Project SIRUB – Sicherheitsrelevante Untersuchungen an Bentonit

Safety-relevant investigations on bentonite

GRS - 854

Gesellschaft für Anlagen-
und Reaktorsicherheit
(GRS) gGmbH

Project SIRUB – Sicherheitsrelevante Untersuchungen an Bentonit

Safety-relevant investigations on bentonite

Michael Kröhn
Klaus-Peter Kröhn
Anke Schneider
Hong Zhao

September 2026

Remark:

This report refers to the in-house research project 02E11880 which has been funded by Federal Ministry for the Environment, Climate Action, Nature Conservation and Nuclear Safety (BMUKN).

The work was conducted by Gesellschaft für Anlagen- und Reaktorsicherheit (GRS) gGmbH.

The authors are responsible for the content of the report.

GRS - 854
ISBN 978-3-911727-47-1

Keywords
bentonite re-saturation, fracture flow, geotechnical barrier, geological repository

Abstract

During research on bentonite re-saturation at GRS, several questions concerning specific aspects have arisen over the years. They could neither be answered immediately nor did they justify a dedicated project. In some cases, a certain effort in classical laboratory work was required. For the majority of questions, however, answers appeared to become attainable only through new technological possibilities. The present report is therefore structured, on the one hand, as a collection of several topics that appear to be linked only by the general theme of bentonite re-saturation. On the other hand, testing and assessment of the new techniques constitute a substantial part of this report. Not only do these techniques require sufficient explanation, but additional tests were also necessary to safeguard the new methods against unforeseen reservations. Consequently, not all topics could be addressed with the originally intended depth. A brief description of the topics and the new measurement techniques is provided below.

Topic 1 concerns a still unexplained detail that has repeatedly been observed in laboratory experiments but is largely ignored by established simulation codes. Re-saturation of compacted and confined bentonite begins with the rapid formation of a narrow, highly saturated zone at the bentonite-water contact, which persists for at least half a year without apparent change. Since the nature of this zone remains largely unknown, Topic 1 was designed to investigate whether different uptake conditions influence the size and development of this zone. For this purpose, non-destructive detection by observation in the visible light spectrum and in short-wave-infrared (SWIR) light was developed. This development required more time than expected, and the results were not always as satisfactory as anticipated. The relationship between greyscale values at the bentonite surface and water content is apparently nonlinear and therefore requires calibration. Such calibration must also account for bentonite density. Interpretation of SWIR-light absorption data by principal component analysis also proved to indicate water content only rather indirectly. Consequently, the narrow, highly water-saturated zone could not be detected reliably with either of the new methods. During the experiment, it was found that water content determination by infrared detection is not possible above a water content of 45 to 60 % for sodium bentonite and above 35 % for powdery calcium bentonite, which may be caused by microstructural changes in the clay particles. At the present state of development, both methods can provide a qualitative impression of a water content distribution. Moreover, in a pre-test, the time required for formation of the narrow saturated zone could convincingly

be determined by the optical method to be less than one minute. By the established gravimetric measurement method, it could be ascertained that the thickness of the narrow zone is limited to 1.5 to 2 mm, irrespective of the density of the bentonite samples, the type of bentonite, or the structure of the material (granular or powdery).

Topic 2 relates to the swelling of compacted bentonite into a limited free space, as may occur in smaller gaps between the bentonite buffer and the host rock or between bentonite pellets in pellet fillings of larger gaps. As observed in several laboratory and in-situ tests, these situations frequently do not result in complete homogenization at the end of re-saturation. A systematic investigation of favourable conditions had therefore been planned. However, the test schedule was substantially affected by the same difficulties encountered in Topic 1. Nevertheless, some insight into the swelling and wetting process could be gained. Effects of gap width on the water uptake rate of the bentonite could be demonstrated. Particularly unexpected and highly remarkable is the resulting notion that the narrow, highly saturated zone investigated in Topic 1 may simply represent a case of incomplete homogenization.

Topic 3 refers to the fact that bentonite is a natural material characterized by different ratios of mono- and divalent cations, with sodium and calcium ions being the most prominent examples. The water uptake behaviour described by isotherms, or by the equivalent retention curves, differs considerably between pure sodium and pure calcium bentonite, so that isotherms need to be determined for each new bentonite. Since the classical procedure required for this task has been laborious in the past and is not free of pitfalls, the possibility of scaling an individual isotherm according to the cation composition was investigated. For 13 samples with known cation characterization, both adsorption and desorption isotherms were measured using a modern Vapour Sorption Analyzer (VSA). The resulting 26 isotherms were scaled using known isotherms for pure sodium and pure calcium bentonite. In 23 of the 26 cases, an excellent to reasonable fit was obtained. However, the remaining three results showed a distinctly poor fit. A reason for these outliers has not yet been identified. Overall, the scaling method nevertheless appears to perform rather well.

Topic 4 addressed the question of the residual bentonite porosity after full saturation by water vapour and by water. For this purpose, two series of long-term uptake tests were performed, running for 1231 and 1232 days, respectively. Each series included confined samples of MX-80 and Calcigel bentonite at four different dry densities. Data from the

uptake phase as well as post-test data were analyzed. The determined uptake rates show no discernible water uptake after 498 days in the case of vapour uptake and after 377 days in the case of water uptake, irrespective of the type of bentonite. As far as can be concluded within the accuracy of the measurements, all 16 samples have therefore reached steady state.

Two phases can be distinguished in the uptake dynamics: a “fast” phase lasting up to 81 and 52 days, respectively, and a subsequent “slow” phase extending until 498 and 377 days, respectively. Since the dynamics of the slow phase cannot be predicted from the evolution during the fast phase, a previously unnoticed or unconsidered process is suspected to be relevant for the later phase, either being present from the beginning or becoming effective at the end of the fast phase. Which process this may be remains to be determined. A relation to the long-term evolution of the narrow, highly saturated zone at the bentonite-water contact cannot be excluded.

The results at full saturation after water uptake were consistent with expectations, yielding a residual porosity of 1 to 3 % and a degree of saturation close to 100 %. By contrast, vapour uptake resulted in rather surprising data. It appears that, in the case of MX-80, more water was taken up from vapour than from water at dry densities above approximately 1.4 g/cm³. This resulted in degrees of saturation exceeding 100 % and negative porosity values. Since such results are non-physical, the data evaluation was scrutinized further, suggesting a higher density of up to 1.2 g/cm³ for hydrated water. A higher density of hydrated water has repeatedly been suggested and rejected in the past. It may therefore be instructive to revisit cases supporting the higher-density hypothesis with regard to the time frame of the related experiments and the form in which water was taken up.

Topic 5 concerns the application of a new technical method for the direct observation of fracture flow using transparent printed fracture replicas. For this application, the complete workflow described in section 2.2 was followed. To address questions concerning the accuracy and reliability of the results, several accompanying tests were performed. These tests confirm a high geometrical fidelity of the results obtained from 3D-scanning and 3D-printing as well as satisfactory repeatability of the test results. Even the results of a percolation test with a micro DFN originally performed at Tohoku University in Japan could be reproduced in the GRS laboratory in Braunschweig. However, a certain uptake of water

by the printed resin was also observed, indicating that care must be taken in longer-lasting hydraulic tests.

The main experiment provided valuable insight into the early phase after closure of a deposition borehole, when water from the depth of the rock returns to a previously dried-out fracture. Two phenomena in particular could be observed. First, in an entirely dried-out fracture, the water did not return as a straight front but instead formed fingers. In some cases, these fingers turned sideways and even backwards while advancing, thereby entrapping larger air bubbles. Second, when such fingers reached the bentonite, suction reduced the pressure in the water to the point at which fingers and narrow water channels were torn apart and the hydraulic connection was interrupted. Interestingly, this did not occur exclusively in the vicinity of the bentonite-water contact, but also close to the injection point. These results imply, on the one hand, a certain reduction in the effective water permeability of a fracture in the vicinity of a borehole due to trapped air bubbles and, on the other hand, self-decelerating water uptake caused by high suction.

Topic 6 is devoted to one of the longest-running in-situ tests in the field of repositories for radioactive waste, the demonstration test Prototype Repository (PR). This test was maintained by the Swedish implementer Svensk Kärnbränslehantering AB (SKB) at the Hard Rock Laboratory Äspö and came to an end during the present project. Within SKB's "Dismantling of the Prototype Repository" project, the opportunity was taken to perform post-test analyses on buffer material that had been exposed to repository-relevant conditions for 20 years. The intention was to investigate the stability of bentonite properties under long-term heating. Using the VSA, adsorption and desorption isotherms were determined for bentonite samples taken from locations close to three of the four heaters of the inner section. These isotherms were compared with isotherms, also determined in this study, for reference material from the production of the buffer blocks. A measurable difference was found between the isotherms of the in-situ bentonite and those of the reference material. Although this difference is probably not of major practical relevance, the results indicate a slightly higher capacity of the in-situ material to buffer water.

Topic 7 covers work on the code COMSOL-VIPER for simulating bentonite re-saturation. Since host rocks suitable for deep geological repositories (DGRs) are characterized by low water permeability, the functionality of the code was extended by including the option of a boundary condition that provides only limited water supply rates (LWSRs) to the

bentonite buffer. The currently one-dimensional implementation of this new option was successfully tested against the results of a corresponding laboratory experiment.

New technique 1 was developed to enable non-destructive and spatially highly resolved observation of the water content in bentonite samples. Two observation methods were tested: one based on visible light and one based on short-wave-infrared (SWIR) light.

The optical method exploits the effect that the colour of bentonite darkens with increasing water content. For practical purposes, a monochrome camera was used to acquire images in which the bentonite colour is translated into shades of grey. This method determines the water content fairly well at an estimated spatial resolution in the range of 100 microns. However, the greyscale distribution over the sample must be scaled to the water content using at least two reference points. In this way, trends in the water content distributions were generally captured, whereas the absolute values were not always consistent with the reference data. Nevertheless, the small fully saturated zone that was the subject of Topic 1 was detected.

Several approaches were tested for detecting the water content by measuring the absorption of SWIR-light. The most cost-effective method was found to be the use of a spectrometer in combination with a moving stage for shifting the sample. This set-up provided data with a spatial resolution of 0.3 mm. The data reflect the absorption characteristics of short-wave-infrared light from the probe and subsequently need to be processed by principal component analysis (PCA). The first principal component (PC1) proved to be the most reliable indicator of the water content, although rather in terms of trends than of absolute values. As with the optical method, the resulting data need to be calibrated using known water contents at at least two different locations. Furthermore, the method is restricted to water contents up to a certain value that depends on the valence of the interlayer cations. Above this critical value, additional quantities, such as the microstructure of the clay particles, apparently become relevant and render the data unusable.

New technique 2 is a fundamentally new procedure that uses 3D-scanning and 3D-printing to produce highly realistic transparent replicas of fractures from crystalline rock. Custom-designed digital test-cell constructions, combined with digital fracture models, enable direct visual observation of hydraulic processes in a fracture. Since the method covers the complete process from acquisition of suitable fracture data by 3D-scanning to evaluation

of the corresponding hydraulic laboratory tests, the workflow is described in detail in section 2.2. Several additional tests were performed to safeguard and further explore different aspects of the developed method based on physical 3D-printed models. These tests are described in the framework of Topic 5.

Zusammenfassung

Im Verlauf der Untersuchungen zur Wiederaufsättigung von kompaktiertem Bentonit bei der GRS sind wiederholt Fragen aufgetreten, die einerseits nicht kurzfristig beantwortet werden konnten, andererseits jedoch kein eigenständiges Projekt rechtfertigten. In einigen Fällen wäre für ihre Bearbeitung ein größerer Aufwand in Form klassischer Laborarbeit erforderlich gewesen. In der Mehrzahl der Fälle rückte eine Beantwortung jedoch erst durch neue technologische Möglichkeiten in Reichweite. Der vorliegende Bericht ist daher zum einen als Sammlung verschiedener Themenkomplexe (Topics) strukturiert, die vordergründig nur durch ihren Bezug zur Wiederaufsättigung von Bentonit miteinander verbunden sind. Zum anderen nimmt das Testen und Überprüfen der neuen Techniken größeren Raum ein, da ihre Arbeitsweisen erläutert und zusätzliche Tests zur Absicherung der Zuverlässigkeit durchgeführt werden mussten, deren Notwendigkeit erst im Verlauf des Projekts deutlich wurde. Aus diesem Grund konnten nicht alle Topics in der ursprünglich geplanten Tiefe untersucht werden. Nachfolgend wird eine Kurzbeschreibung der Topics und der neuen Messverfahren gegeben.

Topic 1 ist mit einem bis heute ungeklärten Phänomen bei der Wiederaufsättigung befasst, das wiederholt in Laborexperimenten beobachtet wurde, von den etablierten Codes zur numerischen Simulation jedoch weitgehend nicht berücksichtigt wird. Die Wiederaufsättigung von kompaktiertem und eingespanntem Bentonit beginnt mit der schnellen Bildung einer schmalen, hoch aufgesättigten Zone am Bentonit-Wasser-Kontakt. Diese Zone bleibt nach ihrer Entstehung für mindestens ein halbes Jahr unverändert. Da nicht geklärt ist, welche Randbedingungen und Materialeigenschaften zu diesem Verhalten führen, wurde in Topic 1 der Einfluss verschiedener Aufsättigungsbedingungen auf Größe und Entwicklung der hochaufgesättigten Zone untersucht. Zu diesem Zweck wurden zerstörungsfreie Beobachtungsmethoden auf Basis sichtbaren Lichts sowie kurzwelligen Infrarotlichts (SWIR) entwickelt. Die technische Entwicklung entsprechender Versuche erforderte mehr Zeit als erwartet, und die Ergebnisse waren weniger zufriedenstellend als erhofft. Die optische Methode, bei der Graustufenwerte in Wassergehalte umgerechnet werden, erfordert aufgrund von Nichtlinearitäten nicht nur eine Kalibrierung als Funktion des Wassergehalts, sondern auch hinsichtlich der Bentonitdichte. Die Interpretation von SWIR-Daten mittels Hauptkomponentenanalyse ergab ebenfalls nur eine schwache Übereinstimmung mit den Referenzkurven aus der etablierten, jedoch zerstörungsbehafteten gravimetrischen Messmethode. Wie sich in den Versuchen zeigte, ist eine Bestimmung

der Wassergehalte über kurzwelliges Infrarotlicht oberhalb von 45 bis 60 % bei Natriumbentonit und oberhalb von 35 % bei pulverförmigem Calciumbentonit vermutlich aufgrund damit einhergehender Mikrostrukturänderungen nicht möglich. Beide neuen Methoden können beim derzeitigen Entwicklungsstand einen groben qualitativen Eindruck der Wassergehaltsverteilung liefern, jedoch keine absoluten Werte. Die hochaufgesättigte Zone konnte daher mit keiner der beiden Methoden verlässlich wiedergegeben werden. In einem Vortest konnte ihre Entstehung jedoch überzeugend beobachtet und die dafür benötigte Zeit mit weniger als einer Minute bestimmt werden. Mit der etablierten gravimetrischen Methode wurde festgestellt, dass die Dicke der hochaufgesättigten Zone auf 1,5 bis 2 mm begrenzt ist, unabhängig von Probendichte, Bentonitart und Materialstruktur (körnig oder pulverförmig).

Topic 2 bezieht sich auf das Quellen von kompaktiertem Bentonit in einen begrenzten freien Raum. Dabei kann es sich einerseits um engere Lücken zwischen Buffer und Wirtsgestein oder andererseits um größere Lücken handeln, die mit Bentonitpellets ausgefüllt werden. In verschiedenen Labor- und In-situ-Experimenten wurde beobachtet, dass solche Randbedingungen am Ende der Wiederaufsättigung zu einer unvollständigen Homogenisierung führen können. Aus diesem Grund sollten in Topic 2 günstige Bedingungen für eine Homogenisierung durch Variation der Versuchsbedingungen identifiziert werden. Aufgrund derselben technischen Schwierigkeiten wie bei Topic 1 wurde der Testplan jedoch stark eingeschränkt. Dennoch konnten bereits aus der Variation der Größe des begrenzten freien Raums wertvolle Erkenntnisse zum Quell- und Befeuchtungsverhalten gewonnen werden. Es konnte gezeigt werden, dass sich die Wasseraufnahmerate des kompaktierten Bentonitkörpers mit zunehmender Größe des freien Raums erhöht. Die stationären Wasserverteilungen zeigten deutlich unterschiedliche Grade der Homogenisierung. Unerwartet und bemerkenswert ist, dass die Verteilungen die Vermutung nahelegen, dass die schmale, hoch aufgesättigte Zone, die Gegenstand der Untersuchungen in Topic 1 ist, einen Spezialfall der Testreihe aus Topic 2 darstellen könnte, nämlich eine unvollständige Homogenisierung bei verschwindendem freien Raum.

Topic 3 befasst sich mit dem Umstand, dass Bentonit ein natürliches Material ist, dessen Tonminerale mono- und divalente Zwischenschichtionen in unterschiedlicher Zusammensetzung aufweisen können. Die wichtigsten Vertreter dieser Kationen sind Natrium und Calcium. Die zugehörigen Isothermen bzw. die äquivalenten Retentionskurven, mit denen das Wasseraufnahmeverhalten der Bentonite charakterisiert wird, unterscheiden sich für

reine Natrium- und Calciumbentonite deutlich. Daher muss die Isotherme für jeden neuen Bentonit mit einem natürlichen Gemisch beider Kationenarten neu bestimmt werden. Da die klassische Methode zur Isothermenbestimmung aufwändig und nicht frei von Schwierigkeiten ist, wurde in Topic 3 untersucht, ob eine individuelle Isotherme auf Grundlage der Isothermen für reine Natrium- und Calciumbentonite anhand der Kationenzusammensetzung skaliert werden kann. Zu diesem Zweck wurden Adsorptions- und Desorptionsisothermen für 13 Bentonitproben mit bekannter Kationenzusammensetzung mithilfe eines im Wesentlichen automatisch arbeitenden Vapour Sorption Analyzer (VSA) bestimmt. Die daraus resultierenden 26 Isothermen wurden anschließend mit skalierten Isothermen verglichen. Für 23 der 26 Isothermen wurde eine hervorragende bis angemessene Übereinstimmung erzielt. Bei den drei übrigen Proben war die Übereinstimmung dagegen sehr schlecht. Eine Ursache hierfür konnte nicht identifiziert werden. Insgesamt liefert die Skalierungsmethode jedoch gute Ergebnisse.

Topic 4 widmet sich der Frage nach der Restporosität nach vollständiger Aufsättigung des Bentonits durch Wasserdampf und Wasser. Zu diesem Zweck wurden zwei Testreihen mit jeweils acht Proben und Laufzeiten von 1231 bzw. 1232 Tagen durchgeführt. Jede Testreihe umfasste MX-80- und Calcigel-Proben mit vier unterschiedlichen Trockendichten. Die berechneten Wasseraufnahmeraten zeigen sowohl für MX-80 als auch für Calcigel im Fall der Aufnahme über Dampf nach 498 Tagen und bei Aufnahme über Wasser nach 377 Tagen keine messbare Wasseraufnahme mehr. Im Rahmen der Messgenauigkeit wurde daher bei allen 16 Proben ein stationärer Zustand erreicht.

Die Wasseraufnahme erfolgte in zwei Phasen: einer „schnellen“ Phase mit einer Dauer von 81 bzw. 52 Tagen und einer anschließenden „langsamen“ Phase, die bis zum Ende der Aufsättigung nach 377 bzw. 498 Tagen andauerte. Da die Aufsättigungsdynamik der langsamen Phase nicht aus der Beobachtung der schnellen Phase abgeleitet werden kann, liegt der Verdacht nahe, dass ein bisher nicht bemerkter oder berücksichtigter Prozess für die spätere langsame Phase relevant ist. Dieser Prozess ist entweder von Beginn an wirksam oder setzt erst mit Beginn der langsamen Phase ein. Welcher Vorgang hierfür verantwortlich ist, bleibt offen. Eine Verbindung zur Langzeitentwicklung der schmalen, hochaufgesättigten Zone am Bentonit-Wasser-Kontakt kann nicht ausgeschlossen werden.

Die Ergebnisse zum Zustand des Bentonits nach vollständiger Aufsättigung stimmen mit den Erwartungen überein, nämlich mit einer Restporosität von 1 bis 3 % und einem Sättigungsgrad nahe 100 %. Die Ergebnisse für die Aufsättigung über Wasserdampf waren dagegen unerwartet. Danach nahm der Natriumbentonit MX-80 bei einer Trockendichte über 1,4 g/cm³ über Wasserdampf deutlich mehr Wasser auf als über flüssiges Wasser. Daraus resultierten Sättigungsgrade von über 100 % und negative Porositäten. Da solche Ergebnisse unphysikalisch sind, wurde die Datenauswertung genauer analysiert. Plausible Ergebnisse ergeben sich danach nur, wenn für die Dichte des hydratisierten Wassers Werte bis zu 1,2 g/cm³ angenommen werden. Vermutungen in diese Richtung wurden in der Vergangenheit wiederholt aufgestellt und verworfen. Eine genauere Untersuchung der Versuche, die die Hypothese einer erhöhten Wasserdichte stützen, könnte mit Blick auf den zeitlichen Ablauf der Experimente und die Art der Wasseraufnahme aufschlussreich sein.

Topic 5 stellt einen Anwendungsfall für die neue Methode 2 (s.u.) dar, mit der eine direkte Beobachtung hydraulischer Prozesse in einer transparenten, 3D-gedruckten Kluftnachbildung ermöglicht wird. Dabei wird der vollständige, in Abschnitt 2.2 beschriebene Arbeitsablauf angewendet. Zusätzlich wurden weitere Tests durchgeführt, um die neue Methode der 3D-gedruckten physikalischen Modelle abzusichern. Diese Tests zeigen eine hohe geometrische Abbildungstreue und eine zufriedenstellende Wiederholgenauigkeit der hydraulischen Versuche. Sogar ein Durchströmungsversuch an einem Mikro-DFN, der ursprünglich an der Tohoku University in Japan durchgeführt wurde, konnte auf Grundlage der originalen Konstruktionsdaten im GRS-Labor in Braunschweig reproduziert werden. Allerdings wurde auch eine gewisse Wasseraufnahme durch das gedruckte Kunstharz beobachtet, die bei länger andauernden hydraulischen Tests besondere Vorsicht und Sorgfalt erforderlich macht.

Das Hauptexperiment lieferte wertvolle Einsichten in die frühe Phase der Wasserbewegung unmittelbar nach dem Verschluss eines Einlagerungsbohrlochs. Zwei Phänomene sind dabei bemerkenswert. Erstens kehrte das Wasser in einer durch Ventilation vollständig ausgetrockneten Kluft nicht als gerade Front zurück, sondern bildete vorauseilende Finger. Diese Finger bewegten sich nicht zwingend geradlinig von der Injektionsstelle weg, sondern bogen seitlich ab oder kehrten die Fortschrittsrichtung sogar vollständig um, wodurch größere Luftblasen eingeschlossen wurden. Zweitens senkte die Saugspannung, sobald ein Finger den Bentonit erreichte, den hydraulischen Druck im Wasser so

weit ab, dass Finger und Brücken zwischen größeren Wasserkörpern auseinandergezogen und die hydraulischen Verbindungen unterbrochen wurden. Interessanterweise geschah dies nicht nur in unmittelbarer Nähe des Kluftwassers zum Bentonit, sondern auch in der Nähe des Injektionspunkts.

Die Beobachtungen implizieren zum einen, dass die effektive Wasserpermeabilität in einer sich wieder mit Wasser auffüllenden Kluft in der Umgebung eines Einlagerungsbohrlochs geringer ist als in der ungestörten Kluft. Zum anderen zeigt sich ein selbstbegrenzender Effekt hoher Saugspannungen auf die Wasseraufnahme.

Topic 6 ist einem der längsten In-situ-Tests im Bereich der Endlagerung radioaktiver Abfallstoffe gewidmet, dem Demonstrationsversuch Prototype Repository (PR). Der Versuch wurde vom schwedischen Betreiber Swedish Kärnbrenslehantering AB (SKB) im Hard Rock Laboratory Äspö durchgeführt und während der Projektlaufzeit beendet. Auf Einladung von SKB wurde die Gelegenheit genutzt, Post-test-Analysen an Buffermaterial durchzuführen, das 20 Jahre lang endlagerrelevanten Bedingungen ausgesetzt war. Ziel war es, den Einfluss der Langzeiterhitzung auf das Wasseraufnahmeverhalten zu untersuchen. Zu diesem Zweck wurden mithilfe des VSA Adsorptions- und Desorptionsisothermen von Proben aus unmittelbarer Nähe zu drei der vier Erhitzer aus der Inner Section bestimmt. Diese Isothermen wurden mit ebenfalls gemessenen Isothermen von Referenzmaterial aus der Produktion der kompaktierten Bentonitblöcke für das PR verglichen. Ein Unterschied zwischen den Isothermen des In-situ-Materials und des Referenzmaterials konnte festgestellt werden. Auch wenn dieser Unterschied wahrscheinlich nicht von größerer praktischer Relevanz ist, deuten die Ergebnisse auf eine etwas höhere Speicherkapazität des In-situ-Materials für Wasser hin, durch die sowohl bei Befeuchtung als auch bei Austrocknung mehr Wasser gebunden wird.

Topic 7 betrifft eine Erweiterung der Funktionalität des Codes VIPER-COMSOL zur numerischen Modellierung der Bentonitaufsättigung. Dazu wurde eine Option für eine spezielle Randbedingung implementiert, mit der ein begrenzter Wasserzufluss berücksichtigt wird. Dieser Fall ist insbesondere für Wirtsgesteine tiefer geologischer Endlager (DGRs) relevant, die anforderungsgemäß eine niedrige Wasserpermeabilität aufweisen sollen. Die bislang nur eindimensional realisierte Implementierung wurde erfolgreich anhand eines entsprechenden Laborversuchs überprüft.

Neue Technik 1 wurde entwickelt, um den Wassergehalt in Bentonitproben zerstörungsfrei und räumlich hochaufgelöst zu bestimmen. Zwei Methoden wurden getestet: eine auf Basis sichtbaren Lichts und eine auf Basis kurzwelligen Infrarotlichts.

Die optische Methode nutzt den Effekt, dass sich die Farbe des Bentonits mit zunehmendem Wassergehalt verdunkelt. Zu diesem Zweck wurde eine Graustufenkamera eingesetzt, mit der die Färbung des Bentonits in Grauwerten erfasst wird. Mit dieser Methode kann der Wassergehalt bei einer räumlichen Auflösung im Bereich von 100 Mikrometern vergleichsweise gut bestimmt werden. Allerdings müssen die Graustufenverteilungen an mindestens zwei Punkten skaliert werden, um Wassergehalte abzubilden. Dadurch konnten Trends im Verlauf des Wassergehalts erkannt werden, während die absoluten Werte nicht immer mit den Referenzwerten übereinstimmten. Dennoch wurde die vollständig aufgesättigte Zone, die Gegenstand von Topic 1 ist, detektiert.

Mehrere Techniken zur Detektion des Wassergehalts mithilfe von infrarotem Licht wurden geprüft. Dabei erwies sich die Methode mit einer räumlich fixierten Spektrometersonde und einem darunter angeordneten Verfahrtisch für die Probe als praktikabel und kostengünstig. Dieser Aufbau lieferte Daten mit einer räumlichen Auflösung von 0,3 mm. Die Daten geben Auskunft über die Absorption des von der Sonde ausgestrahlten kurzwelligen Infrarotlichts und müssen nach der Messung einer Hauptkomponentenanalyse unterzogen werden. Die dabei ermittelte erste Hauptkomponente erwies sich als zuverlässiger Indikator für den Wassergehalt, wobei jedoch eher Trends in der Wassergehaltsverteilung als absolute Werte wiedergegeben wurden. Da die erste Hauptkomponente dimensionslos ist, muss der Kurvenverlauf außerdem, wie bei der optischen Methode, anhand von mindestens zwei Datenpunkten für den Wassergehalt kalibriert werden. Die Infrarotmessung ist dabei auf einen Wassergehaltsbereich begrenzt, der von der Valenz der Zwischenschichtionen abhängt. Oberhalb des kritischen Wassergehalts werden die Ergebnisse anscheinend durch weitere Größen, beispielsweise eine sich ändernde Mikrostruktur der Tonpartikel, beeinflusst, wodurch eine direkte Bestimmung des Wassergehalts unmöglich wird.

Neue Technik 2 ist ein neues Verfahren, mit dem die technischen Möglichkeiten des 3D-Scannens und des 3D-Drucks genutzt werden, um realitätsnahe, transparente Nachbildungen von Klüften in Kristallingestein zu erzeugen. Spezielle digitale Konstruktionen für eine Testzelle ermöglichen, in Kombination mit digitalen Kluftmodellen, die direkte

Beobachtung hydraulischer Prozesse in einer Kluft im Experiment. Dabei wird der gesamte Arbeitsablauf von der Akquisition geeigneter Kluftdaten durch hochauflösende 3D-Scans bis zur Auswertung der daraus hervorgehenden hydraulischen Tests abgedeckt. Der Ablauf wird in Abschnitt 2.2 detailliert beschrieben. Zusätzliche Tests zur Absicherung der Genauigkeit und Wiederholbarkeit der Ergebnisse werden im Rahmen von Topic 5 beschrieben.

Acknowledgements

The research work presented in this report was funded by the Federal Ministry for the Environment, Climate Action, Nature Conservation and Nuclear Safety (BMUKN) under contract number 02E11880.

Particular thanks are due to numerous national and international colleagues who contributed in various ways to substantial progress in the present project. During the preparatory work for Topics 1 and 2, Martin Labus (Laser 2000 GmbH) provided invaluable support in identifying an approach for non-destructive measurement of the water content of compacted bentonite by means of SWIR-techniques. Stephan Kaufhold and Reiner Dohrmann (Bundesanstalt für Geowissenschaften und Rohstoffe (BGR)) provided the 13 bentonite samples for Topic 3, including the characterisation data, in a highly collegial manner. Their support in the search for explanations for poor results is also gratefully acknowledged. With regard to Topic 5, the discussions on fractures and their mechanical and hydrochemical history with Masahiro Uchida (Fracture Flow Solutions, Japan) were highly valuable; his long-standing experience with fractured rock was generously shared, particularly during the identification of suitable field fractures for testing. We are also much obliged to Martin Stigsson (Svensk Kärnbränslehantering AB (SKB), Sweden) for his energetic commitment to enabling the scanning of relevant fractures from the HRL Äspö and from Forsmark. The collaboration has been a pleasure. This also applies to Artu Miettinen and Joni Tanttu (University of Jyväskylä, Finland), who opened up ways to characterize rock samples relevant for Olkiluoto by combining 3D-scanning and CT-measurements. Kaisa Nikkilä (Geologian tutkimuskeskus (GTK, Geological Survey of Finland)) is also thanked for openly providing some of the samples for transport to Germany. The intricate postprocessing of 3D-scan data from the scanning campaigns would not have been possible without the many helpful discussions with and suggestions by Magnus Hund (Hexagon AB). The exchange with Anna Suzuki (Tohoku University, Japan) on a printable micro-DFN, as well as the subsequent invitation to the ICFD 2023 conference in Sendai, was highly valuable. Furthermore, gratitude is expressed to Wei Hsin-Tien (TaiwanTech, Taiwan) for extending his focus and expertise in particle tracking methods to the development of a measurement approach for 3D flow fields in fractures. Thanks are also due to the members of the Task Force on Groundwater Flow and Transport of Solutes for the many discussions and helpful suggestions concerning the new technique for producing transparent fracture replicas for laboratory testing. Particular gratitude is expressed for the group's

willingness to share fracture data from all over the world even before this project had begun.

The involvement of all contributors is gratefully acknowledged.

Table of Contents

Abstract ..... **I**

Zusammenfassung ..... **VII**

1 Introduction **1**

1.1 Background to bentonite re-saturation 1

1.2 Innovative techniques 3

1.2.1 Technique (A): Non-destructive measurement of the water content 3

1.2.2 Technique (B): Visual observation of hydraulic processes in fractures 4

1.3 Topic 1 – Small saturated zone at the water-bentonite contact 5

1.4 Topic 2 – Free swelling into limited space 6

1.5 Topic 3 – Scaling isotherms by bentonite types and clay content 9

1.6 Topic 4 – Porosity at full saturation 10

1.7 Topic 5 – Initial flow dynamics at the bentonite-rock contact 11

1.8 Topic 6 – Stability of bentonite properties against long-term heating 12

1.9 Topic 7 – Extending the functionality of code COMSOL-VIPER 13

2 Preparatory work for innovative techniques **15**

2.1 Non-destructive measurement of the water content of bentonite 15

2.1.1 Observation by visible light 15

2.1.2 Observation by IR light – finding appropriate equipment 17

2.1.3 Observation by IR light – pretesting and method development 19

2.2 Visual observation of hydraulic processes in fractures 23

2.2.1 Sample acquisition 24

2.2.2 3D-scanning 27

2.2.3 Digital post-processing and test cell construction 32

2.2.4 3D-printing of a test cell including the replicated fracture 35

2.2.5 Performing hydraulic tests including imaging 39

2.2.6 Post-processing of the image data 44

3 Topic 1 – Small saturated zone at the water-bentonite contact **47**

3.1 Pre-test 47

3.2 Test set-up 49

3.3 Test procedure 49

3.4 Materials 52

3.5 Evaluation of data 52

3.6 Measurement results 53

3.6.1 Granular MX-80 53

3.6.2 Powdery MX-80 57

3.6.3 Powdery Calcigel 60

3.6.4 Features in the gravimetric data 65

3.6.5 Features in the PC1 data 66
3.6.6 Features in the greyscale data 67

3.7 Interpretation of the results 69
3.7.1 General conclusions 69
3.7.2 Results specifically from the greyscale method 69
3.7.3 Results specifically from the spectrometer measurements 71

4 Topic 2 – Free swelling into limited space 73

4.1 Test set-up 73

4.2 Test procedure 74

4.3 Materials 75

4.4 Measurement results 75

4.5 Interpretation of the results 88

5 Topic 3 – Scaling isotherms by bentonite types and clay content ... 91

5.1 Experimental methods 91
5.1.1 Classic experimental set-up 91
5.1.2 Present experimental set-up 91
5.1.3 Determining isotherms 92

5.2 Materials 98

5.3 Comparing predictions and measurements 99
5.3.1 Procedure of comparison 99
5.3.2 Results 100

6 Topic 4 – Porosity at full saturation 103

6.1 Test I: Water uptake via vapour 104

6.2 Test II: Water uptake via liquid water 107

6.3 Comparison and interpretation of the results from Tests I and II 109
6.3.1 State of the samples in Test I at the end of the test 109
6.3.2 State of the samples in Test II at the end of the test 111
6.3.3 Compilation and comparison of characteristic quantities 113
6.3.4 Interpretation and conclusions 116

6.4 Test III: Water uptake via vapour 119

7 Topic 5 – Initial flow dynamics at the bentonite-rock contact 123

7.1 Accompanying tests 123
7.1.1 Long-term water uptake of the printing material 123
7.1.2 Accuracy of printed planar surfaces 131
7.1.3 Deformation of printed bodys due to water uptake 132
7.1.4 Post-processing induced deformation of printed fracture replicas 134
7.1.5 Repeatability of a wetting test 138
7.1.6 Wetting patterns depending on flow direction 140
7.1.7 Repeatability of a percolation test on a DFN 141
7.1.8 Combining optical 3D-scans with CT images 144

7.2 Main experiment 147

7.2.1 Experimental methods 147
7.2.2 Test procedure 149
7.2.3 Fluid materials 150
7.2.4 Results and interpretation 151

8 Topic 6 – Impact of long-term heating on bentonite properties 159
8.1 The Prototype Repository experiment 159
8.2 Objective 160
8.3 Materials 161
8.4 Temperature and humidity history 162
8.4.1 Background 162
8.4.2 Temperature 164
8.4.3 Relative humidity / water content 167
8.4.4 Essentials 170
8.5 Experimental method 171
8.6 Measurement results 171
8.7 Interpretation of the results 173

9 Topic 7 – Extending the functionality of code VIPER 175

10 Assessment of the new measurement techniques 179
10.1 Technique (A): Non-destructive measurement of the water content 179
10.1.1 Classic gravimetric measurement 179
10.1.2 Visual observation with an optical camera 180
10.1.3 Absorption of SWIR-light 181
10.2 Technique (B): Visual observation of hydraulic processes in fractures . 182
10.2.1 Digital fracture models by high resolution 3D-scanning 183
10.2.2 Producing fracture replicas by additive manufacturing 183
10.2.3 Repeatability of hydraulic tests 183

11 Modelling of special groundwater flow and transport problems ... 185
11.1 Model Development and Validation of the Free Surface and Storage Term Using Analytical and Numerical Benchmarks 185
11.1.1 Introduction 185
11.1.2 Model concept and parameters 188
11.1.3 Evaluation of the results 190
11.2 Modelling radionuclide transport in fractured rock 197
11.2.1 Background 197
11.2.2 The tracer test C2 198
11.2.3 Hydrostructural model and hydraulic properties 200
11.2.4 Hydraulic boundary conditions 203
11.2.5 Primary results 204
11.2.6 Optimization of parameters with inverse modelling 208
11.2.7 Conclusion 211
11.3 Colloid-facilitated contaminant transport 212
11.3.1 Colloid transport 213

11.3.2 Colloid facilitated solute transport 213
11.3.3 Application of the model to a block experiment 216

12 Summary, conclusions, and recommendations 227
12.1 Topic 1 – Small saturated zone at the water-bentonite contact 227
12.2 Topic 2 – Free swelling into limited space 229
12.3 Topic 3 – Scaling isotherms by bentonite types and clay content 231
12.4 Topic 4 – Porosity at full saturation 232
12.4.1 General comment 232
12.4.2 End porosity 232
12.4.3 Water uptake dynamics 233
12.4.4 Swelling of single bentonite pellets 234
12.5 Topic 5 – Initial flow dynamics at the bentonite-rock contact 234
12.5.1 Accompanying tests 234
12.5.2 Main tests 238
12.6 Topic 6 – Stability of bentonite properties against long-term heating 239
12.7 Topic 7 – Extending the functionality of code COMSOL-VIPER 240

References 243

Table of figures 257

List of tables 273

A Appendix: Equations of the quantities of interest for Topic 4 275

B Appendix: Graphical comparison for Topic 3 277

1 Introduction

1.1 Background to bentonite re-saturation

A prominent twofold hazard to the safety of a deep geological repository (DGR) for radioactive waste is posed by water present in the host rock. In contact with waste canisters, it causes corrosion, which may subsequently lead to canister failure and thereby to a release of radionuclides into the geosphere and biosphere.

As part of a multi-barrier protection concept, essentially all worldwide designs for DGRs in crystalline rock or claystone rely on compacted bentonite as a geotechnical barrier. Owing to its specific properties, this material appears well suited for this purpose. Upon water uptake, the bentonite either expands into the available surrounding free space or, under fully confined conditions, increases in density and thereby strongly reduces hydraulic permeability. This response to water impedes water flow towards the canister and thereby reduces both canister corrosion and possible spreading of radionuclides by advective flow away from the canister.

The bentonite buffer around waste canisters is envisaged to be installed in a pre-compacted and air-dry state. Because it is only partially saturated with water, groundwater is drawn into the bentonite, thereby initiating the re-saturation process. The water is hydrated in the interlamellar space of the clay minerals, causing the minerals to expand. Macroscopically, this either causes the clay to swell into any remaining free space or, under fully confined conditions, to expand at the expense of the pore space. The initially entering water is therefore buffered in the clay, while further water inflow is increasingly impeded.

At full saturation, water eventually migrates very slowly through the bentonite because of its low permeability and only in very small quantities because of its low porosity. Long-term in-situ experiments such as the FEBEX at the Grimsel Test Site /KOB 21/ or the recently concluded Prototype Repository at Äspö, e.g. /ÅKE 22/, suggest a time span on the order of decades before full bentonite saturation is reached.

The re-saturation dynamics and the state of the fully saturated bentonite are therefore important bentonite characteristics that define the achievable degree of canister protection provided by buffer and backfill. Direct observation and investigation of the re-saturation

process in the laboratory are, however, precluded by the long time frames involved. Prediction of the performance of a bentonite barrier, particularly during re-saturation, is therefore possible only by means of numerical modelling. Under these circumstances, a sound understanding of the processes involved must be acquired to ensure reliable results from predictive models.

The relatively simple phenomenological description given above obscures the fact that bentonite behaviour during re-saturation is complex and can be influenced by thermal, hydraulic, mechanical, chemical and biological (THMCB) processes. Numerical THM-models have been established for some time to simulate bentonite re-saturation. However, an early review of the conceptual models underlying several THM-codes /KRÖ 04a/ indicated inconsistencies between model assumptions concerning hydraulics and some phenomena at the microstructural level (see also /KRÖ 03a/, KRÖ 03b/, /KRÖ 04c/).

To avoid these inconsistencies, an alternative conceptual model based on vapour diffusion in compacted and fully confined bentonite was developed /KRÖ 04b/. Although the model was initially rather simple, early codes based on this concept were already able to reproduce many results obtained with established THM-models. Comparable problems were calculated much faster, while being based essentially on parameters and relations from textbooks. Since then, the alternative concept has been advanced and refined into the non-isothermal extended vapour diffusion (EVD) model. This model was implemented in the experimental code VIPER (**V**apour transport **I**n **P**artially saturated bentonite as **E**ngineered barrier for **R**epositories) /KRÖ 11/, which allows bentonite re-saturation under repository-like conditions to be simulated.

To bypass restrictions of the code VIPER with respect to dimensionality and to enable full coupling to a simultaneous thermal simulation, transfer of the concept underlying VIPER to COMSOL Multiphysics /COM 26/ was initiated /KRÖ 20a/. This work has resulted in the ongoing development of the new user-written module COMSOL-VIPER /KRÖ 25/.

On the way from the conceptual model to the code VIPER, some open questions remained. Although these questions are not essential for the applicability of the approach in general, they indicate gaps in process understanding and may prove relevant for future extensions of the range of application. These open questions refer to different aspects of bentonite re-saturation. The present report is therefore divided into largely independent

chapters, each addressing one topic. A specific introduction to each topic is provided in the following sections. Before the topics are introduced, however, the new techniques developed and applied in the present project are presented.

1.2 Innovative techniques

During planning of the present project, it had become apparent that substantial benefit could be gained from the innovative application of new technology. Consequently, testing devices and the development of new methodologies became integral, time-consuming components of the project. In principle, two challenges were addressed:

- Technique (A): Non-destructive measurement of the water content of bentonite
- Technique (B): Visual observation of hydraulic processes in fractures of crystalline rock

1.2.1 Technique (A): Non-destructive measurement of the water content

For Technique (A), two different approaches were pursued: observation by visible light and observation by short-wave infrared (SWIR) light. Observation by visible light was motivated by results from the in-situ Buffer-Rock-Interaction Experiment (BRIE) conducted by Svensk Kärnbränslehantering (SKB) at the Hard Rock Laboratory Äspö (HRL) /FRA 17/. In two vertical cylindrical boreholes, with a length of about 3 m and a diameter of 30 cm, closely fitting bodies of compacted bentonite had been installed and thereby brought into contact with the fractured rock for more than one year. After dismantling of the experiment, the surfaces of the bentonite cylinders showed dark grey patterns corresponding to the water-bearing fractures that had been in contact with the bentonite (see Fig. 1.1). Extensive post-test investigations indicated a relation between water content and grey scale value /LAN 15/. This was partly confirmed by a more elaborate analysis of the spontaneously taken photographs obtained during dismantling. However, these photographs were not sufficient for a systematic matching of grey scale and water content /DES 17/. Such matching was intended for Topics 1 and 2 within the present project.

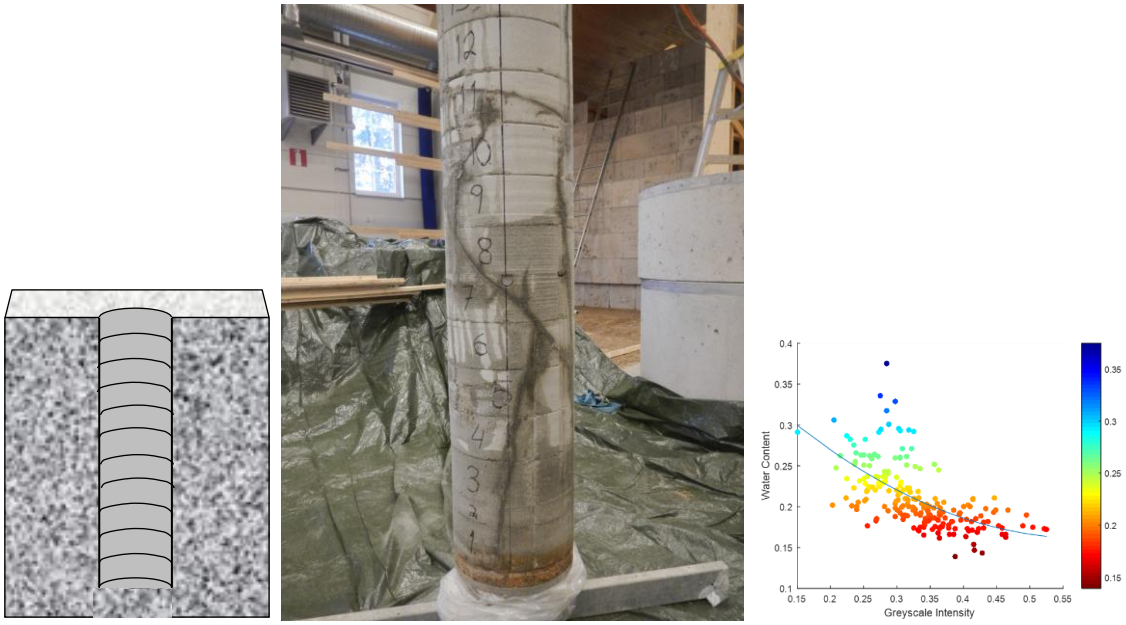


Fig. 1.1 From project BRIE - left: sketch of empty borehole; middle: photograph of the retrieved bentonite column (from /FRA 17/; right: relation of greyscale and water content (from /LAN 15/)

Alternatively, the water content was investigated by analyzing the absorption of SWIR-light. The concept was based on the fact that water absorbs IR-light in the Short Wave InfraRed (SWIR) range at about 1450 nm and 1930 nm, with stronger absorption expected at 1450 nm. This phenomenon allows the presence of water to be detected by strong damping of the reflected IR-light in the vicinity of these wavelengths.

Several different devices and techniques were tested because the method generally did not meet expectations or required equipment exceeding the project budget. Ultimately, the use of a spectrometer was selected.

1.2.2 Technique (B): Visual observation of hydraulic processes in fractures

Because direct visual observation of hydraulic processes in natural rock fractures is not possible, an experimental approach based on 3D-scanning and 3D-printing of natural granitic fracture surfaces was developed. High-resolution surface scans of natural fractures were obtained, and the resulting digital model was further supplemented with features required to produce a functional test cell. This cell was then fabricated by additive manufacturing using a clear resin, thereby enabling optical monitoring. Hydraulic processes

such as wetting or drying of a fracture or tracer transport can be recorded by rapidly acquiring images with an industrial-grade optical camera, which allows animated representation. Image analysis was performed using threshold-based segmentation to generate binary maps at a spatial resolution of approximately 35 × 35 µm. To demonstrate the viability of this methodology, preparatory tests were performed, as described in more detail in chapter 7.

1.3 Topic 1 – Small saturated zone at the water-bentonite contact

To date, many laboratory experiments have been performed on bentonite re-saturation, but little attention has been paid to the state of the bentonite in the vicinity of the water-bentonite contact. Where this aspect has been considered, a rapidly forming narrow zone of highly saturated bentonite (saturated zone SZ) has been observed /KRÖ 04a/, /HAR 15/. Under conditions of unlimited water supply, the SZ is established within minutes. Subsequently, however, it remains stable for a long time, at least for 180 days according to the uptake tests. An illustration of this observation, also relating it to an envisaged storage concept with vertical deposition boreholes, is shown in Fig. 1.2.

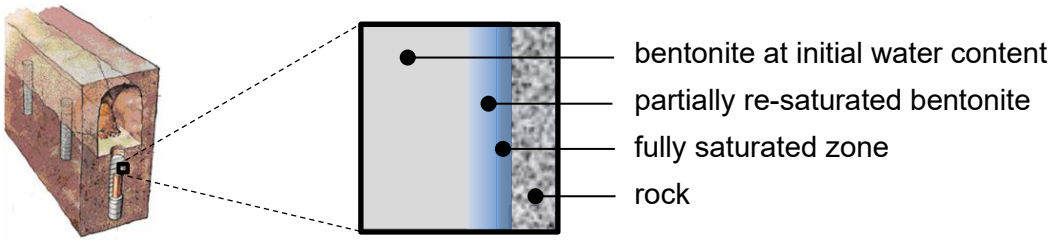


Fig. 1.2 Sketch of a tunnel with deposition boreholes and a close-up of the re-saturating bentonite-rock contact

Although the initial formation of the SZ can readily be explained by water uptake driven by capillary forces, the reason for its subsequent long-lasting and unchanged existence remains unclear. The SZ is not reproduced by the established THM-models. In the EVD-concept, it is deliberately omitted. To obtain further insight into the properties of the SZ, particularly its thickness, uptake tests were performed with MX-80 and Calcigel bentonite at varying dry densities.

1.4 Topic 2 – Free swelling into limited space

After installation, a free space naturally remains between the precompacted blocks of a bentonite buffer and the rock or waste canister, because the buffer cannot fit perfectly into a deposition hole. The remaining gap may have a width of up to several centimetres.

At such dimensions, the open slot is to be filled with bentonite pellets or powder. In a pellet cluster, however, the solid individual pellet bodies leave comparatively large spaces between the pellets. This situation is illustrated in Fig. 1.3.

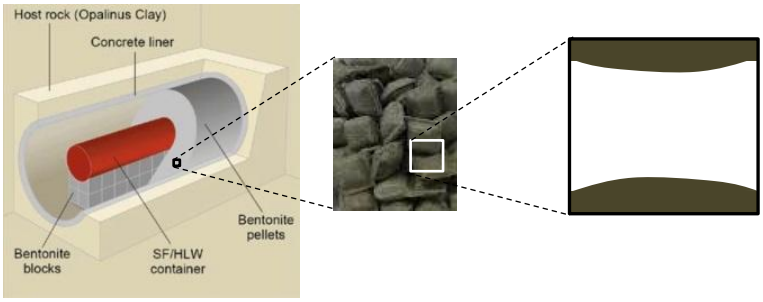


Fig. 1.3 Illustration of the principle of initial swelling of pellets into a limited free space

Finally, gaps between the bentonite blocks may also form free space. According to the construction requirements in the Swedish repository design, however, gaps between bentonite blocks will not exceed a width of 5 mm /ERI 25/.

In all three cases, upon water inflow, the bentonite initially swells freely into a limited space until it reaches more or less firm mechanical barriers against further swelling. Such barriers may be the surrounding rock, the enclosed waste canister, or opposing and likewise swelling bentonite structures. However, complete homogenization may not be achieved, as shown in a technical-scale experiment with a central bentonite core and surrounding pellets /PIN 13/ (cf. Fig. 1.4). The same is indicated by a lab-scale pilot test with MX-80 pellets confined in an acrylic tube /KRÖ 22/ (cf. Fig. 1.5).



Fig. 1.4 Pictures from the TRANSU test; from /PIN 13/; left: experimental set-up, top middle: cross-section before wetting; bottom middle: cross-section after the test; right: close-up of bottom middle

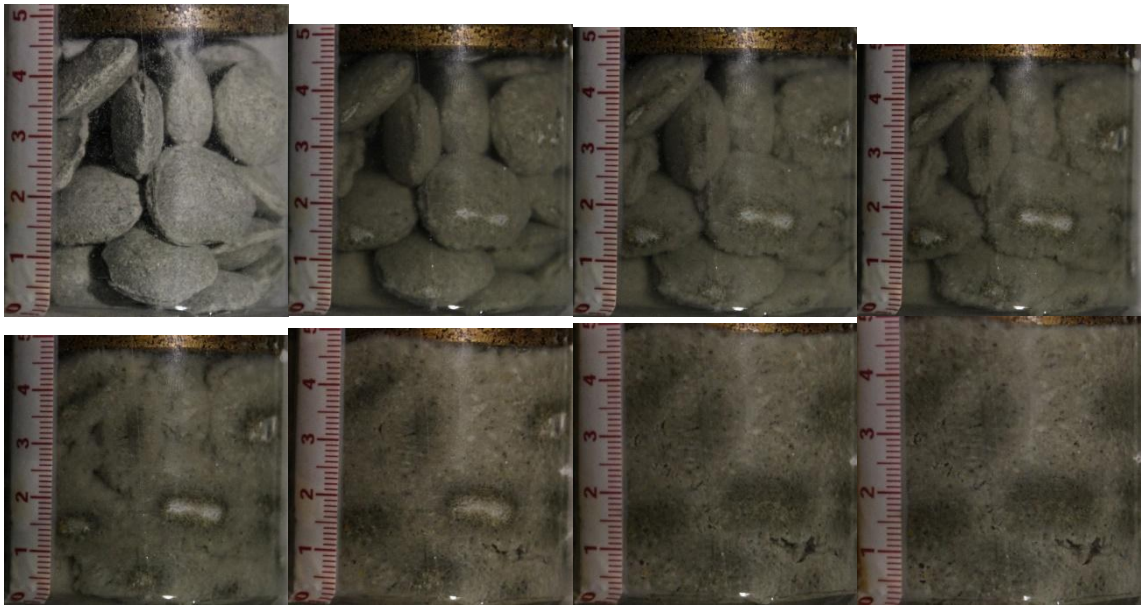


Fig. 1.5 Water uptake by a cluster of MX-80 pellets in an acrylic glass tube;
1. Row: after 0, 1, 10, and 20 min;
2. Row: after 80 and 320 min and after 24, and 74 h; from /KRÖ 22/

The related main test had been set up similarly but in a steel cell /KRÖ 22/. It was not dismantled and therefore ran for almost five and a half years, until the results appeared to be of interest for Topic 1. Despite the long wetting time, the sample was apparently still only partially homogenized, as shown by the left photograph in Fig. 1.6, which was taken

directly after the sample had been pushed out of the cylinder. The photograph on the right-hand side shows the sample after it had been cut along the axis with a scraper, confirming the visual impression of incomplete homogenization from the surface. A remarkable feature of the final sample state should also be noted. A volume suspected to contain approximately the space of a pellet and the attributable free space around it could easily be separated manually from the sample (see Fig. 1.7).

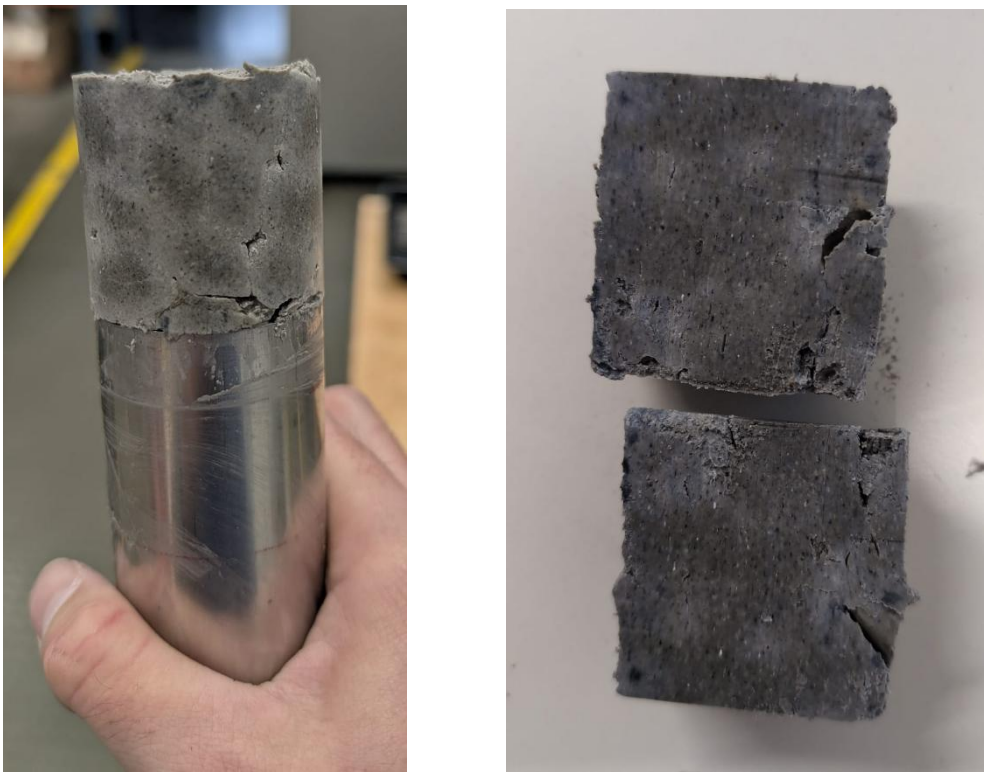


Fig. 1.6 A cluster of MX-80 pellets after long-term wetting in a steel cylinder



Fig. 1.7 Partially homogenized volume of a single pellet manually separated from the sample

The conditions required for full homogenization are currently not known. Further insight was expected from observing swelling into a limited free space while varying the size of this space and the dry density.

1.5 Topic 3 – Scaling isotherms by bentonite types and clay content

Since roughly the early 1990s, thermo-hydraulic-mechanically coupled models have been established to predict the re-saturation process of bentonite, e.g. /STE 01/. Such models depend strongly on a constitutive relation between water content and relative humidity, referred to as an “isotherm”, or, respectively, between suction and water saturation, referred to as a “retention curve”. This relation has therefore repeatedly been determined in the past, e.g. /MOO 52/, /KAH 86/, /GAI 05/, /KRÖ 20b/, and is now used as a basis for numerical modelling.

Characterisation of a specific bentonite with respect to isotherms is therefore a prerequisite for predicting buffer performance by numerical modelling. Since bentonite is a natural product with varying types and contents of minerals, however, the shape of adsorption isotherms varies among individual specimen[1]. Classically, an adsorption isotherm is determined pointwise, e.g. /DUE 04/. This procedure is laborious and time-consuming, but for a long time represented the only available approach for establishing an isotherm. It was therefore hypothesized that the shape of any isotherm could be derived as the weighted sum of isotherms for pure sodium and pure calcium montmorillonite, taking into account the ratio of mono- and divalent cations as well as the smectite content of the bentonite under consideration.

While a laboratory programme to test this concept using classical methods would have been prohibitively expensive, a related investigation became feasible through the use of a comparatively new measurement device. The concept of scaling isotherms was therefore

[1] At that, it is well-known that the shape of the isotherms depends strongly on the interlayer cations. They are decidedly different for Na^{+}- and Ca^{2+}-cations, e.g. /KAH 86/, /KRÖ 20b/, which is a consequence of the different ion charge. In natural clays, however, monovalent and divalent cations can be found at any ratio. Rather obviously, also the smectite content of a bentonite has an impact on the isotherm /KRÖ 11/.

tested using a well-documented set of 13 natural bentonites, e.g. /KAU 12/, provided by the Federal Institute for Geosciences and Natural Resources (BGR). The present work includes the measurement of a complete hysteresis loop consisting of adsorption and desorption isotherms.

1.6 Topic 4 – Porosity at full saturation

Topic 4 addresses the remaining bentonite porosity Φ_v after full saturation by water vapour has been reached. In the EVD-model, this parameter has been freely selectable, with its value constrained only by experience from earlier modelling work. No dedicated test concerning this parameter is known. To reduce the already small number of possible fitting parameters, Topic 4 was initially intended to quantify this parameter by laboratory tests.

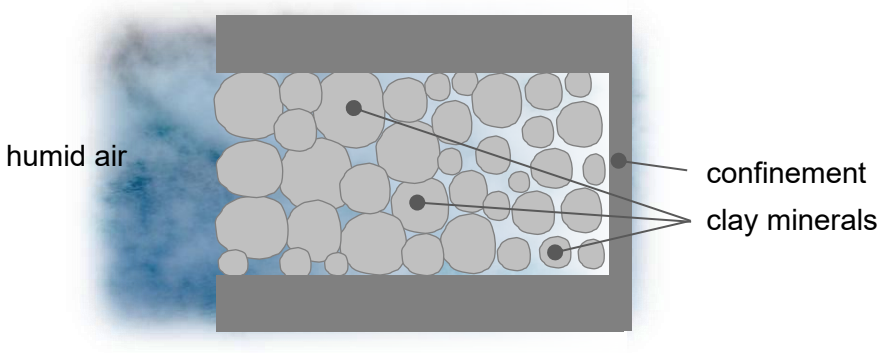


Fig. 1.8 Water uptake by confined bentonite via water vapour

During work on this topic, the possibility appeared relevant that the state of full saturation may depend on the state of the water saturating the bentonite. In other words, the maximum water content, and thereby the final porosity, reached by uptake of liquid water may differ from that reached by uptake from water vapour. Because water vapour at 100 % relative humidity and liquid water have the same chemical potential, it has commonly been inferred that re-saturation from vapour-saturated air follows the same pattern as re-saturation from liquid water.

However, this assumption is contradicted by a late tentative interpretation of test results from /KRÖ 04/, which indicated a significant difference in the final state. In comparable tests, the final water content determined for water inflow amounted to 98 to 99 % of the theoretical maximum, but only to 91 to 92 % for re-saturation by water vapour at 100 %

relative humidity /KRÖ 19/. Since water content complements porosity, the porosity Φ_w remaining after water uptake thus amounted to 1 to 2 % of the porosity Φ_d available after drying according to standard laboratory procedures. By contrast, the final porosity Φ_v after saturation with vapour amounted to 8 to 9 %. This observation may be supported by the consideration that re-saturation solely by vapour should leave the remaining pore space free of water, whereas liquid water should fill the pore space more or less completely.

It was therefore decided that robust data on the final state of bentonite re-saturation and its possible dependence on the state of the water causing re-saturation should be generated. Accordingly, uptake tests with vapour (Test I) as well as tests with water (Test II) were performed under Topic 4.

During a meeting of the Task Force EBS[2] by SKB, a case was discussed in which bentonite pellets had been stored unconfined in vapour-saturated air and subsequently forgotten for several years. When they were rediscovered, they appeared unchanged, particularly with respect to size. Since this observation appeared highly relevant for understanding long-term water uptake from vapour, an additional low-effort test was included under Topic 4. The set-up reproduced the discussed case under controlled conditions using three pellets of MX-80 bentonite[3] and has been operated for nearly two years during the present project. Changes in one pellet with respect to weight and shape are also determined under Topic 4 as Test III. The test is being continued for the two other pellets to ensure that steady-state conditions are reached.

1.7 Topic 5 – Initial flow dynamics at the bentonite-rock contact

The interplay between groundwater originating from crystalline rock, including both matrix and fractures, and water uptake by a bentonite buffer was investigated in Task 8 of the Task Force on Groundwater Flow and Transport of Solutes (TF GWFTS) by SKB /VID 17/. The in-situ BRIE-experiment (see subsection 1.2.1) provided the practical basis for this

[2] This international collaboration coordinates research to improve the understanding and modeling of engineered barrier components in DGRs, and provides a important benchmarks for model validation.

[3] Pellets as installed in the Prototype Repository, courtesy of SKB

exercise, while the Task Force participants contributed advice for test planning, prediction of test performance and interpretation of the measurement results. Water uptake by the bentonite could be monitored well in this experiment, which also applied to the accompanying laboratory tests. By contrast, the impact of water uptake on flow in the rock could not be observed. To achieve a complete process understanding, this aspect is addressed in the work under Topic 5.

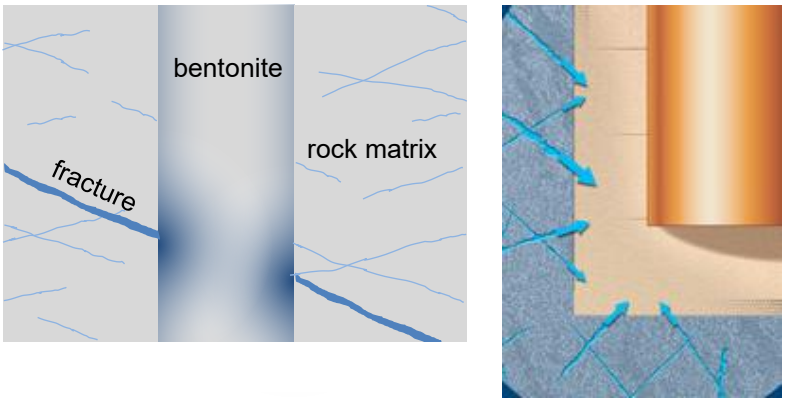


Fig. 1.9 Two schematic visualizations of hydraulic buffer-rock interaction

1.8 Topic 6 – Stability of bentonite properties against long-term heating

In the course of the present project, the long-term in-situ experiment Prototype Repository, maintained by SKB at the HRL Äspö (e.g. /ÅKE 22/), came to an end. It had been running for more than 20 years and is therefore one of the longest-running in-situ tests in the field of repositories for radioactive waste. SKB took this opportunity to invite interested parties to participate in the Dismantling of the Prototype Repository (DPR) Project /SKB 22/, in which post-test analyses by means of modelling or laboratory investigations of material from the test were encouraged.

Participation in this project opened the unique opportunity to investigate a possible influence of about 20 years of heating on the water uptake behaviour of the bentonite. Topic 6 therefore includes the acquisition of samples from the Äspö HRL. Corresponding reference bentonite from the production of the blocks, which had been stored under ambient conditions, could also be acquired. Subsequently, the uptake properties are checked by measuring and comparing isotherms.

1.9 Topic 7 – Extending the functionality of code COMSOL-VIPER

Experimental investigations at GRS /NOS 18/ have demonstrated that the hydration behaviour of bentonite is significantly affected by the amount of water available for uptake. On the one hand, unimpeded access of the bentonite to water (UA) may occur, meaning that the bentonite receives as much water as it can absorb. Such experiments have traditionally been set up in the laboratory and have therefore formed the basis for established modelling approaches. On the other hand, a limited water supply rate (LWSR), in which the external water flux is lower than the potential uptake by the bentonite, is particularly relevant for low-permeable host rocks envisioned for DGRs.

Implementation of a boundary condition for LWSR-conditions in the experimental code VIPER required a special approach, derived in /KRÖ 17/, that could be successfully realized /KRÖ 18/. Since VIPER had already been transferred to COMSOL Multiphysics, the resulting COMSOL-VIPER module was also advanced in this respect. However, to keep the implementation manageable within the framework of the present project, this extension was limited to 1D.

2 Preparatory work for innovative techniques

2.1 Non-destructive measurement of the water content of bentonite

The optical measurement set-up had initially been planned to be rather independent of the lighting, visual or SWIR light. As explained in subsection 2.1.2, the original plans could not be executed, though, which led to a quite different set-up for SWIR-data.

Reproducible lighting conditions are essential for imaging by visible or SWIR light. For this purpose, a dedicated room was used in which the windows could be covered with black foil and all other external light sources could be masked.

The measurement set-ups were based on a NEXUS optical table from Thorlabs /THO 26/, equipped with an array of M6 threads to secure the relative positions of devices and test components. A dedicated damping mechanism absorbs shocks and vibrations from the floor.

2.1.1 Observation by visible light

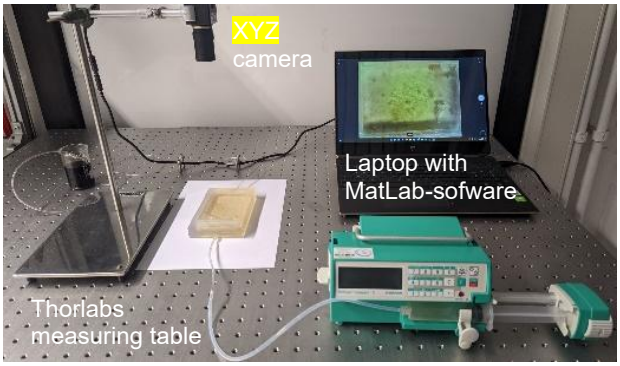


Fig. 2.0 Early set-up for an optical measurement of fracture flow

Image acquisition at predefined times was initially performed using the MatLab software /MAT 26/, specifically the MatLab Image Acquisition Toolbox. Later, ICCapture, the camera software, was used for this purpose. Each image was immediately stored on a laptop computer for subsequent image processing with the MatLab Image Processing Toolbox.

The objective of the image-based analysis for Topics 1 and 2 was to provide an axial profile of the essentially one-dimensional tests while compensating, as far as possible, for unavoidable noise in the data. For this purpose, a structured workflow was established to ensure consistent and reproducible image analysis. First, a two-dimensional region of interest (ROI) was defined individually on the surface of each sample. The ROI was selected to be representative of the sample surface in the lateral direction while avoiding geometric distortions caused by the curvature of the cylindrical sample surface, imaging artefacts and undesired reflections from illumination. Consequently, the ROI covered a rather narrow area with a width of a few millimetres. As a practical consequence for the optical measurements, the camera focus was always set to the outer surface at the minimum distance to the lens, because regions farther away would have been slightly out of focus due to the curvature.

In the axial direction, the ROI covered the complete sample profile, extending from the wet end to the dry end. Only regions with sufficiently uniform and good surface quality were considered for this purpose. The finally selected ROI had a square shape to standardize the evaluation area. From this point onward, all analyses were restricted exclusively to the information contained within the defined ROIs.

Within an ROI, image contrast was enhanced by linear contrast stretching to fully exploit the available greyscale range. The processed ROI was then represented by a two-dimensional array of greyscale values between 0 and 255, with rows arranged perpendicular to the sample axis. To reduce local noise and lateral variability, the mean greyscale value was calculated for each row in the ROI. The resulting one-dimensional vector describes the variation in mean lateral greyscale intensity along the longitudinal axis of the sample. It represents a greyscale profile over the entire sample length and was used as a quantitative descriptor for subsequent analyses.

2.1.2 Observation by IR light – finding appropriate equipment

SWIR-camera

As preparation for the present project, a German company manufacturing SWIR-cameras had been identified and on-site testing of direct SWIR-photography was enabled. The water content of a bentonite sample was intended to be derived from the grey-values in the images acquired by the SWIR-camera. For this purpose, a test body of partially saturated bentonite had been prepared. The tests produced very promising results. Unfortunately, contact was interrupted by the effects of the corona pandemic, and no suitable alternative allowing further product testing could subsequently be identified.

IR-camera in combination with SWIR-lighting

Over time, the committed representative Martin Labus from LASER 2000 GmbH /LAS 26/ pointed out several alternative options and provided the equipment for testing in some cases. To enhance the visibility of absorption at the critical frequencies, an IR-camera in combination with a tunable multispectral light source, which allowed individual narrow light bands to be activated or deactivated separately, was tested on partially saturated bentonite. However, the results were again unsatisfactory (see Fig. 2.2).

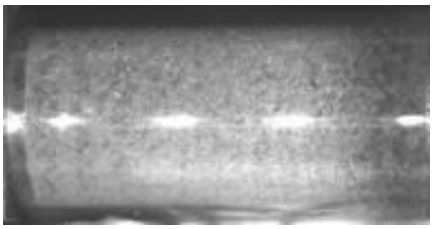


Fig. 2.1 Cylindrical bentonite sample confined in a plexiglas tube for testing SWIR-lighting

Hyperspectral camera

Further testing concerned a hyperspectral line camera, again provided by Martin Labus, which acquires information line-wise in combination with a moving stage to obtain a two-dimensional data field over the sample. For each pixel, the reflected SWIR-light is split by this camera into a considerable number of very narrow wavelength bands. The tested hyperspectral camera proved capable of producing meaningful images of the water-

content distribution along the sample, even under less than ideal test conditions. However, the cost of the camera, including the required equipment, would have far exceeded the project budget.

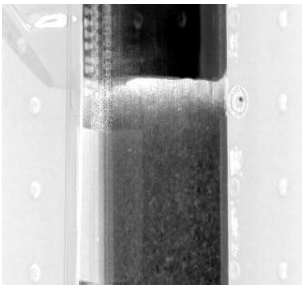


Fig. 2.2 Cylindrical MX-80 sample for testing a hyperspectral camera.

Spectrometer

On the recommendation of Martin Labus, the focus was then shifted from the line-wise imaging of the hyperspectral camera to a more cost-effective point-wise measuring spectrometer with a probe mounted above a moveable stage for the sample. At this point, an exchange with Dr. Janice Bishop from the SETI-Institute & NASA Ames Research Center had been established, whose judgement encouraged pursuing this approach. However, the water-content distribution along a sample could not be determined in the same detail as with the hyperspectral camera, because the resolution of the hyperspectral camera was finer than the diameter of the measurement spot of the spectrometer. Another factor limiting measurement accuracy resulted from ongoing evaporation of water from the bentonite during acquisition of the individual data points, as this effect distorts the resulting water-content data along the profile. Ultimately, the spectrometer SOL™ 2.2A from B&W TEK /BWT 26/ was deployed. It measures SWIR-light in the range from 1088 to 2214 nm, which is divided into 239 bands, resulting in a bandwidth of about 4.7 nm. The test set-up is illustrated by the two photographs in Fig. 2.4.

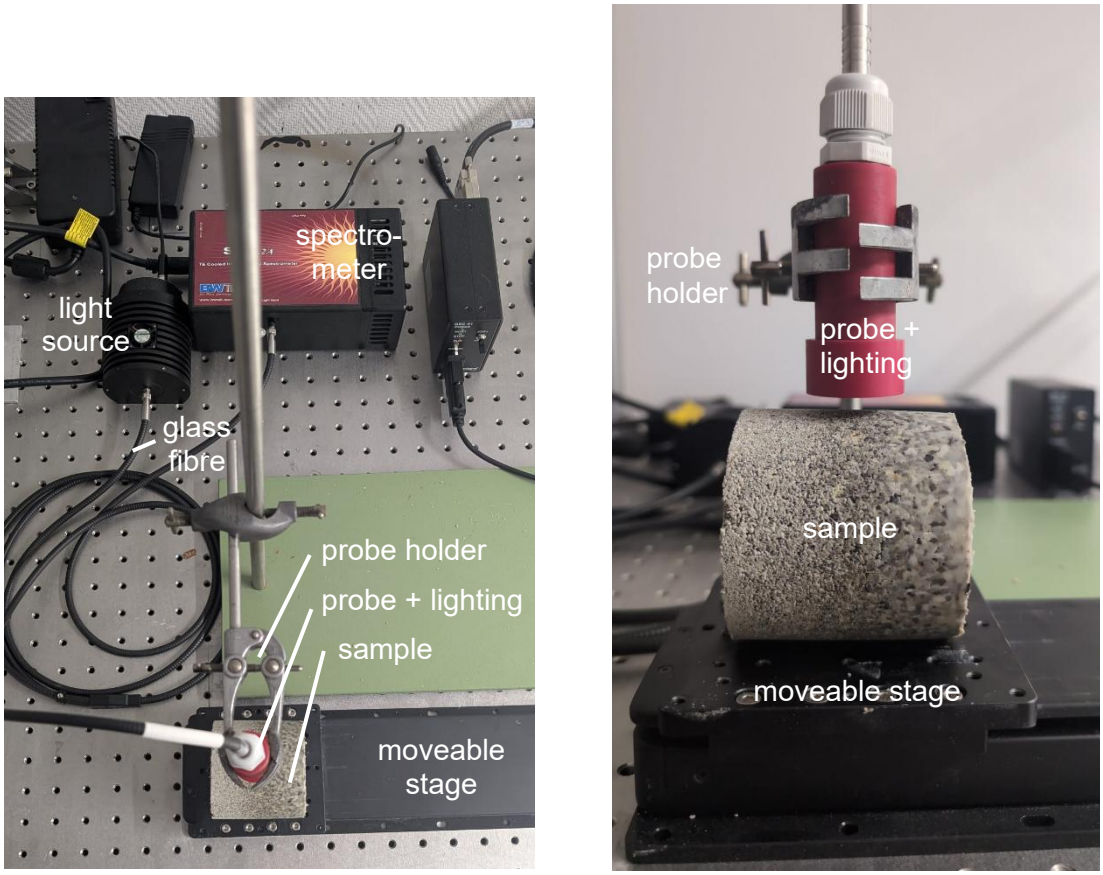


Fig. 2.3 Test setup for spectrometer measurements; complete setup (left) and spectrometer probe, sample and moveable stage (right).

2.1.3 Observation by IR light – pretesting and method development

Focal point

The focal point of the probe is located very close to the tip, at a distance of only a few millimetres. This configuration entails a significant risk of damaging the probe by unintended contact with the sample surface, for example as a result of swelling or handling inaccuracies. Furthermore, measurement through an observation window is not possible in this configuration, because the focal point would be located directly within the transparent window material above the sample surface.

To address this issue, integration of an additional lens into the optical path was investigated to shift the focal point away from the probe tip. Three different lenses were tested: a bi-convex lens (f = 10.0 mm), a bi-concave lens (f = –6.0 mm), and a plano-concave lens

(f = –24 mm). An adjustable adaptor was fabricated to allow variation of the distance between the spectrometer probe and the lens. During the experiments, the distance between lens and probe, the lens orientation, and the distance to the sample surface were systematically varied.

Among the tested configurations, the bi-convex lens provided the best performance. Using this lens, the focal point could be shifted to approximately 10 mm away from the lens, resulting in a significantly more robust measurement set-up.

Measurement of MX-80 samples with different water contents

The capability of the system to detect varying water contents was investigated using partially saturated MX-80 bentonite samples. In the initial test series, two granular samples were examined: one air-dried MX-80 sample and one highly saturated sample. The saturated sample was prepared by spraying granular MX-80 bentonite with water until a high moisture level was achieved. Fifty measurement points were distributed at a constant distance over each sample. A principal component analysis (PCA) was performed on the obtained spectral data. The first principal component clearly differentiated between dry and wetted material, with the sign of the component (positive or negative) indicating whether the sample had been exposed to water.

In a subsequent test series, the granular MX-80 was ground into a fine powder to minimize the influence of varying mineral grains and surface heterogeneity. Five samples were prepared and adjusted to different moisture levels (14 %, 30 %, 50 %, 70 % and 90 %) by controlled water spraying. The samples were stored for several days to allow moisture equilibration throughout the respective sample before measurement. SWIR-reflection data were again measured at 50 measurement points along each sample using the spectrometer, followed by principal component analysis of the collected data. In most cases, differentiation between the various humidity levels was possible. However, some measurements indicated higher or lower moisture contents than expected. These deviations were likely attributable to variations in the measurement distance caused by uneven sample surfaces or to incomplete moisture equilibration within the samples. The initially granular form of the bentonite material in use was also suspected to contribute to the data scatter. This was later confirmed by comparison of the data from granular MX-80 with ground MX-80 and powdery Calcigel (cf. subsections 3.5.1 to 3.5.3).

Suitable materials for the observation window

Additional pre-tests were conducted to evaluate whether the wetting state of MX-80 could be detected through an observation window. For this purpose, a pan filled with MX-80 powder was covered with an 8 mm thick acrylic glass plate, and spectral measurements were performed through the material. Under these conditions, reliable detection of the wetting state was no longer possible.

A subsequent test series focused on the influence of acrylic glass type and thickness. Acrylic glass (PMMA) is available in two main types: extruded (XT) and cast (GS). Extruded PMMA is more cost-effective and offers tighter thickness tolerances but typically exhibits higher internal stresses and slightly lower chemical resistance. Cast PMMA, produced by polymerization between glass plates, is mechanically more stable, less prone to stress and generally provides better optical quality. In SWIR applications, internal stresses and material inhomogeneities, which are more pronounced in extruded PMMA, can affect transmission behaviour and thus influence spectral measurements. For this reason, cast PMMA is generally considered more suitable for precise SWIR measurements, provided that its transmission range for IR-light matches the relevant wavelength region.

In addition to material type, the influence of thickness was investigated. Samples with thicknesses of 3 mm and 5 mm were tested individually, as well as in a combined configuration corresponding to a total thickness of 8 mm. This approach revealed a clear trend: decreasing material thickness improved measurement performance. However, the overall results remained unsatisfactory. Detection of the wetting state remained unreliable, and the rate of false detections increased significantly. This outcome led to the decision to abandon measurements of transient water-content evolution and to rely on post-test measurements that could be performed without a light-attenuating observation window.

Evaluation of spectrometer data

The obtained spectral data were analyzed using principal component analysis (PCA). For this evaluation, the wavelength range between 1380 and 1490 nm was considered. Although the main absorption peak of water is typically reported at approximately 1450 nm, a broader wavelength window was selected as a precaution to provide a sufficiently large dataset for robust PCA. In addition, the water present in the samples is not free water but

is bound within the bentonite structure. This may lead to a shift in the absorption peak position and may also result in spectral changes depending on the degree of saturation.

In addition to the wavelength window around 1450 nm, the spectral region near 1940 nm was also evaluated. The absorption band at approximately 1940 nm corresponds to a strong water combination band (O–H stretching and bending vibration) and is generally more intense than the absorption feature at 1450 nm. For this reason, this region is often considered highly sensitive to variations in water content.

However, the PCA results obtained from the 1940 nm wavelength window were very similar to those derived from the 1450 nm region. In both cases, the first principal component explained nearly the entire variance of the dataset and exhibited the same spatial trend along the sample length.

This similarity can be explained by the fact that both wavelength regions are dominated by water-related absorption features. Since water content is the primary source of variability within the samples, PCA identifies this dominant contribution regardless of whether the 1450 nm band or the 1940 nm band is analyzed. Consequently, both spectral windows capture essentially the same underlying physical gradient, namely the change in bound water content along the saturation profile.

Furthermore, in highly saturated regions, the strong absorption at 1940 nm can lead to reduced penetration depth and increased signal attenuation. Despite this higher absorption intensity, the relative spectral changes along the sample remain governed by the same moisture gradient. As a result, the structure of the PCA results, particularly the dominance of the first principal component, remains comparable to that obtained in the 1450 nm region.

Overall, the consistency between both wavelength ranges confirms that the primary driver of spectral variability is the spatial distribution of bound water within the bentonite samples.

The results from chapters 3 and 4 (Topics 1 and 2) showed that the first principal component (PC1) accounts for 99.9 % of the total variance in the measurement data. This indicates that nearly all variability in the spectral dataset can be described by a single dominant factor, most likely related to changes in water content and saturation state.

2.2 Visual observation of hydraulic processes in fractures

The methodology described in this section is intended to acquire data on hydraulic processes in fractures by visual observation. These processes include wetting of initially dry fractures and, tentatively, tracer tests in water-filled fractures. The related procedure requires a number of different tasks that principally comprise

- Sample acquisition
- 3D-scanning of fracture surfaces
- Digital post-processing and test cell construction
- 3D-printing of a test cell including the replicated fracture
- Performing hydraulic tests including imaging
- Post-processing of the image data

This workflow is described in detail, comprising 21 steps, in the following subsections 2.2.1 to 2.2.6. A graphical summary is shown in Fig. 2.5.

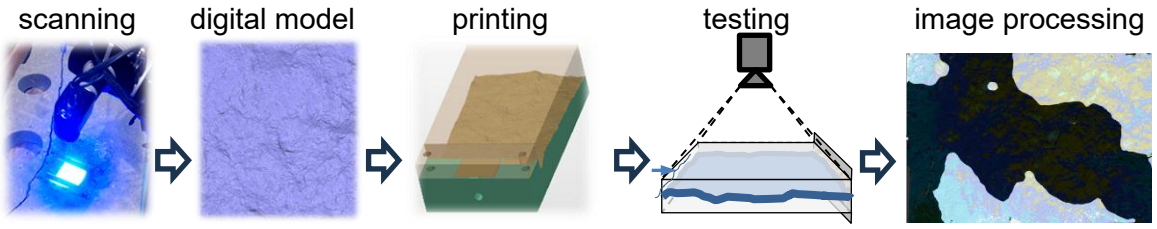


Fig. 2.4 Workflow for the visual observation of hydraulic processes in fractures

During establishment of this workflow, several questions concerning the accuracy of the methodology arose that had not yet been covered by /KRÖ 20b/ (cf. section 7.1). Some of these questions could be addressed by adding further steps to the detailed workflow described below. However, eight accompanying tests were also considered necessary:

(a) long-term water uptake of the printing material
(b) accuracy of printed planar surfaces
(c) deformation of printed bodies due to water uptake
(d) post-processing induced deformations of printed replicas
(e) repeatability of a wetting test
(f) wetting patterns depending on the flow direction
(g) repeatability of a percolation test on an artificial DFN
(h) combining optical 3D scans with CT images

The accompanying tests and their results are described in subsections 7.1.1 to 7.1.8.

2.2.1 Sample acquisition

Step 1: Find intact fracture

Initially, it was assumed that the workflow relevant to hydraulic tests on fractures begins with fracture-surface data suitable for the intended purpose. To this end, it had been planned to build on the long-standing membership of GRS in the Task Force GWFTS and to use fracture data provided by other organisations. Four organisations (SKB, KAERI, NMWO, and JAEA) were indeed able and willing to share fracture-surface data. However, two datasets included only one fracture half, one was too coarse to be useful, and one had been generated artificially by a fractal method. Where two halves were available, no information on their relative position to each other was provided.

Later, scan data of fractures were distributed among the members of the Task Force GWFTS. These data had been obtained by the Research Institutes of Sweden AB (RISE) /RIS 26/ on behalf of SKB for the so-called Task 10.2. An example, the 1N1 fracture, is shown in Fig. 2.6. These data also formed the basis for the first replicas produced in the present project.

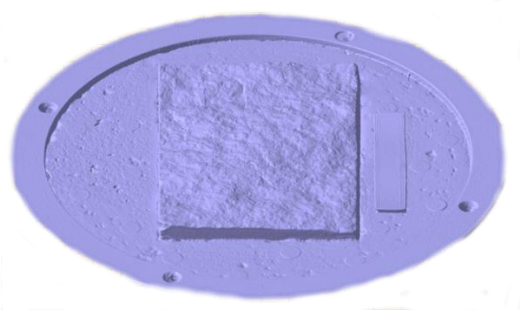


Fig. 2.5 Visualised data of the 1N1 fracture from the data package for Task 10.2

When working with these replicas, however, the problem of aligning two fracture halves became apparent. This issue had previously been treated rather casually. The absence of correct alignment caused considerable confusion among the Task Force members, since even a slight shift between the digital fracture halves resulted in noticeable changes in the

aperture distribution. Against this background, acquisition of dedicated datasets appeared necessary. The workflow therefore begins with identifying suitable fracture samples.

Courtesy of SKB and particularly helpful staff members known from the Task Force GWFTS, access to several promising samples could be arranged for investigation by GRS /KRÖ 26/. Samples from the HRL Äspö were stored in an SKB warehouse at Oskarshamn, Sweden. In the TASS tunnel at Äspö, adjacent to the Prototype Repository tunnel, large slabs had been cut from the wall and contained abundant fractures /OLS 09/. The cutting principle is shown in Fig. 2.7.

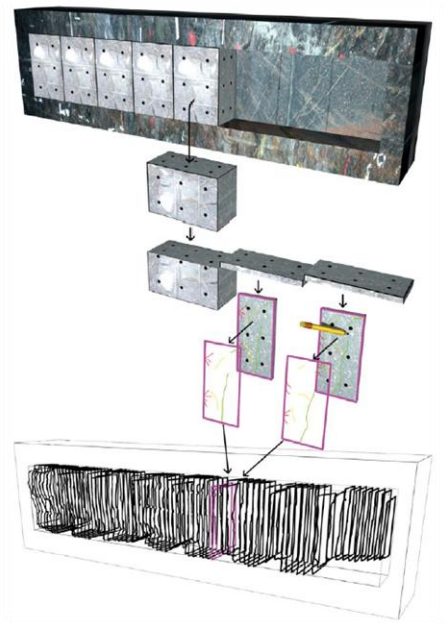


Fig. 2.6 The cutting of slabs from the TASS tunnel at the HRL Äspö; from /OLS 09/

After preselection based on photographs from /OLS 09/, on-site visual inspection identified several promising fractures based on their traces on the rock surfaces, e.g. Fig. 2.8. Fig. 2.9 shows the 3D-scanner in the foreground and some of the stored slabs in the background.



Fig. 2.7 Cleaned rock surface at fracture traces of interest



Fig. 2.8 Scanning samples at a warehouse of SKB at Oskarshamn

Further relevant fracture material was found at the Department of Theoretical Physics at the University of Jyväskylä, Finland, where samples representative of the granitic rock at Olkiluoto /NIK 24/ were available, courtesy of the Geological Survey of Finland (GTK). Several promising fractures were identified by visual inspection and by CT scans previously performed at the University of Jyväskylä, which facilitated the search for suitable fractures. A 3D-scanning campaign was therefore performed at the University of Jyväskylä

with a twofold purpose. On the one hand, additional fracture data from a repository-relevant site were to be acquired. On the other hand, the concept of combining both scanning methods was to be tested, since the 3D-scanning method developed within the present project provides surface data at a higher spatial resolution than the CT data. The results of this specific exercise are presented in subsection 7.1.8.

After some negotiations, material from the site of the Swedish final nuclear waste repository at Forsmark was also investigated at GRS Braunschweig /STI 25/. Several opposing fracture surfaces were obtained from drill cores. Since all investigated fractures had already been opened, possibly due to drilling and handling, the original alignment could not be obtained. A best-fit alignment of the scanned surfaces to the surfaces derived from the CT measurements resulted in realistic aperture distributions.

Overall, fractures from three different rocks relevant to radioactive waste disposal could therefore be investigated in detail within the present project, even though only those from the HRL Äspö have been used so far.

2.2.2 3D-scanning

3D-scanner

Despite a thorough market analysis of available 3D-scanners, the initially acquired scanner soon proved unsuitable. Although the handling of the actual scanning process was highly user-friendly, the device appeared to be designed for industrial applications in which larger smooth surfaces are required, rather than for the rough and detailed topography of fracture surfaces. Automatic and non-adjustable post-processing therefore produced very coarse, smoothed grids where surface details had been expected. A further disadvantage was recognized only later. The scanned object had to be placed in a light-shielded scanning chamber, which inherently restricted the size of the object that could be scanned.

After the return process for the first scanner had been initiated, the Hexagon SmartScan-HE R12 scanner /HEX 26/ (see Fig. 2.10) was favoured instead. It essentially consists of a scanner head containing the hardware for structured light scanning, which is mounted on a photogrammetry tripod. All additional electronic devices are physically separated and connected by cables. This configuration enables objects to be scanned whose size is

theoretically limited only by the storage capacity for the scanning data. It therefore became possible to move the scanning equipment to the samples instead of transporting the samples to the GRS geotechnical laboratory in Braunschweig.



Fig. 2.9 Hexagon SmartScan-HE R12 scanner on a photogrammetry tripod

Step 2: Apply reference markers to the rock surface

To preserve the original alignment of the opposing fracture surfaces in the digital model, only intact rock samples containing fractures can be considered. Before the fracture was opened, the area of the rock surface surrounding the fracture trace of interest was therefore equipped with circular reference markers (see Fig. 2.11), which are recognized by the scanning software.



Fig. 2.10 Sample surface with applied reference markers

Step 3: 3D scan the rock surface to obtain the relative positions of the markers

By 3D-scanning the surface of the intact sample, including the fracture trace and reference markers, the relative position of each marker point with respect to the other markers is measured. Based on this information, a common reference coordinate system covering both sides of the fracture is established, which can be referred to after the sample has been split along the fracture. Scanning of a square area on the surface of a rock slab with markers around a fracture trace is shown in Fig. 2.12.

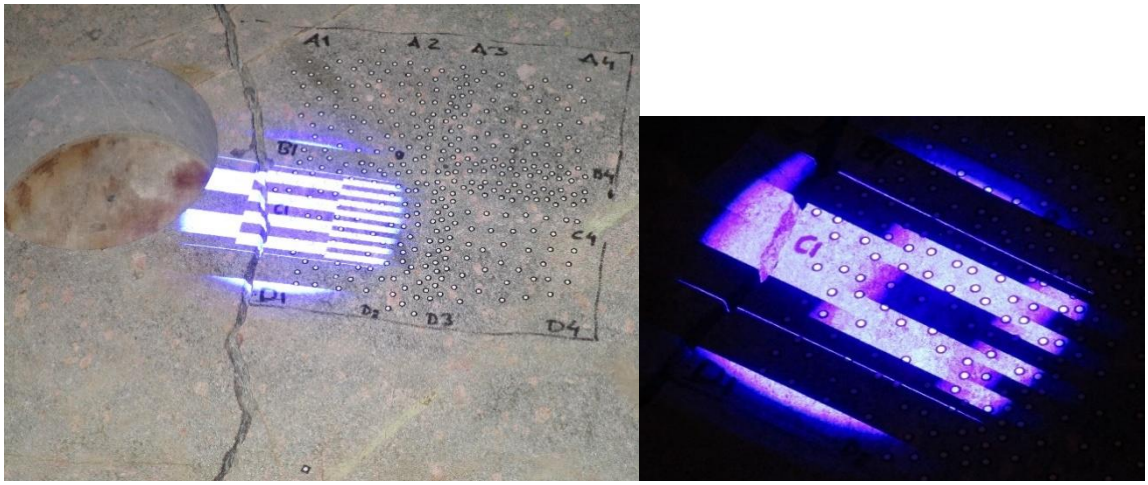


Fig. 2.11 Left: scanning of the slab surface including markers before opening the fracture; right: close-up

Step 4: Open fracture

Different methods for opening fractures along the visible trace were tested. Tapping near or directly at the fracture trace with a hammer proved to be the most feasible approach. While some fractures had already opened during sawing, others were tightly closed and therefore required careful use of a sledgehammer.

Step 5: Preparation and 3D scan of the rough fracture surfaces

The Hexagon scanner used for all reported scanning exercises applies an optical measurement technique referred to as “structured light”. This technique is based on striped light patterns projected onto the sample surface by a central projector in the scanner head. The illuminated surface is observed and recorded by two optical cameras, also mounted on

the scanner head, which capture the field of view (FOV) at slightly different angles and thereby allow reconstruction of a complex three-dimensional topography.

Two peculiarities are associated with the optical scanning method. First, the employed structured-light technique performs optimally at an angle of about 85° between the optical axis from the scanner head and the sample surface. Since a fracture surface can be regarded as a fine grid of connected but differently oriented very small planes, scan quality may vary considerably at the local scale. To avoid areas with low-quality elements, surface scans are performed at different angles and from different directions. An example of such a quality plot is given in Fig. 2.13.

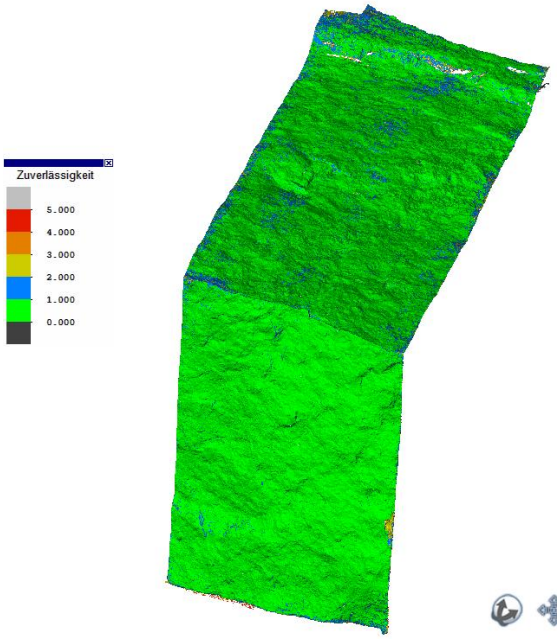


Fig. 2.12 Confidence plot showing the quality of the obtained data. Green: high confidence, red: low confidence

Second, the optical mapping technique is impaired by reflecting minerals. Since such minerals occur abundantly in crystalline rock, this problem had to be addressed. The preferred solution was to matt the fracture surface using a special chalk suspension applied with an airbrush. Because the applied chalk layer has a finite thickness, an optimum must be found between layer thickness and sufficient attenuation of reflected light.

Step 6: Aligning of the single scans to each other

During acquisition of the scanner, high spatial resolution of the scanned grid was prioritized over faster scanning using a larger FOV. The achievable resolution of about 17 µm is therefore associated with a comparatively small FOV of only 70 x 55 mm. The accuracy achieved by high resolution can be demonstrated visually by comparing two printed fracture surfaces. Fig. 2.14 shows a fracture from the VS0040B03-slab scanned with the Hexagon scanner at GRS and a comparable section from the 1N1 fracture obtained with a hand-held scanner at RISE, providing a resolution of about 200 µm.



Fig. 2.13 Photograph of two printed fracture surfaces; same scale, different scanners, different resolution of the resulting digital models;
left: 40B03 cropout section (GRS); right: 1N1 (RISE)

To obtain fracture-surface data from samples larger than the FOV, several individual scans had to be acquired, each overlapping previously obtained scans by at least 20 %. While individual scans near the boundaries of the rough fracture surfaces included information from the reference markers, the other scans could be aligned only on the basis of topographic features. This automatic alignment is performed after each scan but may lead to misalignments in the overlap zones of individual scans, particularly in areas containing lower-quality elements. At a later stage, such misalignments lead to artificial surface features (e.g. Fig. 2.15), which are time-consuming to remove. After all necessary scans have been obtained, they are therefore realigned using a weighted alignment algorithm that allows prioritization of marker-based alignment, because the markers provide higher positioning accuracy. The quality of the surface elements is also considered by this alignment algorithm. An example of realignment is shown in Fig. 2.16.

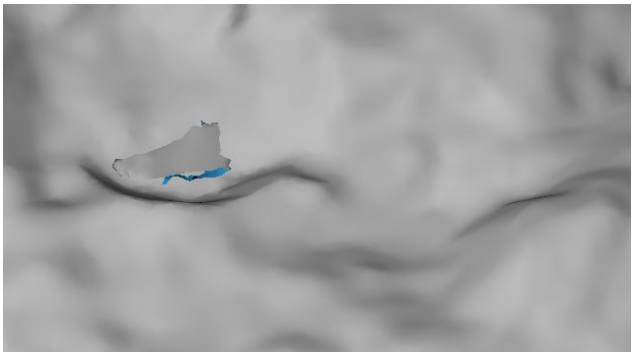


Fig. 2.14 Surface artefact caused by misaligned single scans

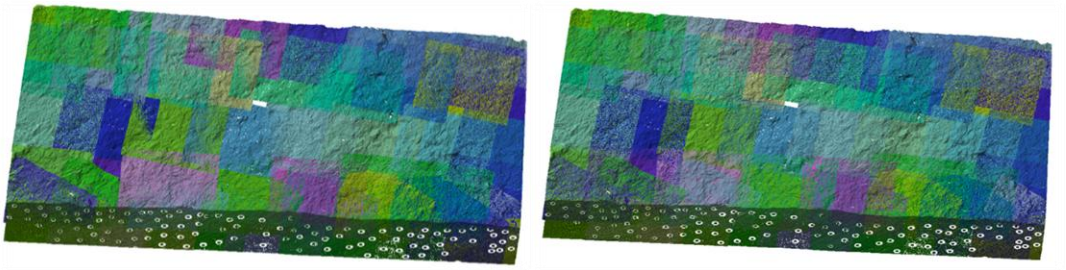


Fig. 2.15 Realignment of the single scans; before realignment (left), afterwards (right)

2.2.3 Digital post-processing and test cell construction

Step 7: Stitching of the single scans to two larger files each representing one half of the fracture

Low-quality elements in the previously aligned individual scans are then deleted in each scan to avoid reducing element quality during stitching by combining elements of higher and lower quality. Stitching itself is performed by the scanner software “OptoCat”. The resulting datasets still include the position data of the reference markers on the scanned rock piece. They are then aligned to each other based on the initially obtained marker point cloud, which includes the relative positions of all markers. All surfaces of an investigated fracture can then be exported in .stl format, with all surfaces oriented relative to each other in their original configuration within a common coordinate system. Such a processed fracture surface is shown in Fig. 2.17.

Step 8: Repairing imperfections of the two topographical grids

Problems related to reflections, shadows in deep and very narrow areas, and alignment issues lead to a number of imperfections in the topographical grid of a fracture surface, such as holes or separate but very close grid nodes. These imperfections can be repaired semi-automatically using the software Polyworks Modeller from InnovMetric /PWM 26/.



Fig. 2.16 Surface of the fracture from slab VS0037B03 representing an area of about 40 cm x 13 cm

Step 9: Digital fracture model

After all files constituting a fracture have been loaded into the software Polyworks Inspector from InnovMetric Software Inc. /PWI 26/, two different approaches can be followed to calculate the distance between .stl surfaces. The first approach determines the distance in the element-normal direction, starting from one of the two fracture surfaces. Since these fracture surfaces are not perfect mirror images of each other, even when correctly aligned, the determined aperture depends slightly on the selected reference surface. Alternatively, a median plane can be constructed from the fracture surfaces, and the orthogonal distance to the two fracture surfaces can be determined for each point in the median plane. Because both approaches produced very similar results, with only minor local variations, measurement in the element-normal direction was used subsequently because of its higher repeatability. The aperture distribution of the digital fracture, measured in the element-normal direction, can then be visualized as shown in Fig. 2.18.

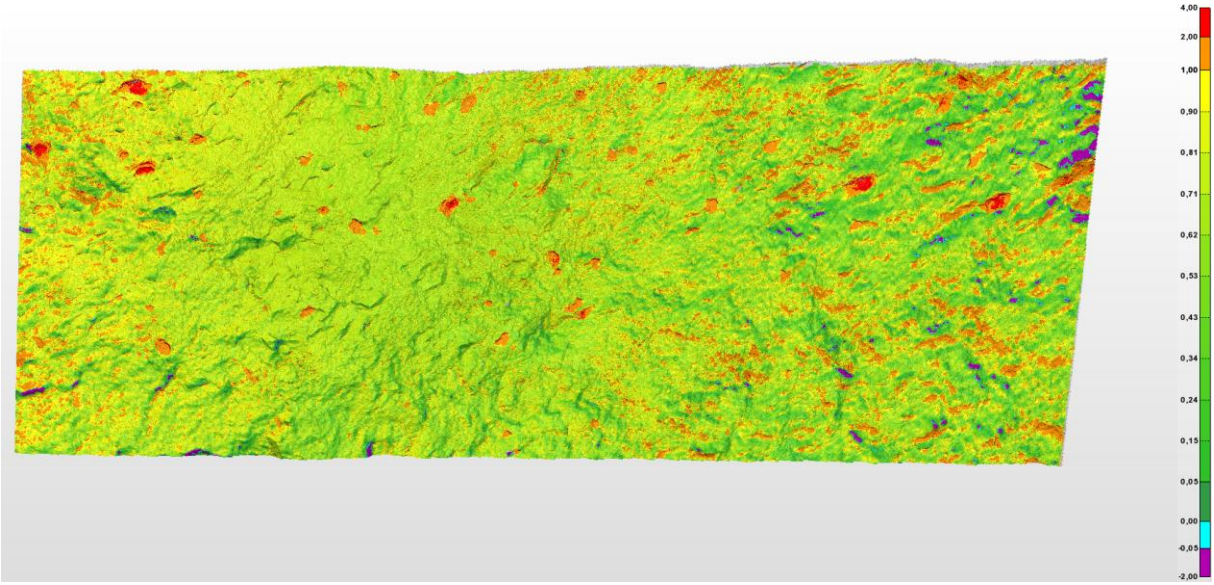


Fig. 2.17 Sample from slab VS0037B03; aperture distribution of the fracture along D1D5; scale in mm

Step 10: Design of the test cell using CAD

An individual test cell can be digitally custom-designed for the intended purpose. Therefore, connectors for the inflow and outflow tubing, as well as other attachments such as sealing surfaces, are designed in the CAD software SolidEdge from Siemens /SIE 26/. After export, also using .stl format, these parts are aligned relative to each other as a digital pre-assembly for the inflow and outflow sides.

Step 11: Crop out a smaller dataset using Boolean operators

Because the obtained fracture datasets, particularly those obtained from the Äspö slabs, are larger than the build volume of the currently used 3D printer, they must be digitally cut to size to fit the intended test cell. Boolean operators were used for this purpose in the open-source software Blender. The use of these operators required preprocessing of the datasets to achieve a homogeneous element size, because differences in element size can lead to faulty elements and major holes in the mesh.

Step 12: Unify CAD model with crop out sections using Boolean operators

The previously created inflow and outflow sections are then joined with the cropped-out fracture section in two stages. First, rough alignment is calculated based on the selection of at least three corresponding features. Subsequently, manual fine alignment is performed. When all parts are aligned and no edges between the individual parts remain visible, they are joined using the Boolean operator “union”. An example of a completed test cell with top and bottom parts immediately before unification is shown in Fig. 2.19.

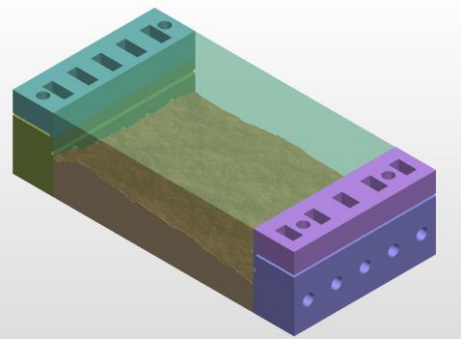


Fig. 2.18 Digital model of a test cell including a cropped out fracture; top half in transparent green, bottom half in brown, additional test features in solid green and violet

2.2.4 3D-printing of a test cell including the replicated fracture

Step 13: 3D print the resulting model

For 3D-printing of the complete test cell, a Form 3 printer from Formlabs /FOR 26/ was used. The printer is based on the SLA-technique (Stereo Lithographic Apparatus) and prints from bottom to top in an upside-down orientation. This method may require additional support structures when inclined or overhanging objects are printed. The potential need for such structures is checked by the printer software, which suggests additional supports where required. The support structures are removed after printing and curing. An example of this process is depicted in Fig. 2.20. The digital test cell model is shown on the left-hand side, and the model after addition of support structures is shown on the right-hand side. The top half of the fracture is included in the printing model.

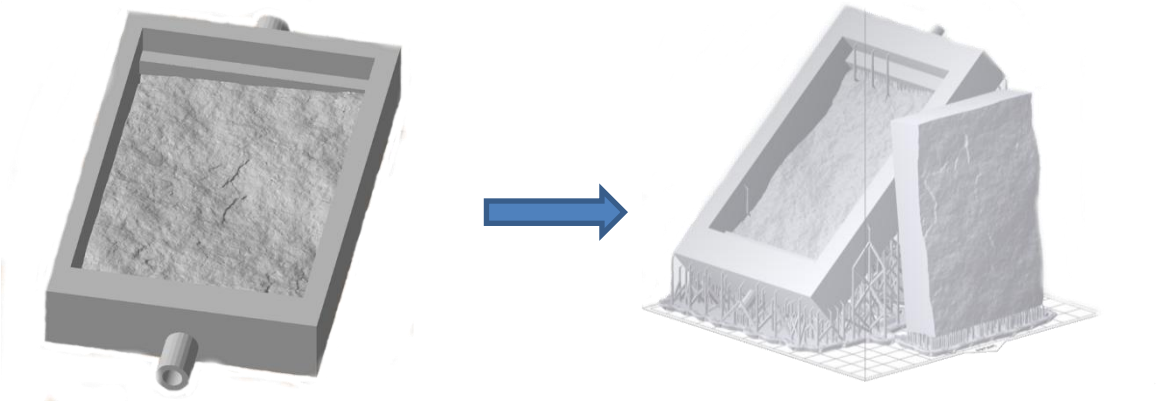


Fig. 2.19 Simple test cell; lower half of digital model (left) and printing model including top plate (right)

The open Form 3 printer after completion of a print is shown in Fig. 2.21. A key performance characteristic of the printer is its high printing resolution. The lateral (XY) positioning accuracy of the laser spot is specified as 25 µm, thereby enabling accurate fabrication of fine features and sharp edges. The vertical resolution is determined by the adjustable layer thickness in the Z-direction, ranging from 25 µm to 300 µm, which directly affects surface smoothness and printing time. With a build volume of 145 × 145 × 185 mm, the Form 3 is particularly suitable for printing high-resolution fracture replicas with a high level of detail and repeatability. A printed fracture half is shown in Fig. 2.22.



Fig. 2.20 Completed printing of a fracture half with a Form 3-printer; from /FOR 24/

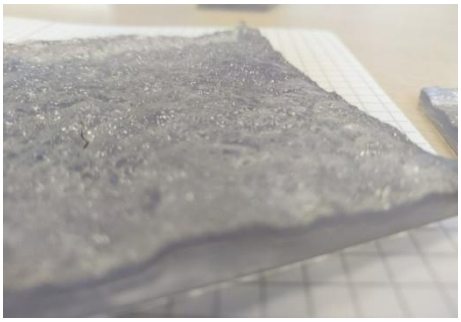


Fig. 2.21 3D-printed fracture half

Step 14: Washing and curing of the printed model

Right after printing, the object is still comparatively soft and also covered in liquid resin. It therefore gets washed in isopropyl alcohol for a certain period of time and after that it is cured (hardened) under UV-light at elevated temperatures. The times for washing and curing as well as the curing temperature can be chosen by the user. By these means, the properties of the printed object can be influenced to a certain extent.

Step 15: 3D scan the printed model to check for deformations

Ideally, the fracture replicas would exactly reproduce the fracture surfaces within the accuracy of the measuring tools. This has been the general goal of the presented methodology. However, perfect reproduction cannot not be expected. Already the printing process may lead to slight distortions of the replica but also washing and curing may lead to

measurable deformations. An optimization study to archieve the desired material parameters while minimizing the deformation has been performed. The replicated fracture surfaces are therefore scanned again when the production process is completed and compaired with the digital model of the test cell. An example is given in Fig. 2.22.

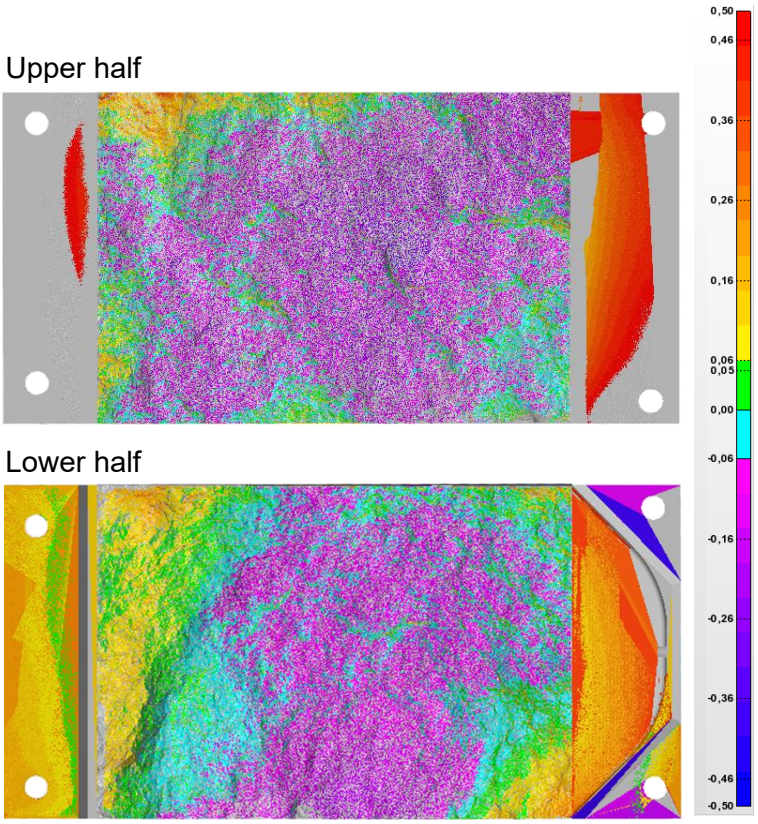


Fig. 2.22 Differences between digital model and 3D-printed testcell, plotted in mm

Step 16: Grinding and polishing of the printed model.

Next, the support structures are removed from the model. This leaves pimply surfaces, that require machining. Support structures are therefore only attached to the flat surfaces of the test cell and not the rough fracture surfaces.

In the following step, holes e.g. for centering pins to maintain the alignment during the machining are cleared before such pins are inserted. Then the surfaces on the sides of the cell are milled to create smooth and even surfaces for sealing the fracture. Afterwards, the top and bottom surface of the cell are grinded to smooth the surfaces. The top surface is then polished until a clarity comparable to acrylic glass is achieved.

Step 17: 3D scan the printed model to check for deformations

Another check of the fracture topography at this point serves two purposes. On the one hand, it indicates a possible influence of the post-processing on the replicated fracture surfaces. On the other hand, performed shortly before a hydraulic test, it provides a reference for the initial topography of the fracture in this particular test.

Step 18: Assembling the printed model parts

Up to this point, the complete test cell comprises at least two parts, one for each fracture surface, in order to avoid support structures from the printing process. All parts are now assembled in an appropriate way to ensure alignment and water tightness. Different techniques have been used for that purpose. Fig. 2.23 shows an early configuration where a top plate has been inserted into a fitting bottom half ensurig the alignment of the fractures halves and the remaing gaps between the two parts are sealed with silicon to achieve water tightness.



Fig. 2.23 The assembled test cell from the digital and the printing model in Fig. 2.19

2.2.5 Performing hydraulic tests including imaging

Step 19: Perform experiments

Basically the same optical observation technique that is applied in for the work on Topics 1 and 2 is also used here. The optical industrial camera is mounted above the test cell and directed downwards (cf. chapters 3 and 4).

To fathom the potential of using 3D-printed transparent replicas of fractures for hydraulic test, three types of tests have been performed tentatively and are discussed subsequently:

(1) Wetting of a dry fracture
(2) Tracer migration in a steady-state flow field
(3) Particle tracking in a steady-state flow field

(1) Wetting of a dry fracture

Type (1) experiments have been performed as a preparation for the fracture-bentonite interaction tests under Topic 5. Especially the handling of the fracture replicas as well as the fluid detection have been developed on this simplified system. Instead of tap water, a tracer solution to increase observability of the water phase was found to be appropriate.

An example based on the 1N1 fracture (see subsection 2.2.1) is given in Fig. 2.24. Tracer solution has been injected point-wise by a syringe pump at a rate of 0.1 ml/h. The image shows the tracer solution in black overlain over a plot of the variyble fracture aperture.

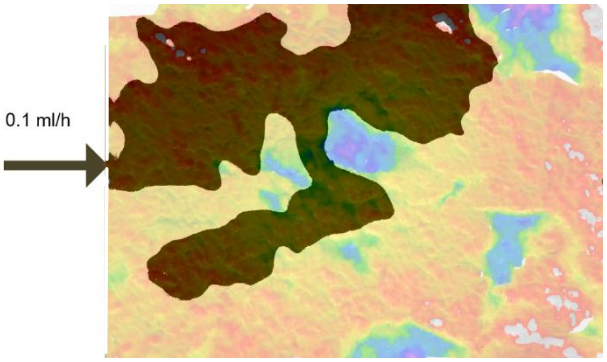


Fig. 2.24 Wetting of a dry fracture by constant point-wise inflow; tracer solution in black; otherwise color-coded aperture

Beyond the initial purpose, some of the the type (1) tests showed interesting wetting patterns due to the varying aperture and the ensueing varying local capillary pressure. At a sufficient distance from the inflow point where the influence of the hydraulic pressure induced by the forced injection becomes small, the wetting is basically driven by capillary pressure. As a consequence, the progressive movement of the water-air interface becomes seemingly erratic to the extent that fast extending fingers can even turn direction and even move backwards towards the inflow point. It has also been observed that air gets trapped by that movement (see Fig. 2.24). Such air bubbles vary in extent and could

apparently not be moved by the surrounding flow. Even applying some short term fast flow using a syringe didn't lead to a significant mobilization of the entrapped air.

(2) Tracer migration in a steady-state flow field

The exchange with members of the TF GWFTS regarding fracture surface data sets, as well as the presentation of tracer tests conducted in a dry fracture, raised the question of this method being also applicable to water-filled fractures. Since the same experimental set-up could be used as for Topic 5, additional tests were carried out with a modified test cell (see Fig. 2.25) at rather little effort. However, the flooding of the fracture proved to be challenging due to the occurrence of air entrapments. To enable the detection of different tracer concentrations, the replica was flushed with tracer solutions of varying concentrations prior to the experiments. As these tests had generated considerable interest within the TF GWFTS, sub-task 10.3.0.2 was dedicated to one of the tracer experiments[4].

[4] From the perspective of the present project, the purpose of this experiment was to enable direct observation of tracer distribution within a water-filled fracture by applying the previously developed replica method, originally designed for air-filled fractures. The approach required only minimal effort, demonstrating the versatility and ease of adapting the method to different research questions. The test setup consisted of a 7 × 10 cm fracture surface equipped with five inflow points and five corresponding outflow sections on the opposite side, with a constant pressure head maintained on both ends. The procedure began with a 3D scan of the fracture replica, followed by careful flooding of the fracture. Entrapped air bubbles were initially observed, whose evolution was mitigated by flooding the fracture from the bottom and tilting and tapping the replica to prevent air entrapment. After establishing a constant head at the inlet and outlet, measurements were carried out sequentially under various inflow scenarios. Each run lasted approximately 30–40 minutes, and the replica was flushed with clear, degassed water between runs to avoid air bubble formation. After completing all inflow scenarios, the sample was flushed with degassed tracer solutions of increasing concentrations (0 %, 20 %, 40 %, 60 %, 80 %, 100 %) to calibrate the resulting tracer distributions (cf. step 20). A final 3D scan was performed to verify that no significant deformation occurred during testing. The short duration of individual runs made it possible to efficiently investigate multiple inflow scenarios within a single experimental session.

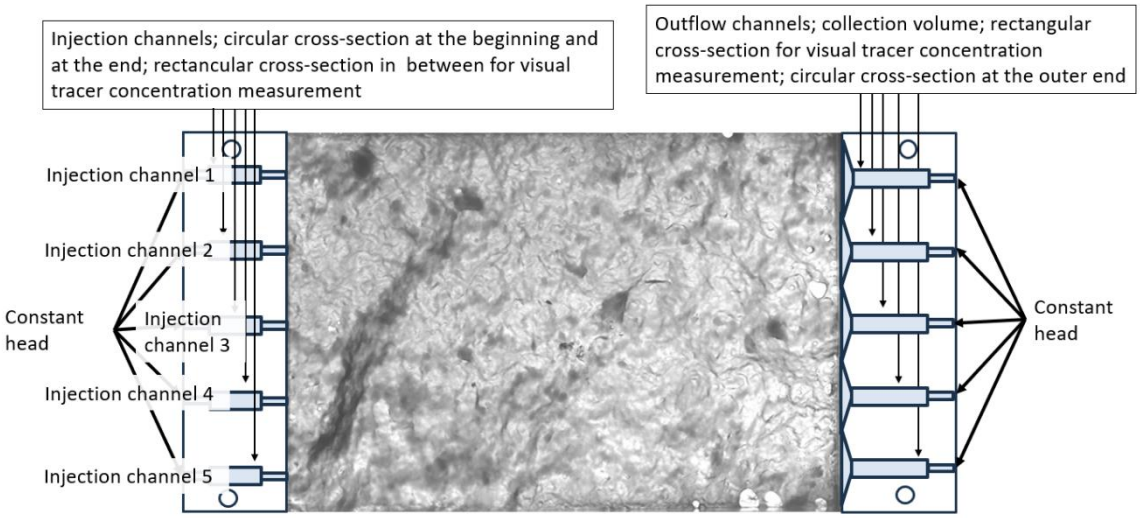


Fig. 2.25 Cell for tracer tests; from the description of Task 10.3.0.2 of the TF GWFTS

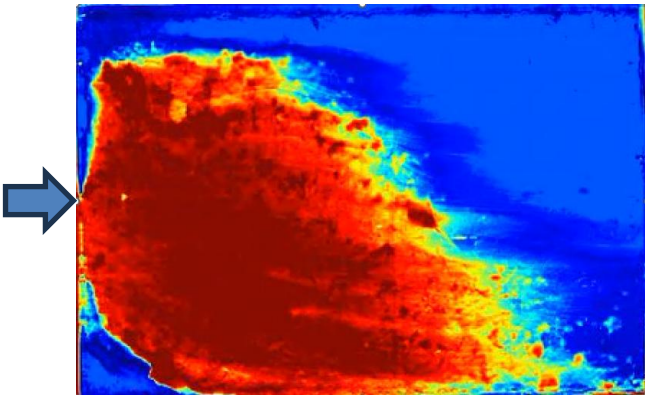


Fig. 2.26 Tracer distribution after continuous pointwise tracer injection; red colour: high tracer concentration, blue colour: no tracer

(3) Particle tracking in a steady-state flow field

The presentation of the developed fracture replica method at the International Conference on Fluid Dynamics (ICFD) 2023 led to a still ongoing collaboration with leading experts in particle tracking from Taiwan Tech (cf.subsection 7.1.7). A mutual interest in particle tracking methods with respect to fracture flow had been identified as this was for Taiwan Tech a welcome additional application of the newly developed tracking methods while it had obviously potential to characterize flow from a practical test with replicas in great detail. Different kinds of particle tracking methods were discussed and it was decided that particle image velocimetry (PIV) would be the most suitable method for this application.

Suitable particles with an diameter of 48.5 µm have been procured and injected into the fracture replica using a syringe pump with a set flowrate of 5 ml/h. Due to this low injection rate, a sedimentation of the particles in the syringe and also a clustering of the particles have been observed. To prevent this, a drop of dishsoap was added to the water, to act as a surface-active agent. As more of the particle surfaces got wetted by this solution, the cluster formation was reduced but not entirely prevented. Some work on this problem therefor remained to be done. The obtained image data was processed using the open source PIVlab toolbox /PIV 26/ to calculate the velocity fields based on the time resolved particle images.

The observation of the particles proved to be difficult, because of the narrow depth of field of the deployed camera. As Taiwan Tech has the dedicated equipment in their lab for such measurements, they kindly offered to perform tests on a fracture replica in their lab. As the field of view of the event camera, that is used for the experiments in Taiwan, is only 2.88 by 2.16mm a smaller version of the test cell has been 3D printed and scanned and then send on loan to Taiwan Tech.

Currently two students are working on this experiment who were able to observe the particle flow within the field of view. To obtain the flow field for the whole sample, it may work to move the event camera over the fracture in a grid, so that the single datasets could be combined afterwards.

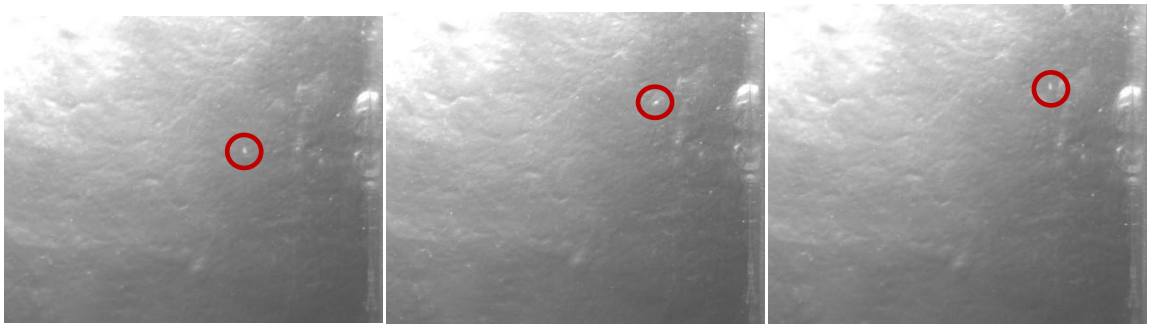


Fig. 2.27 Observed movement of a particle through a fracture from slab VS0040B03

Step 20: 3D scan the printed model to check for deformations

After terminating a hydraulic test, the fracture surfaces are 3D-scanned again to investigate a possible deformation of the replica by water uptake during the test.

This is the fifth and final scanning event in the workflow. The different scans are required to provide a replica with a true and fair view of the real fracture as well as the best possible fracture description for an actual hydraulic test:

- Step 3: Scanning of the matrix surfaces containing fracture traces as well as reference markers to ensure a correct later alignment of the fracture surfaces.
- Step 5: Scanning of the fracture surfaces after opening the fracture including the reference markers. This provides the orientation data for the fracture surfaces.
- Step 14: Scanning of the 3D-printed replica surfaces right after printing for evaluating the accuracy of the printing process.
- Step 16: Scanning of the replica surfaces before a test as a reference for possible deformations of the replica that may be caused by wetting of the replica.
- Step 19: Scanning of the replica surfaces after a test to check for possible deformations of the replica against the reference scan.

2.2.6 Post-processing of the image data

Step 21: Image analysis by MatLab

Several image-processing tasks were addressed using MatLab to support the evaluation of the fracture experiments. First, dry and wet areas on the fracture surface were distinguished by enhancing the contrast of the acquired images and applying threshold-based segmentation. The segmentation quality improved with increasing tracer coloration, whereas experiments requiring pure water necessitated the use of GraphCut segmentation. In this case, wet and dry regions were selected manually, after which MatLab proposed a segmentation mask that required manual refinement along the air–water interface. As only partial automation was achievable, the workflow remained labor-intensive.

Second, tracer concentrations were determined from local greyscale values, which required a prior calibration to differentiate between tracer concentration and aperture thickness. For this purpose, the fracture was filled with tracer solutions of known concentrations (0 %, 20 %, 40 %, 60 %, 80 %, 100 %), and greyscale values obtained during the experiments were compared with these reference images. To avoid misalignment, reference images ideally needed to be taken directly before or after a series of experimental runs;

otherwise, image registration became necessary, a challenging task due to the lack of visible features in a tracer-filled fracture.

Third, the repeatability of the tests was examined by overlaying segmented images to visualize consistent or differing wetting patterns (see Fig. 2.28 and subsection 0). This process was straightforward for short-term tests, which caused minimal disturbance of the test cell and often required little to no alignment. In contrast, water-injection tests in initially dry fractures had runtimes of several days, making image registration essential. Different feature-based algorithms were tested, starting with manual feature selection for coarse alignment, followed by automated registration using a feature-based ORB (Oriented FAST and Rotated BRIEF) algorithm. ORB combines the FAST (Features from Accelerated Segment Test) keypoint detector with the BRIEF (Binary Robust Independent Elementary Features) descriptor, extended to be rotation invariant. In the registration workflow, corresponding keypoints between images are matched, and a geometric transformation is estimated based on these matches. The approach provides robust performance while remaining computationally efficient, making it well suited for practical image alignment tasks.

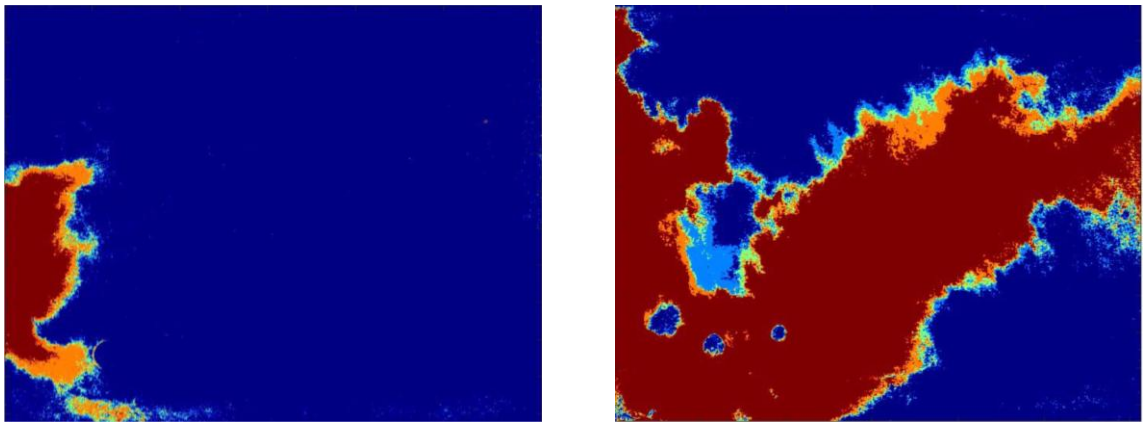


Fig. 2.28 Overlays of four inflow tests at two different times; pixelwise colour-coding: water in four tests – red, in three tests – orange, in two tests – light green, in one test – light blue, in no test – dark blue

Finally, working up a series of single images to an animation of the dynamic hydraulic processes.

3 Topic 1 – Small saturated zone at the water-bentonite contact

3.1 Pre-test

Topic 1 is concerned with the highly saturated narrow zone of a few millimetres thickness that develops in compacted and confined bentonite bodies at the bentonite-water contact. Since the evolution dynamics of this zone have not yet been investigated in detail, a simple ad hoc test was performed to clarify the process velocity associated with the formation of this zone. MX-80 bentonite was compacted to a density of 1400 kg/m³ in an acrylic glass cylinder; subsequently, the sample was wetted from above while mechanical confinement was maintained (see Fig. 3.1).

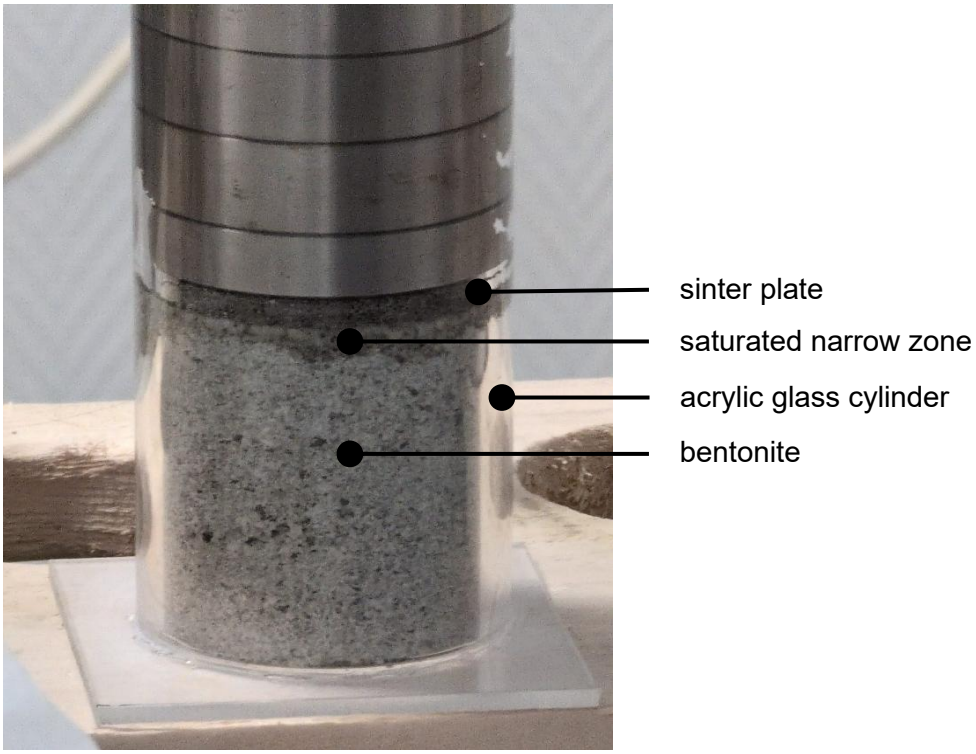


Fig. 3.1 Set-up of the pre-test

Using the optical observation method with the same equipment as in the main tests, the water uptake dynamics were determined qualitatively, and the time required for the zone to fully develop was identified from the evaluated optical data shown in Fig. 3.2.

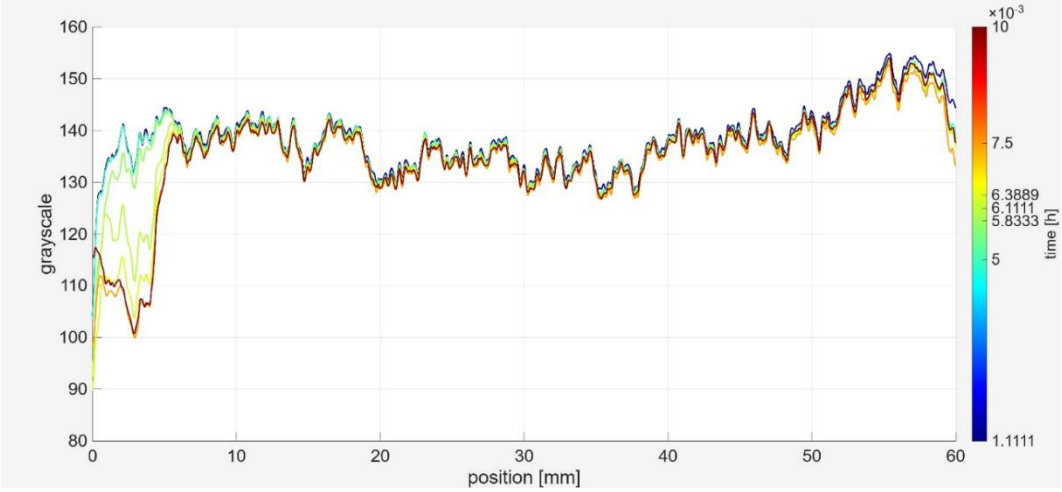


Fig. 3.2 Greyscale values over the sample as a function of time up to 36 s

The plot in Fig. 3.2 is given in terms of greyscale values and shows the rapid darkening of the sample at the water contact (left-hand side of the plot). The evolution dynamics can be inferred from a series of curves coloured according to elapsed time. The process is rapid and is completed in less than half a minute. In the present test, the thickness of the resulting highly saturated zone ranges from 3 to 4 mm, which is consistent with the conclusion drawn from the uptake tests in /KRÖ 04a/. The plot in Fig. 3.3 shows the same type of curves over a longer period to demonstrate that the zone remains steady after its rapid formation. To obtain results comparable with earlier uptake tests (/NOS 18/, /NOS 12/, /KRÖ 04a/), the tests were performed with Äspö-solution.

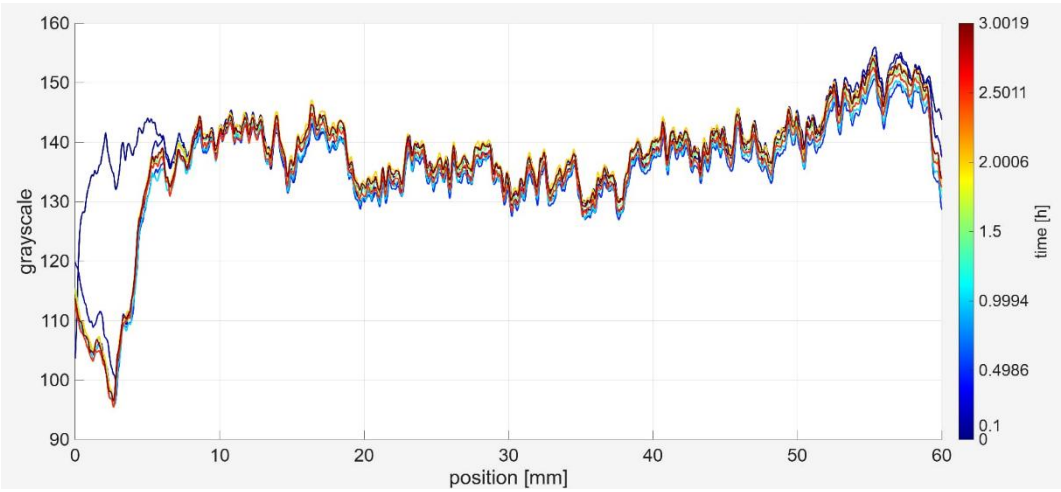


Fig. 3.3 Greyscale values over the sample as a function of time up to 3 h

3.2 Test set-up

For the measurements with SWIR-light, a motorized stage holding the cylindrical sample was installed beneath the fixed spectrometer probe. The probe was optically coupled to the spectrometer via a fibre connection and simultaneously connected to an external light source through a dedicated illumination channel, as depicted in Fig. 3.4.

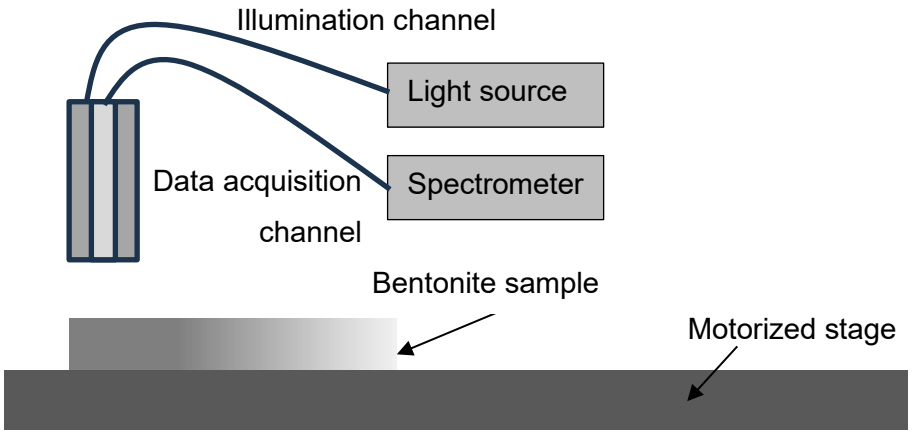


Fig. 3.4 Sketch of stage, spectrometer probe and light source

The motorized stage enabled precise and reproducible positioning of the sample relative to the probe. By moving the sample in defined increments, measurements were carried out systematically in the axial direction along a selected profile across the sample surface. In the tests, the motorized stage was set to increments of 0.3 mm. This set-up ensured consistent measurement conditions and enabled spatially reasonably resolved analysis of the sample properties.

Before the bentonite sample was placed on the motorized stage, photographs of the sample were taken for subsequent evaluation. To account for local differences, the sample was rotated between photographs so that the entire outer surface of the sample was covered.

3.3 Test procedure

To conduct parallel experiments, existing test cells from another project were reused. Three cylindrical bentonite samples were compacted in layers directly within these cells to a diameter of 50 mm and a total height of 40 mm. The effect of different densities was first

tested on MX-80; subsequently, the tests were repeated with Calcigel. Sample saturation was achieved by connecting burettes filled with Äspö solution to the bottom of the test cells, thereby providing unrestricted access to water.

Compaction was executed in three fractions of the total bentonite mass, called layers further on, to ensure a higher degree of homogeneity of the sample by minimizing the effect of wall friction. This procedure had a strange side effect, though, that was observed when preparing the Calcigel samples. The contact zone between the layers appeared to be brighter than the rest of the material. The effect has been observerved in the tests for Topic 1 and Topic 2 alike.

Fig. 3.5 shows on the left hand side the situation where two layers of material had already been compacted and the third layer had been loosely filled in. This brightness pattern became even more prominent over the test as the photo of a squeezed out sample on the right hand side shows. This observation is reflected in the grey scale images from visual light (see subsection 3.6.3).

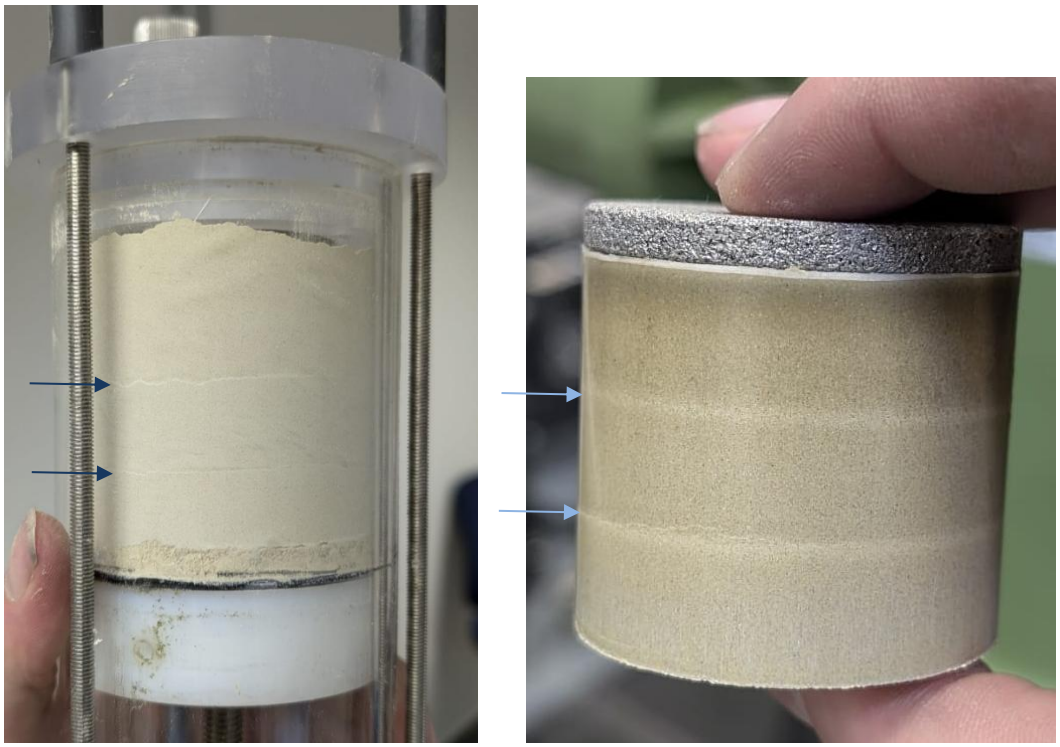


Fig. 3.5 Calcigel samples; left: before compaction of the final layer, right: after squeezing out at the end of the test; layer contacts indicated by arrows

When the test was terminated after the allocated time had elapsed, one of the three test cells was set aside for gravimetric measurement of the water content distribution along the sample as a reference. The sample was sectioned into thin discs, which were heated at 105°C for 24 hours to remove moisture. The water content was then calculated from the mass difference of the discs before and after drying.

Spectrometer and optical measurements were performed on the remaining two samples. Each sample was removed from the test cell, photographs of the surface were taken, and the sample was then rapidly placed on the movable stage. The spectrometer probe was positioned close to the sample surface to ensure proper focus. The stage was then moved in 0.3 mm increments, with one SWIR spectrum recorded at each step. To reduce the influence of local heterogeneities caused by the mineralogical variability of bentonite, measurements were performed along three separate profiles for each sample.

As the samples began to dry rapidly after extraction from the test cell, the time required for image acquisition had to be minimized. Prolonged exposure to ambient conditions resulted in progressive drying, which caused cracks to form on the sample surface, as shown in Fig. 3.6. These structural changes limited the number of measurements that could be performed before the evolving sample conditions started to influence and potentially bias the results. Whereas the optical data could be obtained comparatively quickly, acquisition of a full profile with the spectrometer required approximately 20 minutes.

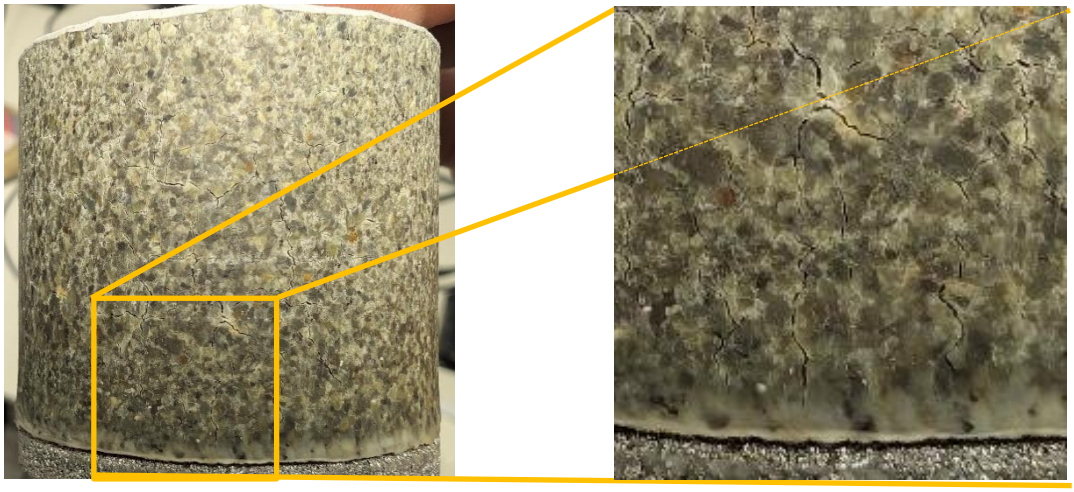


Fig. 3.6 Cracks on the surface of a MX-80 sample with a dry density of 1.4 g/cm³ evolving during SWIR measurements

3.4 Materials

For the present purpose, MX-80 was used as sodium bentonite, while Calcigel was used as calcium bentonite. MX-80 samples were compacted from granular material with a grain size of less than 2 mm to densities of 1.4 g/cm³ and 1.6 g/cm³, respectively. Alternatively, the granular bentonite was ground, and the resulting powder was compacted to densities of 1.4 g/cm³ and 1.6 g/cm³. Powdery Calcigel bentonite was compacted to densities of 1.4 g/cm³, 1.6 g/cm³, and 1.8 g/cm³. In all cases, a second sample was prepared to assess the repeatability of the results. The densities refer to bentonite under ambient storage conditions in the laboratory. Äspö solution was used for wetting.

3.5 Evaluation of data

Evaluation of the optical data followed the procedure described in subsection 2.1.1. The number of rows was then scaled to the total sample length of 40 mm, enabling spatially resolved comparison along the sample axis.

A further scaling step concerns the water content data. Neither the greyscale data nor the spectrometer data provide direct water content values. Instead, only the indirect optical intensity and the more abstract first principal component (PC1) derived from the SWIR spectra can be plotted. Since the gravimetric method is the only method from which the water content can be calculated directly, it was used here as the reference for scaling the optical and SWIR data.

To adjust the scales of the greyscale and PC1 data to the reference water contents, two data points from the reference curve are required. One data point is needed to assign an absolute water content level to the greyscale and PC1 curves, while one additional piece of information is required to adjust the span between the minimum and maximum values. The latter can either be the difference itself or another reference point. For practical purposes, use of the minimum water content at the dry side and the maximum water content at the wet side is recommended, since the corresponding gravimetric measurements refer to the two outer slices, which can most easily be cut from the sample.

3.6 Measurement results

In this section, the results obtained with all three methods for determining the water content, i.e. the gravimetric method, greyscale interpretation, and principal component analysis of spectroscopy data, are compared. For this purpose, the scaling described in section 3.5 was applied. However, the data for the wet side of the MX-80 samples could not be scaled in this way. At this location, the gravimetric method yielded water contents of approximately 100 % or higher, which flattened the curves to nearly horizontal lines when used for calibration. In these cases, a fit by eye was applied instead, comprising calibration at the dry side and subsequent alignment of the PC1 and greyscale data to the gravimetric data. For the comparisons, the water content determined by the established gravimetric method is assumed, as mentioned above, to represent the reference.

All processed data are plotted together for each sample in subsections 3.6.1 to 3.6.3 to enable an integrated interpretation of the moisture distribution. The results are arranged by material type, with the data for granular MX-80 presented first, followed by the results for ground MX-80 and, finally, those for powdery Calcigel.

Several features in the water content data derived from PC1 and greyscale data are repeatedly recognizable in the plots; therefore, they are briefly summarized in subsections 3.6.4 to 3.6.6.

3.6.1 Granular MX-80

The measured and derived water content distributions for the MX-80 samples with a density of 1.4 g/cm³ are shown in Fig. 3.7 and Fig. 3.8. For sample 1, the fit appears very good over the first part of the reference curve, i.e. up to 30 mm, where a water content of 35 % is reached. This value is slightly higher than the water content of 32 % at the dry end. Subsequently, the PC1 data increase slightly above the gravimetric reference. At the wet end, however, they do not exceed a water content of 45 % and therefore do not approach the gravimetric data. Consequently, the highly saturated zone cannot be identified from the PC1 data, either in terms of extent or water content.

For sample 2, a substantially larger scatter is observed in the PC1 data than for sample 1. According to the gravimetric data, the water content at the dry end is slightly lower than

for sample 1, at approximately 30 %. The PC1 data follow the reference curve very well up to 20 mm but then remain constant up to 32 mm, while the reference curve indicates an increase. At 32 mm, the PC1 data increase more rapidly than the reference curve, which is therefore crossed, reaching a peak at 38 mm and 43 % water content before decreasing again. The wet zone is again indicated, but its position is reached too early.

The greyscale data for sample 2 show no increase in water content up to 10 mm. Subsequently, they increase rapidly, reaching a plateau at 36 mm at approximately the same water content of 43 % as derived from the PC1 interpretation. The highly saturated zone at the wet end is also indicated by the optical method, but is represented even less accurately than by the PC1 data.

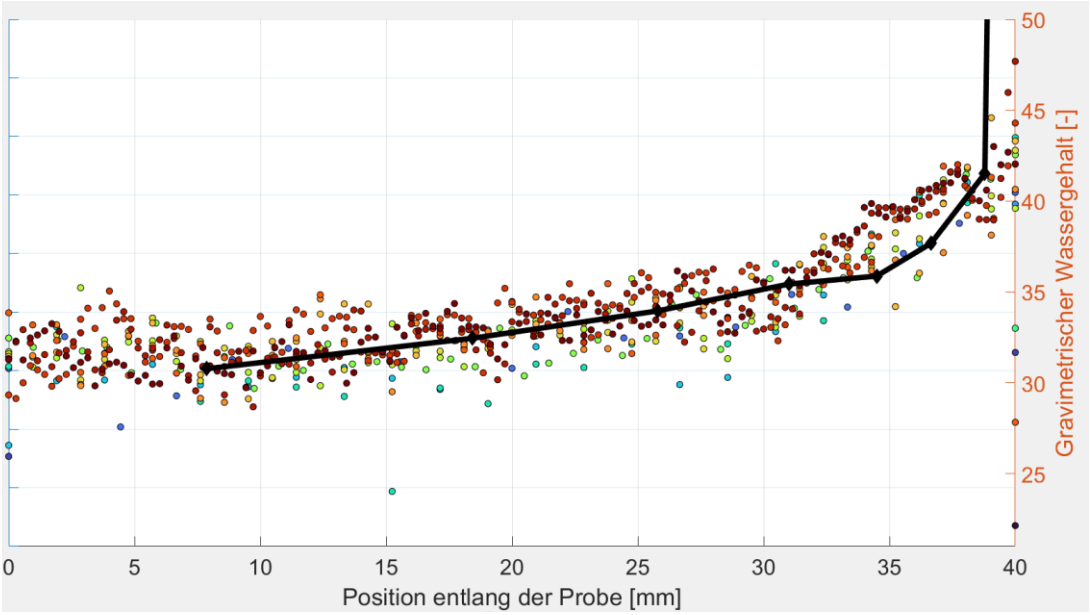


Fig. 3.7 Gravimetric and spectrometer data for sample 1 of granular MX-80 with a density of 1.4 g/cm³

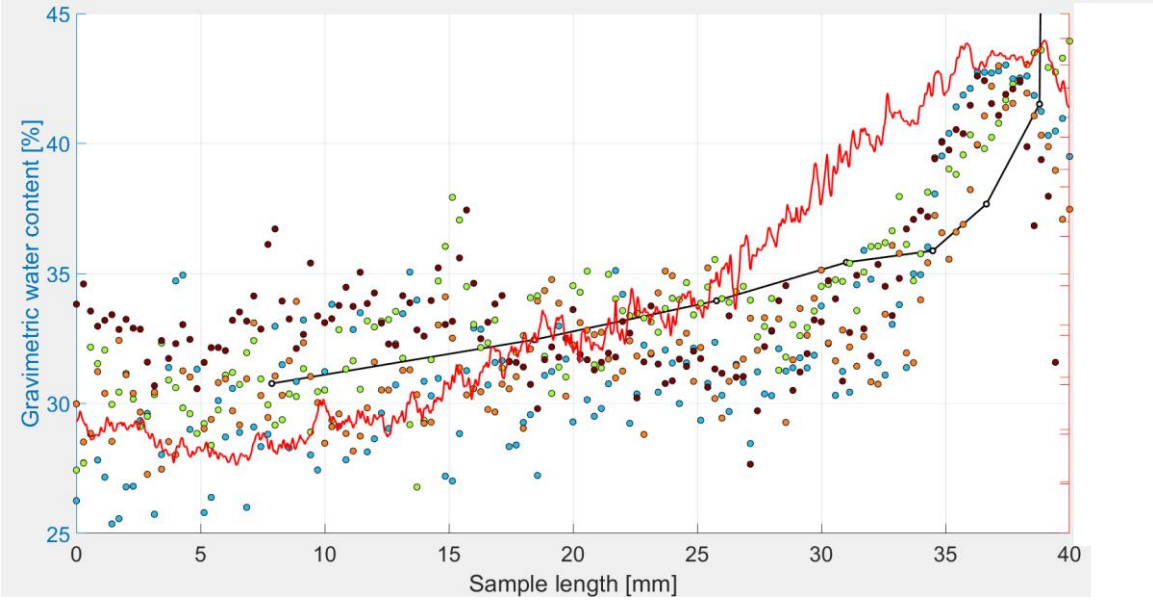


Fig. 3.8 Gravimetric, greyscale and spectrometer data for sample 2 of granular MX-80 with a density of 1.4 g/cm³

Results for the two samples with a density of 1.6 g/cm³ are depicted in Fig. 3.9 and Fig. 3.10. Scatter in the PC1 data lies between that observed for sample 1 and sample 2 with a density of 1.4 g/cm³. At the dry end of the samples, the gravimetric data indicate a water content of 20 %.

Overall, however, the two data sets do not match satisfactorily. In sample 1, a slight downward trend in water content is observed over the first 10 mm, and in sample 2 over the first 20 mm, whereas the gravimetric data show the expected increase. This is followed by an excessively rapid increase in water content. At the wet end, the gravimetric measurements yield water contents slightly above 45 % for both samples, which are barely reached before the PC1 data decrease again.

By comparison, the greyscale data mostly fit the gravimetric results reasonably well, deviating from the reference curve by no more than 5 % water content. However, sample 1 shows the same unphysical downward trend at the wet end as the PC1 data. In addition, the highly saturated zone is not reflected in the greyscale data. By contrast, the wet zone at the right-hand side of sample 2 appears to be represented comparatively well. A sharp increase and a plateau-like end of the greyscale curve indicate the highly saturated zone, even though the extent of this zone is slightly larger than indicated by the gravimetric measurements and apparently occurs at a lower level.

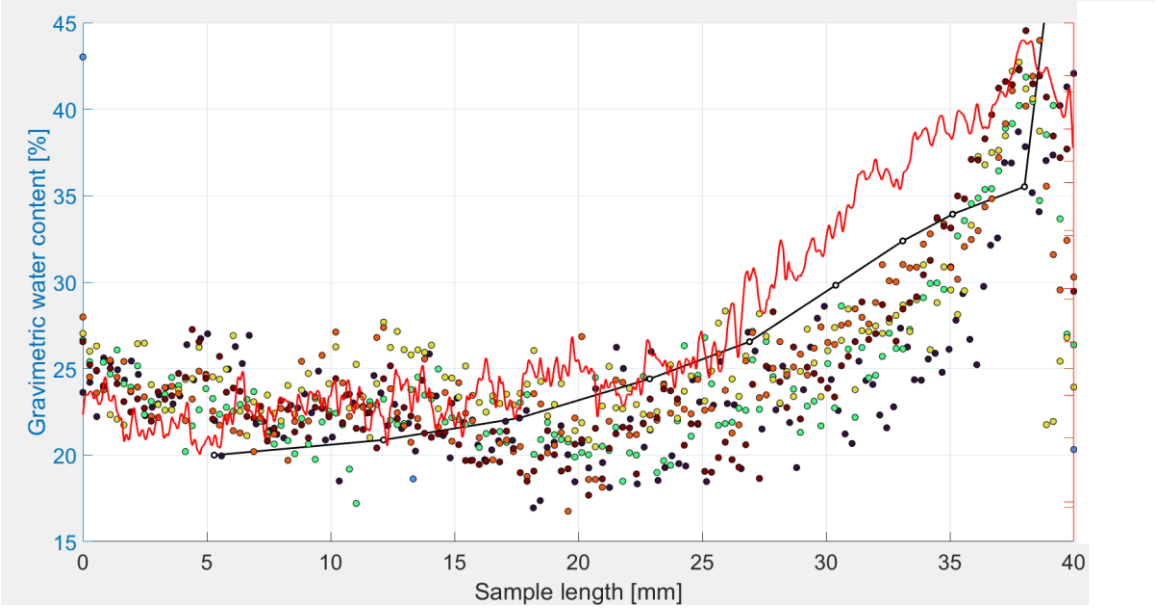


Fig. 3.9 Gravimetric, greyscale, and spectrometer data for sample 1 of granular MX-80 with a density of 1.6 g/cm³

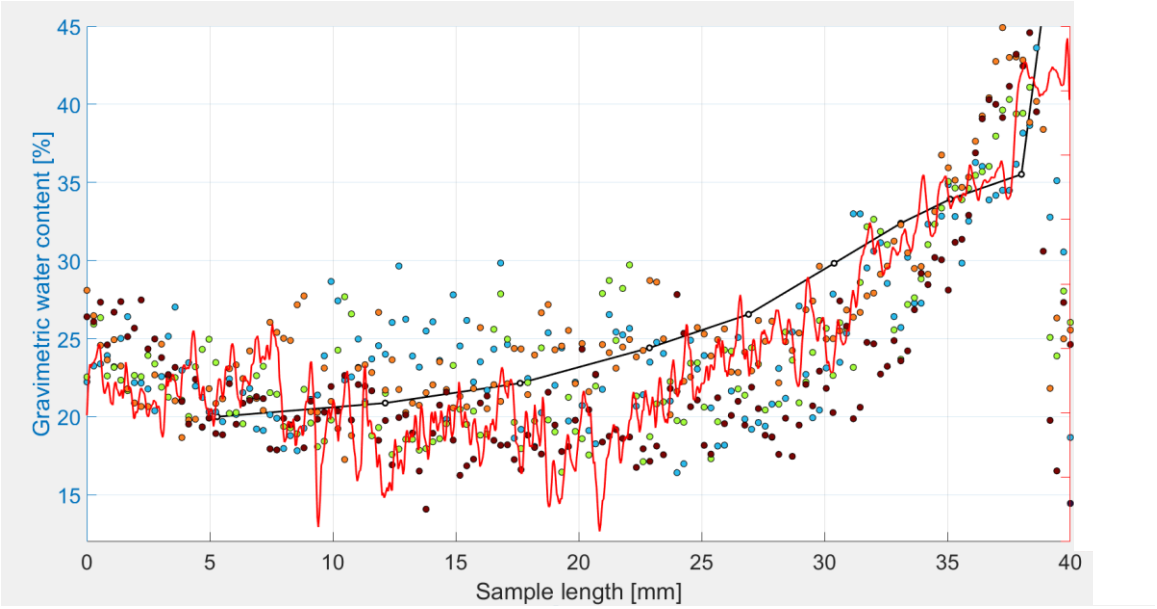


Fig. 3.10 Gravimetric, greyscale, and spectrometer data for sample 2 of granular MX-80 with a density of 1.6 g/cm³

3.6.2 Powdery MX-80

Measurement results for samples 1 and 2 of powdery MX-80 with a density of 1.4 g/cm³ are shown in Fig. 3.11 and Fig. 3.12, while the results for the density of 1.6 g/cm³ are shown in Fig. 3.13 and Fig. 3.14. In general, the scatter in both the greyscale and PC1 data is much less pronounced than in the data for granular MX-80. The degree of particle mixing in the bentonite therefore appears to have a significant effect on the smoothness of the greyscale and PC1 data. This effect can be seen particularly clearly by comparing sample 2 of granular MX-80 with sample 1 of powdery MX-80, for which essentially the same characteristics can be identified, while the trend is much more clearly recognizable for the powdery sample.

The gravimetric measurements also show that the water content at the dry end of the powdery MX-80 samples is generally lower than for samples prepared from the same bentonite in granular form. For the samples with a density of 1.4 g/cm³, this water content amounts to approximately 20 %, whereas values of 15 % to 18 % are obtained for a density of 1.6 g/cm³.

The favourable agreement between the gravimetric and PC1 data observed for sample 1 of granular MX-80 with a density of 1.4 g/cm³ is confirmed by the results for sample 2 of powdery MX-80. A plateau at the wet end of the sample is even indicated in both the greyscale and PC1 data. However, the plateau occurs too early, shows no preceding sharp increase in water content, and is not sufficiently elevated to account for the highly saturated zone. Essentially the same description also applies to the greyscale data for sample 2 of powdery MX-80.

For powdery sample 1, the data obtained with the SWIR-method provide an almost constant value over approximately the first 25 mm of the sample. This is followed by an increase up to 64 % before the PC1 data decrease again, contrary to physical evidence. The optical method provides reasonably good fits to the gravimetric data up to approximately 27 mm; thereafter, at approximately 35 % water content, the greyscale data show an unrealistic overshoot above the gravimetric data, which also obscures the location and extent of the highly saturated zone.

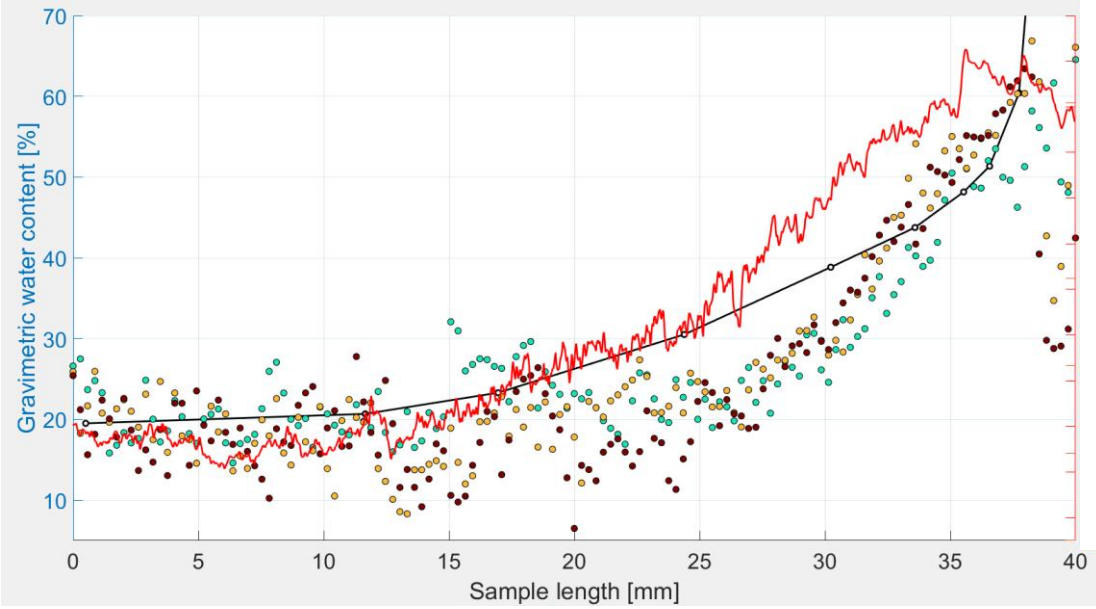


Fig. 3.11 Gravimetric, greyscale, and spectrometer data for sample 1 of powdery MX-80 with a density of 1.4 g/cm³

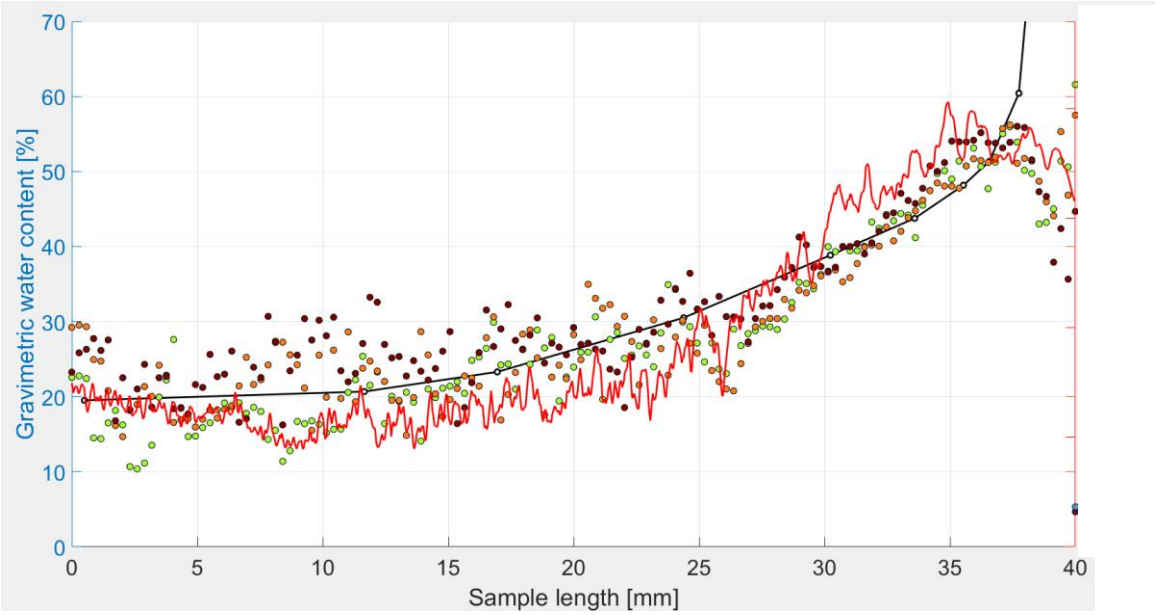


Fig. 3.12 Gravimetric, greyscale, and spectrometer data for sample 2 of powdery MX-80 with a density of 1.4 g/cm³

The water content data determined for the powdery MX-80 samples with a density of 1.6 g/cm³ are plotted in Fig. 3.13 and Fig. 3.14. The PC1 data for sample 1 show an unphysical downward trend over the first 23 mm of the sample, followed by an apparently exponential

increase up to 63 % water content at 38 mm. This increase ends as a peak rather than a plateau, since the derived water content values decrease again over the final 2 mm.

At the dry end of sample 1, the greyscale data also decrease, similar to the PC1 data, but more rapidly and only over the first 13 mm. The subsequent increase in water content is also stronger, resulting in larger deviations from the reference curve than for the PC1 data. At the wet end, the data obtained with the optical and IR-methods converge again; however, the greyscale data form a plateau before decreasing again, in contrast to the peak observed in the SWIR-data.

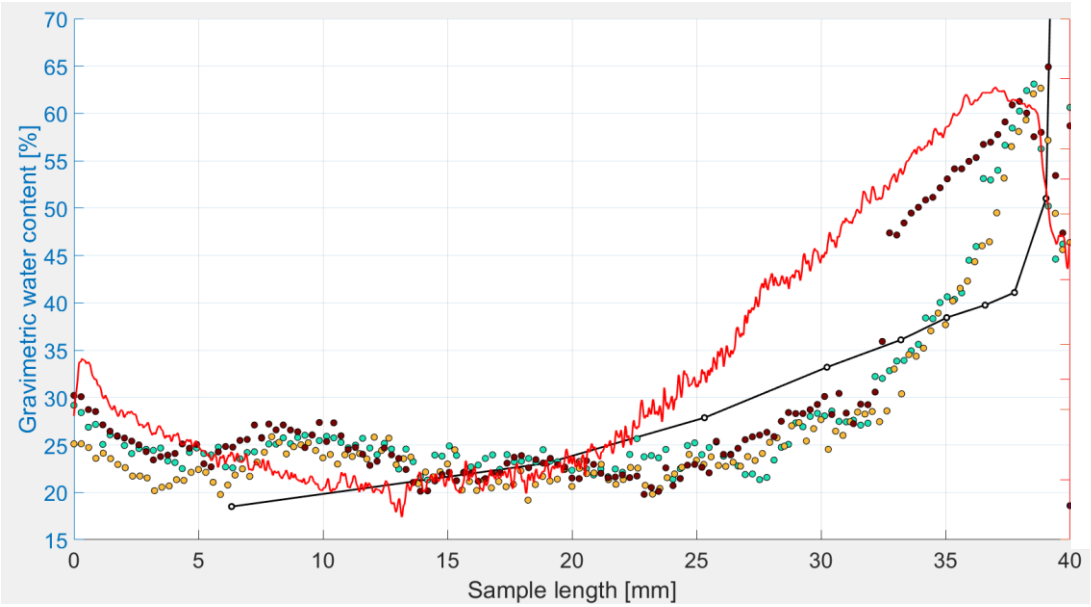


Fig. 3.13 Gravimetric, greyscale, and spectrometer data for sample 1 of powdery MX-80 with a density of 1.6 g/cm³

The PC1 data for sample 2 show a slight decrease over the first 20 mm, followed by a stronger, exponentially converging decrease up to 25 mm and then an exponential increase ending in a small plateau at 38 mm at a water content of 43 %. No decrease in water content after reaching the maximum is observed, so that the highly saturated zone appears to be detected reasonably well in terms of location, although the water content is much too low.

The greyscale data show an approximately constant water content up to 23 mm, followed by an approximately linear increase leading to a plateau beginning at 36 mm at about 50 % water content, which is eventually followed by a decrease over the final 2 mm.

Along the greyscale curve for sample 2, sharp depressions can be observed at approximately 13 mm and approximately 26 mm. A similar, but less pronounced, phenomenon can also be identified in sample 1, although not in the vicinity of 26 mm. This phenomenon is discussed in subsection 3.6.3 in the context of the measurements for Calcigel with a density of 1.6 g/cm³.

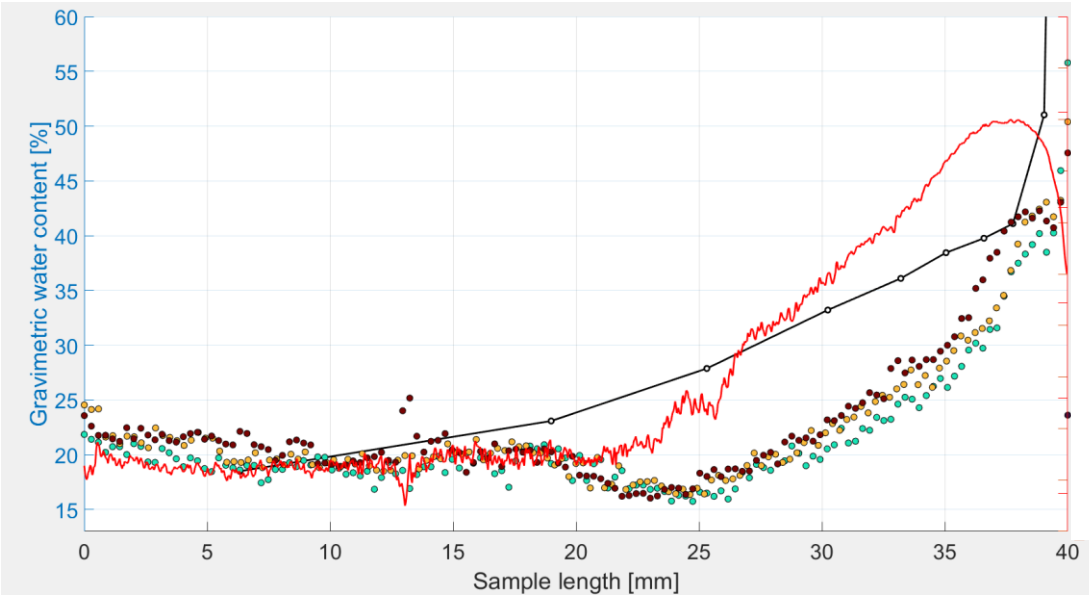


Fig. 3.14 Gravimetric, greyscale, and spectrometer data for sample 2 of powdery MX-80 with a density of 1.6 g/cm³

3.6.3 Powdery Calcigel

As in the preceding subsections, the water content data obtained for the Calcigel samples are shown in Fig. 3.15 to Fig. 3.20 for different degrees of compaction. The comparatively narrow data scatter appears to confirm the positive effect of a small maximum particle size.

The gravimetric measurements indicate a water content of approximately 10 % at the dry sample ends, except for the two high-density samples, for which values of approximately 14 % are obtained.

The PC1 and gravimetric reference curves coincide well for the two samples with a density of 1.4 g/cm³. Some deviations are observed at the very ends of the samples; however, these may represent artefacts from the spectrometer measurements when the sample ends are reached. It should be noted that the water content does not exceed 35 %. The SWIR-method indicates a comparatively narrow highly saturated zone without the final decrease that appeared to be typical for the MX-80 samples. The maximum value is also consistent with the gravimetric data for both samples.

By contrast, for a density of 1.4 g/cm³, the greyscale data fit the reference data poorly. For sample 1, agreement appears satisfactory over the first 13 mm, but deviations increase beyond this distance and above a water content of 15 %. After a maximum deviation of approximately 13 % water content is reached between 25 and 30 mm, the curves converge again. The greyscale curve for sample 2 with a density of 1.4 g/cm³ also initially fits the reference curve reasonably well, except for upward shifts at 13 and 23 mm. From 27 mm onward, however, the same deviation pattern as for sample 1 is observed: initially, strong divergence occurs until a maximum difference of 10 % water content is reached between 30 and 35 mm, followed by convergence towards the sample end. The actual shape of the water content curve at the wet end is not captured for either sample.

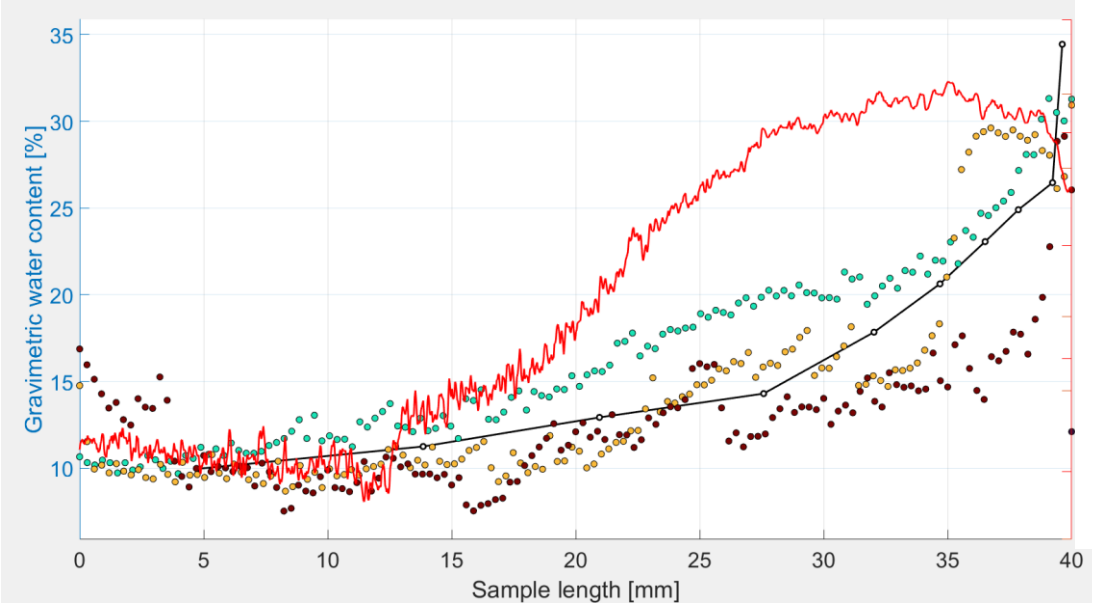


Fig. 3.15 Gravimetric, greyscale, and spectrometer data for sample 1 of Calcigel with a density of 1.4 g/cm³

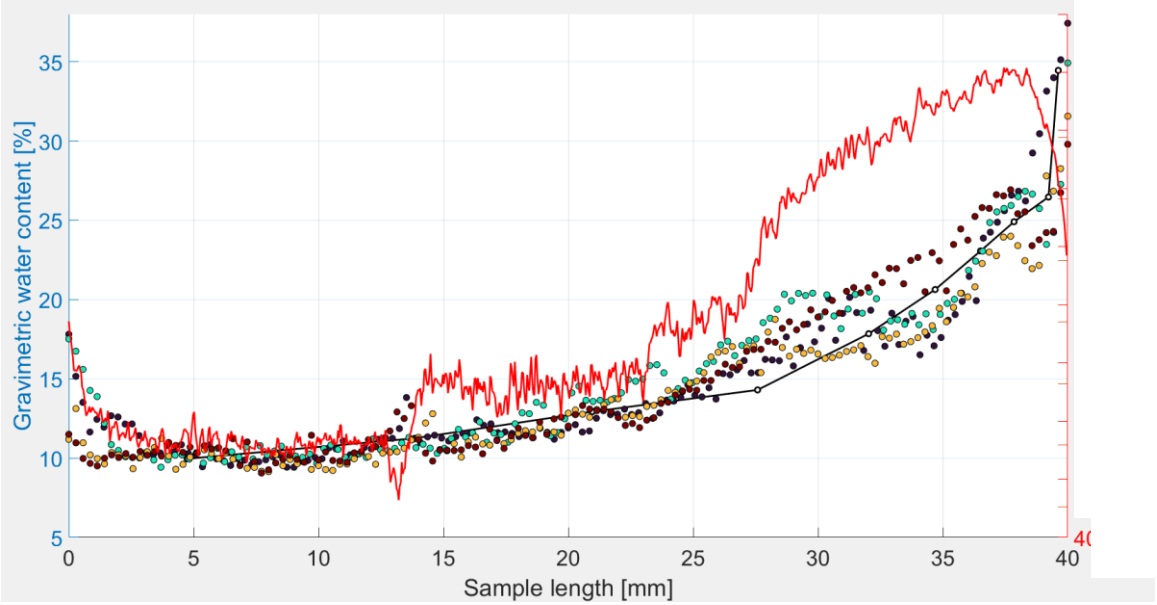


Fig. 3.16 Gravimetric, greyscale, and spectrometer data for sample 2 of Calcigel with a density of 1.4 g/cm³

The fit of the PC1 data to the reference curve for sample 1 with a density of 1.6 g/cm³ appears reasonable, although it is less satisfactory than for the low-density samples. However, the PC1 curve remains nearly constant over the dry half of the sample, whereas the reference curve shows a slight increase in water content.

The PC1 data for sample 2 with a density of 1.6 g/cm³ and for both samples with a density of 1.8 g/cm³ show poor agreement with the reference curve, since they decrease where an increase would be expected. No plausible reason for this effect has yet been identified.

By contrast, for sample densities higher than 1.4 g/cm³, the greyscale data and the reference curves agree reasonably well for water contents up to approximately 25 %. However, two prominent local deviations are observed. At approximately 12 to 13 mm, a depression is found that indicates a brighter grey value, which in turn would be associated with a lower water content. This depression becomes more distinct in samples with a density of 1.8 g/cm³. A second depression is observed at 26 to 27 mm. Such depressions are not observed for the samples with 1.4 g/cm³, but the corresponding positions coincide with the upward shifts observed for sample 2 with a density of 1.4 g/cm³.

Above 25 % water content, the greyscale curve increases above the reference curve, as observed for the low-density samples. This phenomenon is restricted to the final 8 mm, however, which includes the highly saturated zone at the bentonite-water contact. Although it can be interpreted as indicating this zone, the true extent of the zone appears to be obscured, since its thickness, as determined from the gravimetric measurements, lies in the range of 2 to 3 mm.

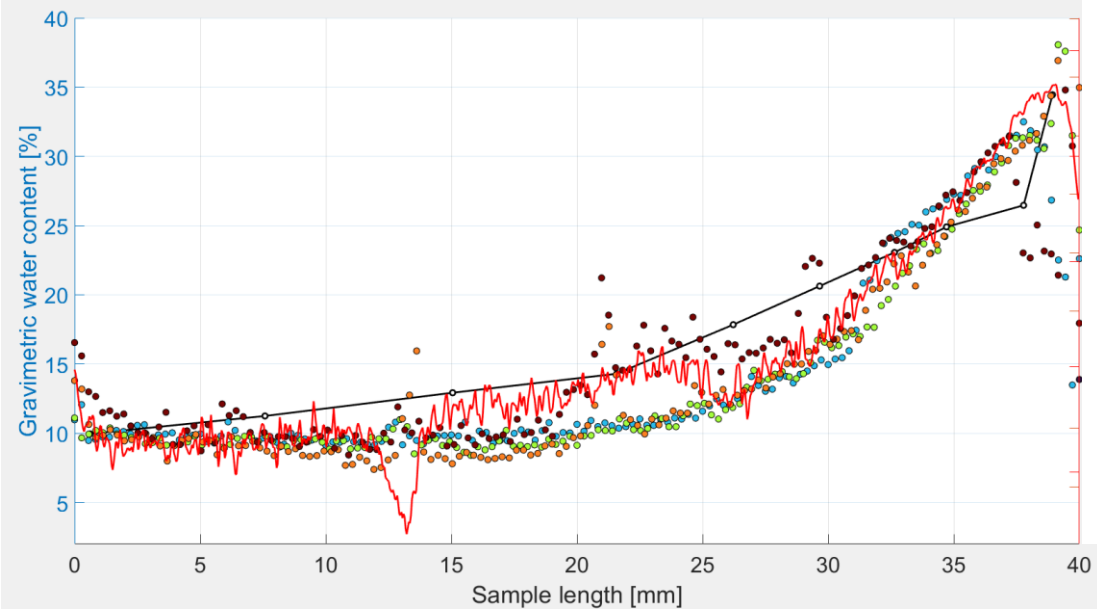


Fig. 3.17 Gravimetric, greyscale, and spectrometer data for sample 1 of Calcigel with a density of 1.6 g/cm³

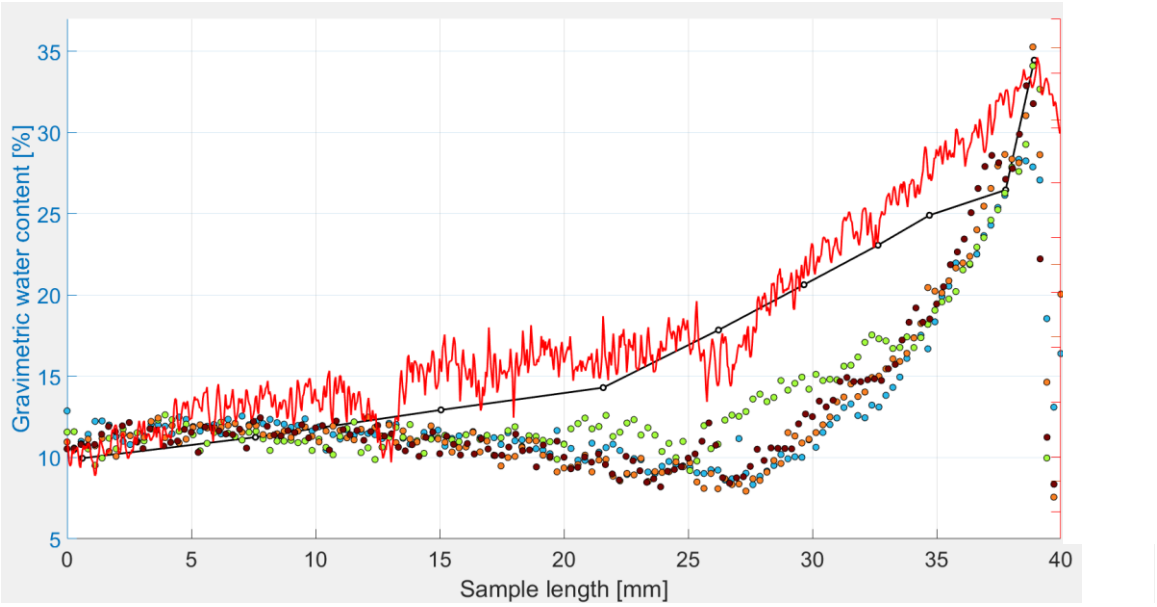


Fig. 3.18 Gravimetric, greyscale, and spectrometer data for sample 2 of Calcigel with a density of 1.6 g/cm³

Finally, the PC1 data appear to lose their relation to the water content entirely once a water content of approximately 35 % is exceeded. This applies to the two medium-density samples and sample 1 with a density of 1.8 g/cm³.

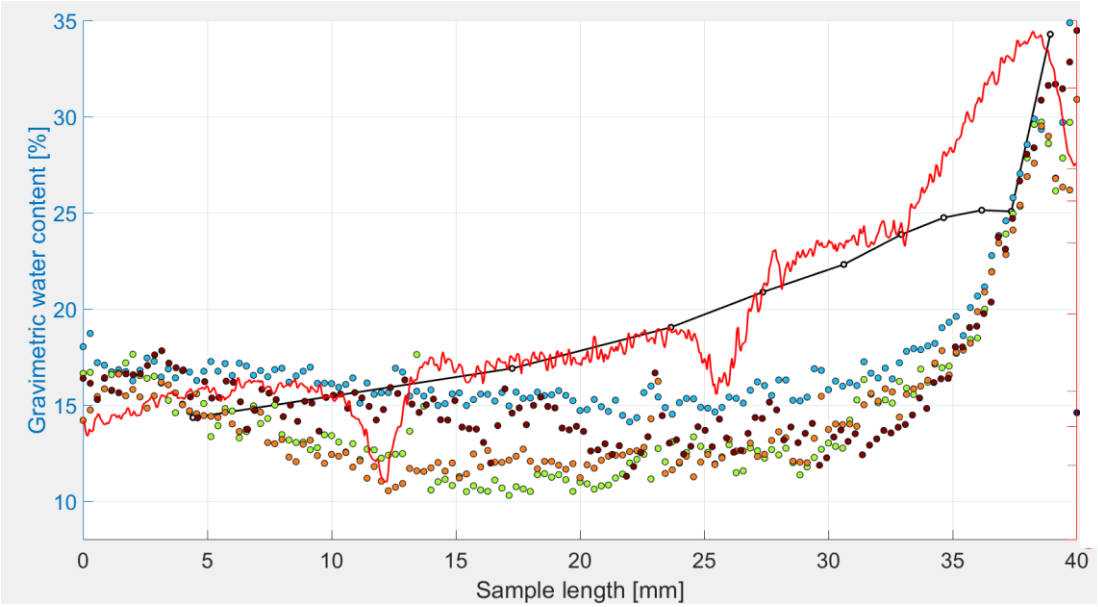


Fig. 3.19 Gravimetric, greyscale, and spectrometer data for sample 1 of Calcigel with a density of 1.8 g/cm³

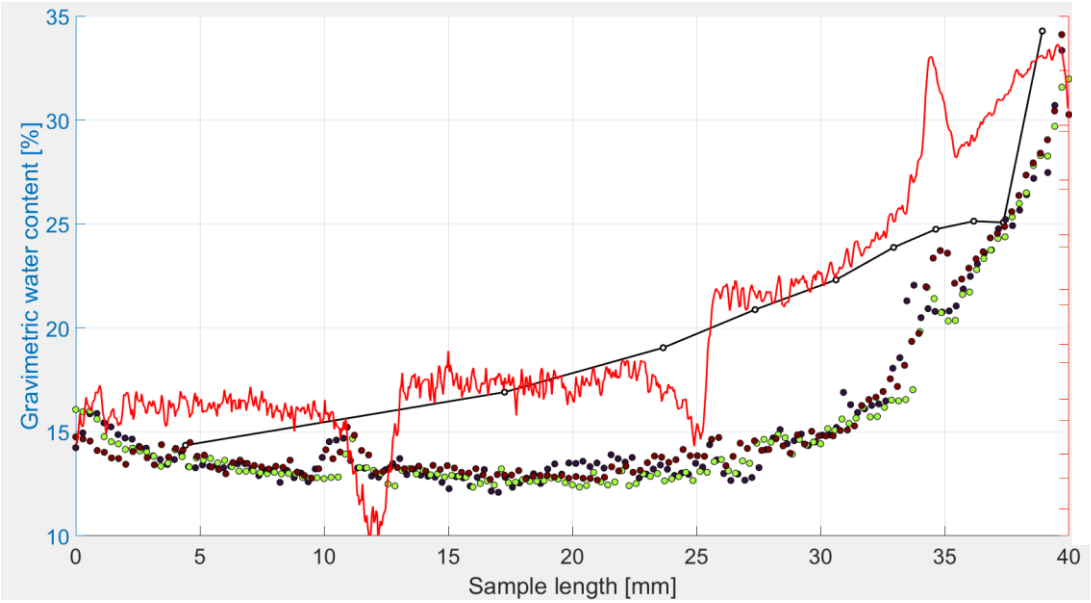


Fig. 3.20 Gravimetric, greyscale, and spectrometer data for sample 2 of Calcigel with a density of 1.8 g/cm³

3.6.4 Features in the gravimetric data

(1.1) Three characteristic sections can be identified in the gravimetrically determined water content curves.

- Starting from the dry end (left-hand side in the plots), the first section shows a slow but steady increase in water content.
- In most cases, a second section with a somewhat higher, but still moderate, increase follows.
- In the third section, a very strong increase is observed. The final high water content marks the position of the highly saturated zone at the wetted end of the sample (right-hand side of the plots).

(1.2) The water content at the dry side of the MX-80 samples was determined to be around 30 % for samples prepared from granular MX-80 bentonite with a density of 1.4 g/cm³ and around 20 % for granular material with a density of 1.6 g/cm³. For powdery material, values of 20 % were measured for samples with a density of 1.4 g/cm³, and values of 15 % to 18 % were obtained for a density of 1.6 g/cm³.

(1.3) At the dry side, the powdery Calcigel samples displayed a water content of approximately 10 %, except for the samples with a density of 1.8 g/cm³, for which values of approximately 14 % were measured.

(1.4) At the wet side, water contents in the range of 100 % and higher were measured for MX-80.

(1.5) In contrast to the MX-80 samples, the water content of Calcigel at the wet side amounted to only approximately 35 %.

(1.6) The thickness of the narrow, highly saturated zone appears to be in the range of 1 to 2 mm for both MX-80 and Calcigel.

3.6.5 Features in the PC1 data

(2.1) Starting from the dry sample end, the PC1 data remain nearly constant over 1/3 to 2/3 of the sample length, whereas the reference data indicate an increase. This applies to four samples: samples 1 and 2 of granular and powdery MX-80 with a density of 1.4 g/cm³.

(2.2) In the data of seven samples, even a slight decrease is observed: samples 1 and 2 of powdery MX-80 with a density of 1.6 g/cm³ and all Calcigel samples except sample 2 with a density of 1.6 g/cm³.

(2.3) In five samples, an additional stronger initial decrease over approximately 10 mm is observed:

- sample 2 of granular MX-80 with a density of 1.6 g/cm³
- sample 1 of powdery MX-80 with a density of 1.6 g/cm³
- samples 1 and 2 of Calcigel with a density of 1.4 g/cm³
- sample 1 of Calcigel with a density of 1.6 g/cm³
- sample 2 of Calcigel with a density of 1.8 g/cm³

(2.4) At the wet end, two characteristic features are observed in the PC1 data. Either the determined water content increases continuously up to an end value (5 samples), as observed for

- sample 1 of granular MX-80 with a density of 1.4 g/cm³

- sample 2 of powdery MX-80 with a density of 1.6 g/cm³
- samples 1 and 2 of Calcigel with a density of 1.4 g/cm³
- sample 2 of Calcigel with a density of 1.8 g/cm³

or a peak value is reached at a short distance from the wet end, after which the water content values decrease steeply again (9 samples), as observed for

- sample 2 of granular MX-80 with a density of 1.4 g/cm³
- samples 1 and 2 of granular MX-80 with a density of 1.6 g/cm³
- samples 1 and 2 of powdery MX-80 with a density of 1.4 g/cm³
- sample 1 of powdery MX-80 with a density of 1.6 g/cm³
- samples 1 and 2 of Calcigel with a density of 1.6 g/cm³
- sample 1 of Calcigel with a density of 1.8 g/cm³

(2.5) The highly saturated zone is detected in terms of location in four samples:

- sample 2 of powdery MX-80 with a density of 1.6 g/cm³
- samples 1 and 2 of Calcigel with a density of 1.4 g/cm³
- sample 1 of Calcigel with a density of 1.8 g/cm³

(2.6) Detection of the water content by the SWIR-method is sensitive to the structure of the bentonite material before compaction. Greater scatter of data points is observed for granular material than for powdery material.

3.6.6 Features in the greyscale data

(3.1) Constant values over the first 10 to 20 mm are observed in seven samples:

- sample 2 of granular MX-80 with a density of 1.4 g/cm³
- sample 1 of granular MX-80 with a density of 1.6 g/cm³
- sample 1 of powdery MX-80 with a density of 1.4 g/cm³
- sample 2 of powdery MX-80 with a density of 1.6 g/cm³
- sample 2 of Calcigel with a density of 1.4 g/cm³
- sample 1 of Calcigel with a density of 1.6 g/cm³
- sample 2 of Calcigel with a density of 1.8 g/cm³

(3.2) A slight decrease over the first 10 to 20 mm is observed in four samples:

- sample 1 of granular MX-80 with a density of 1.6 g/cm³
- sample 2 of powdery MX-80 with a density of 1.4 g/cm³
- sample 1 of powdery MX-80 with a density of 1.6 g/cm³
- sample 1 of Calcigel with a density of 1.4 g/cm³

(3.3) An additional strong initial decrease is observed in two samples:

- sample 1 of powdery MX-80 with a density of 1.6 g/cm³
- sample 2 of Calcigel with a density of 1.4 g/cm³

(3.4) An increase from the beginning is observed in two samples:

- sample 2 of Calcigel with a density of 1.6 g/cm³
- sample 1 of Calcigel with a density of 1.8 g/cm³

(3.5) At the wet end, two characteristic features can also be differentiated in the greyscale data. Either a peak value is reached at a short distance from the wet end, after which the water content values decrease steeply again (9 samples), as observed for

- sample 1 of granular MX-80 with a density of 1.6 g/cm³
- samples 1 and 2 of powdery MX-80 with a density of 1.6 g/cm³
- all Calcigel samples

or a plateau is observed at the wet end that is usually larger than the highly saturated zone indicated by the gravimetric data (4 samples):

- sample 2 of granular MX-80 with a density of 1.4 g/cm³
- sample 2 of granular MX-80 with a density of 1.6 g/cm³
- samples 1 and 2 of powdery MX-80 with a density of 1.4 g/cm³

(3.6) Characteristic local depressions in the water content data at approximately 13 mm and 26 mm are identified in seven samples:

- sample 2 of powdery MX-80 with a density of 1.6 g/cm³
- samples 1 and 2 of Calcigel with a density of 1.4 g/cm³, only at 13 mm
- samples 1 and 2 of Calcigel with a density of 1.6 g/cm³ and 1.8 g/cm³

(3.7) The highly saturated zone is detected in terms of location in one sample:

- sample 2 of granular MX-80 with a density of 1.6 g/cm³

(3.8) Detection of the water content by the greyscale-method is sensitive to the structure of the bentonite material before compaction. Greater scatter of data points is observed for granular material than for powdery material.

3.7 Interpretation of the results

3.7.1 General conclusions

Although the results obtained with the two investigated new measurement methods differ in several respects from the gravimetric measurements described above, low water contents at the dry end of the samples and high water contents at the wet end are consistently indicated by all three methods. At the present stage of development, however, the new methods provide only a qualitative impression of the strongly varying water content distribution rather than precise values, despite their superior spatial resolution.

The location of the thin, highly water-saturated zone could be identified from the PC1 data in one MX-80 sample and three Calcigel samples, whereas it was detected by the optical method in only one MX-80 sample. The maximum water content was reproduced for the Calcigel samples, but was clearly underestimated for MX-80. These observations support the conclusion that meaningful application of the new detection methods may be limited to qualitative investigations of water content distributions.

As a potentially relevant side aspect, it should be noted that this Topic was not intended to investigate possible effects of the initial bentonite material used for compaction—powder or granules—on water uptake. However, the pronounced difference in the detected water content at the dry side of the MX-80 samples strongly suggests substantially faster water uptake for bentonite compacted from granular material.

3.7.2 Results specifically from the greyscale method

The depressions and shifts observed in the greyscale data (see subsections 3.6.2 and 3.6.3) appear to coincide with the transition zones between the three sequentially compacted bentonite layers described in section 3.3. These transition zones are directly visible

in the photographs of two Calcigel samples in Fig. 3.5. Although they were not directly documented, the interfaces between the three material layers appear from the data to be located at 12 to 13 mm and approximately 25 mm. Similar conditions can also be assumed for the MX-80 samples.

Two observations indicate that the brightness of the transition zone is not related to water content. First, the brightness can already be observed after the loose material has been filled into the test cell, before initiation of the third and final compaction step. Second, the local brightness at the transition zones is not reflected in the highly resolved PC1 data; it would also have been lost in the comparatively coarse gravimetric measurements. The effect therefore appears to be caused by the procedure used to fill the bentonite powder into the test cell, although a conclusive explanation has not yet been identified.

In terms of absolute values, the optical method appears to provide rather unreliable results for the strongly varying water content in MX-80 samples, since the reference curves from the gravimetric measurements are not reproduced in most cases. In this context, feature (3.5) listed in subsection 3.6.6 indicates that, in the majority of cases (9 out of 14), the water content decreases at the wet end in an unphysical manner. This observation was entirely unexpected and coincides with similar results obtained with the SWIR-method (see subsection 3.7.3). No explanation for this phenomenon was identified.

However, the results appear to agree more closely in the range of lower water contents. For Calcigel, the water contents are reproduced satisfactorily up to 15 % for sample densities of 1.4 and 1.6 g/cm² and up to 25 % for a density of 1.8 g/cm³. Beyond these ranges, the optical method can provide only a qualitative impression of the water content distribution, since the absolute values may deviate substantially.

The strong deviations of the greyscale data for the two low-density samples above 15 % water content, and the less pronounced deviations for the samples with higher densities above 25 %, are essentially continuous. They therefore appear to be attributable to nonlinearity in the relationship between greyscale value and water content, which is less pronounced in samples with higher densities.

The latter observation may indicate that the nonlinearities are related to the amount of hydrated water in the bentonite. In principle, variation of the bentonite density at constant

water content results in a change in porosity. Although the ratio of water to solid particles remains constant, this does not apply to the volumetric ratio of pore air to solid particles, which is likely to affect light reflection at the sample surface.

In principle, all these effects could be corrected by calibration. To be useful, however, such calibration would have to account not only for water content, but also for bentonite density and possibly even for the grain size of the original material. Calibration would therefore require sufficient resolution at least with respect to both water content and density, which made the required effort impracticable within the framework of the present project.

The optical measurement set-up was initially planned to be largely independent of the illumination type, i.e. visible or SWIR light. As explained in subsection 2.1.2, the original plans could not be implemented, resulting in a substantially different set-up for SWIR-data.

3.7.3 Results specifically from the spectrometer measurements

At the present stage, it must be concluded that spectrometer measurements can provide reasonably good results for water content at low bentonite densities. For bentonite at medium and higher densities, however, reasonable values cannot be obtained. As with the visual light measurements, only a qualitative impression of the water content distribution can be provided.

The relationship between spectrometer data and water content is even more complex than the evaluation of visual light measurements. SWIR-data must be evaluated by principal component analysis, which identifies general changes but does not assign them to a specific cause. The pronounced profiles observed for the first principal component (PC1) may therefore result not only from variations in water content, but also from other quantities, such as variations in density.

For the low-density samples, water content indeed appears to be the main factor controlling the characteristics of the PC1-curves. For the medium- and high-density samples, however, additional effects also appear to be relevant, since larger parts of the curves seem to be largely unaffected by water content. Identification of the additional influencing quantities would require further investigations that could not be covered within the

framework of the present project. Moreover, even if these additional quantities were known, it currently remains unclear whether correction by calibration would be possible.

Finally, observation under SWIR-light was found to be impossible at water contents exceeding 45 % for granular MX-80 and 55 to 65 % for powdery MX-80. These critical values are subject to considerable uncertainty, since robust scaling (cf. section 3.6) was not possible for MX-80. However, after a critical water content had been exceeded, the spectrometer data indicated a strong decrease, although a further increase was expected (cf. feature (2.4) in subsection 3.6.5).

The situation differed for Calcigel, because the gravimetrically determined maximum water content was comparatively low at 35 %. In several cases, the same effect of a strong decrease instead of a high end value was observed when this critical water content was approached or exceeded.

4 Topic 2 – Free swelling into limited space

The initial objective of the work under this topic was to investigate options for optimizing the swelling behaviour of pellet fillings towards full homogenization. However, this objective was compromised by the unsatisfactory results obtained during development of an operational online SWIR-observation method. The results therefore constitute a proof of concept for this type of test rather than a comprehensive and systematic investigation.

4.1 Test set-up

The test set-up was similar to that used for Topic 1. Since one end of the compacted bentonite samples was intended to adjoin a limited free space for swelling, wetting was planned to be applied from above, in contrast to the tests conducted under Topic 1. For this purpose, the free space was to be flooded as rapidly as possible to mimic instantaneous wetting.

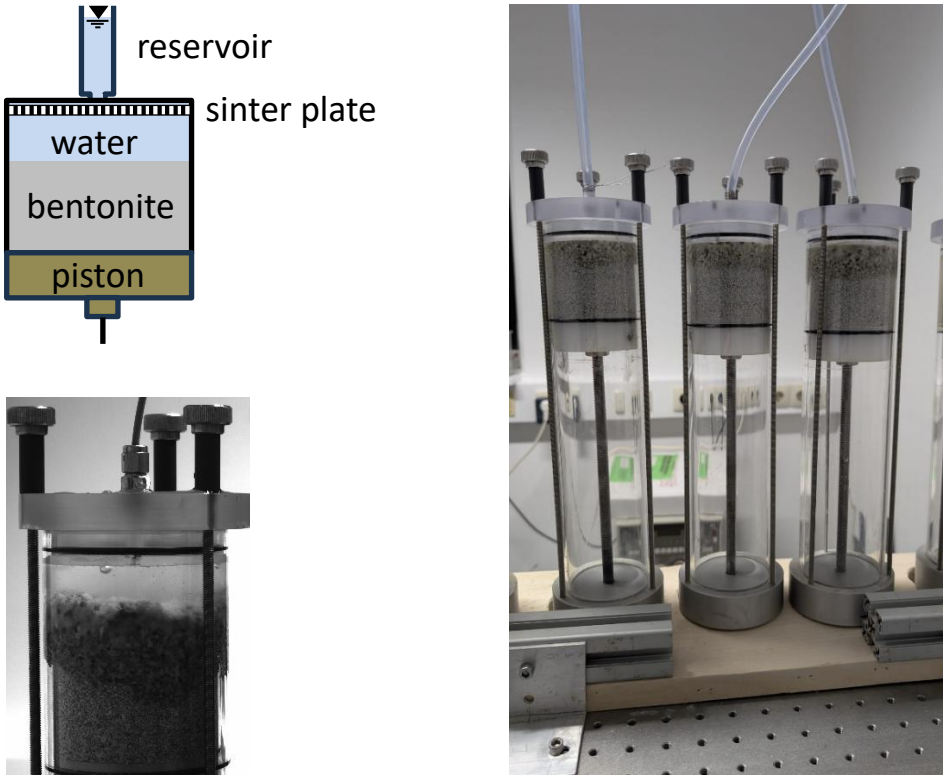


Fig. 4.1 Sketch of the test principle (top left), photographic close-up of a flooded test cell at the beginning (bottom left), actual test set-up (right)

4.2 Test procedure

The samples were compacted directly in the test cell in three layers to a height of 50 mm to prevent gaps between sample and cell wall. Subsequently, the free volume above the sample was adjusted by positioning the piston of the test cell. The assembled test cells were then placed on the optical table, and the camera was aligned accordingly. A water reservoir was connected to the top of each test cell to enable rapid flooding. To prevent trapped air in the void volume from hindering water ingress, an additional air outlet was installed at the top of the cell.

After image acquisition had been initiated, the test cells were flooded sequentially. For technical reasons, the first sample was connected to the reservoir 4 minutes after image acquisition had started. Once water emerged from the additional outlet, a silicone plug was inserted to prevent further leakage. This procedure required approximately 5 minutes; consequently, flooding of the second cell was started after approximately 9 minutes and flooding of the third cell after 14 minutes. Particularly during this period, disturbances of the lighting by the operator could not be avoided. These disturbances may explain some unusual curve shapes obtained with the optical method in the general area of the vanishing gap. The connections between the gaps and the reservoir were maintained throughout the entire test period. The testing times were 290 hours for MX-80 and 522 hours for Calcigel.

After terminating the tests, the samples were removed from the test cells for further investigation using the SWIR spectrometer. The samples were immediately placed on the movable stage, with the spectrometer probe positioned directly above the sample surface. By translating the stage beneath the stationary probe, complete profiles across the samples were acquired. A step size of 0.3 mm was selected to achieve a high spatial resolution while keeping the measuring period for each profile short to prevent significant drying of the sample during the measurement procedure. To account for local mineralogical heterogeneity, three measurement profiles were recorded for each sample.

4.3 Materials

The samples were compacted from granular MX-80 with a grain size of less than 2 mm to a density of 1400 g/cm³ and from powdery Calcigel to a density of 1400 g/cm³. Wetting was performed with tap water.

4.4 Measurement results

Three exemplary images of an MX-80 specimen swelling into the limited free space at the top of the test cell are shown in Fig. 4.2 for the test times 0 s, 1 min, and 2 h. They show rapid filling of the available space. Greyscale images of the swelling samples were recorded at one-minute intervals throughout the entire test duration to monitor the temporal evolution of the swelling process.

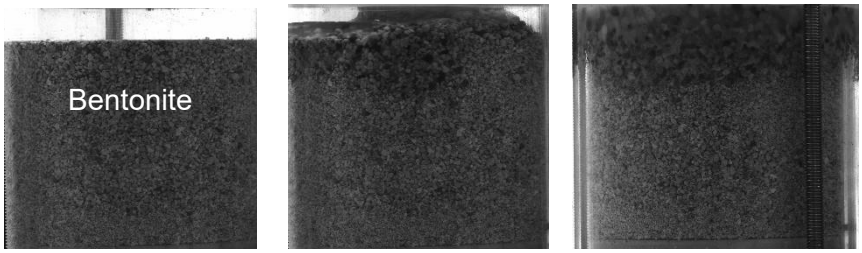


Fig. 4.2 Swelling of the sample into a gap of 1 cm width, initial conditions (left), after 1 minute (middle) and after 2 hours (right)

After terminating a test, spectral data were collected along three profiles on each sample with the spectrometer. A principal component analysis (PCA) was then performed on the spectral dataset. It revealed that the first principal component (PC1) accounted for 99 % of the total variance, indicating that it captured the dominant changes related to moisture distribution and possibly structural alteration.

In principle, spectrometer data were acquired at the end of the tests in the same way as for the samples investigated under Topic 1, where the samples were also subjected to strong wetting at one end. Based on the experience from Topic 1 that the SWIR-method would not provide reliable absolute water content values, no effort was made to scale the spectral data. Instead, only a qualitative interpretation of the SWIR-data is provided here.

The PC1 scores for the MX-80 samples and the Calcigel samples are shown in Fig. 4.3 and Fig. 4.4, respectively. They are plotted over the entire sample length in such a way that the dry end is always located at the right-hand side. The position of the sample and thus its dry end therefore shifts to the right with increasing gap size.

In general, the PC1-data for MX-80 indicate approximately two sections. At the wet end of the sample, a depression-like shape can be observed. This shape is probably attributable to pronounced swelling into the gap, resulting in very low dry density and high water content. This process is accompanied by structural alterations and, consequently, by changes in the optical properties of the material, as observed under Topic 1. The size of the depression increases with gap size, whereas the length of the second section with converging values remains largely unchanged.

Beyond the depression and towards the dry end, a subsequent decrease converging towards a value representing the initial water content was found. This section is assumed to approximately reflect the actual course of the water content curve.

By contrast, the data for the Calcigel samples show a comparatively constant level of PC1 scores. It therefore appears that the experiments with MX-80 ended after 290 hours while the dynamic water uptake process was still ongoing, whereas this process had already been completed after 520 hours for the Calcigel samples.

At the end of the experiment, complete filling of the entire test volume, including the initially void space, by swollen bentonite was observed in all samples. This observation again confirms pronounced and rapid volumetric expansion into unconfined space.

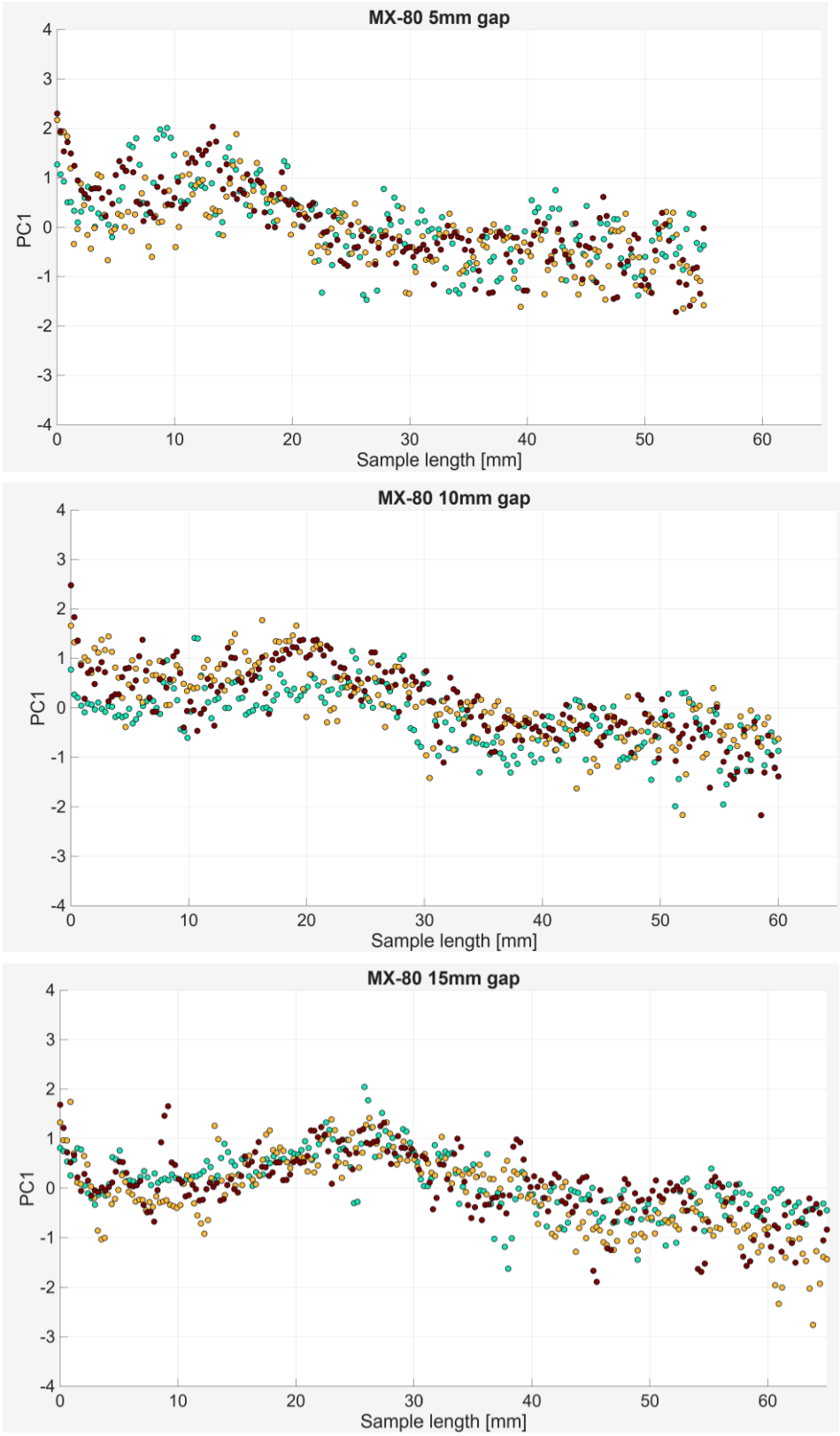


Fig. 4.3 PC1 scores for MX-80 samples with a target gap of 5 mm (top), 10 mm (middle), and 15 mm (bottom); wet end on the left, dry end on the right

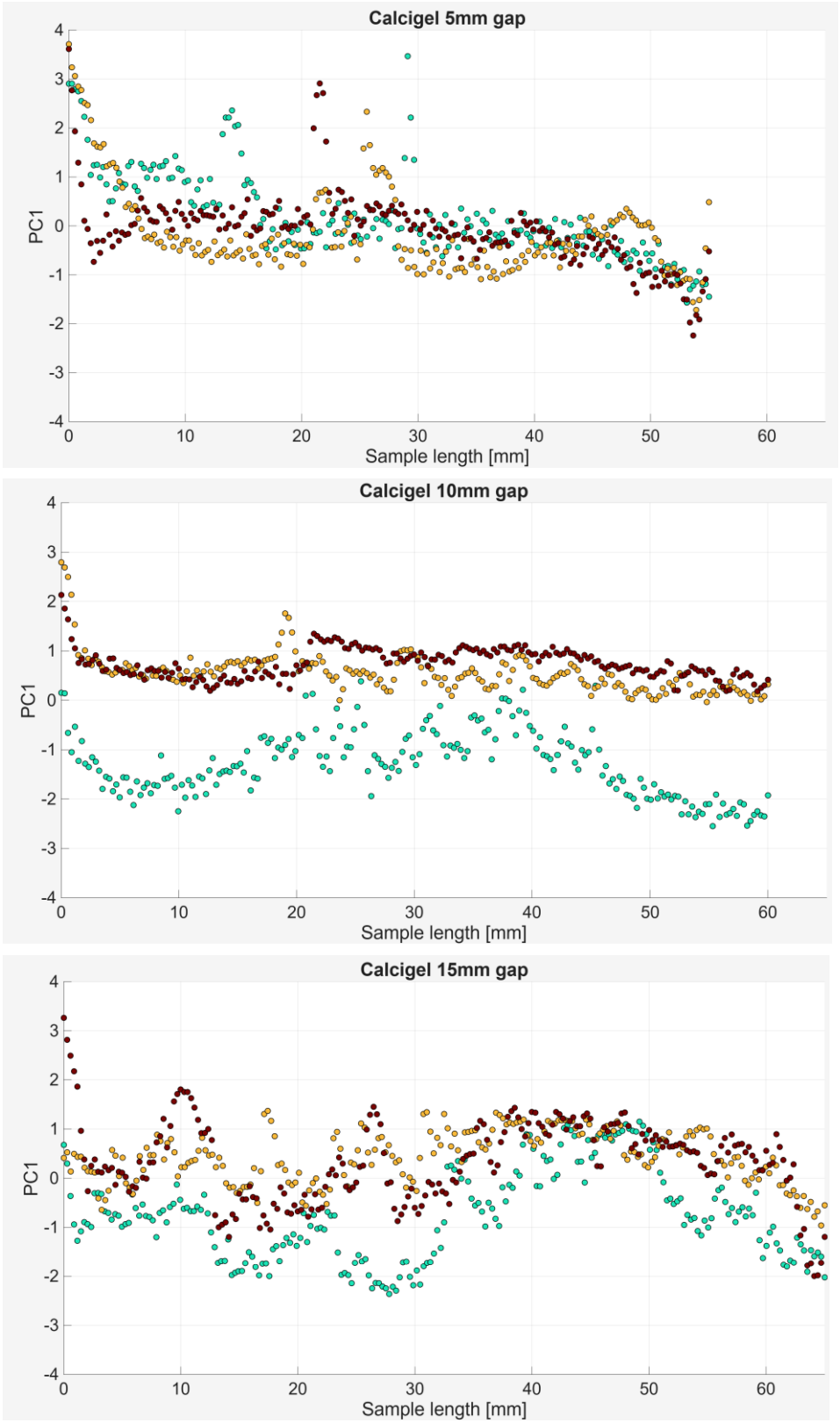


Fig. 4.4 PC1 scores for Calcigel samples with a target gap of 5 mm (top), 10 mm (middle), and 15 mm (bottom); wet end on the left, dry end on the right

In contrast to the spectrometer measurements, which could only be performed after the tests, the transparent cells allowed the optical measurement to be applied throughout the entire test duration. This approach enabled observation of gap filling by the swelling bentonite as well as qualitative assessment of water migration into the bentonite samples. However, for the same reason as for the SWIR-data, the data were not scaled.

For evaluation of the optical data, all recorded images were processed according to the workflow described in subsection 2.1.1 The plots shown in Fig. 4.5 for MX-80 and in Fig. 4.6 to Fig. 4.8 for Calcigel illustrate the temporal evolution of greyscale values along the samples. A series of curves, coloured according to elapsed time, is used to facilitate intuitive recognition of the process. Greyscale curves are plotted in Fig. 4.5 to Fig. 4.8 for the same testing times, where applicable, to facilitate comparison of the results. The selected time points were chosen to illustrate both gap filling and, subsequently, the progression of water into the bentonite. These times are: 0, 1, 3, 5, 6, 12 minutes and 1, 10, 20, 40, 60, 80, 100, 150, 200, 250, 300, 350, 400, 450, and 500 hours.

Initially, the gap was air-filled and therefore appeared almost white in the images, corresponding to high greyscale values or very low water contents. In the presence of water, the shades of grey were darker than for air but brighter than for bentonite at the initial water content. For the bentonite part of the samples, an essentially constant initial water content was indicated. With increasing local water content, however, the greyscale values decreased. These observations apply to all samples.

The optical data from the gap systematically indicate smaller gap widths than the target widths of 5, 10, and 15 mm, with differences of approximately 2 to 3 mm in all cases. Since the piston above the bentonite samples was positioned rather precisely, the reason for this observation is not entirely clear. It may, however, be caused by optical distortion, since the camera axis was directed towards the centre of the test cell set-up.

The individual process dynamics are subsequently evaluated according to the following characteristics:

- time required for the bentonite to reach completely into the gap
- velocity of the wetting front into the sample

- reaching of steady-state within the testing times

- shape of the (expected) steady-state distribution of greyscale values

Since the gaps were not instantaneously flooded with water but were instead filled by a rapid succession of droplets, the point in time at which the expanding bentonite reached the sinter plate representing the limit of the available swelling space is difficult to define. Overall, all gaps were filled by the expanding bentonite within less than 10 minutes. The filling time was approximately the same for MX-80 and Calcigel.

In all plots, a steep greyscale gradient can be observed advancing into the bentonite. As a proxy for the second characteristic, the velocity of this wetting front into the sample, the front position relative to the initial bentonite boundary after 1 hour wetting time is used. Tab. 4.2 compiles the resulting penetration depths. An increasing penetration depth with increasing gap width is apparent.

Tab. 4.1 Penetration depth after 1 hour relative to the initial bentonite boundary

Bentonite	5 mm gap width	10 mm gap width	15 mm gap width
MX-80	(16 mm)[5]	13 mm	13 mm
Calcigel sample 1	11 mm	18 mm	25 mm
Calcigel sample 2	10 mm	20 mm	22 mm

The next characteristics evaluated from the greyscale plots are whether steady-state was reached within the testing time and which shape of the steady-state curve can be observed or inferred. Due to the different testing times for the MX-80 and Calcigel batches, direct comparison between the two bentonite types is not possible.

Only the MX-80 sample with a 5 mm gap, Calcigel sample 1 with a 5 mm gap, and the two Calcigel samples with a 15 mm gap appear to have reached steady-state, as indicated by convergence of the greyscale curves towards a specific distribution. Among these samples, the two samples with a 5 mm gap indicate pronounced heterogeneity. The steady-state greyscale distribution appears as if the wetting process had simply terminated

[5] The one hour curve also marks the steady-state curve

prematurely. By contrast, the two Calcigel samples with a 15 mm gap show an essentially constant shade of grey over the entire sample.

The MX-80 samples with 10 mm and 15 mm gaps still indicate a moving wetting front. A steady-state distribution can therefore not be inferred. The remaining Calcigel samples have not yet reached steady-state, but suggest residual inhomogeneity. The data indicate that this inhomogeneity becomes less pronounced with increasing initial gap size for swelling.

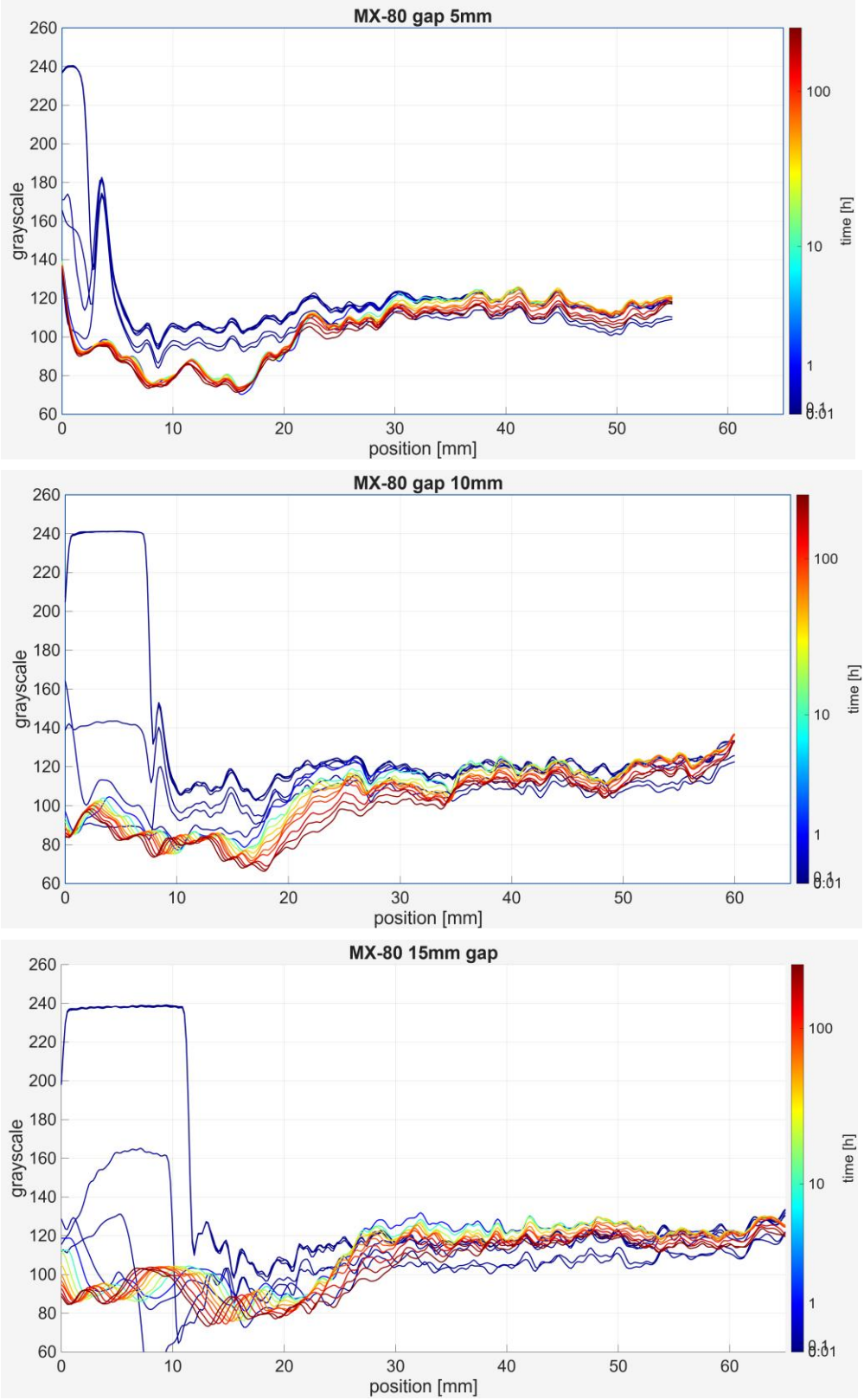


Fig. 4.5 Evolution of greyscale values along the MX-80 samples; target gap size 5 mm (top), 10 mm (middle), and 15 mm (bottom); gap → left, dry end → right

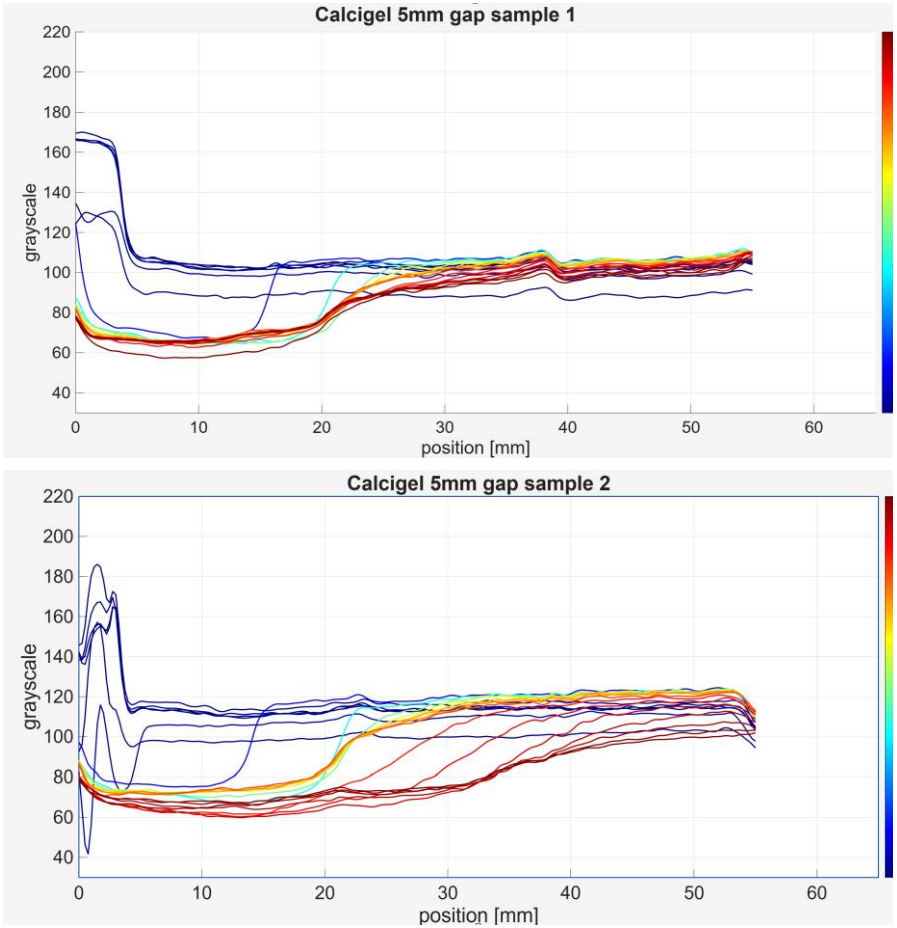


Fig. 4.6 Evolution of greyscale values along the two Calcigel samples; target gap size 5 mm; sample 1 (top), sample 2 (bottom); gap to the left, dry end to the right

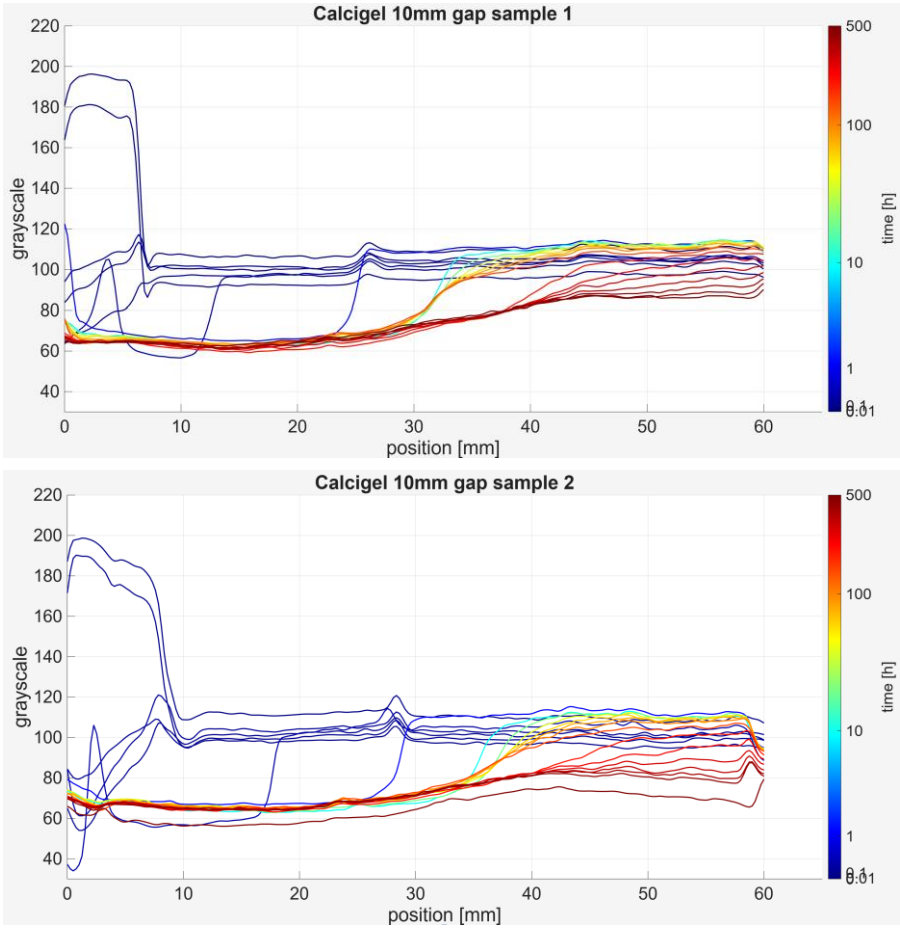


Fig. 4.7 Evolution of greyscale values along the two Calcigel samples; target gap size 10 mm; sample 1 (top), sample 2 (bottom); gap to the left, dry end to the right

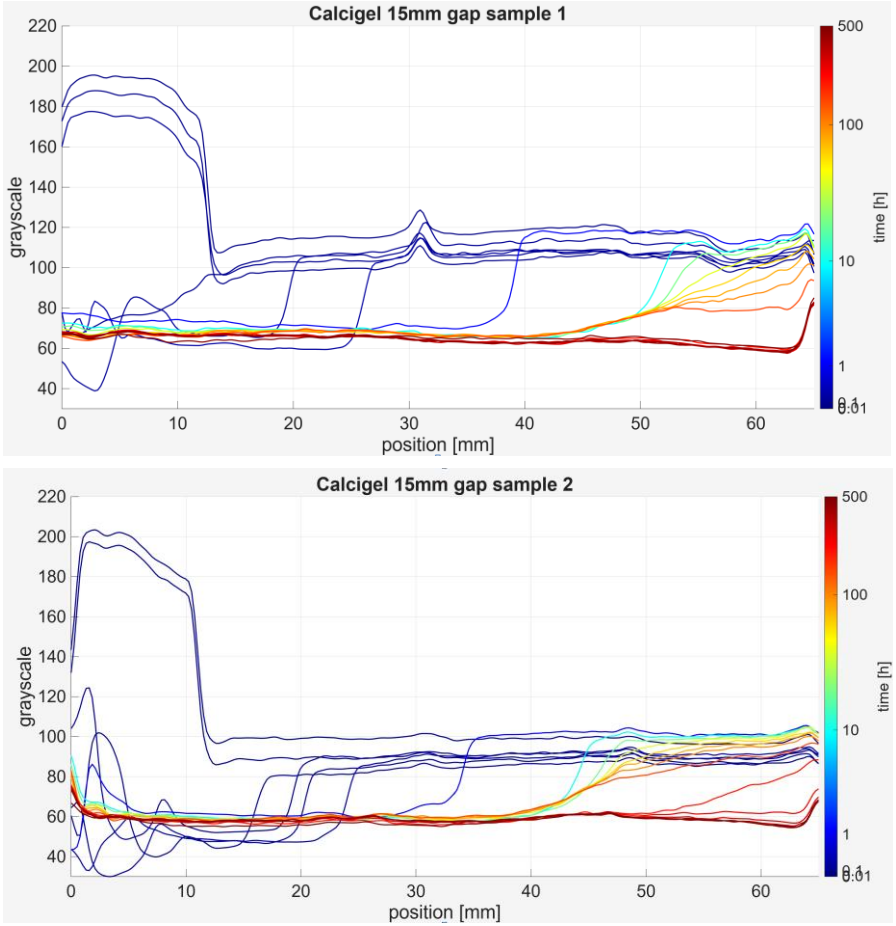


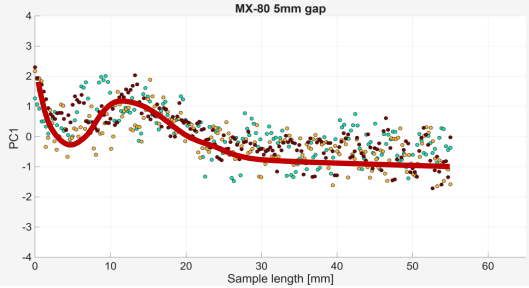
Fig. 4.8 Evolution of greyscale values along the two Calcigel samples; target gap size 15 mm; sample 1 (top), sample 2 (bottom); gap to the left, dry end to the right

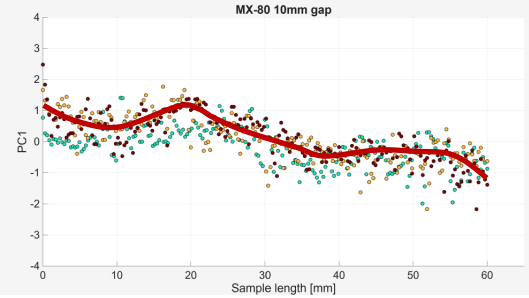
A final analysis concerns the consistency of visual and SWIR data. For this purpose, two arrays of plots are arranged with Fig. 4.9 to Fig. 4.11 for MX-80 and with Fig. 4.12 to Fig. 4.14 for Calcigel, respectively. The first columns of plots (Fig. 4.9 and Fig. 4.12, respectively) show the SWIR-data over the sample length ordered by the gap width. These data are overlain by a mean PC1 score that was fit by eye. The second column (Fig. 4.10 and Fig. 4.13, respectively) is built up by copies of the optical data plots where the curves for the latest time points are highlighted by a thick line. These curves are closest to the end-of-test conditions at which the spectrometer measurements had been performed.

In the third column (Fig. 4.11 and Fig. 4.14, respectively), the two thick lines from the first and the second column are arranged by eye in such a way that the sections representing the dry end of the samples are optimally aligned to each other. To that end, the curves from the optical data were vertically mirrored as the PC1 data are proportional to the water content but the greyscale values are inverse proportional.

The comparison of optical and SWIR-data for MX-80 shows a quite striking resemblence of the two curves. For the Calcigel samples, the two curves are reasonably similar as well but the fit is not as good as for MX-80. While this may have to do with the type of bentonite, another explanation can be speculated about. The three profiles taken by the spectrometer along each sample show quite different curve shapes. There is no obvious way to determine a characteristic shape. Quite a number of differently assumed shapes appear to fit the SWIR-data for Calcigel, so the correct one is anyone’s guess. As mentioned already, a curve reasonably fitting also the optical data has been found, though.

The reason for the diverging three profiles from the Calcigel samples is also not entirely clear. However, the tests for MX-80 did not last as long as those for Calcigel. As a consequence, the true water content profiles at the end of the tests were more pronounced in the MX-80 samples than in the Calcigel samples. Less differences in the spectrometer data for Calcigel may have aggravated difficulties of the PCA to represent an only little varying water content.





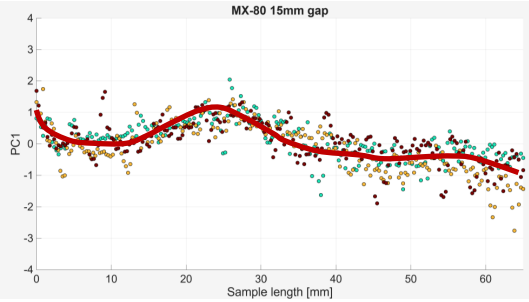
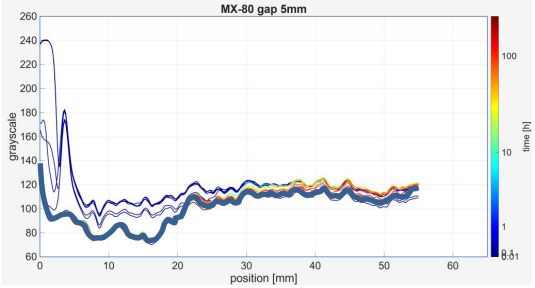
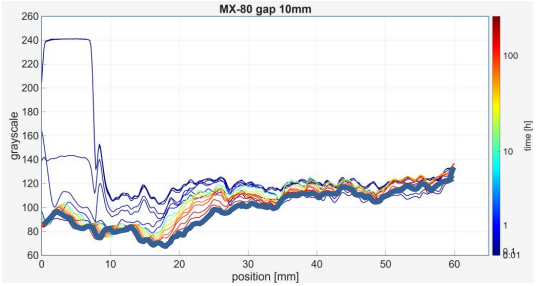


Fig. 4.9 Mean SWIR-data on MX-80 samples; fit by eye





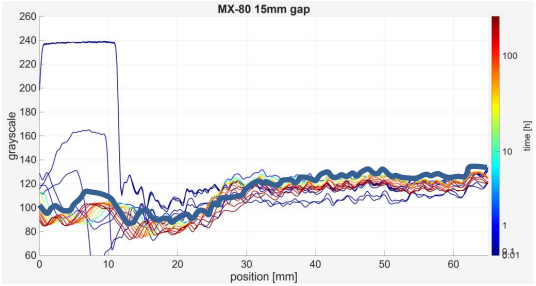
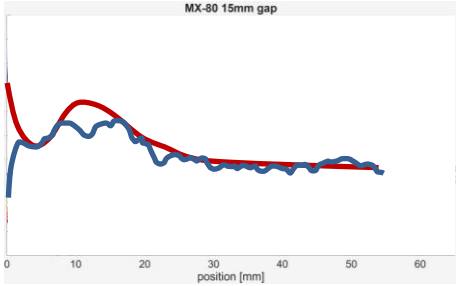
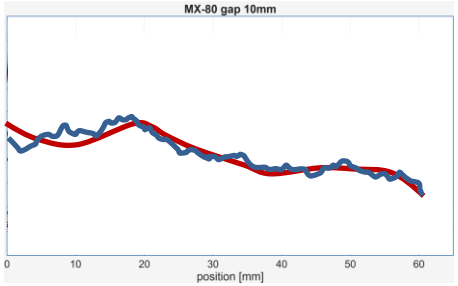


Fig. 4.10 Optical end-of-test data on MX-80 samples





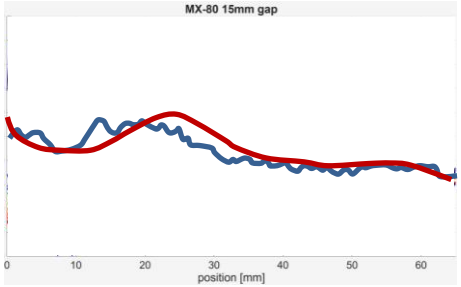
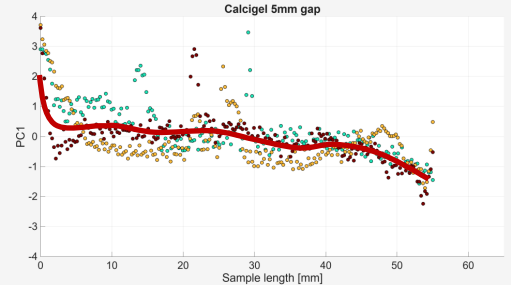
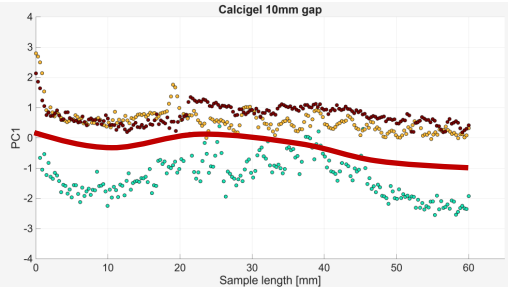


Fig. 4.11 Overlay of the curves from Fig. 4.9 and vertically mirrored curves from Fig. 4.10





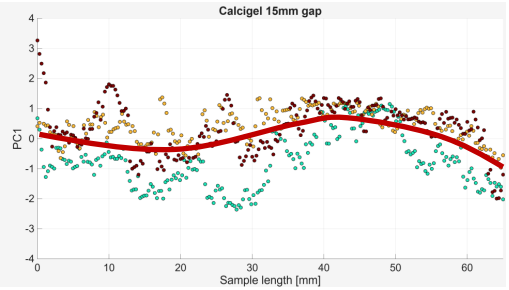
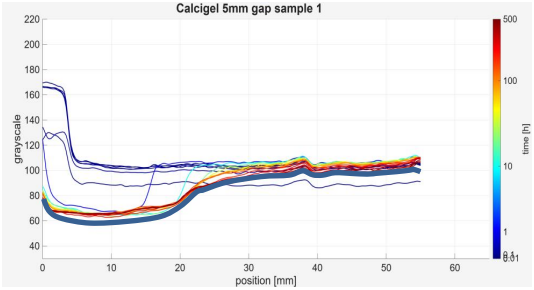
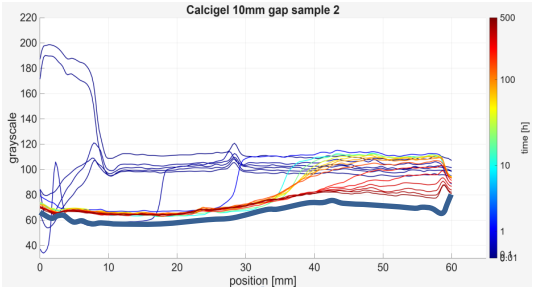


Fig. 4.12 Mean SWIR-data on Calcigel samples; fit by eye





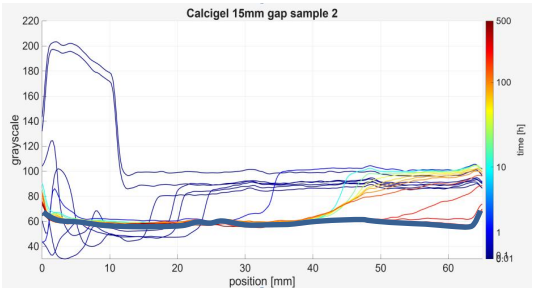
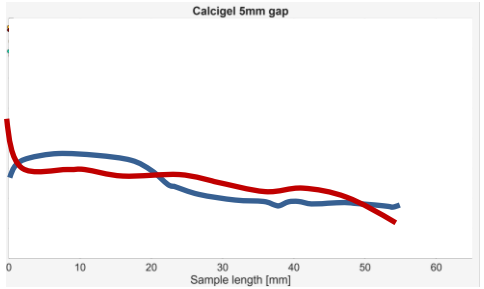
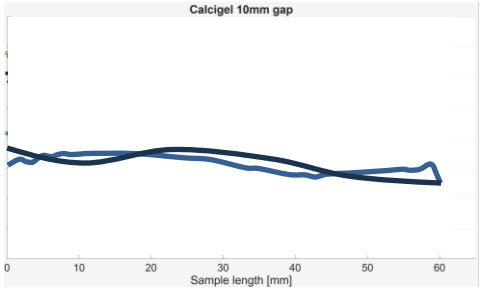


Fig. 4.13 Optical end-of-test data on Calcigel samples





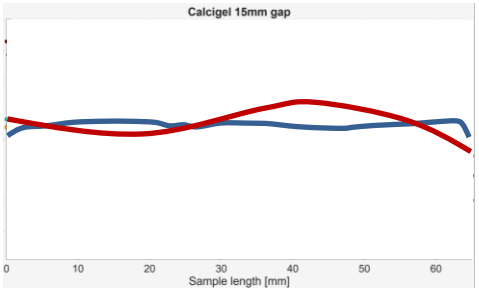


Fig. 4.14 Overlay of the curves from Fig. 4.12 and vertically mirrored curves from Fig. 4.13

4.5 Interpretation of the results

SWIR-method

Water uptake by compacted bentonite without initial confinement is accompanied by pronounced swelling. Initially, very high water content values are therefore reached in the swelling-affected zone of the bentonite. As already suggested by the results from Topic 1, no conclusive data from the SWIR-method could be expected for early test times.

However, spectrometer measurements could only be performed at the end of a test. Due to homogenization, the initially high water content at the wet end decreases as water from the gap is redistributed over the sample. For a state of complete homogenization, as apparently observed for Calcigel, the test design allows the final constant water content to be estimated. Depending on the initial water content and gap width, this final water content should range between 20 % and 35 %. These values are well within the detection range of the SWIR-method.

This interpretation is supported by the fact that the breakdown of PC1-data observed under Topic 1 is not observed in the results for Calcigel under Topic 2. Furthermore, the bentonite density lies within the range identified under Topic 1 as providing reliable SWIR-data for the water content. The spectrometer measurements are therefore meaningful in that they indicate a constant water content.

In the results for MX-80, the penetration depth of water into the samples can clearly be determined from a peak between approximately 10 and 25 mm, depending on gap width. The water uptake process in these MX-80 samples was therefore evidently still ongoing at the end of the tests. By contrast, the comparatively constant profiles for Calcigel indicate that an end state of homogenization had been reached. They suggest a high degree of homogenization.

Optical method

With the optical method, the transient wetting process becomes observable, providing insight into the water uptake dynamics. These dynamics reveal characteristic features of the process and provide a basis for determining whether steady-state conditions have been

reached and what the associated water content distribution looks like. If transient wetting has advanced sufficiently, the steady-state distribution can at least be estimated.

Since the Calcigel samples were wetted for a longer period than the MX-80 samples, the optical results for Calcigel provide a clearer representation of the wetting process. After the gap had been partly filled by bentonite, a steep wetting front with a length of not more than 1 to 2 mm was observed to advance into the sample. At a distance depending on gap width, however, this steep front began to level out and, in the long term, converged towards a steady-state distribution.

Two principal end states of the water content distribution can be differentiated from the results. In the samples with the narrow gap, a rapid transition from strongly wetted bentonite to the initial water content can be observed. In the case of the large gap, wetting resulted in a fully homogeneous water distribution.

In the samples with an intermediate gap, steady-state has not been reached yet. However, the water content profiles indicate a steady-state distribution that has a much larger transition zone which is also located much deeper into the samples. It thus seems, that the length of the transition zone as well as the location is a function of the gap width. Indeed, the results give rise to the hypothesis that the ratio of gap width to sample length determines the degree of steady-state heterogeneity.

5 Topic 3 – Scaling isotherms by bentonite types and clay content

5.1 Experimental methods

5.1.1 Classic experimental set-up

Isotherms are usually determined pointwise from the water content of bentonite samples at equilibrium with a predefined relative humidity in the ambient atmosphere. This is commonly achieved by placing the bentonite in a desiccator above a salt solution that provides a controlled relative humidity (e.g. /WAD 04/). The sample mass is monitored at regular intervals to identify mass constancy. At equilibrium, the water content is determined by weighing and drying. The data pair consisting of water content and relative humidity from one sample defines one point on the isotherm. In the following, each data point characterising the course of an isotherm is referred to as a “sample point”, whereas the process of measuring such a data point is referred to as “sampling”.

Equilibrium in a single test is reached only after a considerable time; consequently, sampling an isotherm with a sufficient number of data points is highly time-consuming. To reduce the overall experimental duration, such tests are generally performed in parallel. In addition to the time required, the desiccator must be opened for weighing, thereby repeatedly disturbing the contained atmosphere.

5.1.2 Present experimental set-up

These disadvantages were circumvented by applying an automated procedure using an AquaLab Vapour Sorption Analyzer (VSA) /MET 23/, depicted in Fig. 5.1, left. In principle, this device is a small programmable climate chamber containing a high-precision balance. It enables continuous mass measurements of bentonite samples up to a mass of 5 g at controlled temperature and relative humidity, as illustrated in Fig. 5.1, right. The conditions of interest are selected and preset by the experimenter. Each condition, i.e. each temperature-humidity pair, is maintained until the mass changes determined by the integrated microbalance remain below a predefined threshold for a predefined number of consecutive measurements. In the present study, a mass change of less than 0.02 %/h for four

consecutive measurements was defined as the steady-state criterion. The mass was measured approximately every six minutes. After equilibrium had been reached, the chamber climate was automatically adjusted to the next preset temperature-humidity condition.

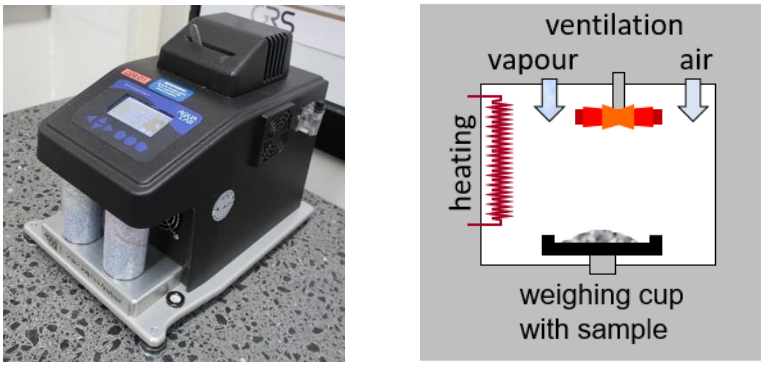


Fig. 5.1 Photo of the VSA during measurement (left), working principle (right); from /KRÖ 20/

Although the measurement principle is essentially identical to that used in classical methods, substantially less attendance is required. Owing to the small sample mass, the alternative technique is considerably faster and thus permits less laborious but nevertheless detailed sampling of isotherms. In addition, the complete data set is obtained from the same sample, thereby providing maximum consistency among the data points.

5.1.3 Determining isotherms

A comparatively large number of isotherm measurements has been reported for MX-80 bentonite compared with other bentonites. Among the most detailed data are those from /KAH 86/ and /SEI 14/, which are depicted in Fig. 5.2. These data probably show the most complex shape among the isotherms to be considered in the context of radioactive waste storage. This chapter therefore refers exemplarily to isotherms for MX-80.

When directly compared, the isotherms for MX-80 reported in the literature generally differ substantially in shape and absolute value /KRÖ 11/. Therefore, three aspects explaining these differences and providing a basis for a sound comparison are discussed below.

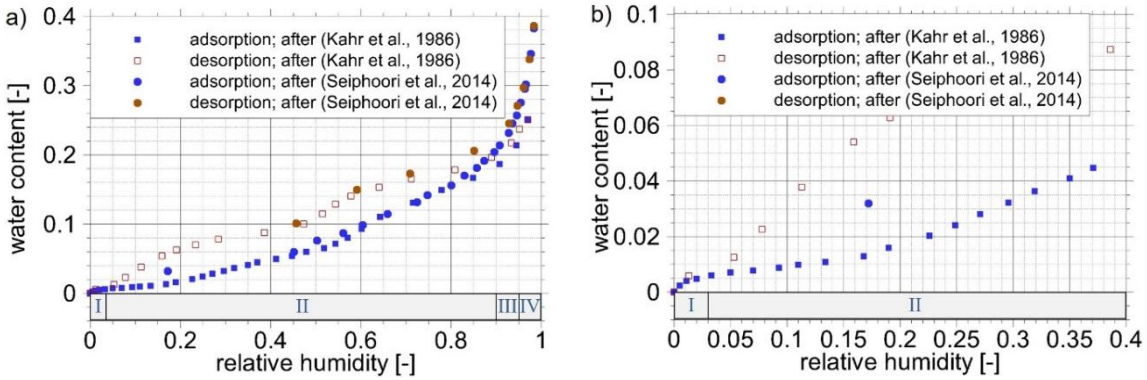


Fig. 5.2. Sections of the isotherms for MX-80 bentonite; a) full range, b) enlargement

Aspect 1: Smectite content

The most evident aspect is that bentonite is a natural product whose smectite and accessory mineral composition may vary even within a single quarry. Consequently, because the isotherm of MX-80 has been determined in several laboratories and at different times, the smectite content cannot have been identical in all cases. Since only smectite can take up water, variations in smectite content lead to differences between the corresponding isotherms that increase linearly with relative humidity. Accounting for the smectite content has already been shown to reconcile the measured isotherms to an encouraging degree /KRÖ 11/.

Aspect 2: Sampling data density

The possibility of programming the VSA comparatively freely with respect to the number and position of sample points on the isotherms required consideration of an appropriate best practice for data acquisition. This is particularly relevant for subsequent modelling of the re-saturation process, because numerical results are sensitive to the retention curves (e.g. /GEN 19/).

Since only discrete points can be determined in laboratory experiments, the true shape of the isotherm is effectively represented by a polygon. Because isotherms are generally curved, a minimum number of sampling points is required for a reasonable representation; this number increases with curvature and slope. Accordingly, relevant characteristics of the isotherm may be missed if an insufficient number of sampling points is used.

To derive a reasonable sampling scheme, either the true shape or an appropriate approximation must be known in advance. For this purpose, the detailed measurement results shown in Fig. 5.2 are sufficient. The agreement between the data sets is not exact but reasonably good, particularly considering that more than 30 years separate the individual measurements.

With respect to slope and curvature, these isotherms can be roughly divided into four sections. For reference, these sections are numbered from I to IV from left to right in Fig. 5.2. Below 3 % relative humidity (section I), the isotherms are strongly curved and connect the origin with an almost plateau-like part at the beginning of section II. Although slightly undulating, the major part of the isotherms between 3 % and 90 % relative humidity (section II) exhibits only a moderate slope. In section III, between 90 % and 95 %, the isotherms are again strongly curved. Section III merges smoothly into section IV, which exhibits a steep course and, in a mathematical sense, appears to converge towards a singularity at full vapour saturation. Indeed, no data point for 100 % could be found in the literature.

The technical limitations of the VSA did not permit sampling in the ranges of sections I and IV. However, excluding section I is probably not critical, because dry conditions below 3 % relative humidity, or a corresponding water content of approximately 0.6 %, are rarely expected under repository conditions.

Section IV of the isotherms is also of limited interest. Wetting at approximately 95 % relative humidity corresponds to full water saturation of compacted MX-80 at a dry density of 1500 kg/m³. This density approximately marks the minimum dry density required for buffer and backfill in a repository to ensure a minimum swelling pressure, e.g. /KRO 20/. At higher dry densities, less water can be taken up, thereby preventing a wetting state in section IV from being reached.

Against this background, a simple sampling scheme covering sections II and III with sample points at intervals of 0.05 (5 %) relative humidity was adopted. For procedural consistency, the same scheme was also applied to the Ca-bentonite Calcigel. The resulting sampling scheme is illustrated in Fig. 5.3.

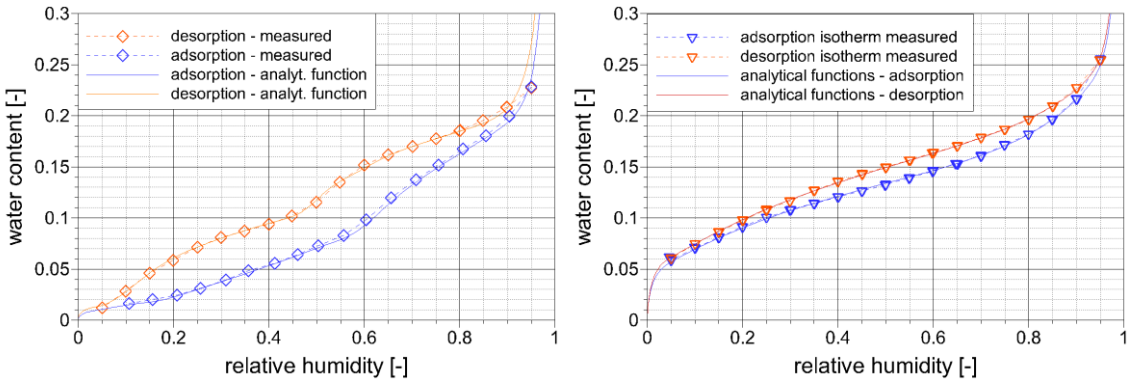


Fig. 5.3. Comparing sampled isotherms with analytical solutions; left: MX-80, right: Calcigel; from /KRÖ 20b/

The sampled isotherms of MX-80 appear to be just representative of the true shape. It is therefore evident that using fewer sample points may result in relevant features of the true isotherm shape being missed.

It should be noted that the isotherms for Calcigel were found to be considerably smoother than those of MX-80, with only one inflection point instead of several. The sampling scheme considered appropriate for MX-80 therefore provides a somewhat excessive resolution for Calcigel.

Aspect 3: Hydration history

The third aspect causing differences between isotherms measured by different parties concerns possible changes in the hydration path. For instance, when the path changes from wetting to drying, a drying path must branch off from the adsorption isotherm at the corresponding state and proceed towards the desorption isotherm. Such a path is referred to as a “scanline”; in this specific case, it is termed a “desorption scanline” to distinguish it from “adsorption scanlines”, which analogously branch off from the desorption isotherm (see Fig. 5.4).

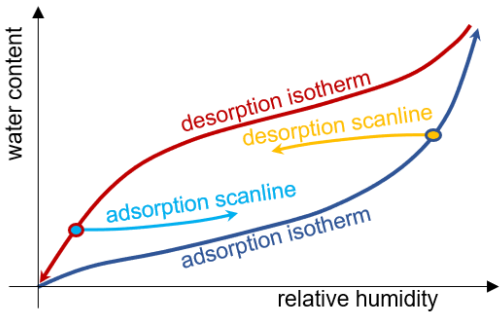


Fig. 5.4. Principle sketch of isotherms and scanlines

Isotherms as well as scanlines have been determined in detail for the Na-bentonite MX-80 and the Ca-bentonite Calcigel /KRÖ 20b/. The results indicated that, after branching off, the scanlines do not intersect the opposite isotherm at an as-yet undefined point. Instead, they converge towards the opposite isotherm and reach it only at the endpoint, i.e. at a completely dry or fully saturated state, respectively. This behaviour is shown in Fig. 5.5, which presents the results from measurements of adsorption and desorption scanlines for MX-80.

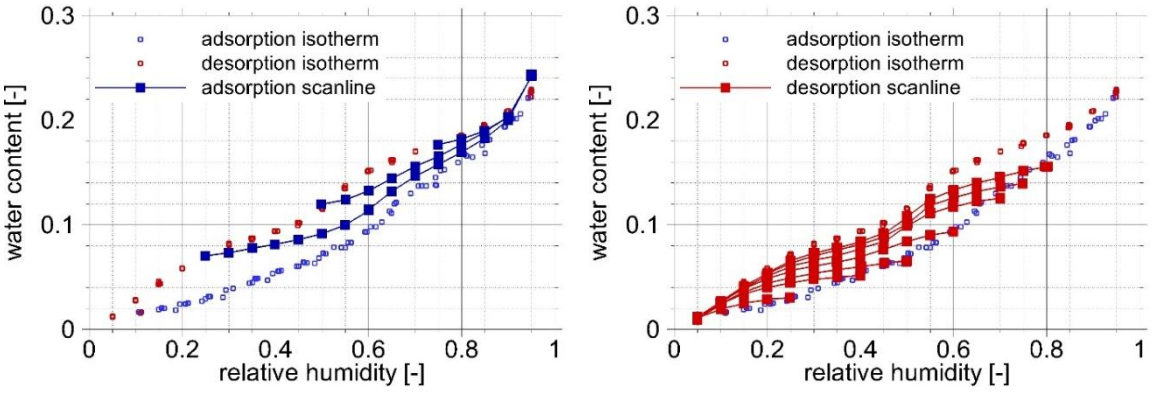


Fig. 5.5. Measured scanlines for MX-80 including the data for isotherms for reference, left: desorption scanlines, right: adsorption scanlines; after /KRÖ 20b/

Since the VSA permits measurements only between 3 % and 95 % relative humidity, the isotherms presented here can, in a strict sense, only be regarded as scanlines that approximate the isotherms, albeit closely. However, both the measurements from /KRÖ 20b/ and those of the present study were performed in the same manner: (1) lowering the relative humidity to 5 % and waiting for equilibrium, (2) increasing the humidity in steps of 5 % up to 95 %, and, finally, (3) decreasing the humidity again in steps of 5 % down to

5 %. The results from /KRÖ 20b/ imply that isotherms can be regarded as special cases of scanlines. The present work therefore represents a consistent comparison of scanlines that closely approximate the corresponding isotherms. These particular scanlines are therefore nevertheless referred to as “isotherms” in the following.

Of greater practical relevance, however, was the conclusion that the actual state of a bentonite, in terms of relative humidity and water content, may occur anywhere between the adsorption and desorption isotherms, depending on its hydration history. Determination of an isotherm therefore ideally requires starting either from a completely dry or from a fully wetted state. Otherwise, only scanlines are determined.

A striking example of the relevance of hydration history may be provided by the work of /DUE 04/ on MX-80 bentonite, in which the impact of different initial conditions, namely water contents of 0 %, 10 %, 17.5 % and 27 %, on the adsorption isotherm was investigated. In Fig. 5.6, these data are shown and may, upon cursory inspection, suggest that different initial water contents result in different isotherms. However, comparison with the analytical functions for isotherms and adsorption scanlines from /KRÖ 20b/ suggests a different interpretation. After high saturation had been reached during sampling of the preceding curve, the bentonite appears to have been dried to the desired initial water content, thereby following a drying path along the desorption isotherm. In this case, subsequent wetting would have followed an adsorption scanline rather than the adsorption isotherm. This conjecture is supported by the overlay of the results from /DUE 04/ with analytical solutions for isotherms and scanlines from /KRÖ 20b/, as shown in Fig. 5.6.

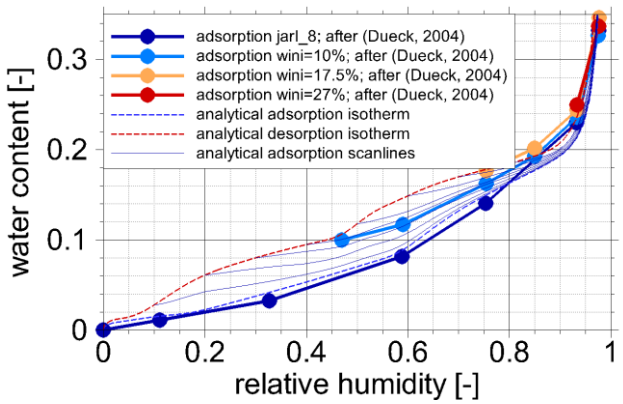


Fig. 5.6. Data points for the adsorption isotherm from /DUE 04/ and analytical solutions for isotherms and scanlines from /KRÖ 20b/

Unfortunately, the actual testing procedure could not be reconstructed from the otherwise thorough description in /DUE 04/, so that this interpretation remains a strongly supported conjecture. It should be noted that these considerations explicitly do not question the quality of the measurements themselves. However, this example demonstrates the importance of controlling the wetting history when determining isotherms.

5.2 Materials

Previously, a pure Na-bentonite MX-80 with a smectite content of 80 % and a pure Ca-bentonite Calcigel with a smectite content of 75 % had been used to determine reference isotherms and corresponding analytical relations /KRÖ 20b/. For the present study, a batch of 13 bentonites with varying fractions of Na- and Ca-content, provided by BGR, was used. These bentonites had been characterized in /KAU 08/, /KAU 12/ and /KAU 13/. They were intentionally randomized and coded as B01, B02, B03, etc. The characteristics relevant here are compiled in Tab. 5.1. For visualization, these data are shown in Fig. 5.7 and scaled such that the length of the coloured bar represents the smectite content in the samples, whereas the lengths of the blue and red bars represent the fractions occupied by monovalent and divalent cations, respectively, in the interlamellar space.

Tab. 5.1 Sample characteristics after /KAU 12/ and /KAU 13/

sample	smectite content [%]	interlayer cation occupancy	
		Na [%]	Ca+Mg [%]
B04	91	18	82
B09	74	100	0
B10	89	31	69
B11	89	71	29
B12	91	56	44
B13	84	1	99
B16	70	0	100
B19	75	24	76
B23	80	69	31
B31	81	62	38
B36	75	1	99
B37	80	1	99
B38	63	21	79

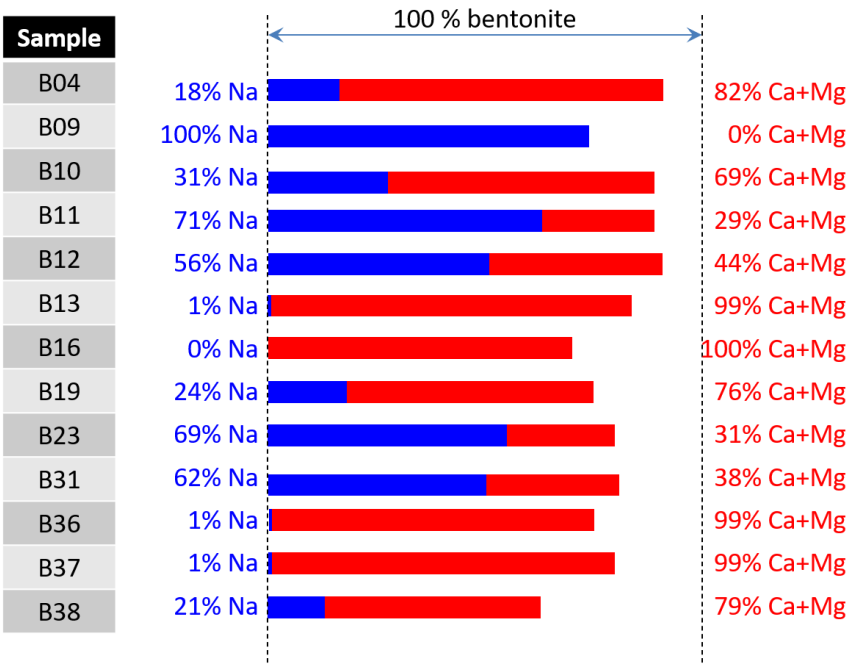


Fig. 5.7. Smectite content and fractions of mono- and divalent cations in the 13 samples

Finally, ultrapure water was used to generate the required humidities in the climate chamber in order to protect the VSA against deposits from tap water.

5.3 Comparing predictions and measurements

5.3.1 Procedure of comparison

For each bentonite sample, the complete hysteretic loop of adsorption and desorption was determined in two ways. First, the shape of the hysteretic loop was predicted theoretically based on the analytical functions for MX-80 and Calcigel from /KRÖ 20b/, with the water content scaled to a smectite content of 100 %. For each bentonite sample, the percentages of monovalent and divalent cations in the interlamellar space were then used to calculate a weighted mean of the adsorption isotherms for MX-80 and Calcigel. The same procedure was subsequently applied to the desorption isotherm, thereby completing a full hysteretic cycle. Second, the loop was measured with the VSA, and the water content was then scaled to a smectite content of 100 %.

As a performance measure for each isotherm, the following ad hoc procedure was adopted. The water content at 20, 40, 60, and 80 % relative humidity was determined for both the predicted and the measured curve, and the difference Dw' was calculated for each sampling point. The arithmetic mean Dw of the four difference values Dw' was used to define the quality of the fit according to the criteria listed in Tab. 5.2.

Tab. 5.2 Assessment scheme for the fit of predicted and measured isotherm.

Quality	Condition
excellent	$\Delta w < 1$ %
reasonable	1 % < $\Delta w < 2$ %
bad	$\Delta w > 2$ %

5.3.2 Results

Adsorption and desorption isotherms were examined for 13 bentonite samples. For clarity, the results for adsorption and desorption isotherms are shown separately in all cases. For each bentonite, the measured and subsequently scaled isotherm for both the wetting and the drying path is plotted together with the predicted curve based on the interlayer cation composition. For reference, the bounding isotherms for Na- and Ca-bentonite are also included. All resulting plots are compiled in Appendix B.

According to the assessment scheme in Tab. 5.2, the fit between predicted and measured isotherms was evaluated for all bentonite samples and compiled in Tab. 5.3. Of the 26 predictions, 12 were classified as excellent, 11 as reasonable, and 3 as bad. The performance measures of the three bad matches deviate strongly from those of the other fits. However, a thorough post-test examination of the smectite and cation contents revealed no peculiarities in the corresponding materials.

The results for bentonite B31, shown in Fig. 5.8, are discussed as an example. According to the assessment scheme in Tab. 5.2, the agreement between prediction and measurement was assessed as reasonable for both isotherms of B31 (see Tab. 5.3).

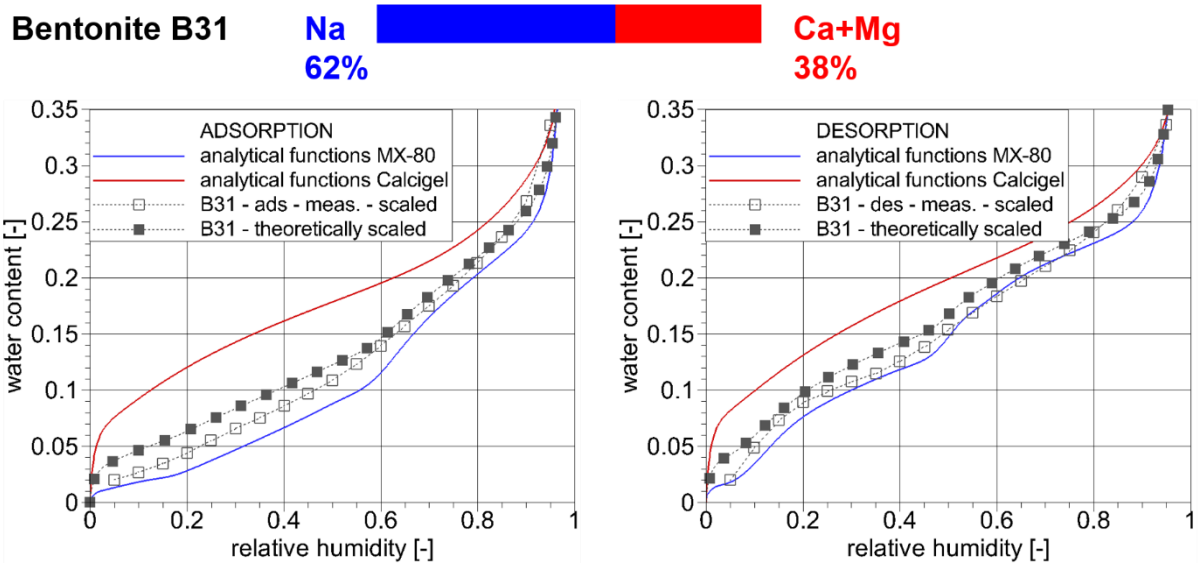


Fig. 5.8. Predicted and measured isotherms for bentonite B31; bounding isotherms for pure Na- and Ca-smectite added for orientation

In bentonite B31, approximately two thirds of the interlayer cations are Na+-ions, whereas only one third is divalent. As expected from the prediction, the measured and scaled isotherms are more closely related to the isotherms for Na-bentonite than to those for Ca-bentonite. Even the curvature and bends characteristic of Na-bentonite can be recognized in the results for B31.

Somewhat unexpected is the observation that the prediction does not deviate systematically from the measurement. For B31, the adsorption isotherm is predicted much more accurately above 50 % relative humidity than below this value. By contrast, the desorption isotherm deviates less strongly, but over the entire humidity range.

Tab. 5.3 Assessment of the fits of predicted and measured isotherms.

B04	adsorption	0.50	excellent
	desorption	0.35	excellent
B09	adsorption	1.95	reasonable
	desorption	1.10	reasonable
B10	adsorption	0.56	excellent
	desorption	0.47	excellent
B11	adsorption	1.29	reasonable
	desorption	1.54	reasonable
B12	adsorption	4.32	bad
	desorption	4.29	bad
B13	adsorption	0.79	excellent
	desorption	0.71	excellent
B16	adsorption	1.76	reasonable
	desorption	0.90	excellent
B19	adsorption	0.29	excellent
	desorption	0.41	excellent
B23	adsorption	2.97	bad
	desorption	1.91	reasonable
B31	adsorption	1.20	reasonable
	desorption	1.01	reasonable
B36	adsorption	1.06	reasonable
	desorption	1.44	reasonable
B37	adsorption	0.83	excellent
	desorption	0.63	excellent
B38	adsorption	1.84	reasonable
	desorption	0.74	excellent

6 Topic 4 – Porosity at full saturation

As introduced in section 1.6, Topic 4 investigates the end state of bentonite after re-saturation with vapour (Test I) and with water (Test II), with particular regard to porosity. Test I and Test II each comprise 8 confined bentonite samples. Four samples each of the sodium bentonite MX-80 and the calcium bentonite Calcigel were prepared at different target dry densities (1300, 1400, 1500, and 1600 kg/m³). In parallel, a long-term test on three pellets of MX-80 bentonite in a vapour-saturated atmosphere (Test III) was performed.

Initially, it had been planned to perform the uptake tests of Test I sequentially, with the compacted bentonite confined in a stainless-steel tube whose ends were closed by sinter plates. These plates were intended to be fixed by specially designed 3D-printed caps. However, this approach failed because of the mechanical instability of the printed resin during long-term contact with water. The cell broke, as shown in Fig. 6.1, left. It should be noted that protecting the printed cell caps with a water-repellent coating reduced water uptake only slightly and only for a few days. Subsequently, no difference from the uncoated cap was observed. At the end of the test, the coating appeared to be cracked (see Fig. 6.1, right), which probably eliminated its protective effect.

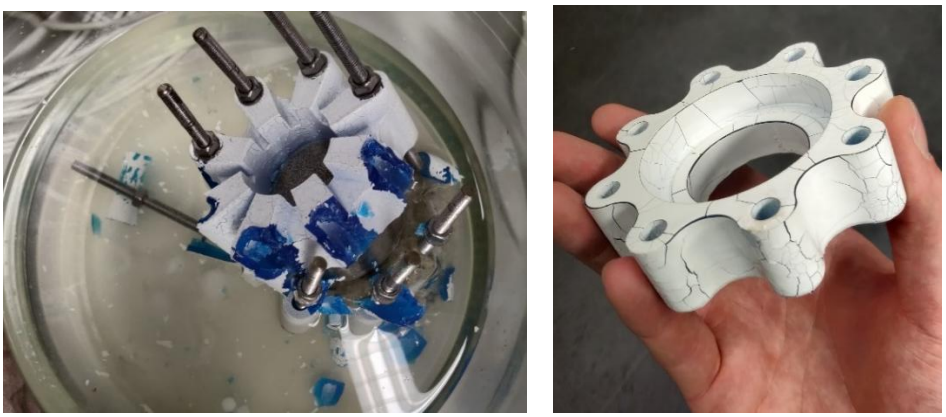


Fig. 6.1 Failed pre-test with a 3D-printed test cell under Test II-conditions; left: broken cap – right: cracked coating

As an alternative to the printed caps, two aluminium plates with large holes were prepared to confine the samples, as shown in Fig. 6.2, left. However, this approach introduced another problem. Since the test was performed with tap water, aluminium chloride formed within a few days and appeared to begin clogging the sinter plates (see Fig. 6.2, right).

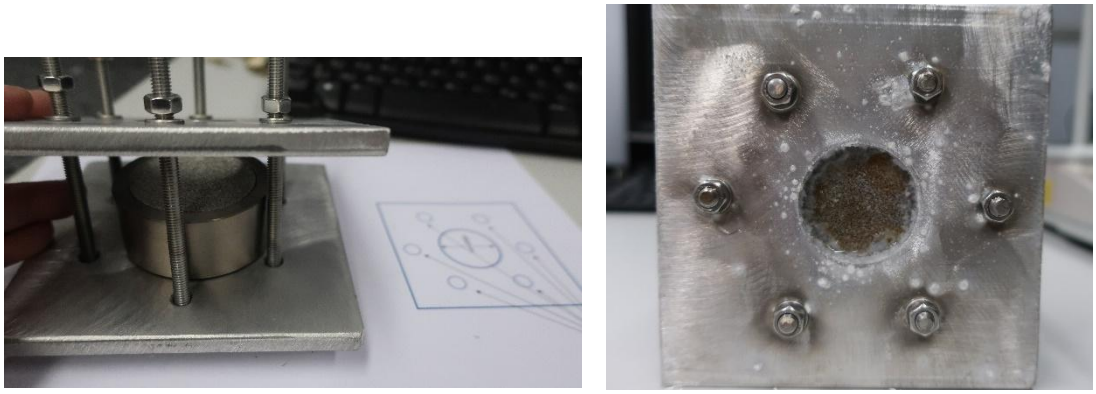


Fig. 6.2 Failed pre-test with aluminum plates as caps under Test II-conditions; left: open test set-up – right: aluminumchloride evolution at the bottom

To compensate for the time lost during the pre-tests, additional time was allowed until a batch of suitable conventional test cells from other projects became available, enabling the tests to be performed in parallel.

6.1 Test I: Water uptake via vapour

For Test I, 8 cylindrical test cells were used that allowed air to enter the cell from both ends. The installed bentonite samples had a height of approximately 2 cm and a diameter of 5 cm. They were compacted in two layers directly in the cell. Each cell was placed in a desiccator and kept above tap water on a ceramic sieve, thereby ensuring a vapour-saturated atmosphere. The cluster of the 8 desiccators is shown in Fig. 6.3.

Each desiccator was equipped with a temperature and humidity sensor to monitor the ambient conditions during water uptake. To accommodate the demand for desiccators in other projects, all four test cells with MX-80 samples were stored together in one desiccator, and the four test cells with Calcigel samples were also placed in one desiccator after 980 days. Re-saturation was assumed to be advanced at that time; therefore, evaporation of the tap water from below was considered sufficient to meet the water demand of four bentonite samples. Until termination of the test after 1231 days, each remaining desiccator therefore contained four test cells. The temperature data obtained over time are shown in Fig. 6.4. The temperatures were essentially identical in all 8 desiccators, except for desiccator 8, where slightly lower temperatures were recorded while the overall trend remained unchanged.

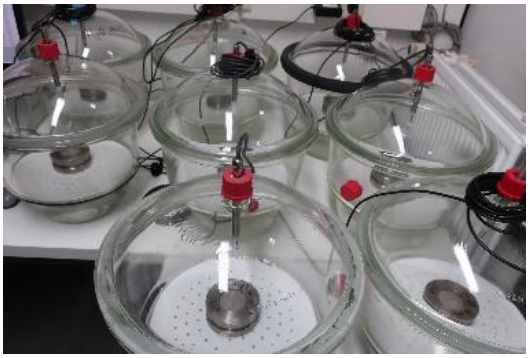


Fig. 6.3 Test cells for water uptake via vapour in desiccators

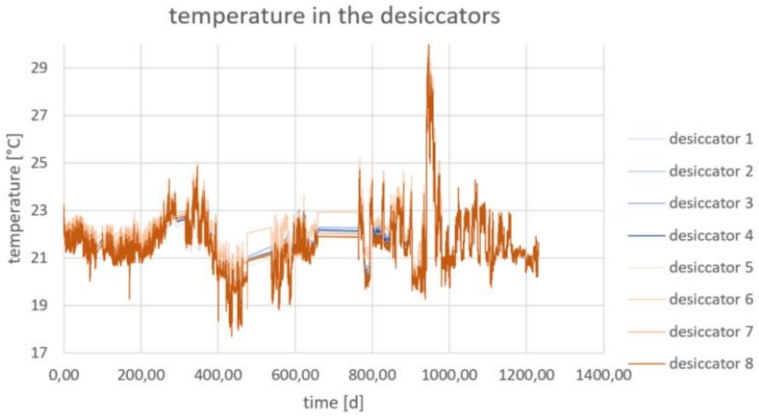


Fig. 6.4 Temperature evolution in the eight desiccators

By contrast, the recorded humidity data were less uniform than the temperatures, as shown in Fig. 6.5. In desiccator 3, approximately 60 days were required to reach full vapour saturation. A similar behaviour was observed in desiccator 1; however, after approximately 80 days the relative humidity decreased again to approximately 91 % by day 980. All other desiccators showed full vapour saturation throughout the test. The humidity evolution in desiccators 2 and 4 is shown in Fig. 6.5 as representative of the other desiccators. After the test cells had been concentrated in two desiccators, the humidity was stabilized at 100 % in both remaining desiccators.

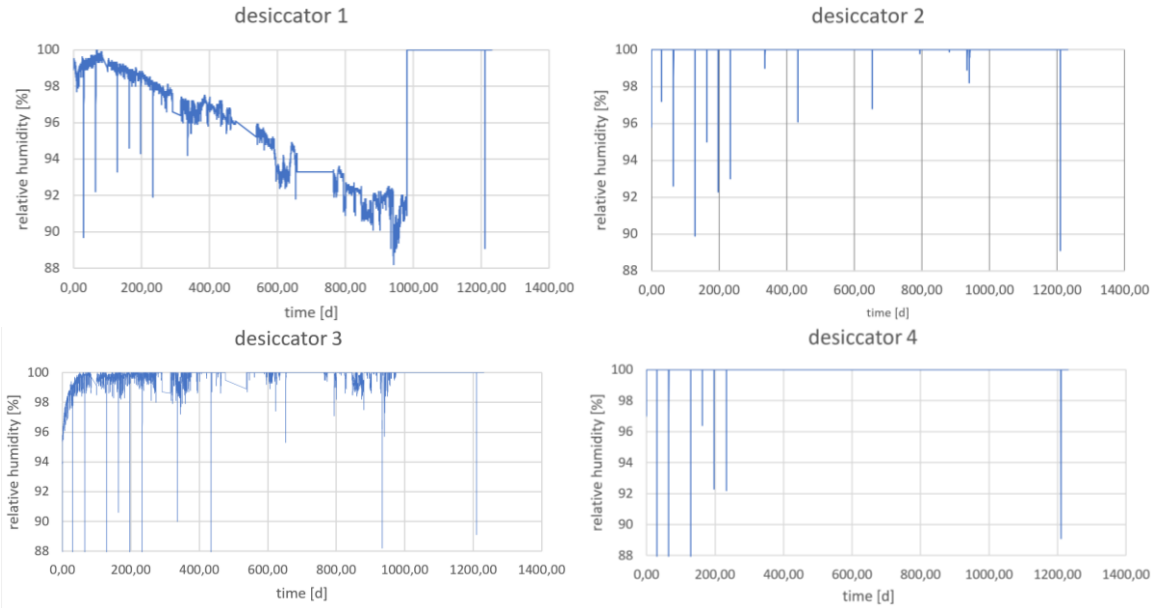


Fig. 6.5 Humidity in the desiccators 1 to 4, 2 and 4 being representative for all others

Model calculations had indicated a time of approximately 7 days for nearly complete saturation. This was not observed in the laboratory test. Compared with the numerical model, convergence towards steady state appeared to be very slow. Therefore, each cell was removed briefly from the desiccator approximately once per month, weighed to monitor the progress of re-saturation, and returned to the desiccator. From the increasing weight of the test cells, the mass of water taken up by the samples could be determined directly. The resulting curves for all 8 cells are shown in Fig. 6.6.

When Test I was terminated after 1231 days, the samples were pressed out of the cells and cut into 4 discs with a height of approximately 5 mm. The height of each disc was determined from three caliper measurements, which were averaged. The wet weight of the discs and the weight after heating at 105 °C for 24 hours were determined. The results and their comparison with the results from Test II are presented in section 6.3.

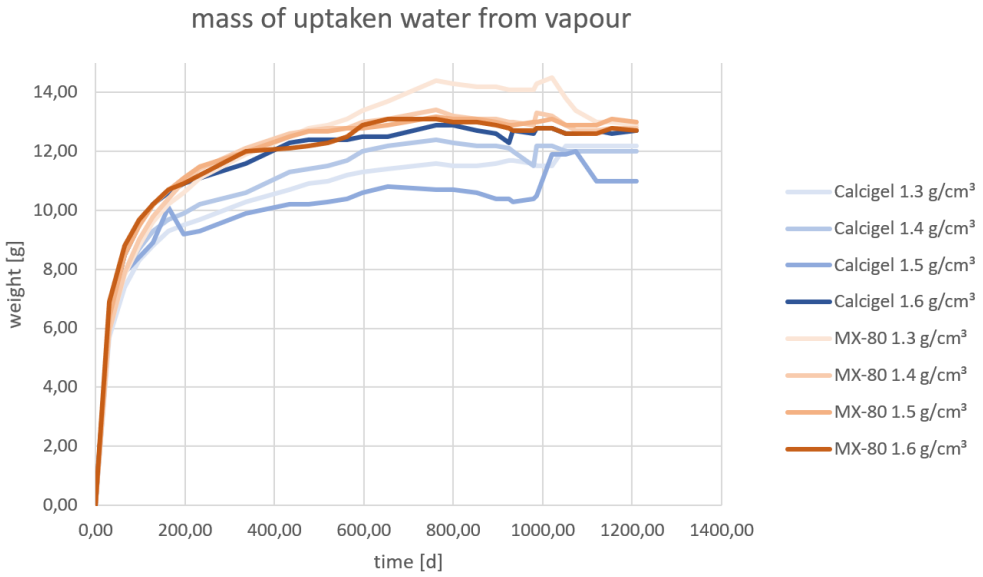


Fig. 6.6 Dynamics of water uptake from vapour by MX-80 and Calcigel for different dry densities

6.2 Test II: Water uptake via liquid water

For Test II, the eight samples were also compacted in the test cells to a height of 20 mm and a diameter of 50 mm. Sample saturation was achieved by attaching burettes filled with distilled water to the bottoms of the test cells. The experimental set-up is shown in Fig. 6.7. After an initial phase of rapid water uptake, burette readings were recorded monthly. They are graphically compiled in Fig. 6.8. Further data evaluation and comparison are provided in the next subsection.

Test II was terminated after 1232 days. As in Test I, the samples were sectioned into discs with a thickness of approximately 5 mm. Water content profiles across the samples were then determined by weighing and subsequent heating at 105 °C for 24 hours. These measurements were used to verify full saturation at the end of the test.



Fig. 6.7 Array for water uptake tests via liquid water, two different views

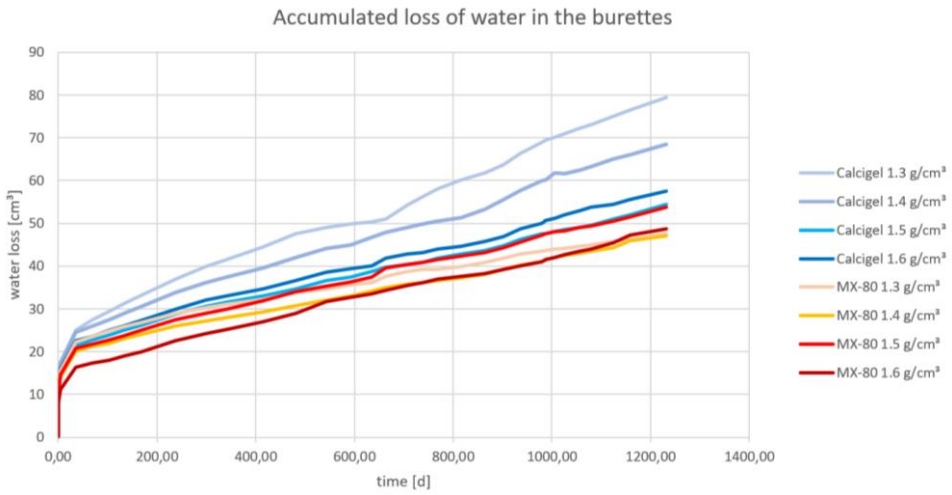


Fig. 6.8 Losses of water from the burettes over time

6.3 Comparison and interpretation of the results from Tests I and II

6.3.1 State of the samples in Test I at the end of the test

Although the curves of water uptake over time (cf. Fig. 6.6) are reasonably smooth, the corresponding uptake rates shown in Fig. 6.9 are comparatively scattered because they represent the derivative of weight with respect to time.

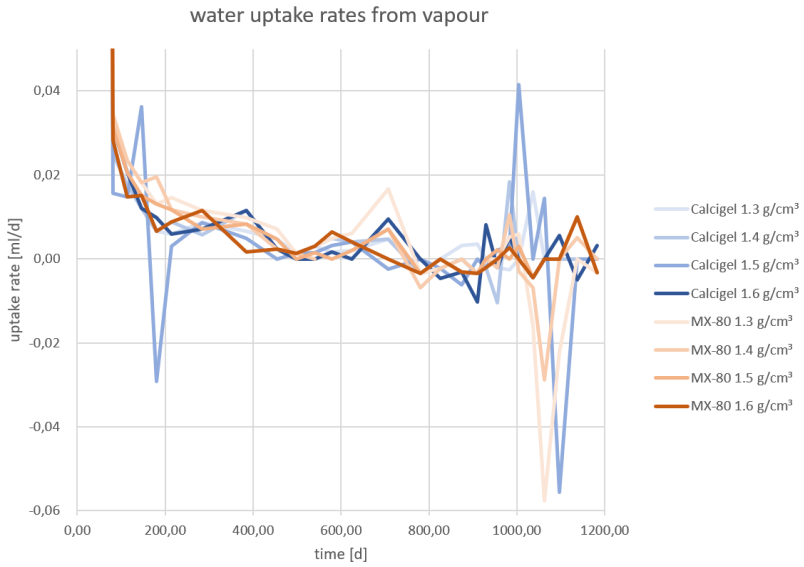


Fig. 6.9 Uptake rates of the bentonite samples in the desiccators

As a first observation, the uptake rate over time does not appear to depend on the type of bentonite. Overall, this also seems to apply to dry density.

Against this background, medians of the uptake rates were calculated for the MX-80 and Calcigel samples, respectively. They are plotted on a semilogarithmic scale over the full data range in Fig. 6.10 (left) and on a linear scale for small values, including negative values, in Fig. 6.10 (right). The evolution of the curves during the first year is particularly relevant. During the first 81 days, a linear trend is observed in the semilogarithmic plot, indicating an exponentially decreasing uptake rate. This behaviour is typical of the diffusion-like uptake process in bentonite and has been observed repeatedly. Subsequently, however, the curves show a much slower decrease in uptake up to 215 days; the rate then appears to increase slightly before eventually decreasing to zero after approximately 498 days. Thereafter, the data appear to reflect measurement errors rather than actual uptake

rates (cf. Fig. 6.9). With regard to the present test, it can therefore be concluded with high confidence that maximum saturation in the samples of Test I had been reached well before termination of the test.

The very long time required to reach full saturation is in strong contradiction to the model calculations, which predicted complete water uptake within approximately one week (cf. section 6.1). The disproportionately slower decrease in uptake rates after an initial period of exponential decrease suggests that the physico-chemical processes close to maximum water uptake cannot be extrapolated from the behaviour at lower saturations. A closer investigation of hydration processes at the microscopic level and at high degrees of saturation therefore appears advisable.

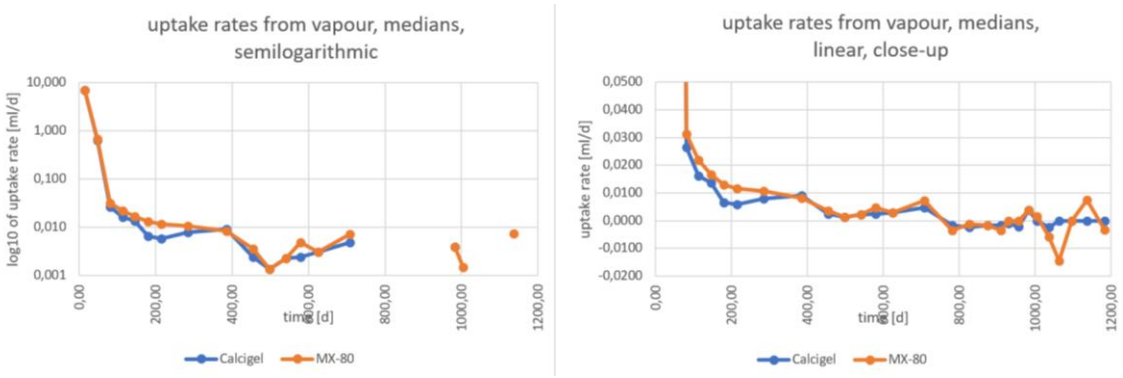


Fig. 6.10 Uptake rates in the desiccators; medians for MX-80 and Calcigel; left: semi-logarithmic plot over the whole data range, right: linear plot for small values

Similar observations concerning uptake dynamics were already reported by Kahr et al. /KAH 86/, who specifically measured water uptake times from vapour for MX-80 and Montigel[6]. However, the tests performed by Kahr et al. differed from the present tests in several aspects. The results are therefore only qualitatively comparable. Nevertheless, in the double-logarithmic plot of water content over time in Fig. 6.11 (right), an initial increase in water content is observed that shows a continuously decreasing uptake rate, followed by an even slower decrease.

[6] a precursor to Calcigel from the same company.

The linear plot on the left in Fig. 6.11 indicates that at least the Montigel samples had not reached steady state at the end of the test. The results for MX-80 are less clear because water uptake in two samples was terminated early. However, the third sample also appears to show a tendency for further water uptake. These observations corroborate the present results, indicating that very long times are required to reach full saturation.

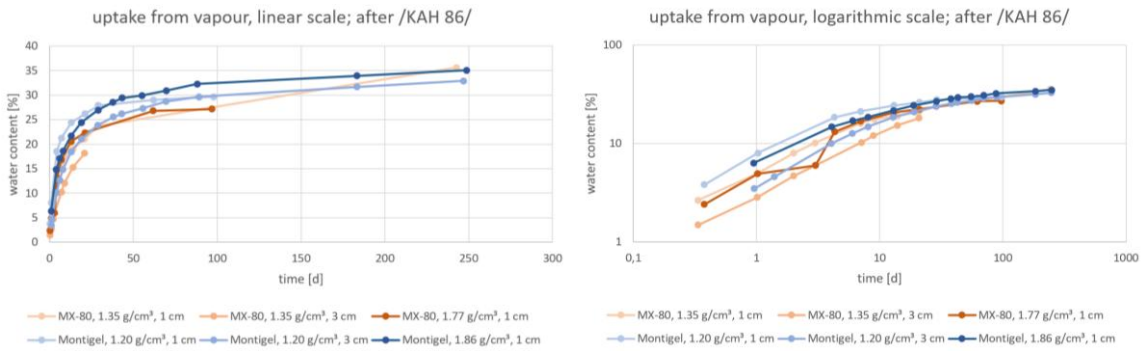


Fig. 6.11 Evolution of the water content during uptake from vapour for MX-80 and Montigel; after /KAH 86/; left: linear scale, right: logarithmic scale

6.3.2 State of the samples in Test II at the end of the test

In contrast to the weight data from Test I, the data from Test II do not converge towards a steady-state value but rather towards a linear gradient. A linear increase is confirmed by calculating “uptake” rates from the data in Fig. 6.8, as shown in Fig. 6.12. This type of data suggests leakage or evaporative loss at this constant “uptake” rate. However, because rate calculations increase scatter in the volume data, it is difficult to determine conclusively how much water was actually lost. The dynamics of the true water uptake by the samples could therefore not be determined.

The data from Test II shown in Fig. 6.12 exhibit trends similar to those in Test I (cf. Fig. 6.9). The only exception appears to be the sample with Calcigel at a dry density of 1.5 g/cm³. Therefore, medians were calculated for each type of bentonite. They are shown as a semilogarithmic plot over the full data range in Fig. 6.13 (left) and as a linear plot for small values in Fig. 6.13 (right).

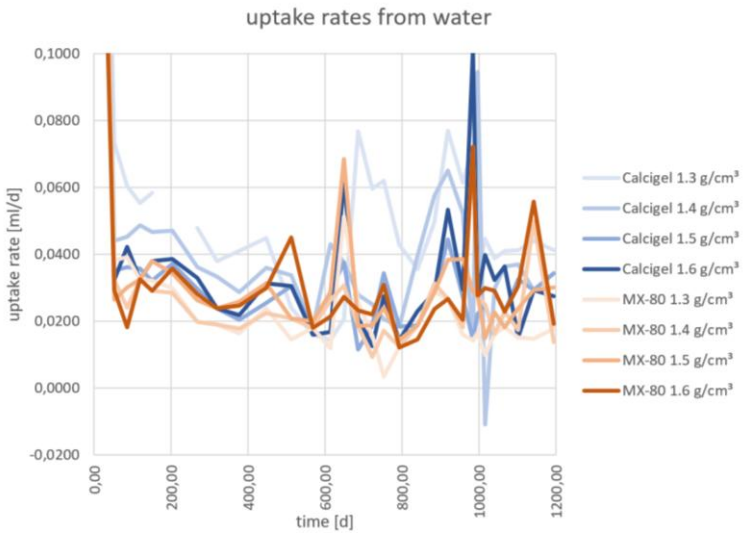


Fig. 6.12 Uptake rates according to the burette readings

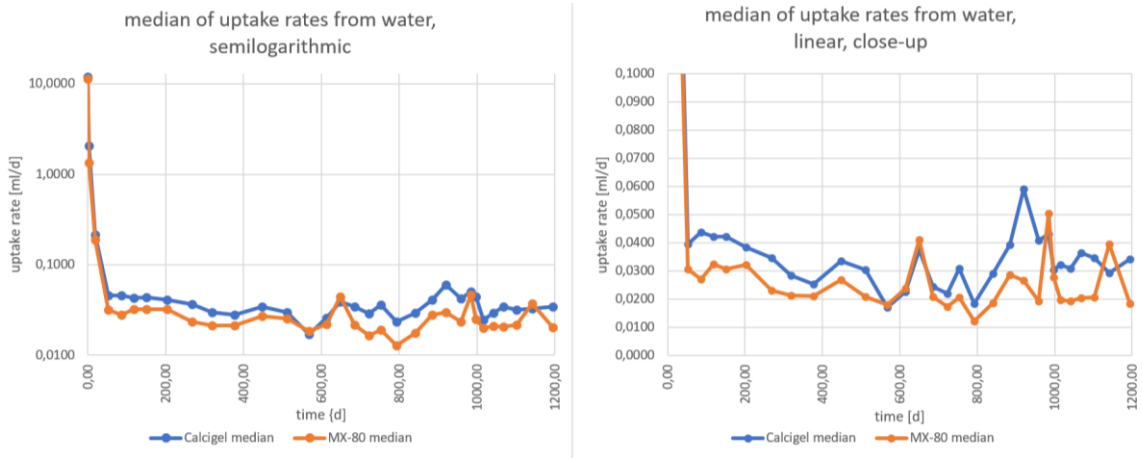


Fig. 6.13 Uptake rates via liquid water; medians for MX-80 and Calcigel; left: semilogarithmic plot over the whole data range, right: linear plot for small values

The calculated uptake rates are slightly higher for Calcigel than for MX-80; qualitatively, however, the uptake behaviour is the same. As in Test I, water is initially taken up in a diffusion-like manner until a rate of approximately 0.03 (MX-80) / 0.04 (Calcigel) ml/day is reached after approximately 52 days. From this point onward, the rate decreases much more slowly, reaching approximately 0.025 / 0.021 ml/day on day 377.

During the remaining part of the test, the rate appears to be constant and is affected only by unavoidable measurement errors. A rate of approximately 0.025 ml/day therefore represents a constant loss of water along the path from the burettes to the bentonite samples.

Consequently, the same conclusions as drawn for Test I regarding an as yet unknown additional process and the state of full saturation at the end of the test also apply to Test II. Whether this process is identical to the one becoming effective in Test I remains to be demonstrated.

6.3.3 Compilation and comparison of characteristic quantities

The data obtained from cutting and weighing the bentonite discs were processed according to the set of equations presented in Appendix A. First, the water content of each individual bentonite disc was calculated and plotted against its position in the test cell. As an example, the data for Calcigel at a target dry density of 1,5 g/cm³ are graphically compared in Fig. 6.14 for uptake from vapour and water.

The water content data for the discs appear to indicate a characteristic overall value for the sample, although they are affected by measurement inaccuracies. A larger influence on the data is introduced by the determination of the disc volume, which depends on caliper measurements of the disc height. Even after repeating the height measurements twice and using the average, the resulting errors introduce considerable deviations.

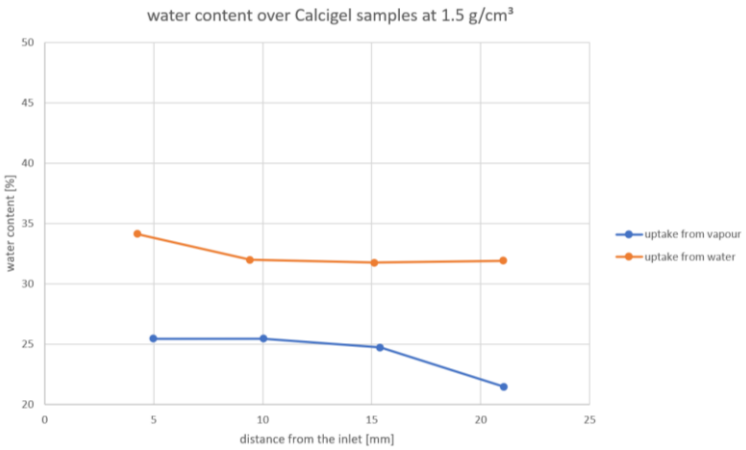


Fig. 6.14 Water content distributions for Calcigel (1.5 g/cm³); water (red), vapour (blue)

In response to these challenges, two measures were taken. The adverse influence of individual off-trend values was reduced by using the median instead of the mean of all values. In addition, errors in the height measurements of individual discs partly compensate each other when summed to obtain the height of the complete sample. Therefore, only integral values for each of the 16 samples were considered in the subsequent evaluation.

The integral values were calculated according to Appendix A, assuming a water density of = 1.0 g/cm³ and a mineral density of = 2.78 g/cm³. The median dry density was found to deviate somewhat from the target dry density in some cases. Therefore, the water content, degree of saturation, and porosity in Fig. 6.15 to Fig. 6.17 are plotted against the dry density determined after the test rather than against the target dry density.

Several expected and unexpected observations in Fig. 6.15 are of interest.

(1) In general, the water content decreases with increasing dry density. This was expected, because increasing dry density is associated with more bentonite in the same volume and therefore with progressively less free pore space available for water.

(2) The water contents of MX-80 and Calcigel in Test II are more or less identical. This result is consistent with equation (A.4) for the maximum water content when the same densities and are used in both cases.

(3) By contrast, the water content curves from Test I are clearly separated, with the water content of MX-80 being approximately 10 % higher than that of Calcigel.

(4) In addition, the gradient of the water content in the Test I data is considerably lower than in the Test II data, resulting in an intersection of the curves for MX-80 slightly below 1.4 g/cm³.

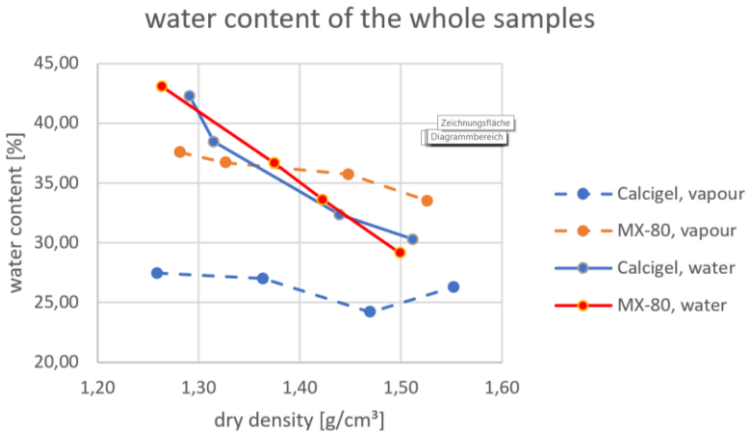


Fig. 6.15 Water content in all 16 samples over the determined dry density

At completed saturation, the degree of saturation indicates the extent to which the pore space available under dry conditions has been filled with water. Several observations can again be derived from Fig. 6.16:

(5) The degrees of saturation in Test II are all close to 100 %, indicating that water uptake proceeded as anticipated.

(6) The opposite is observed in Test I. The saturation curves not only show an upward trend with dry density, but are also separated by an approximately constant value. Moreover, the saturation of MX-80 exceeds 100 % above a dry density of 1.4 g/cm³.

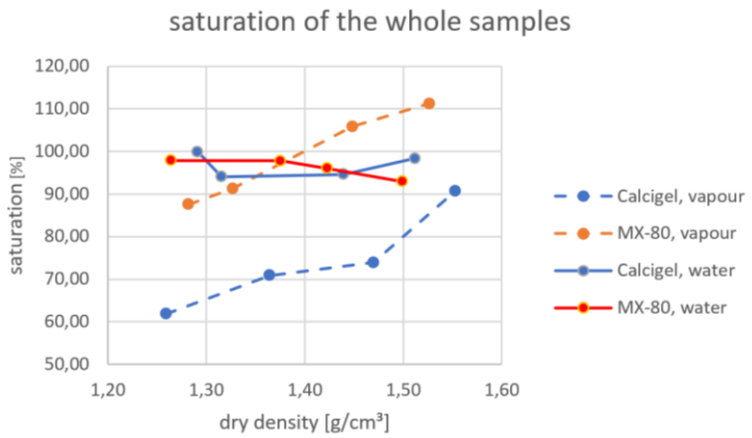


Fig. 6.16 Degree of saturation in all 16 samples over the determined dry density

The porosities shown in Fig. 6.17 also follow the expected behaviour for Test II, whereas a distinctly different trend is observed for Test I:

(7) The derived porosity values for Test II generally lie in the range between 1 % and 3 %.

(8) As the saturation values increase with dry density in Test I, the corresponding porosity values decrease. The curve for MX-80 intersects the 0 % line at 1.4 g/cm³, as expected from the saturation data. The same also applies to the intersection of the two curves for MX-80.

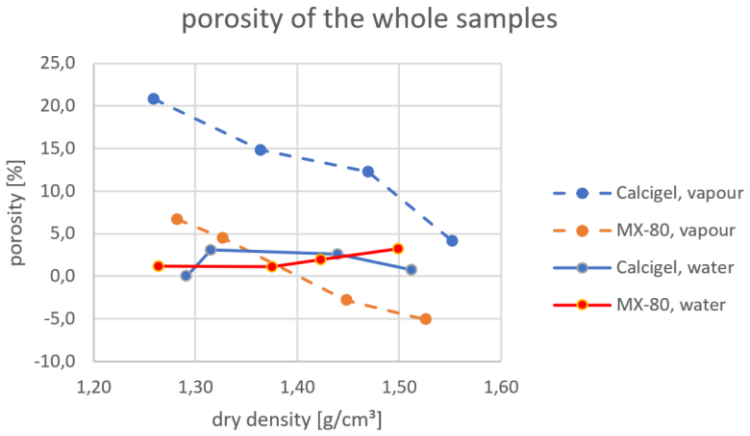


Fig. 6.17 Porosity in all 16 samples over the determined dry density

6.3.4 Interpretation and conclusions

Test II proceeded as anticipated and yielded plausible results: the water content decreases with increasing dry density, the degree of saturation is close to 100 % in all cases, and the end porosity ranges between 1 % and 3 %. This range covers well the range of 1 % to 2 % determined in /KRÖ 19/ for early uptake tests at GRS /KRÖ 04/ (cf. section 1.6). The only unexpected observation is that these data are essentially identical irrespective of the type of bentonite or the dry density and therefore appear to be generally applicable to uptake from water.

By contrast, Test I produced highly unexpected data. The final water content also decreased with dry density in this test, but the decrease was considerably less pronounced than in Test II. In the case of MX-80, more water appears to have been taken up from vapour than from water at dry densities above approximately 1.4 g/cm³. Although this was not observed for Calcigel, the trends of the corresponding curves nevertheless indicate an intersection of the final water content curves at a dry density above the range investigated in the present tests.

The observation for MX-80 that final water contents after uptake from vapour exceed those after uptake from water is also reflected in the degrees of saturation: after uptake from vapour, saturation exceeds 100 % above a dry density of approximately 1.4 g/cm³. Consequently, negative porosity values were obtained in this dry-density range. These results for uptake from vapour are physically unreasonable and therefore require further discussion.

All uptake tests were performed in accordance with proven standard procedures. A review of the test execution indicated that the results are not affected by systematic errors. Nevertheless, the most robust data are the water contents, because they are based only on two weight measurements after termination of an uptake test (cf. equation (A.1) in Appendix A). Some scatter was observed in the data from the four segments of each sample, although identical values would be expected. However, averaging over the segments yielded a representative value for each sample, which in turn produced clear trends when the representative values of all samples were compared. The water content data are therefore most likely to reflect the actual condition of the fully saturated samples. All other quantities considered here involve additional measured data and therefore also include the corresponding measurement errors.

Calculating the dry density of a sample according to equation (A.3) in Appendix A additionally requires the sample volume. When the bentonite is pressed out of the cylindrical cell, the cross-sectional area is known with comparatively high accuracy. However, the height of a cut-off disc is difficult to determine with sufficient accuracy, which introduces an additional uncertainty.

The evaluation of the degree of saturation and porosity is even more affected by unavoidable measurement errors, because both quantities depend on water content and dry density (cf. equations (A.5) and (A.6) in Appendix A). Moreover, saturation and porosity also depend on the density of the interlayer water and the particle density, both of which remain subject to discussion.

The equations provided in Appendix A are derived from general geometrical considerations and should therefore strictly apply. The only degree of freedom in evaluating data with these equations arises from the parameters, namely the densities of the taken-up water and of the clay particles . Because bentonite is a natural material, the particle density may vary to a certain extent. While a particle density of 2.78 g/cm³ is generally assumed for MX-80, a range of values for Calcigel is reported in the literature. According to /ASA 25/, the grain density determined over the last 40 years lies between 2.65 and 2.847 g/cm³. In the present work, the same value of 2.78 g/cm³ as for MX-80 is adopted for Calcigel, which is close to the most recently determined value of 2.738 g/cm³ reported by /ASA 25/. However, varying the particle density within the ranges indicated by /ASA 25/

has a comparatively small effect on the saturation and porosity curves in Fig. 6.16 and Fig. 6.17.

The only remaining option for obtaining physically reasonable results for saturation and porosity would be a modification of the water density. Indeed, a tentative increase in water density by no more than 20 % shifts the curves into plausible ranges. This is noteworthy because the density of hydrated water in bentonite has been a long-standing controversial issue. At present, the majority of the community working with compacted bentonite appears to assume that hydrated water has the same density as free water (view 1). This assumption was also used in the present data evaluation. However, experiments have repeatedly shown that confined compacted bentonite may take up more water than theoretically predicted, and this observation has been explained by a higher density of hydrated water (view 2).

Against this background, the present results appear ambiguous: Test II appears to confirm view 1, whereas Test I would support view 2. Whether this represents a viable explanation can only be determined through a thorough investigation of relevant experiments.

It had been planned to derive a mathematical formulation for the end porosity as a function of dry density, type of water supply, and type of bentonite. However, the results from Tests I and II do not support such a formulation. For uptake from water, a value of 1 % to 3 % appears appropriate, irrespective of the type of bentonite or the dry density.

For water uptake from vapour, the results appear physically unreasonable. This may be caused by an incomplete understanding of the density of hydrated water, suggesting that further investigations focusing on the density of hydrated water are advisable. It is further conceivable that additional information on microstructural effects during long-term water uptake may contribute to resolving this issue.

Comment on the residual porosity values as determined in /KRÖ 19/

The analysis of residual porosities in /KRÖ 19/ was based on uptake tests from /KRÖ 04/. These tests are in principle similar to the present tests, because both liquid water and water vapour were used as media for re-saturation. However, several practical differences preclude a direct comparison of the results, particularly because steady state had not yet been reached at the end of the earlier tests. Instead, the highly saturated zone at the

bentonite-water contact was used as a proxy for fully saturated conditions. Nevertheless, the analysis in /KRÖ 19/ led to the expectation that the residual porosity remaining after uptake from water would also be higher than that after uptake from vapour in the present tests. This expectation was not confirmed.

A direct quantitative comparison of the test results is not possible because of the experimental differences. However, at least one qualitative conclusion can be drawn from two facts. (1) The earlier tests with water had been running for up to 189 days, whereas the tests with vapour had been added later in the project and therefore ran for only approximately 90 days. (2) The uptake dynamics in the present tests with water were much faster than those in the tests with vapour. It is therefore evident that the state reached in the earlier tests with water was considerably closer to steady state than that reached in the tests with vapour. It can therefore be assumed that the final porosity in the tests with vapour would have been significantly higher if the tests had been continued for a longer period.

6.4 Test III: Water uptake via vapour

A discussion within the Task Force EBS on the behaviour of bentonite pellets under high-humidity conditions raised the question of whether the pellets would swell or retain their shape. While experimental evidence suggested that the pellets would maintain their shape, this conclusion was challenged by other members of the group. To verify either assumption, a long-term laboratory experiment was initiated in March 2024. Three MX-80 pellets, as used in the Prototype Repository, were 3D-scanned, weighed, and subsequently placed in a desiccator at 100 % relative humidity (see Fig. 6.18).

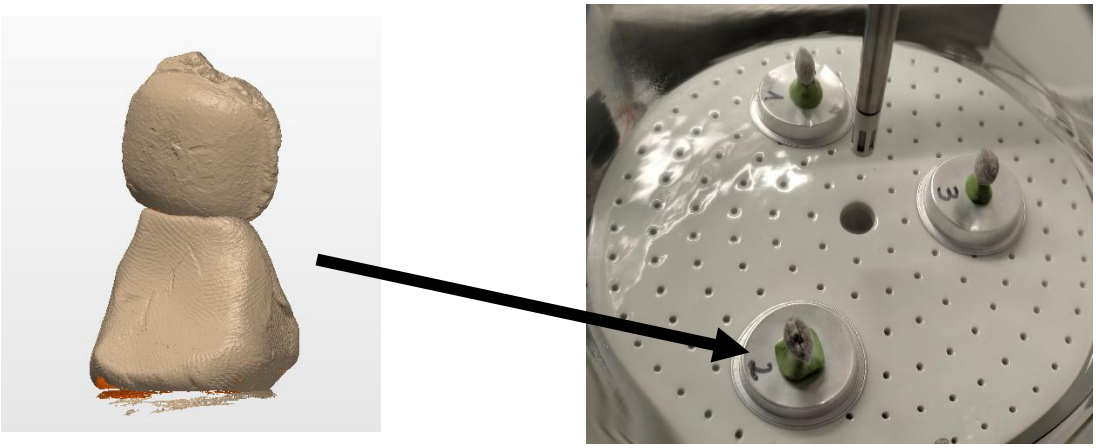


Fig. 6.18 Pellets in a desiccator for testing long-term uptake of vapour

One pellet was removed from the desiccator in late January 2026 after 22 months and immediately subjected to 3D scanning. During scanning, cracks began to appear on the pellet surface as a result of drying. The water content amounted to 24 % and had therefore approximately doubled over the 22-month period.

After data processing, the scanned surface data acquired before and after the experiment were aligned using the PolyWorks best-fit algorithm, including pre-alignment based on user-defined point pairs. Swelling was first visualized by overlaying the initial pellet geometry with a transparent representation of the swollen pellet (see Fig. 6.19). Subsequently, the distance between the two datasets was calculated along the surface-element normals and displayed as a false-colour comparison plot, revealing an expansion of approximately 1–2 mm across the entire pellet.

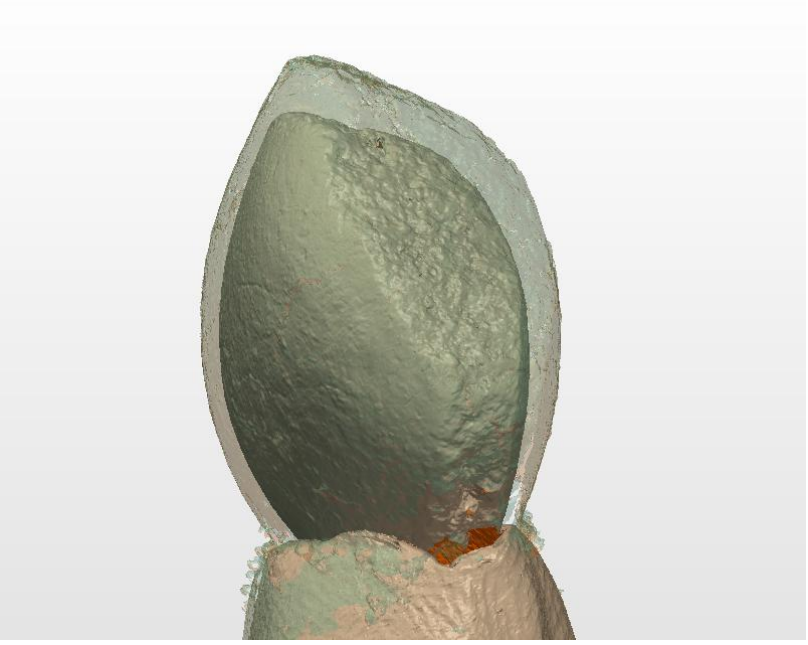


Fig. 6.19 Swelling of a MX-80 pellet after 2 years exposure to high humidity

The results for the first pellet showed substantial water uptake and swelling. The discussion within the Task Force EBS was therefore resolved clearly. With regard to Test I, however, uncertainty remained as to whether steady state had actually been reached within 22 months. In Test I, substantially more time was required for water uptake to cease. However, Test I involved confined samples, whereas Test III was performed as a free-swelling test. Because Test III requires very little maintenance, it was decided to continue the test and examine the remaining two pellets at a later time.

7 Topic 5 – Initial flow dynamics at the bentonite-rock contact

Topic 5 concerns the physical simulation of the interaction between groundwater flow and bentonite re-saturation at the buffer-rock contact. In a real deposition situation, it is expected that the walls of tunnels and deposition boreholes have been dried by ventilation. The dried-out fringe zone must therefore be re-saturated by water from deeper parts of the rock before water can be taken up by the bentonite. Due to the natural aperture variation in the fractures, a straight wetting front is not expected to form during this process; instead, a locally concentrated, finger-like flow pattern is likely to develop. In this situation, these fingers encounter comparatively dry bentonite, which exerts high suction on the approaching water.

Such a scenario had already been proposed in /KRÖ 17/, although the underlying hypothesis could not be substantiated at that time. The expected effects can now be observed directly using the new method for producing detailed, realistic, and transparent fracture replicas. Accordingly, two phenomena are addressed here: fingering during fracture saturation and the influence of high suction on a partially water-saturated fracture. The investigations under Topic 5 are based on fracture surface geometries obtained with the support of SKB from material originating from Äspö /KRÖ 26/ (cf. subsection 2.2.1).

During development of the new method for realistic printed fracture replicas, several questions arose that could not be answered directly. These questions were addressed by a series of accompanying, limited-scope tests, which are described below before the main experiment is presented.

7.1 Accompanying tests

7.1.1 Long-term water uptake of the printing material

Preliminary tests on the water uptake of printed resin materials had already been performed in a previous project /KRÖ 20b/. Two objectives were pursued in this context. First, different resins from different manufacturers were compared to support the selection of printer and printing materials. The tested array of sample cubes is shown in Fig. 7.1. In general, the uptake dynamics appeared diffusion-like, as the water uptake rate decreased

with time. With regard to total water uptake, the Formlabs materials intended for further use showed favourable properties.

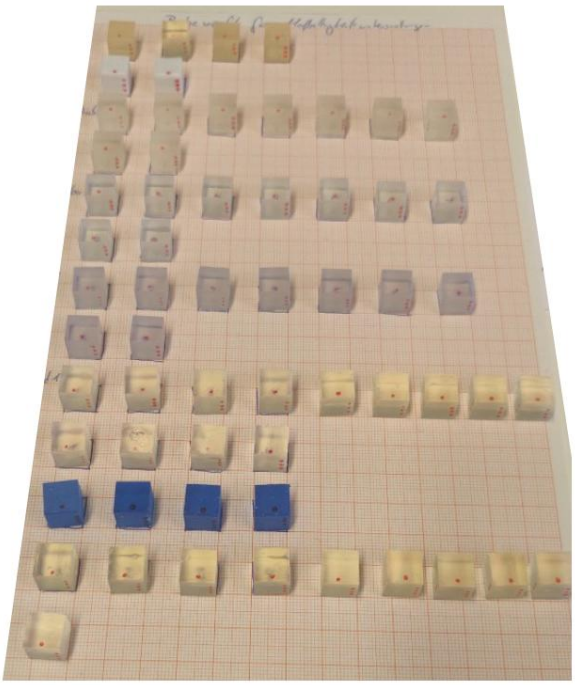


Fig. 7.1 Array of printed test cubes for different printing materials; from /KRÖ 20b/

Subsequently, uptake from water and from vapour was investigated for the Clear resin from Formlabs. Cubes with a side length of 1 cm were submerged in potassium permanganate solution for 53 days. After the cubes had been opened along a mid-plane, they were found to be completely and uniformly dyed (see Fig. 7.2), indicating that steady state had been reached. By placing a test cube in the Vapour Sorption Analyzer (cf. subsection 5.1.2), it was demonstrated that printed resin takes up water from water vapour. Furthermore, it was shown that printed resin may contain a certain amount of water immediately after printing, which can be removed when the material is placed in a sufficiently dry atmosphere. The measurement protocol of the corresponding test is shown in Fig. 7.3.

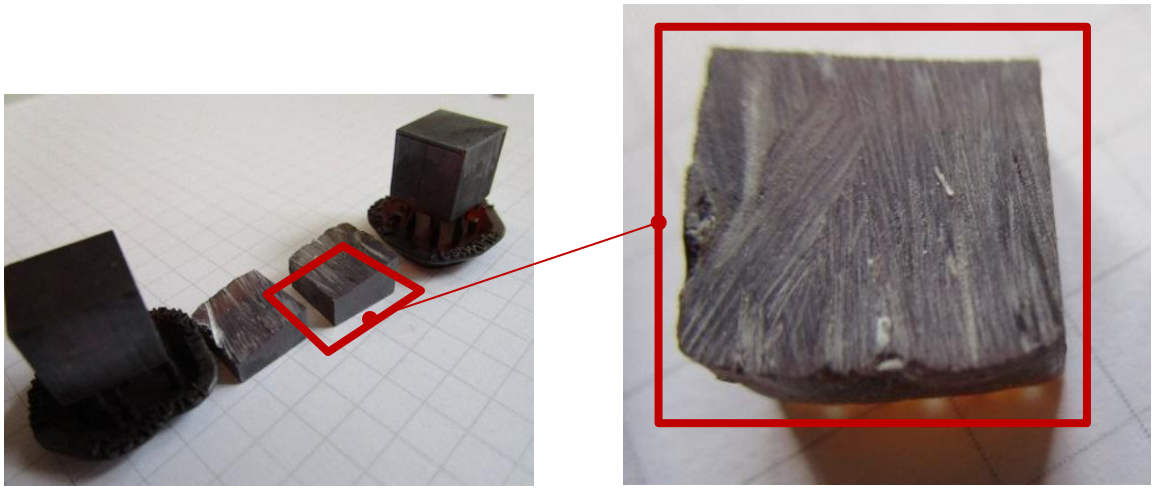


Fig. 7.2 Uptake of potassium permanganate by transparent printed cubes; from /KRÖ 20c/

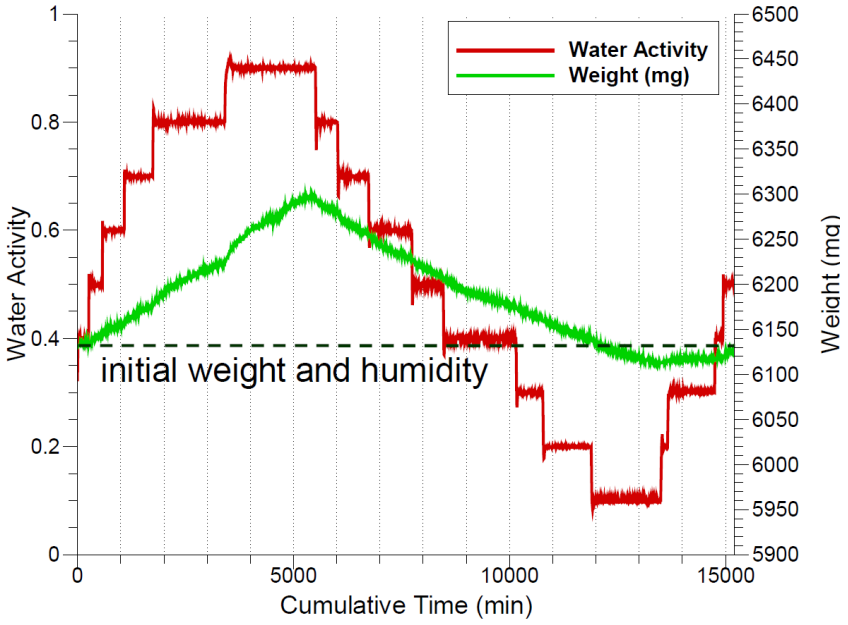


Fig. 7.3 Weight and water activity at varying relative humidity; from /KRÖ 20c/

The present accompanying tests also had two objectives. On the one hand, the water uptake dynamics were investigated, particularly with regard to a possible steady state. On the other hand, the post-processing procedure for the printed objects, namely washing time, curing time, and curing temperature, was optimized.

For this purpose, cubes with a side length of 1 cm were printed under identical conditions using Formlabs Clear V4 resin with a layer height of 25 µm. Washing time, curing time,

and curing temperature were systematically varied. As a reference, the settings recommended by Formlabs, namely curing for 15 minutes at 60 °C, were applied. A first series of 21 cubes with varying post-printing conditions was started and informally designated the “yellow series”. The varied post-processing conditions are compiled in Tab. 7.1.

After printing and post-processing, the support structures were carefully removed from the cubes. Each cube was then weighed and fully submerged in an individual small glass jar filled with water. A single test cube and the glass jars containing the test cubes are shown in Fig. 7.4.



Fig. 7.4 Printed test cube (left), test cubes in small jars with solution (right)

At predetermined intervals, the cubes were removed, gently blotted with a lint-free cloth to remove surface water, weighed, and then re-immersed. Initially, measurements were performed daily. As the water uptake rate decreased, the measurement intervals were progressively extended to reduce unnecessary handling. Sample #18 rapidly showed printing defects that rendered it unsuitable and was therefore removed from the test.

After 5 weeks, favourable conditions appeared to become identifiable in the yellow series (cf. Fig. 7.5, left). This observation motivated the start of a second series, the blue series, in which specifically these conditions were varied (for details, see Tab. 7.1). In parallel, samples #12, #14, and #21 of the yellow series, which were considered unfavourable, were transferred to a desiccator containing a drying agent to investigate drying dynamics. Tests on the remaining unfavourable samples #1, #2, #4, #5, #7 to #9, #11, #13, #17, and #20 were stopped in order to optimize the handling of the measurements.

Tab. 7.1 Post-processing conditions of the test cubes; colours according to Fig. 7.6

yellow series sample #	washing time [min]	curing time [min]	curing temperature [°C]	layer height [µm]	comments
1	5	0	-	25	stopped after 35 days
2	15	0	-	25	stopped after 35 days
3	20	0	-	25	strange late evolution
4	5	30	35	25	stopped after 35 days
5	15	30	35	25	stopped after 35 days
6	20	30	35	25	
7	5	30	80	25	stopped after 35 days
8	15	30	80	25	stopped after 35 days
9	20	30	80	25	stopped after 35 days
10	5	15	80	25	
11	15	15	80	25	stopped after 35 days
12	20	15	80	25	drying after 35 days
13	5	30	60	25	stopped after 35 days
14	15	30	60	25	drying after 35 days
15	20	30	60	25	
16	5	15	60	25	
17	15	15	60	25	stopped after 35 days
18					dropped
19	5	15	35	25	
20	15	15	35	25	stopped after 35 days
21	20	15	35	25	drying after 35 days
blue series sample #					
31	3	10	60	25	high water uptake
32	3	15	60	25	
33	3	20	60	25	
34	5	0	60	25	strange late evolution
35	5	15	60	25	
36	5	30	60	25	
37	5	15	60	50	
38	5	15	60	100	
39	8	10	60	25	
40	8	15	60	25	
41	8	20	60	25	

In Fig. 7.5, right, the starting point of the blue data series was shifted to 0 days to facilitate comparison with the yellow series. In principle, the curves of the blue series form a narrower band and are generally located in a more favourable part of the range spanned by the yellow series. However, the results are not improved to a highly significant extent.

Moreover, after analysis of the post-printing conditions in Tab. 7.1, no clearly advantageous pattern was identified.

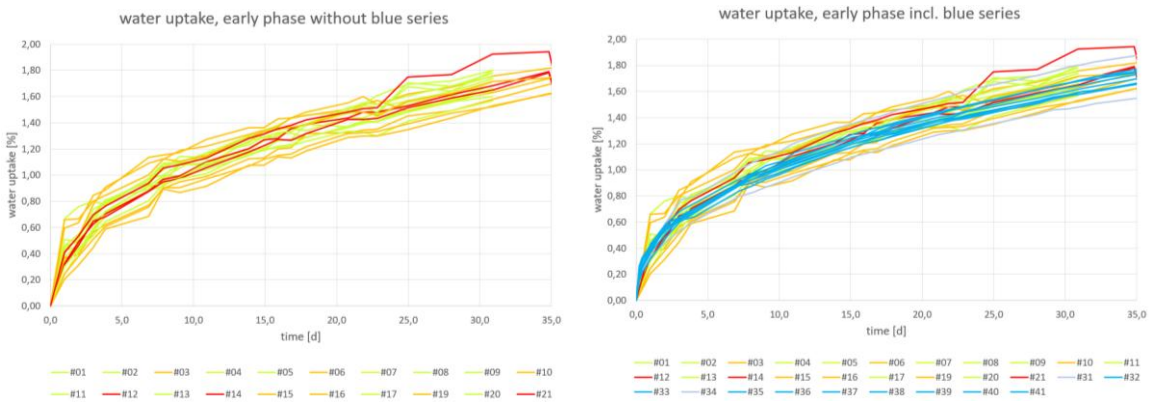


Fig. 7.5 Early water uptake; without blue series (left) including blue sries (right)

The tests ended after 765 days for the yellow series and after 730 days for the blue series. The complete evolution of the amount of water taken up, referenced to the initial weight, is plotted in Fig. 7.6. The data indicate that no further water was taken up or lost at the end of the tests.

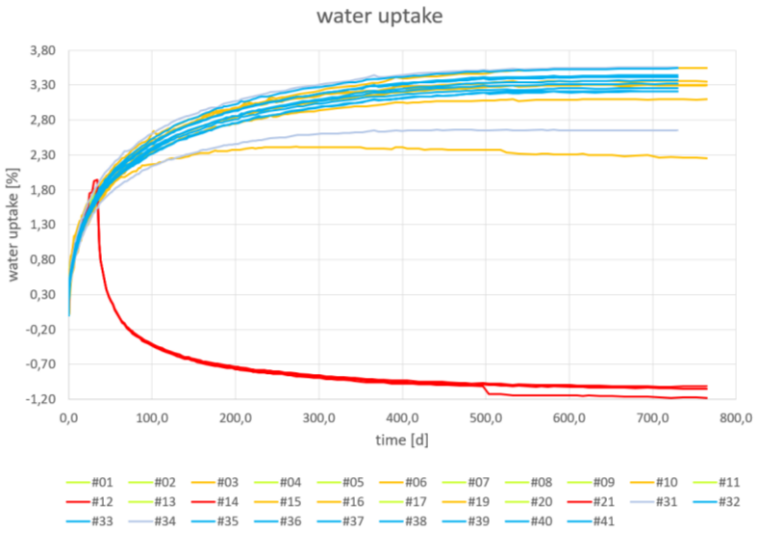


Fig. 7.6 Uptake of water in all test cubes over time

The tests ended after 765 days for the yellow series and after 730 days for the blue series. The complete evolution of the amount of water taken up, referenced to the initial weight,

is plotted in Fig. 7.6. The data indicate that no further water was taken up or lost at the end of the tests.

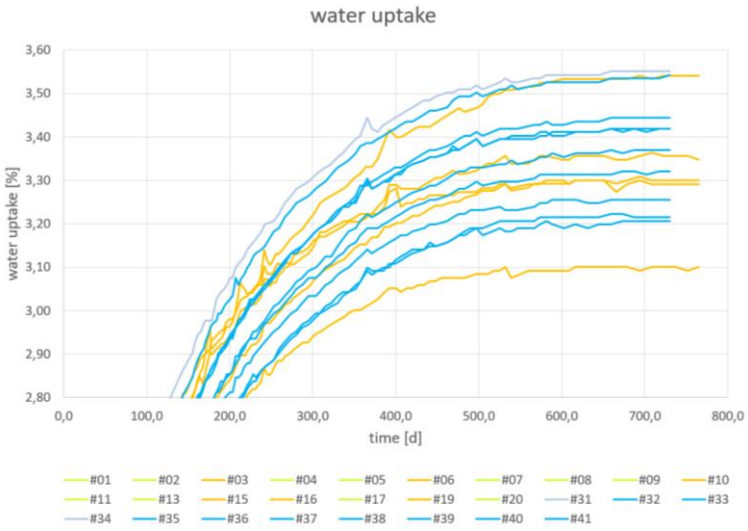


Fig. 7.7 Uptake of water in all test cubes over time, first enlargement

For further assessment, the uptake rates were calculated and are shown in Fig. 7.8 and, at higher resolution, in Fig. 7.9. The rates become very low towards the end of the tests and are therefore strongly affected by unavoidable measurement errors[7]. Maximum water uptake therefore appears either to have been reached already or to be very close in terms of mass, although not necessarily in terms of time.

[7] Note that the time to lose 1 mg of water from a cube was checked twice and amounted to a range between 2 and 18 seconds. The weight measurements of the cubes were therefore performed as quickly as possible.

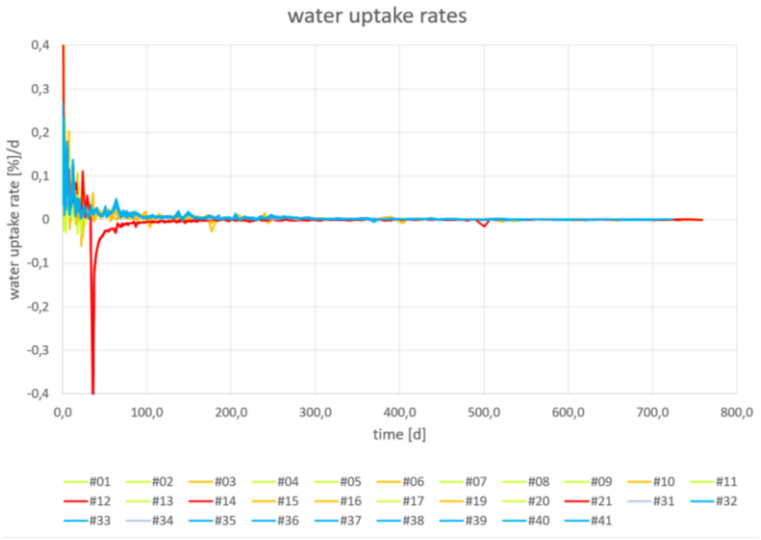


Fig. 7.8 Uptake rate in all test cubes over time

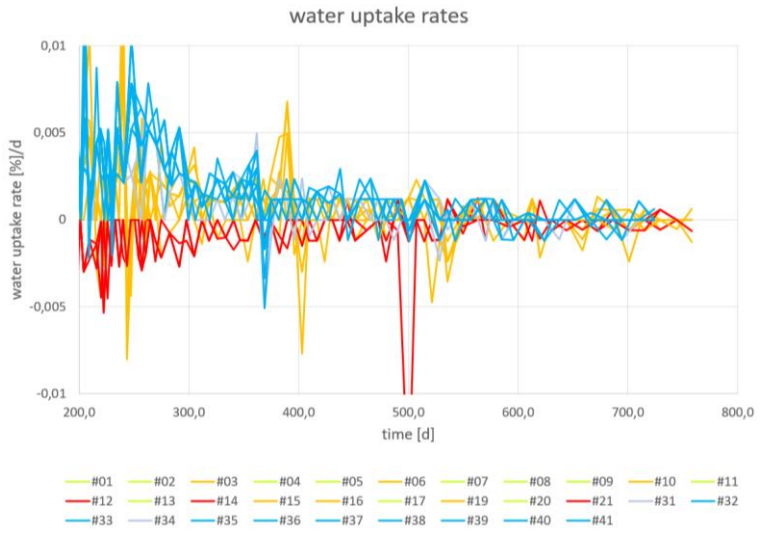


Fig. 7.9 Uptake of water in all test cubes over time, higher resolution

In the drying case, steady state clearly had not been reached, as shown in Fig. 7.10, and is expected to occur well below -1 %.

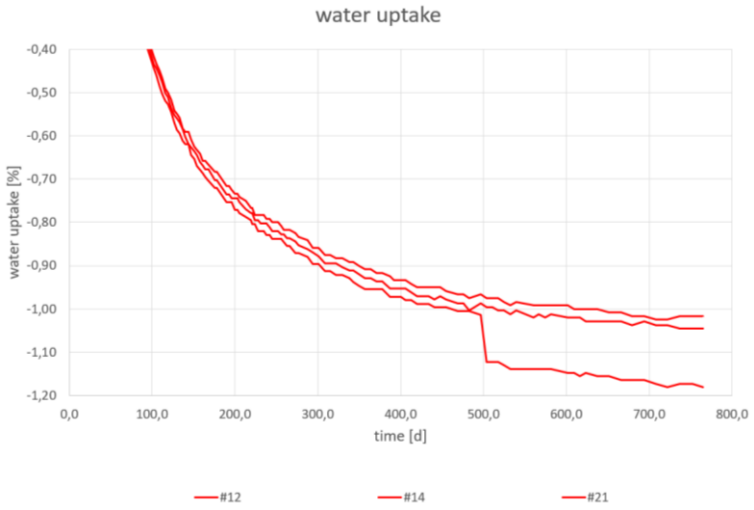


Fig. 7.10 Uptake of water in all test cubes over time, second enlargement

Overall, the following conclusions can be drawn:

- water uptake and water loss due to ambient conditions converge approximately exponentially towards maximum and minimum values, respectively;
- more than two years were required to reach steady state in the tests;
- the scatter in the obtained uptake curves cannot be satisfactorily explained by the post-printing conditions during washing and curing;
- no post-printing procedure was identified that clearly minimized water uptake.

7.1.2 Accuracy of printed planar surfaces

Since the accuracy of a printed rough fracture surface is difficult to assess directly, printing accuracy was evaluated for planar surfaces oriented at different angles. For this purpose, a test body was designed with three planar surfaces inclined at angles of 30°, 45°, and 65° relative to the printing platform (see Fig. 7.11). The visibility of layer-induced steps varies depending on the surface angle. Because the test body was printed using Formlabs Clear resin, the part had to be slightly tarnished before 3D scanning could be performed.

Close inspection of the steps in the resulting dataset showed that they did not exhibit sharp edges but appeared comparatively uneven. To verify that this effect was not caused by limitations of the 3D scanner, the obtained triangular mesh was overlaid onto the determined geometry, as shown in Fig. 7.12. The analysis showed that each step was resolved

by 2–3 mesh elements, indicating that the observed unevenness is an artifact of the printing process rather than of scanning. However, Fig. 7.12, left, indicates that the printing errors are generally smaller than the layer thickness of 25 µm set on the printer.

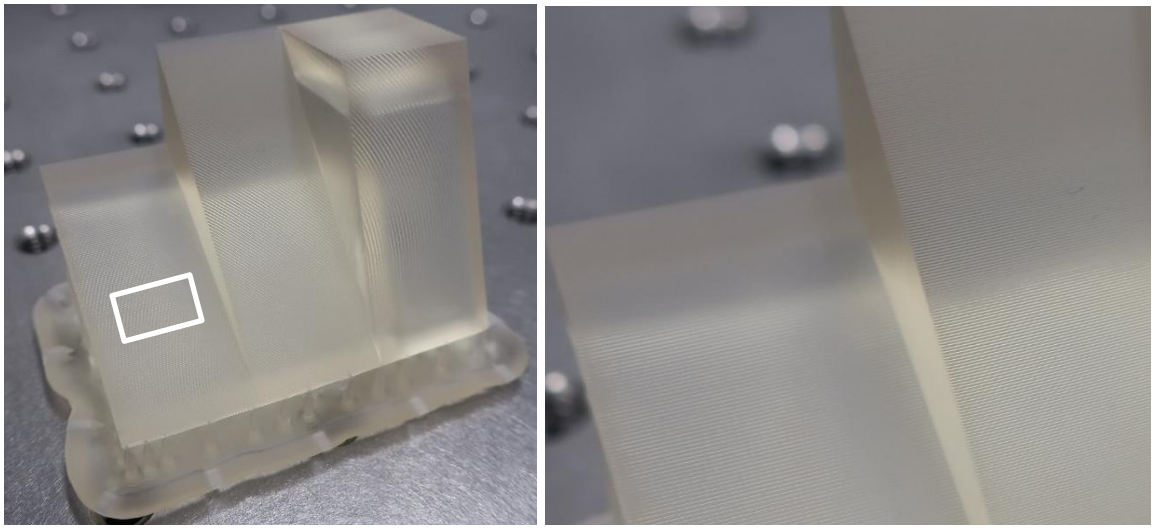


Fig. 7.11 Printed test body with differently slanted planes (left), close-up (right)

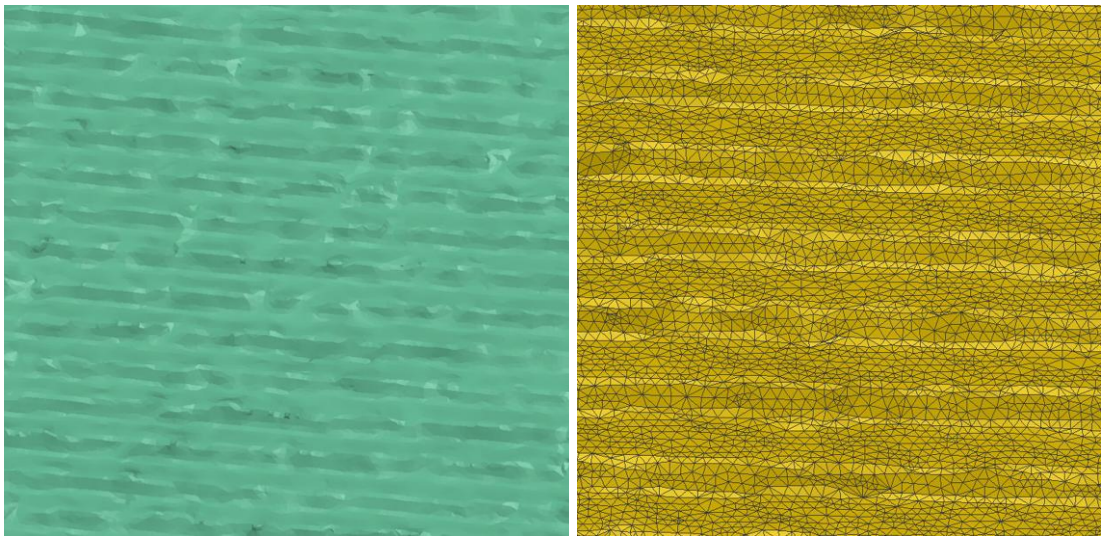


Fig. 7.12 Scan of slanted plane (30°), without scanning grid (left), with grid (right)

7.1.3 Deformation of printed bodys due to water uptake

The same test body was subsequently used in an additional water uptake test to investigate potential deformations. Before the test, the part was thoroughly cleaned to remove

residual tarnishing spray from the surface. It was then fully submerged in water for 24 hours, corresponding to the default test duration for uptake measurements performed by Formlabs. After removal from the water, the piece was gently blotted with a lint-free cloth to remove surface water. The test body was then re-tarnished and 3D scanned. The datasets acquired before and after wetting were compared, and the geometric differences were visualized using a false-colour comparison (see Fig. 7.13).

The comparison revealed systematic deformations of up to approximately 300 µm. The spatial distribution showed a clear gradient from the central region of the sample towards the edges, with comparatively small deviations in the interior and progressively larger displacements near the boundaries. This deformation pattern suggests that water uptake primarily caused global expansion of the part, while local amplification occurred at geometrically exposed regions such as edges and corners. The pronounced edge deformations were therefore probably not caused solely by uniform material swelling, but may also have been influenced by residual internal stresses originating from the printing process and released during wetting. Geometry-dependent stress redistribution appears to have accentuated deformation at the sample margins. Overall, the observed magnitude and pattern of deformation indicate that water uptake can induce measurable but spatially heterogeneous geometric changes. While the central regions remained largely stable within the observed tolerance range, edge effects should be considered when high-resolution geometric measurements on water-exposed printed specimens are interpreted.

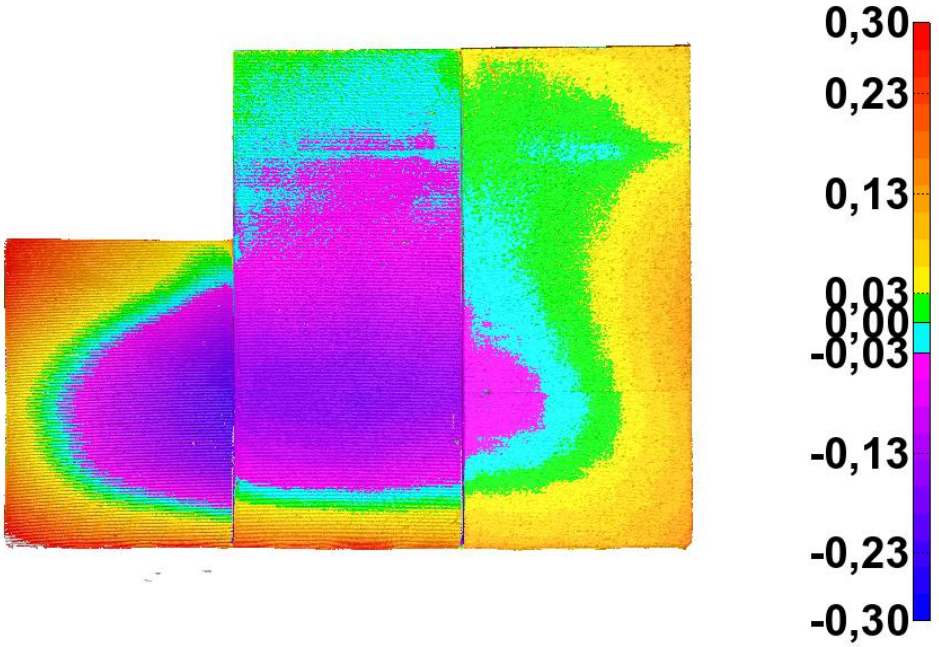


Fig. 7.13 False-colour comparison, printed test body before and after 24h of exposure to water

7.1.4 Post-processing induced deformation of printed fracture replicas

Several post-processing steps are required between removal of a printed fracture replica from the printer and its use in subsequent experiments. These steps include washing, curing, machining (milling and grinding), polishing, and, in some cases, exposure to water. Each procedure may induce geometrical deviations from the original digital dataset. To systematically evaluate and quantify these effects, the fracture surfaces were 3D scanned before and after each individual processing step. This approach enabled deformation visualization and workflow optimization to minimize geometrical alterations.

Comparison between digital dataset and washed replica

A first comparison was performed between the original digital dataset and a 3D scan of the printed fracture replica after washing with isopropyl alcohol (IPA). Scanning before washing was not feasible because residual resin remained on the fracture surface.

The comparison showed that deviations from the digital dataset occurred predominantly in the edge regions of the printed replica. These deviations are likely related to insufficient

structural support during printing. A lack of support structures in edge regions may result in reduced dimensional stability and slight warping.

To improve the dimensional accuracy of the printed objects, several measures were implemented:

- the total number of support structures was increased;
- the density of support contact points was increased specifically in boundary regions;
- overall stability was enhanced by placing the replica directly on the build platform instead of using a raft structure.

These modifications significantly improved geometric fidelity, particularly at the replica edges, as shown in Fig. 7.14.

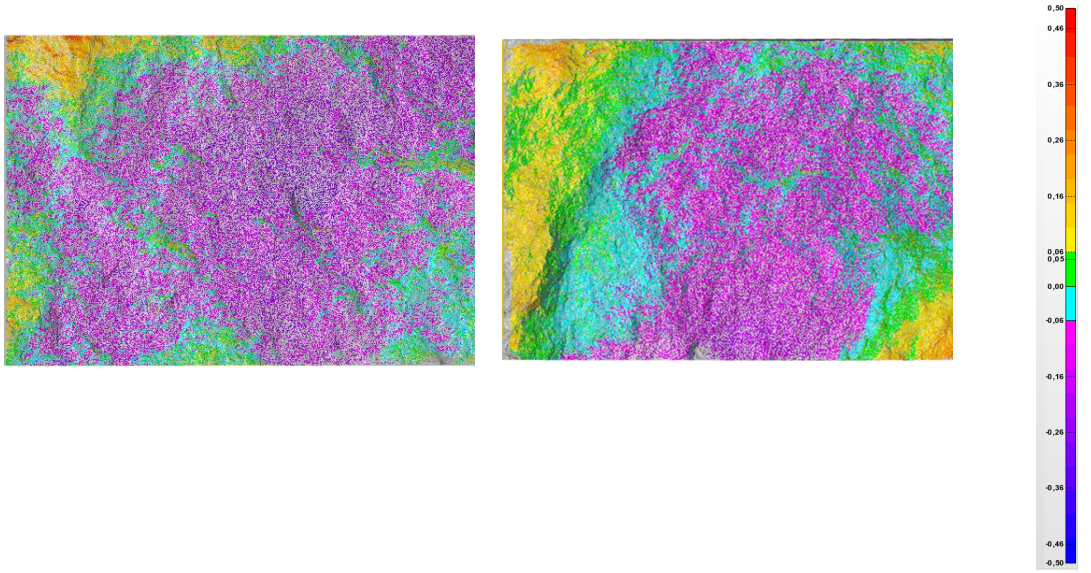


Fig. 7.14 False colour comparison, printed dataset vs digital data; left: top surface; right: bottom surface

Deformation due to curing

The influence of curing was evaluated by performing 3D scans before and after the curing process. Deformations of up to approximately 100 µm were observed. These deformations are attributed to UV exposure at elevated temperatures, which induces additional cross-linking and internal stress redistribution within the polymer (see Fig. 7.15).

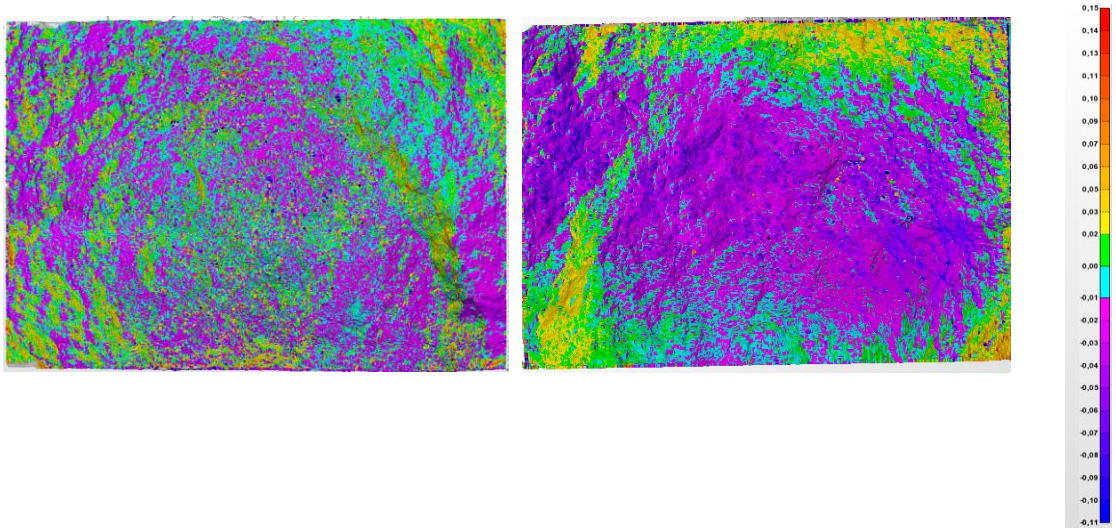


Fig. 7.15 False colour comparison, replica before vs after curing; left: top surface; right: bottom surface

Curing was performed using a Formlabs curing unit. A key limitation of this system is that UV light is applied predominantly from above, resulting in uneven exposure of the replica. Turning the specimen during curing was not possible without risking damage to the fracture surface, because the material had not yet reached its final mechanical stability.

When replicas were placed directly on their rough fracture surfaces during curing, increased deformation was observed. The uneven support conditions appear to amplify distortion.

Process analysis revealed the following trends:

- shorter curing times resulted in reduced deformation;
- lower curing temperatures led to decreased geometric deviation.

Curing parameters were therefore adjusted to balance deformation minimization with sufficient polymerization, which was required to reduce water uptake during later processing steps.

Deformation due to milling, grinding, and polishing

Subsequent mechanical processing steps also contributed to surface deformation. During milling and grinding, local temperature increases occurred due to friction and material

removal. In addition, mechanical energy was introduced into the material, which may cause stress relaxation and localized distortion.

During polishing, the replica was continuously cooled with water to reduce friction-induced heating. Although thermal effects were effectively limited, water exposure introduced a secondary deformation mechanism due to moisture absorption. The resulting deviations were distributed across the entire surface, occurred in both positive and negative directions, and exhibited a non-uniform spatial pattern.

Swelling due to water exposure

To further isolate the influence of water uptake, a dedicated swelling experiment was conducted. The fracture replica was first 3D scanned in dry condition, subsequently submerged in water for 24 hours, and then scanned again after removal. The scanning results are shown in Fig. 7.16.

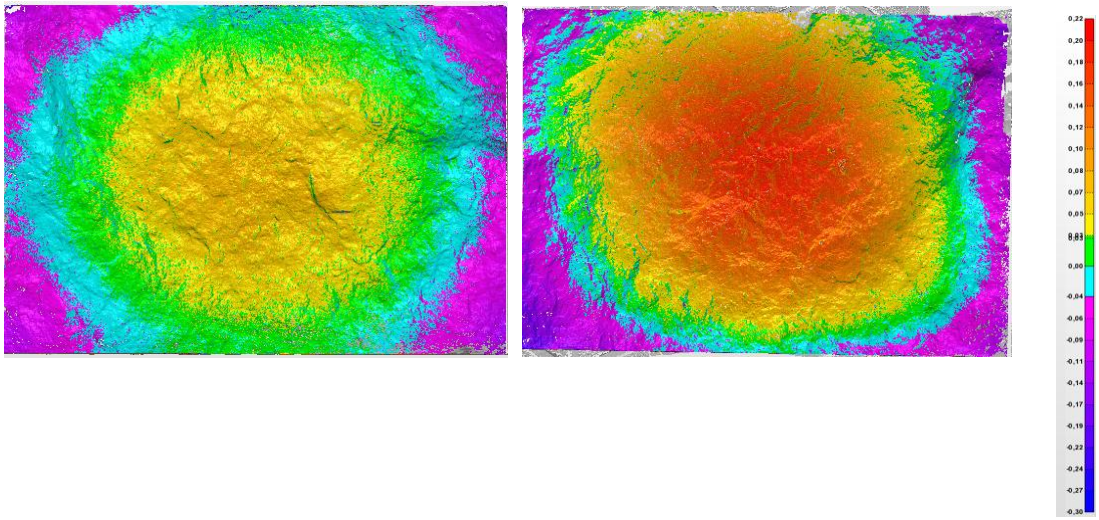


Fig. 7.16 False colour comparison, replica before vs after wetting; left: top surface; right: bottom surface

The deformation pattern was similar to that previously observed for the test specimen with tilted planar surfaces. On a larger scale, expansion occurred predominantly in the central region of the replica, leading to relative displacement of the boundary areas. Due to these large-scale effects, the expected small-scale deformations were not measurable across

the entire surface, because both 3D scan datasets were aligned using a feature-based alignment algorithm in Polyworks Inspector.

These results indicate that water absorption contributes significantly to geometric changes in the printed polymer and may partly explain the deformation observed during polishing. It is therefore advisable to check for deformations by 3D-scanning before and after a hydraulic test.

7.1.5 Repeatability of a wetting test

As preparation for the fracture-bentonite interaction experiments, the repeatability of wetting an air-dry fracture was investigated. For this purpose, a replica of a cropout section of the VS0040B03 fracture was used. A tracer solution was injected pointwise into the fracture at a constant flow rate using a syringe pump. The tests were repeated three times under identical conditions.

Since the test cell had to be cleaned and resealed between individual tests, minor shifts in cell position prevented direct image overlay. To compensate for these shifts, the images were registered to each other. Characteristic features of the rough fracture surfaces were manually selected to guide the registration process and to account for the movement of the air–water interfaces over time. After segmentation of the registered images, the resulting binary arrays were overlaid to visualize test repeatability in greyscale plots. In these plots, white indicates air, whereas black represents tracer detected in all three tests. Areas in which tracer was detected in only one or two tests are shown in shades of grey.

The results demonstrate satisfactory repeatability of the wetting pattern, particularly with regard to repeated air entrapment at several locations.

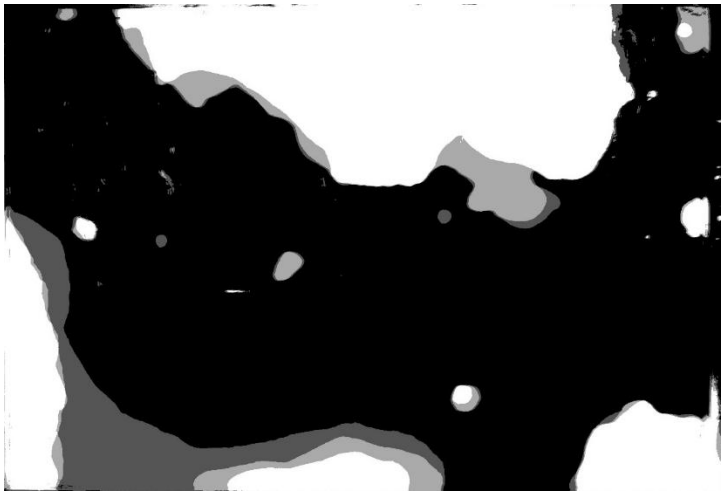


Fig. 7.17 Repeatability of the wetting from the left of a single fracture including air enclosure; pixel-wise overlay of 3 tests; colour code: tracer detected in all 3 tests (black), in 2 tests (grey), in 1 test (light grey), no tracer (white)

A preliminary test was conducted at an injection rate of 0.5 ml/h to compare two physical replicas produced by different additive manufacturing systems. One replica was fabricated in-house using a Formlabs printer, whereas the second replica was produced by Anna Suzuki at Tohoku University, Japan, using a Keyence 3D printer. Both replicas were printed from the same underlying dataset, ensuring identical geometric input for the manufacturing process.

To assess potential differences in the experimental response arising solely from the printing technology, segmented images acquired at identical time points were used for comparison. The segmented datasets were spatially aligned and overlaid to enable direct visual and quantitative comparison of the evolving structures. This overlay approach enabled deviations in morphology and temporal development between the two replicas to be identified under otherwise identical experimental conditions, as shown exemplarily in Fig. 7.18.



Fig. 7.18 Repeatability of the wetting of a single fracture from the left including air enclosure; pixel-wise overlay of tests in replicas produced on 2 different printers; colour code: tracer detected in both tests (black), in 1 test (light grey), no tracer (white)

7.1.6 Wetting patterns depending on flow direction

An experiment was conducted to investigate the dependence of wetting patterns on the flow direction through the fracture. In both tests, fluid injection was performed at a constant flow rate of 0.5 ml/h, while the injection direction was reversed between the two cases. The images shown in Fig. 7.19 were acquired after 1 h 15 min of injection. In the images, dark regions correspond to tracer-saturated areas, whereas bright regions indicate air-filled parts of the fracture. Despite identical injection rates and observation times, the resulting wetting patterns differed noticeably between the two flow directions, indicating a clear influence of flow direction on the spatial development of re-saturation within the fracture.

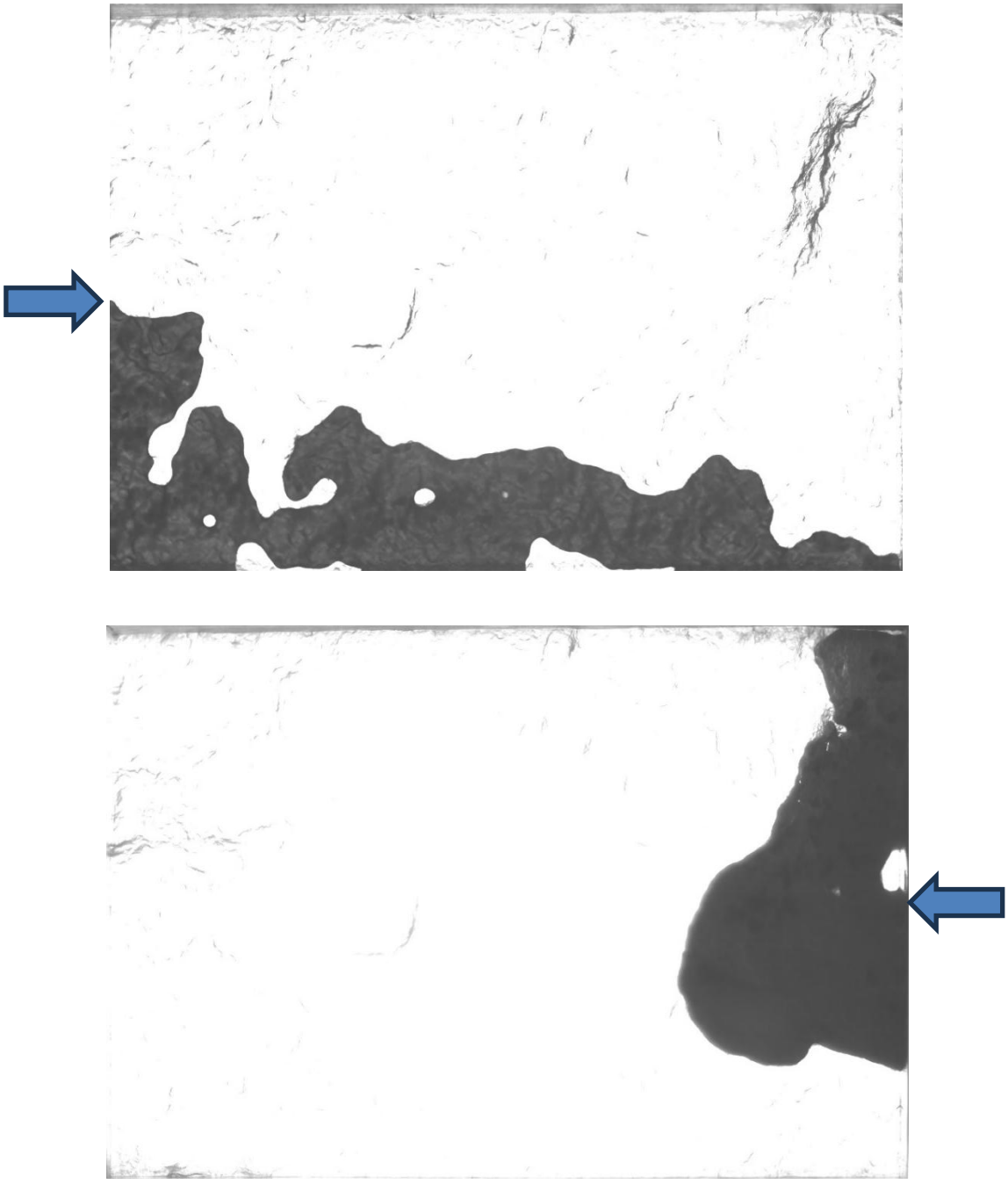


Fig. 7.19 Wetting patterns depending on the flow direction; top: inflow from the left, bottom: inflow from the right

7.1.7 Repeatability of a percolation test on a DFN

After the work of Anna Suzuki from Tohoku University, Japan, on percolation tests using printed micro-DFNs /SUZ 17/ had been noticed, contact was established to exchange

ideas on hydraulic tests with printed fracture replicas. During these discussions, the repeatability of experiments performed on 3D-printed fractures or fracture networks derived from the same digital model but manufactured using different printers was addressed. It was therefore agreed that comparative tests should first be performed on the fracture network based on /SUZ 17/.

After the geometry file had been shared, initial attempts were made to print the model. Due to the complex internal structure of the micro-DFN, support structures would have been required to make the model printable on the Form 3 printer. Since this limitation is inherent to the printing technique rather than to the specific printer, the DFN was fabricated externally using a Stratasys PolyJet printer. This printer uses two different materials, one forming the rigid model and the other serving as water-soluble support material. Removal of the support material from the fracture network proved to be time-consuming. The digital model from /SUZ 17/ and the newly printed physical model are shown in Fig. 7.20.



Fig. 7.20 Micro-DFN used in /SUZ 17/ (left), DFN printed from the digital model (right)

For the intended permeability measurements, a silicone cap with an integrated hose fitting was printed on the Form 3 printer and attached to one end of the cylindrical micro-DFN sample. The sample was connected to a water reservoir providing a constant hydraulic head and was positioned above a beaker to collect the outflowing water. The beaker was placed on a balance to measure the amount of outflowing water over time. From these data, the integral permeability of the micro-DFN could be determined. A photograph of the set-up is shown in Fig. 7.21.

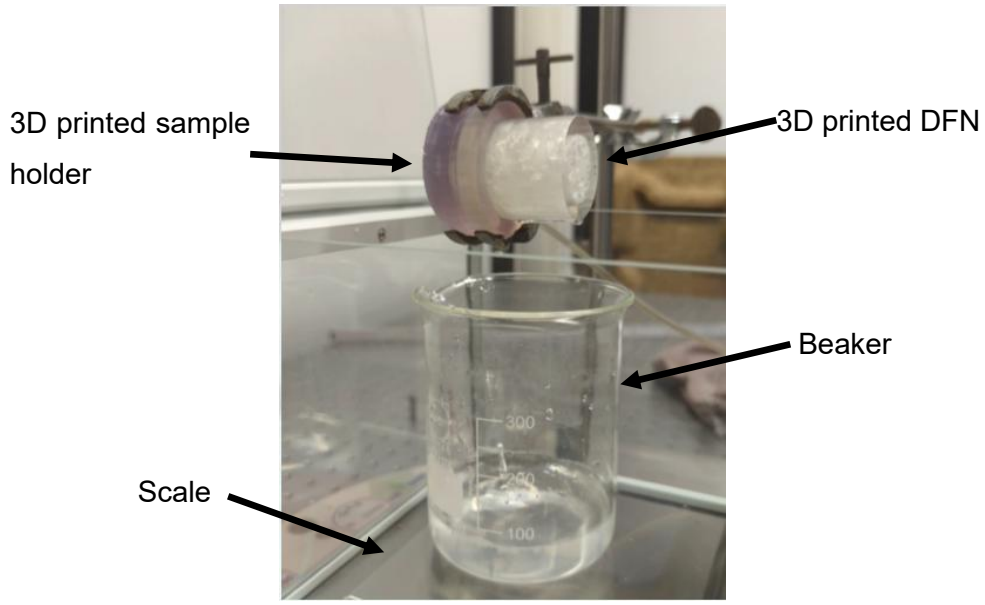


Fig. 7.21 Permeability test on the 3D-printed DFN

The measured permeabilities were within the same range as those reported by Anna Suzuki, although they were slightly higher, as shown in Fig. 7.22. The differences may be attributed either to the varying effectiveness of different fluids in removing residual support material or to printing artifacts within the DFN. Although residual support material in the present sample could not be quantified by CT scanning, as in /SUZ17/, the comparable permeability values suggest a higher solubility of the support material, resulting in more open fractures within the micro-DFN and consequently in higher permeability.

The results obtained at GRS attracted sufficient interest that an invitation to the International Conference on Fluid Dynamics ICFD 2023 in Sendai, Japan, was received. A presentation was given on the tests performed on the micro-DFNs and on the method of hydraulic testing using physical models. The presentation received a best presentation award and raised the interest of Abdul Quadir, at that time a master student of Prof. Wei Hsin-Tien, thereby initiating a collaboration with TaiwanTech.

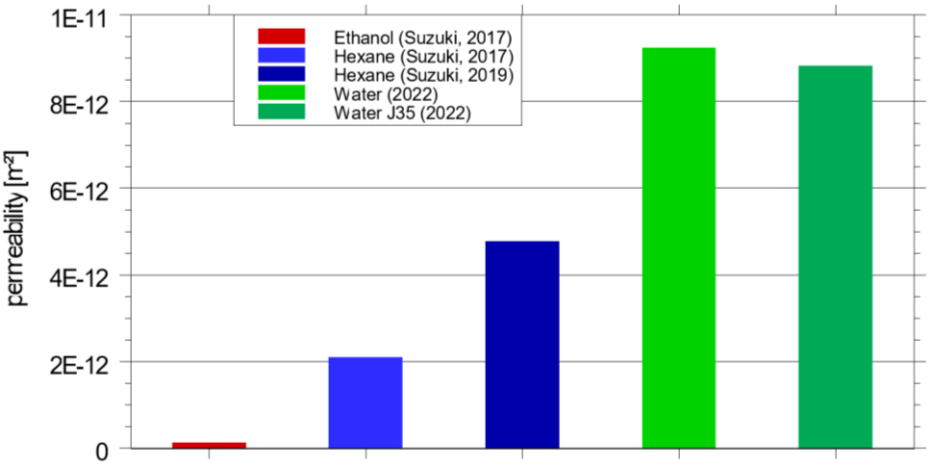


Fig. 7.22 Total permeability of two 3D-printed micro-DFNs using different solutions for dissolving support material

7.1.8 Combining optical 3D-scans with CT images

At the University of Jyväskylä, fracture surfaces are measured using X-ray computed tomography (CT). This technique has the advantage that data can be acquired from undisturbed samples. Interesting fractures can therefore be detected non-destructively, and artefacts such as flakes, which may occur during sample opening or due to rock relaxation processes, can be avoided. These measurements were carried out in collaboration with the Geological Survey of Finland (GTK) on representative material from the Olkiluoto area within the FLOP project /VYR 23/.

Because the 3D scanning method developed within the present project provides surface data at a higher spatial resolution than the CT data, complementary 3D scans were considered to combine the advantages of both methods. Since some of the fractures had been opened in the meantime, the CT data of the intact fracture were used as a reference for aligning the 3D scanning data. The STL-format was selected for data exchange because it could be generated and processed by both systems. While conversion of the 3D scanning data was straightforward, conversion of the CT data proved to be more challenging.

The CT data acquisition and conversion into the STL-format were performed by the University of Jyväskylä. Since the CT output consists of intensity maps for each acquired slice, segmentation was required to extract the fracture surfaces. This step was performed using Fiji /SCH 12/ with the FeatureJ plugin /MEI 02/ to detect edges in the X and Y directions. The spacing of the resulting point clouds in the Z direction corresponds to the slice spacing of the CT scan. By adjusting the segmentation threshold, either additional very narrow fractures could be captured or noise could be reduced. However, filtering the data was challenging, because clusters of points representing small fractures were frequently removed by the noise-filtering algorithm due to their limited size. After optimization of the segmentation parameters, an STL-file with a resolution of approximately 60 µm was exported.

Although the major fractures in sample 04B were already open, the sample was reassembled to reconstruct the original alignment as accurately as possible. Following the standard workflow for acquiring fracture surfaces by 3D scanning, reference markers were attached to the outer surface of the sample. After scanning, the relative positions of the markers and fracture surfaces were determined, and the resulting datasets were used to calculate aperture distributions. To further improve alignment accuracy, each 3D scanning dataset was re-aligned according to the CT-derived fracture topography using the best-fit algorithm implemented in PolyWorks Inspector. An example of combined CT and 3D scan data for localizing fractures in sample 04B is shown in Fig. 7.23. The determined fracture apertures are shown in Fig. 7.24.

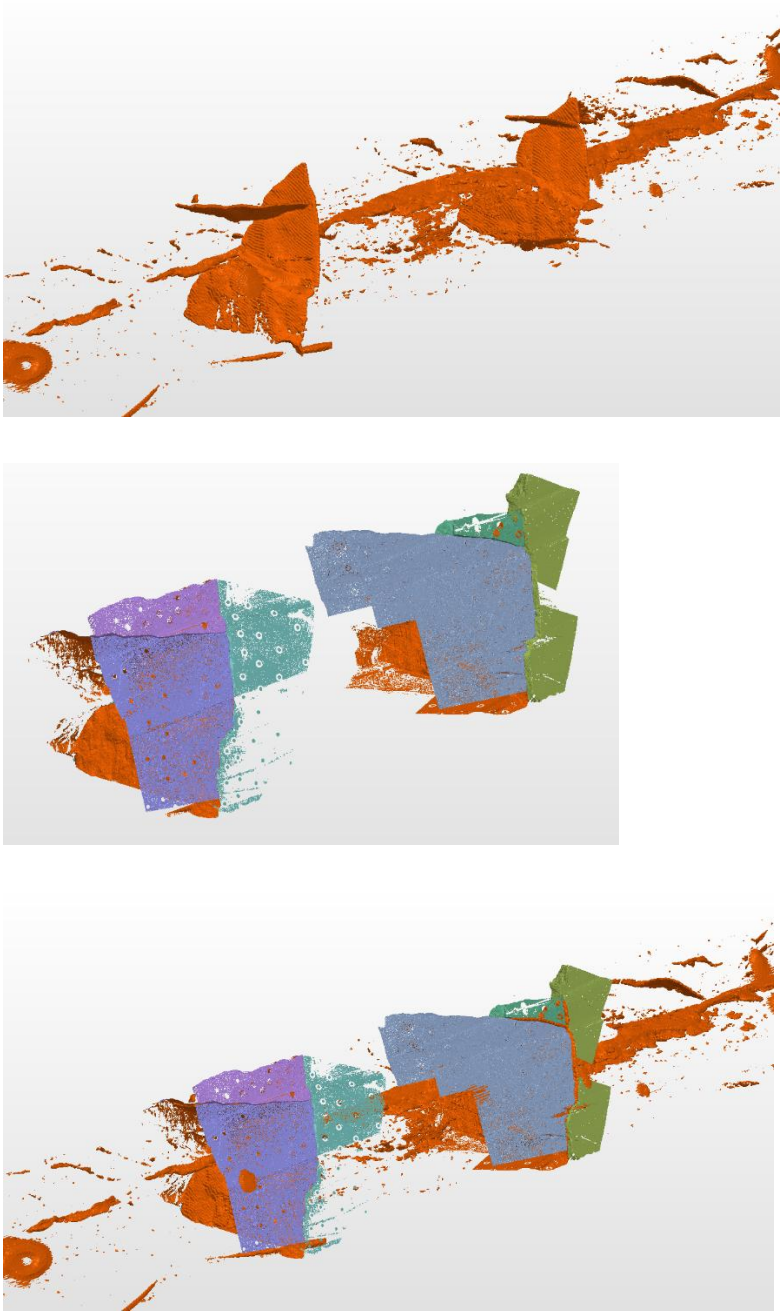


Fig. 7.23 3D-data on a fracture 04B by different techniques, CT by University of Jyväskyla (top), 3D-scan by GRS (middle), overlay (bottom)

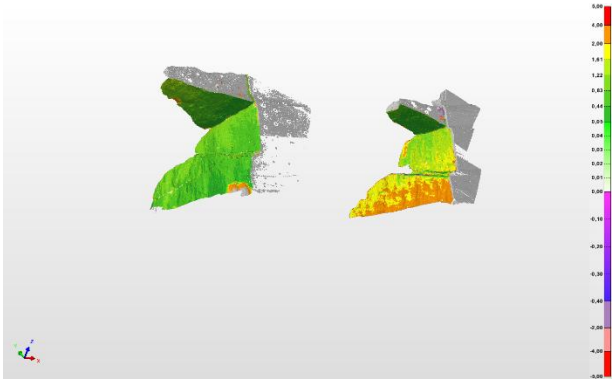


Fig. 7.24 Fracture apertures from 3D-scans

The present study demonstrates that CT and 3D scanning data can be effectively combined to generate a comprehensive dataset that exploits the strengths of both techniques. By aligning the 3D scan data with the CT images, high spatial accuracy based on the CT data was achieved while detailed surface information from the 3D scanning data was retained. This integration places the detailed but local 3D scan data into the broader context of the CT scan and improves the reliability of geometric and volumetric analyses. The combination of both methods therefore provides a more comprehensive representation of the sample structure than either method alone.

7.2 Main experiment

In this experiment, the interaction between a compacted bentonite body and water in a resaturating fracture was observed. For this purpose, an initially dry transparent 3D-printed fracture replica was brought into contact with a compacted bentonite body. Subsequently, water was injected at the fracture side opposite to the fracture-bentonite contact.

7.2.1 Experimental methods

In this experiment, the method for observing hydraulic processes described in section 2.1.3 was extended by attaching a compacted bentonite body to the outflow side of the fracture, as indicated in the principle sketch in Fig. 7.25. A test cell including hydraulic connectors was designed on the basis of a 7 × 10 cm outcrop section of the fracture from the VS0040B03 dataset with a mean aperture of about 190 µm. The cell provides pointwise inflow on one side and visible fracture traces on the remaining three sides after

assembly. To preserve the original alignment of the two fracture halves, cylindrical holes for two alignment dowels were included on either side of the injection point.

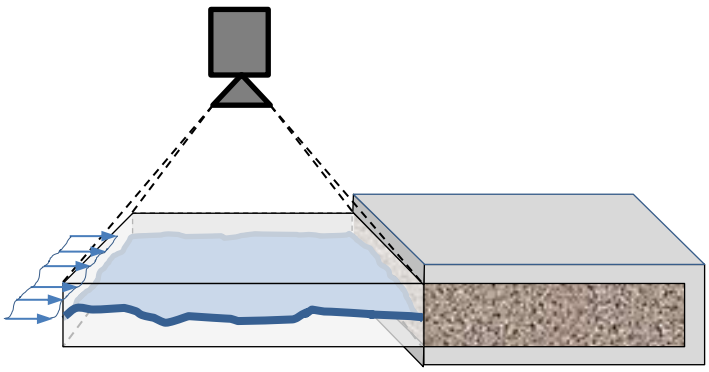


Fig. 7.25 Principle of the tests under Topic 5

Since the 3D-printed material was not sufficiently strong to withstand the swelling pressure of the bentonite body, a rigid test frame was constructed from solid square steel bars. Acrylic glass plates were mounted on the top and bottom of the frame to enable visual observation of the experiment. A visualization of the reinforcement frame from the CAD-file is shown in Fig. 7.26.

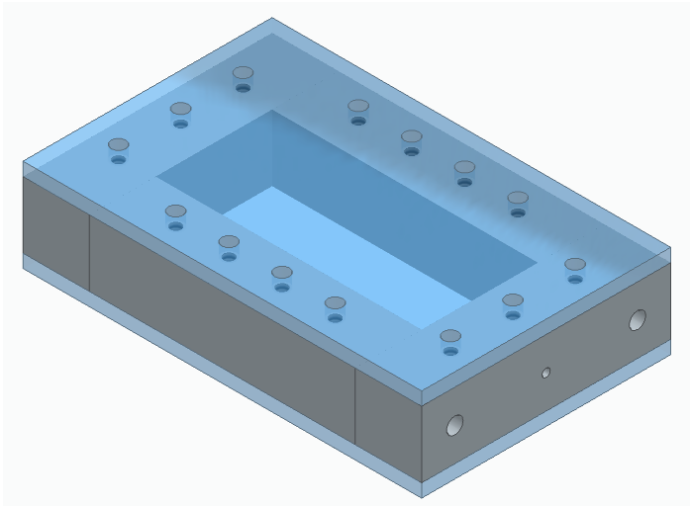


Fig. 7.26 CAD construction of the reinforcement frame for the Topic 5 experiments

Assembly of the reinforced test cell is illustrated in Fig. 7.27. The photograph on the left shows the frame and the bottom half of the fracture replica, the photograph in the middle

shows the open frame with the complete replica, and the photograph on the right shows the fully assembled reinforced test cell. To ensure good contact between the fracture replica and the bentonite body, the bentonite sample was compacted directly within the reinforced test cell.

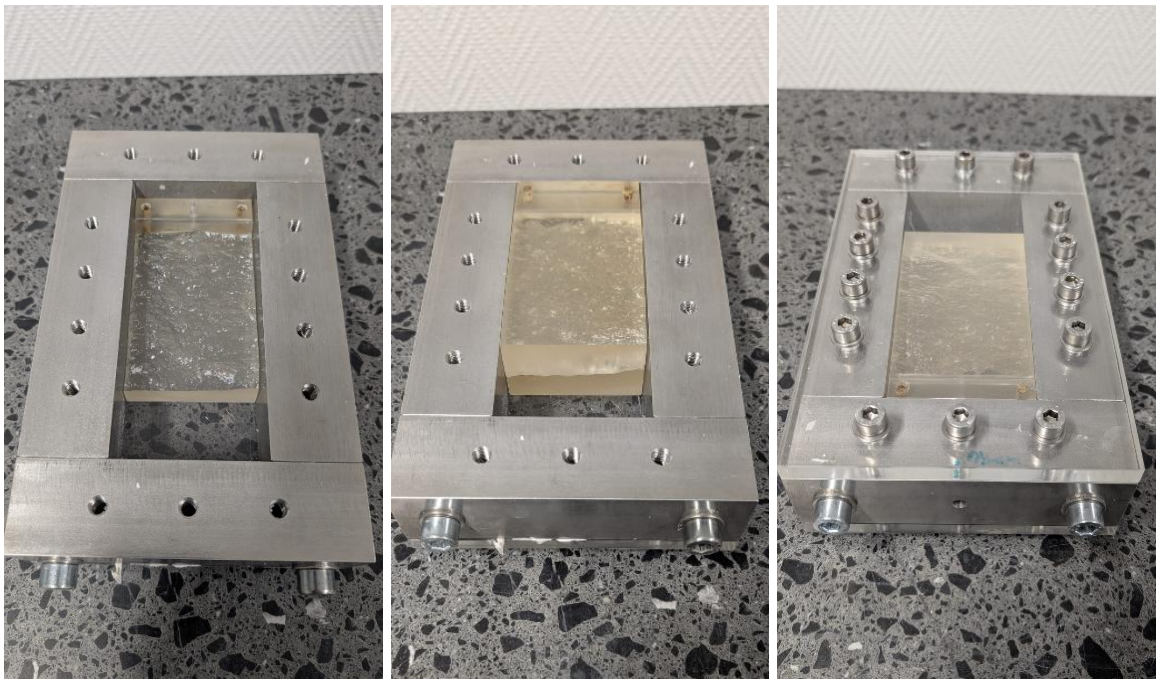


Fig. 7.27 Photos of the reinforced test cell for the Topic 5 experiments; frame and lower half of the replica (left), frame and complete replica (middle), and fully assembled reinforced test cell (right)

7.2.2 Test procedure

Before a test was started, the fracture replica was tarnished and subsequently 3D scanned to record the geometry prior to the experiment. After removal of residual tarnishing spray from the surface, the fracture replica was sealed at the inflow side using Neukasil RTV 1703 silicone. While the silicone was still curing, the centering pins were inserted. Excess silicone material was then carefully removed, and the long sides of the fracture replica were sealed using adhesive tape.

The prepared fracture replica was subsequently placed into the test frame. To prevent bentonite from entering the fracture during sample compaction, a fine steel mesh was positioned between the fracture replica and the bentonite body. It was later discovered

accidentally that this precaution would not have been necessary. The bentonite sample was compacted directly inside the test cell to a density of 1400 g/cm³ using a specially designed attachment to prevent displacement of the fracture replica during compaction.

After assembly, the test cell was placed above a light source on the optical table, and flow processes within the fracture were recorded using a camera positioned above the set-up. After the inlet of the fracture replica had been connected to a syringe pump, image acquisition was initiated at one-minute intervals. Subsequently, injection of Äspö solution was started. Inflow rates between 0.02 ml/h and 0.2 ml/h were used for the tests. Afterwards, the fracture surfaces were scanned again according to the workflow (see section 2.2). Only minor deformations were detected.

7.2.3 Fluid materials

To enhance the contrast between water and air in these experiments, the addition of a colour tracer to the water was initially considered, following the approach used in the re-saturating fracture experiments. Several tracers, including potassium permanganate, methylene blue, and E150, were tested. Although all three tracers provided a clearly detectable water–air interface, each introduced specific problems. In particular, potassium permanganate and methylene blue caused permanent staining of the fracture replica, resulting in false tracer detection in areas exposed to the tracer for extended periods. In addition, potassium permanganate solution tended to decolour rather quickly due to a reaction with the sealing silicone. In a pre-test, this effect was already detected after about two hours, as demonstrated in Fig. 7.28. While E150 did not cause staining or decolouring, it was found to influence the water uptake behaviour of the bentonite.

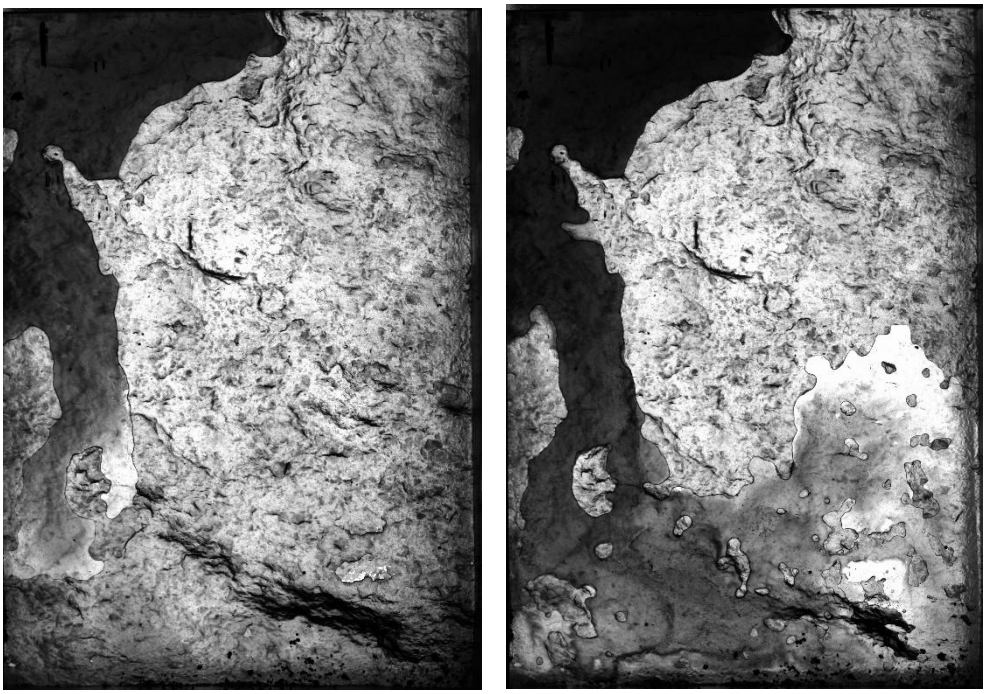


Fig. 7.28 Wetting test with potassium permanganate solution at an inflow rate of 0.5 ml/h applied to the top; images after 2.15 h (left) and after 4.1 h (right)

To minimize interactions between the tracer and the bentonite, pure Äspö solution without any colour tracer was therefore used. In the resulting images, water-filled areas appear brighter and smoother, whereas air-filled regions exhibit more pronounced fracture surface details and a slightly darker appearance.

7.2.4 Results and interpretation

The acquired images were compiled into a time-lapse movie to facilitate identification of key events in the swelling and fluid-flow process. These events are illustrated by image series in Fig. 7.29 to Fig. 7.31 for inflow rates of 0.02 ml/h, 0.1 ml/h, and 0.2 ml/h, respectively.

An early test had previously been conducted at an injection rate of 0.1 ml/h and represented the first test in which flow disruption was observed. This test was performed without proper alignment of the fracture assembly, because the centering pins had been removed. Consequently, the fracture aperture distribution was not reproducible and could not be reliably determined afterwards. In addition, the aperture distribution may have been altered during disassembly due to stress release. The lack of alignment probably resulted

in locally reduced fracture apertures caused by compression of the fracture surfaces. Nevertheless, the test provided interesting results, which are shown in Fig. 7.32.

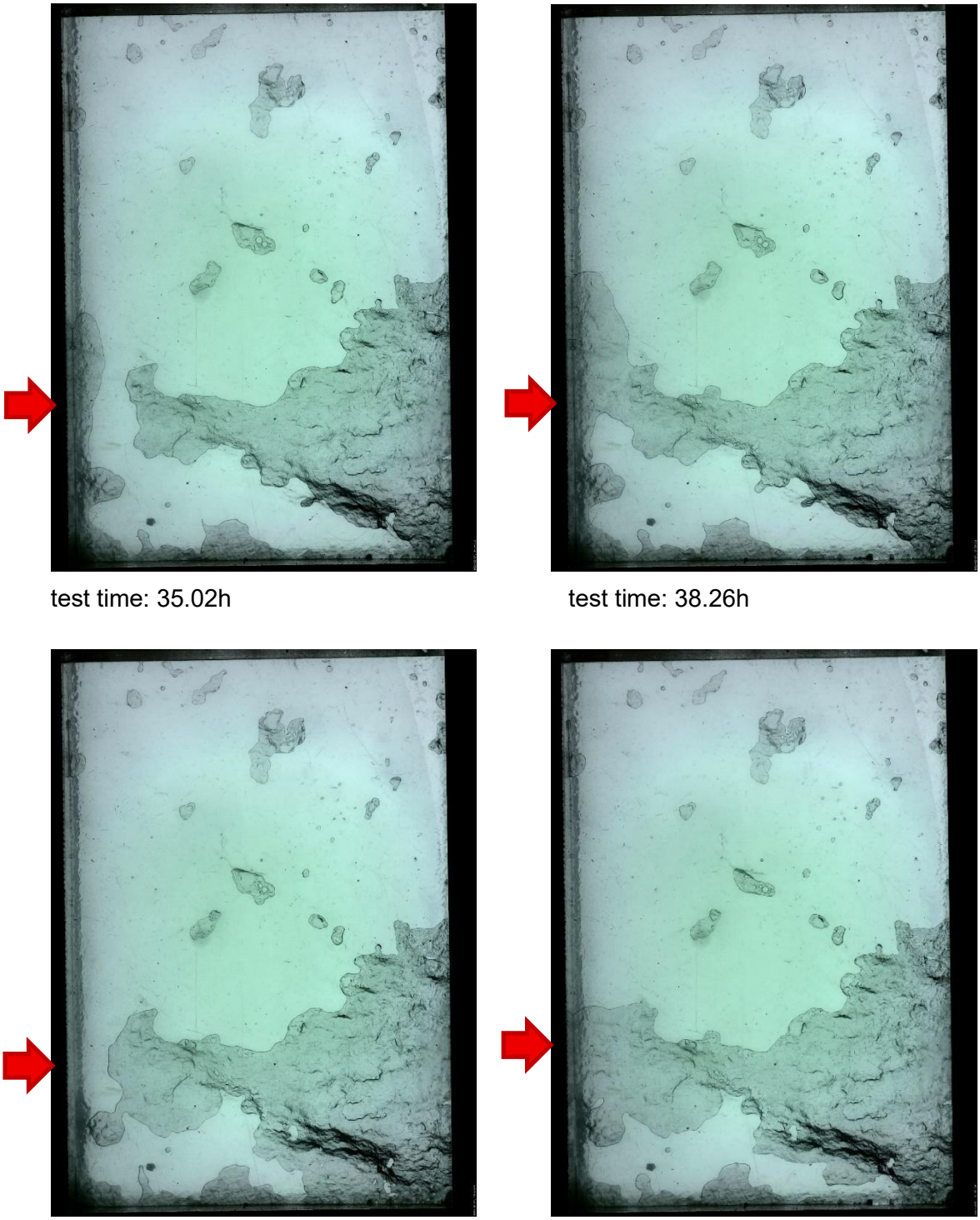
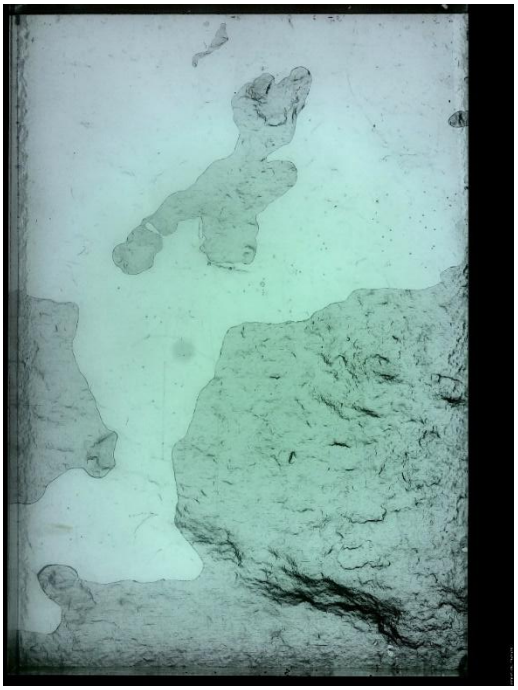
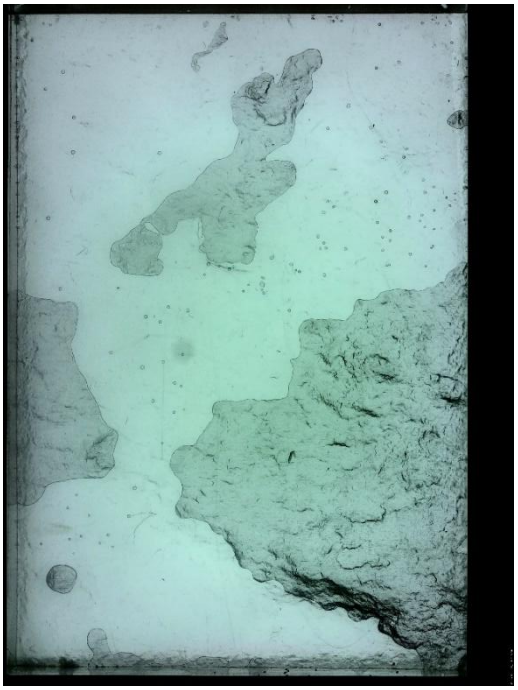


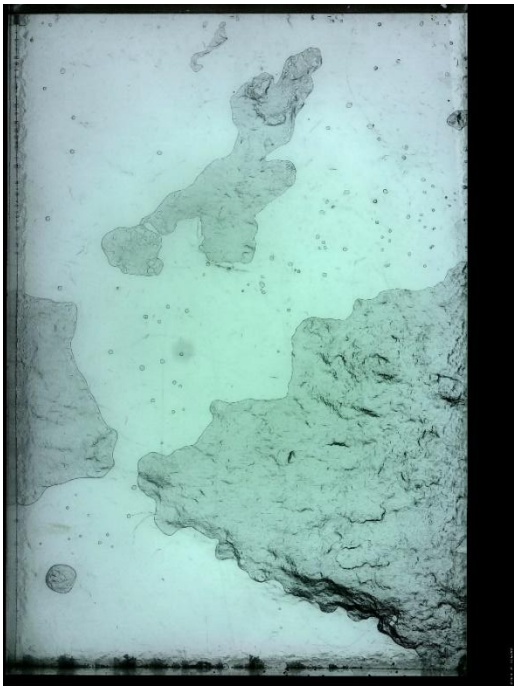
Fig. 7.29 Breaking off of water fingers after contact with bentonite; water in bright grey, air in structured dark grey; inflow from the top, bentonite at the bottom; pointwise water injection of 0.02 ml/h



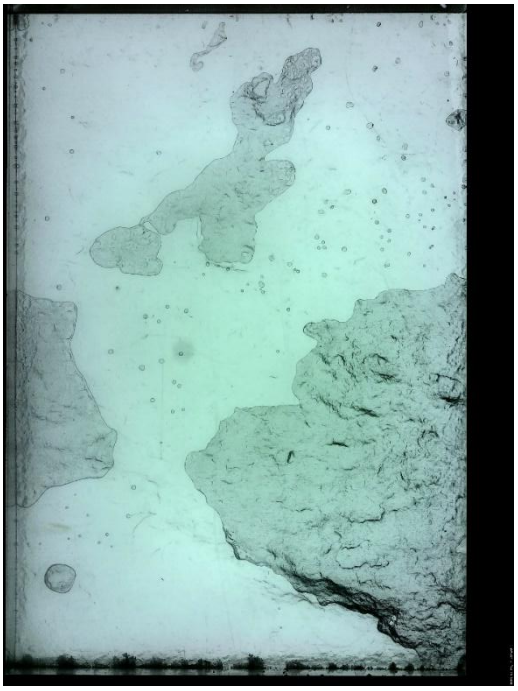
test time: 2.4h



test time: 7.24

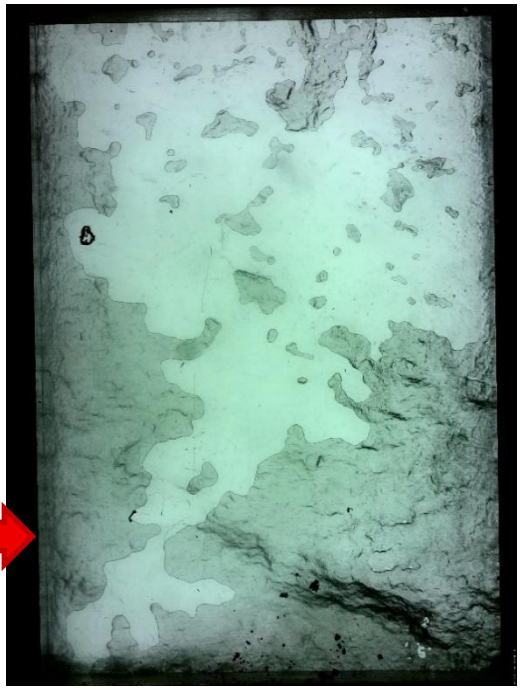


test time: 14.75

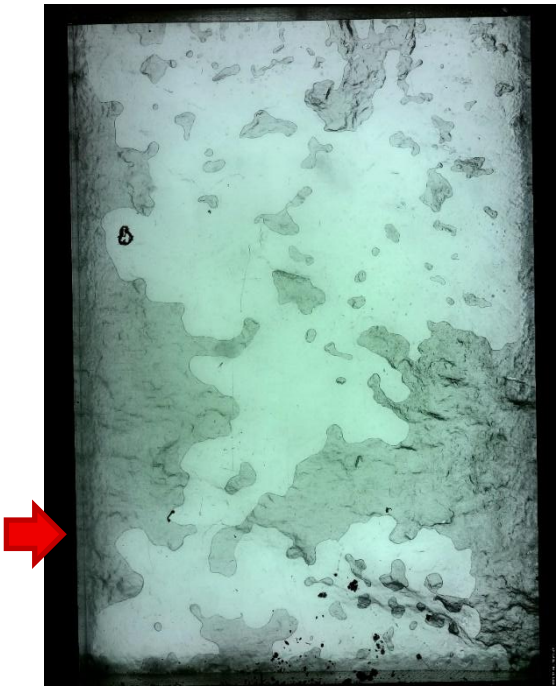


test time: 28.1h

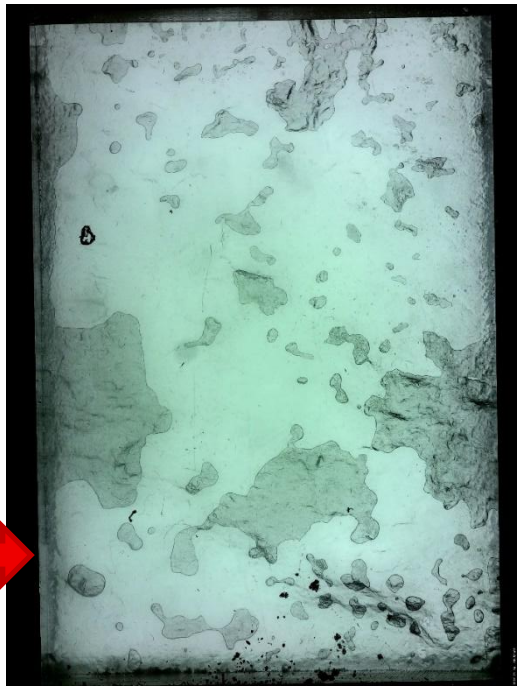
Fig. 7.30 Almost breaking off of water fingers after contact with bentonite; water in bright grey, air in structured dark grey; inflow from the top, bentonite at the bottom; pointwise water injection of 0.1 ml/h



test time: 6.12h



test time: 7.26h



test time: 11.31h

Fig. 7.31 Almost breaking off of water fingers after contact with bentonite; water in bright grey, air in structured dark grey; inflow from the top, bentonite at the bottom; pointwise water injection of 0.2 ml/h



test time : 10.62h



test time: 10.87h



test time: 11.27h

Fig. 7.32 Breaking off of water fingers after contact with bentonite; water in bright grey, air in structured dark grey; inflow from the top, bentonite at the bottom; pointwise water injection of 0,1 ml/h, narrower but undeterminable aperture field

Throughout the experiment, repeated disruption of the advancing fluid finger was observed, indicating intermittent flow instabilities. These interruptions lasted from a few minutes to up to 10 hours, depending on the inflow rate. Lower inflow rates caused a higher number of disruption events, indicating that flow dynamics and capillary effects play a significant role in controlling the shape of the fluid front. At inflow rates of 0.1 ml/h and higher, no further breaking off was observed. This rate is assumed to correlate approximately with the mean fracture aperture of about 340 µm.

Breaking off of water fingers due to suction exerted by the air-dry bentonite was found not to be limited to the immediate vicinity of the bentonite-water contact. In the early test with a narrower fracture, it was observed at the opposite side of the replica (see Fig. 7.32). The configuration of the aperture field therefore also affects the location where disruptions of the water fingers occur.

If inflow into the bentonite is temporarily interrupted after flow disruption, water at the bentonite-water contact has time to migrate further into the bentonite. This implies partial drying at the contact, which in turn increases suction and may amplify subsequent repeated flow disruption by breaking off water fingers. Although this may represent a secondary effect, disruption delays bentonite re-saturation.

During re-saturation of the fracture, air bubbles were frequently enclosed within the fluid phase, highlighting the complex interaction between fluid movement, fracture geometry, and trapped air.

8 Topic 6 – Impact of long-term heating on bentonite properties

8.1 The Prototype Repository experiment

The Prototype Repository (PR) experiment, conducted by SKB, represents the longest-running full-scale in situ test of its kind. The test was installed in two sections. The inner section, containing four deposition holes, had been operated for more than 20 years at the Äspö Hard Rock Laboratory in Sweden and was reopened in 2022 /SKB 22/. The layout of HRL Äspö, the PR, and the opening of the inner section are illustrated in Fig. 8.1.

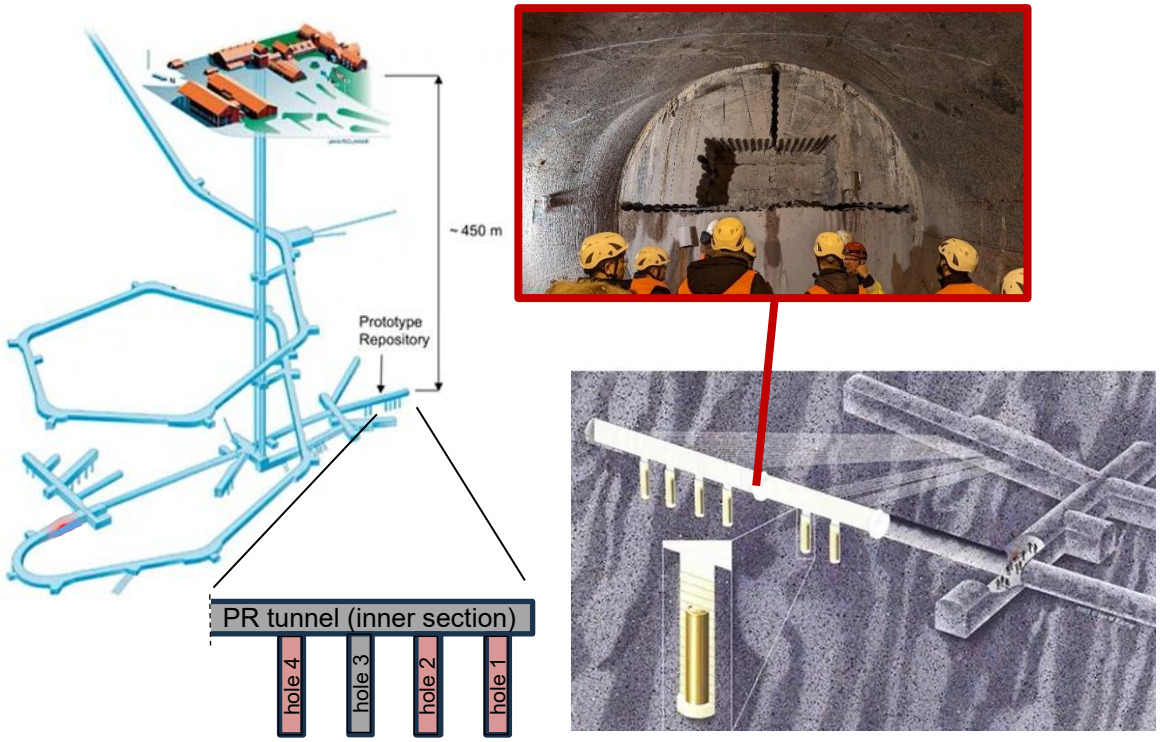


Fig. 8.1 Location (left), set-up of the PR (bottom right) and opening of the inner section (top right) of the PR; from /SKB 22/

All six deposition holes had the same dimensions, and the installation of the buffer and heater was identical in each case. The buffer was assembled from circular bentonite plates and rings labelled according to Fig. 8.2.

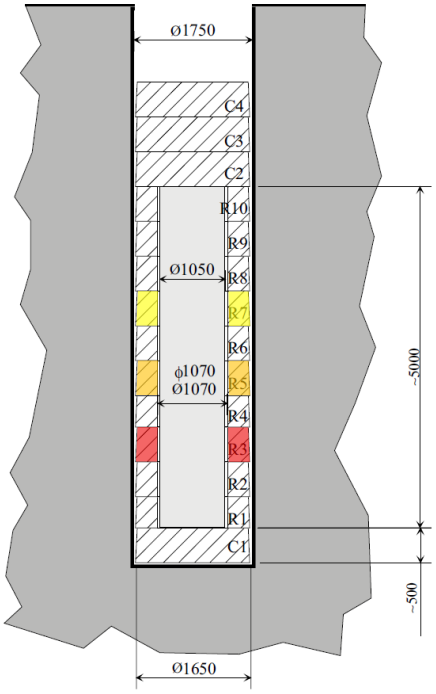


Fig. 8.2 Schematic drawing of a deposition hole with buffer and canister including standardized labelling of buffer rings and plates; rings 3, 5, and 7 marked for reference;after /VID 17/

Owing to the extensive instrumentation and the detailed post-mortem programme, parameters such as water content and dry density were measured on hundreds of samples. Because these samples were distributed throughout the bentonite buffers, the evolution of buffer hydration could be reconstructed. Due to locally varying inflow into the deposition holes caused by fractures and to specific events such as heater failure in one of the holes, the bentonite buffers were exposed to different, well-documented conditions over the course of the experiment.

8.2 Objective

To involve international partners in the analysis of samples and data, SKB initiated the Dismantling of the Prototype Repository (DPR) project in 2023. Through German participation in this international project, bentonite samples could be collected from the site for further investigations. The opportunity was therefore used to assess a potential impact of long-term heating on the water uptake behaviour by determining and comparing isotherms with the Vapour Sorption Analyzer (VSA).

8.3 Materials

Suitable bentonite samples at different distances from the heater were collected directly on site from deposition holes 1 and 2 during the ongoing excavation work in 05/24 and 11/24. Vacuum-sealed material from deposition hole 4 was collected on these occasions as well. The material was taken along transects from the heater surface to the surrounding rock, as indicated in Fig. 8.3 (bottom middle), extracted (see Fig. 8.4), and vacuum-sealed on site.

Reference material from the production of each installed bentonite ring or plate had been stored separately by SKB, as shown in Fig. 8.5. A generous quantity of the reference material corresponding to the sampled bentonite from the site was also kindly provided by SKB.

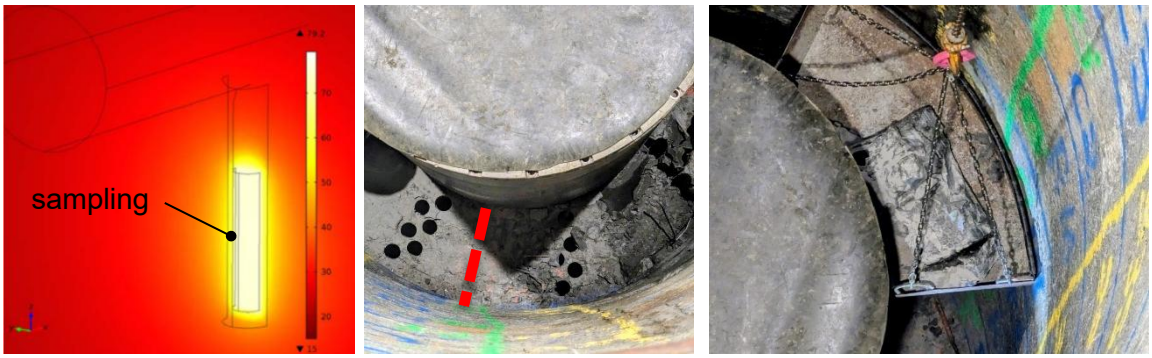


Fig. 8.3 Taking samples from deposition hole 3; sketch of deposition hole 1 during operation (top left), relation of sampling to the experiment (bottom left), position of samples in the buffer ring (bottom middle), lifting sample material in the ring (bottom right)



Fig. 8.4 Bentonite samples taken from deposition hole 1



Fig. 8.5 Storage of reference bentonite material for each buffer ring

8.4 Temperature and humidity history

The description of the evolution of the PR mainly follows SKB's final sensor data report /GOU 23/ and the evaluation of the extensive sample collection from dismantling /SAN 25/. Additional references are cited where appropriate.

8.4.1 Background

The condition of the buffer in the deposition boreholes was monitored by numerous pressure, temperature, and relative humidity sensors. By the time the PR was shut down at the end of 2022, all temperature and relative humidity sensors in the buffer had failed. The total number of sensors still operating in the inner section over the running time of the PR is plotted in Fig. 8.6.

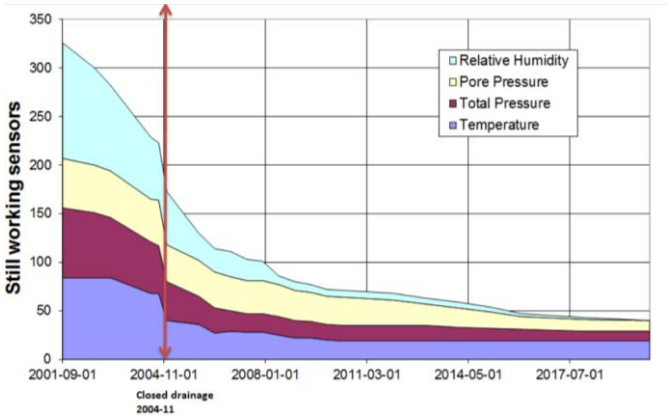


Fig. 8.6 Number of still working sensors in the inner section; from /GOU 23/

As many of the temperature and relative humidity sensors failed comparatively early, the corresponding conditions cannot be reconstructed directly over time. Therefore, the history of heater power consumption in the canisters is also important for indirectly, albeit only approximately, deriving these conditions. Since heating in the three deposition holes considered here was far from uniform, the evolution of power consumption is briefly discussed for each of the three heaters.

Heating of all canisters began with a power of 1800 W in September 2001. To mimic the decrease in heat production by radioactive decay, the power had been planned to be reduced by 20 to 40 W every one to three years. For DH1, this plan was followed until 2013-03-06 (day 4188), when the power had to be reduced due to electrical heater failure. Further failures occurred over the following years and eventually resulted in the power being switched off on 2019-12-17 (day 6665).

The heaters in DH2 experienced an unexpected temperature increase after 450 days due to difficulties in measuring the power. The actual power at that time was probably higher than 1800 W /GOU 09/. Otherwise, the heaters followed a similar failure pattern to those in DH1, although at a much earlier stage. They were determined to be permanently damaged, which led to final shut-off in December 2004. The temperature on the canister surface decreased accordingly and stabilized at about 30 °C.

Heating of DH4 also did not proceed according to plan. Irrecoverable heater failures forced a severe power reduction in 2016, around day 5500. However, heating could be continued at a level of 300 W and, between 2018 and 2021, even at 570 W. The power for DH4 was

eventually switched off on 2023-01-02 (day 7778), the first day of actual dismantling. Curves showing the power consumption over time are depicted in Fig. 8.7, top left for DH1, top right for DH2, and bottom for DH4.

Comparison of the plots in Fig. 8.7 shows that high temperatures were maintained longest in DH4. However, the total heat energy supplied to DH1 may have been close to that supplied to DH4. By comparison, considerably less energy was supplied to DH2, where the canister surface temperature remained only slightly above room temperature for most of the time. The strongest effect of heat on the properties of the bentonite buffer should therefore be observable in the acquired samples from DH4, followed by those from DH1 and then by the samples from DH2.

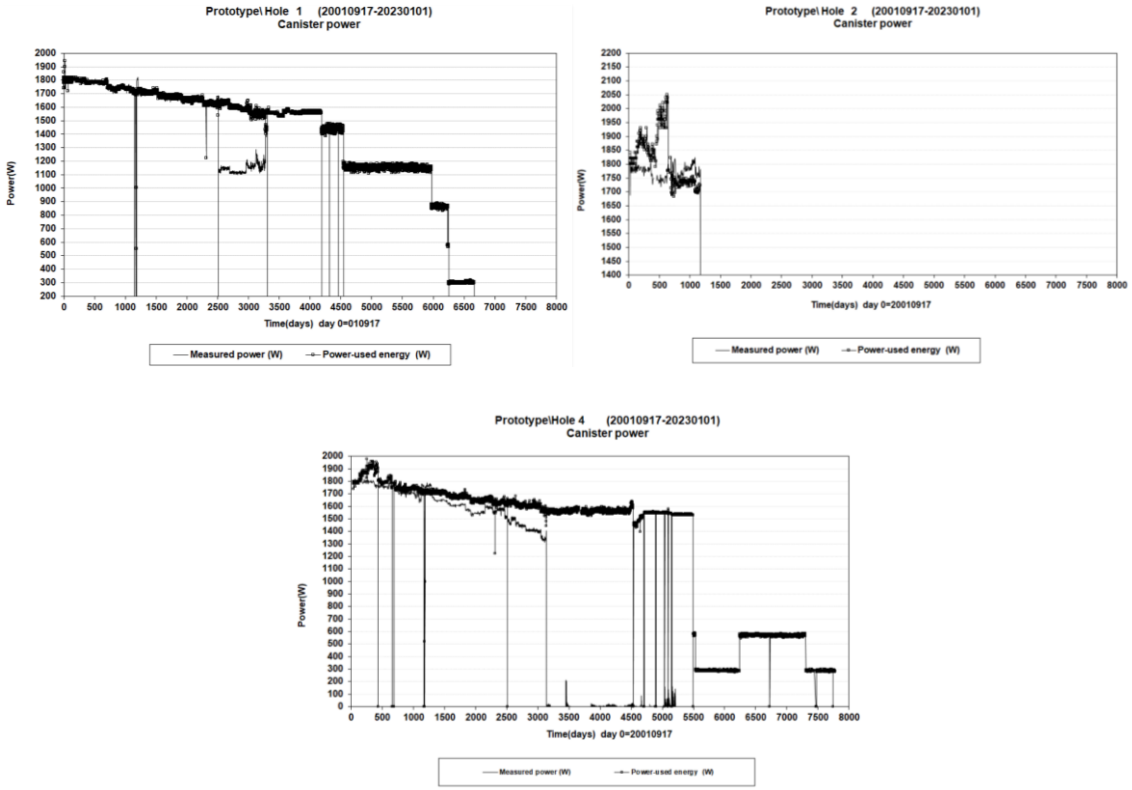


Fig. 8.7 Power consumption by heaters in DH1 (Top left), DH2 (top right) and DH4 (bottom); from /GOU 23/

8.4.2 Temperature

The most pronounced influence of long-term heating on the properties of bentonite is expected where the highest temperatures prevailed in the buffer. Since this is undoubtedly

the case in the immediate vicinity of the canister, the canister surface temperature is considered first.

Direct measurement was enabled by optical fibre cables positioned vertically along the canisters. The maximum temperatures measured along the cables are plotted over time in Fig. 8.8, top left for DH1, top right for DH2, and bottom for DH4.

A nearly constant maximum temperature of 75 °C was reached in DH1 in all three cables after approximately 650 days. The four cables in DH2 indicated temperatures between about 90 and 100 °C before the increased power input raised these values to about 100 to 110 °C, before power management returned to normal. Immediately before heating was switched off in DH2, a maximum temperature of 96 °C was measured. The maximum canister surface temperature in DH4 was 88 °C.

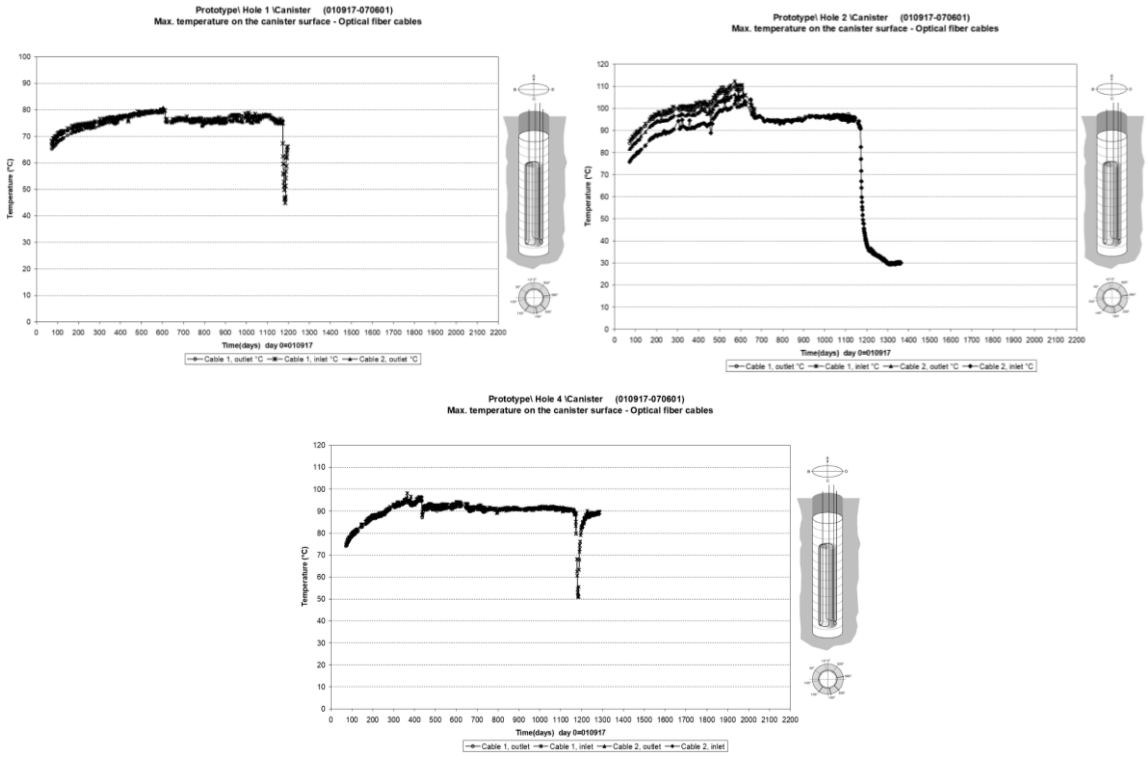


Fig. 8.8 Maximum temperature on the canister surface in DH1 (Top left), DH2 (top right) and DH4 (bottom); from /GOU 23/

Assuming ad hoc that the maximum canister surface temperature was maintained as long as the heating schedule was followed as planned, DH4 was exposed longest, for about 5500 days, to high temperatures close to 90 °C. DH2 experienced the highest

temperatures, ranging from 96 to 110 °C, but only over a period of about 1200 days. The maximum temperatures in DH1 were considerably lower at 75 °C and were maintained for about 4500 days.

Data from ring 5 of deposition hole 1 have been particularly well documented in SKB's literature and also provide insight into the temperature evolution within the ring. Four types of temperature measuring devices were distributed in ring 5 in four radial directions. From the sensor data representing the temperatures in these four radial directions in ring 5, as depicted in Fig. 8.9, rotational symmetry of the temperature distribution could be derived. The resulting overall temperature profile accounting for all sensor types is shown in Fig. 8.10.

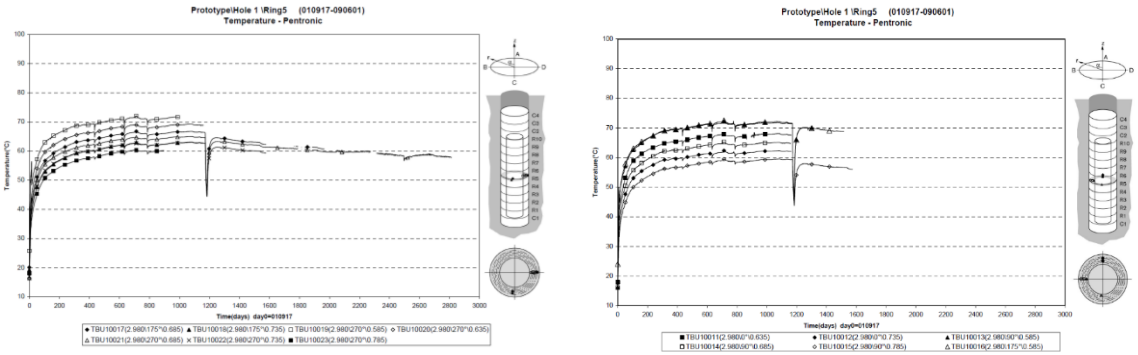


Fig. 8.9 Temperature sensor data for DH1 R5; from /GOU 09/

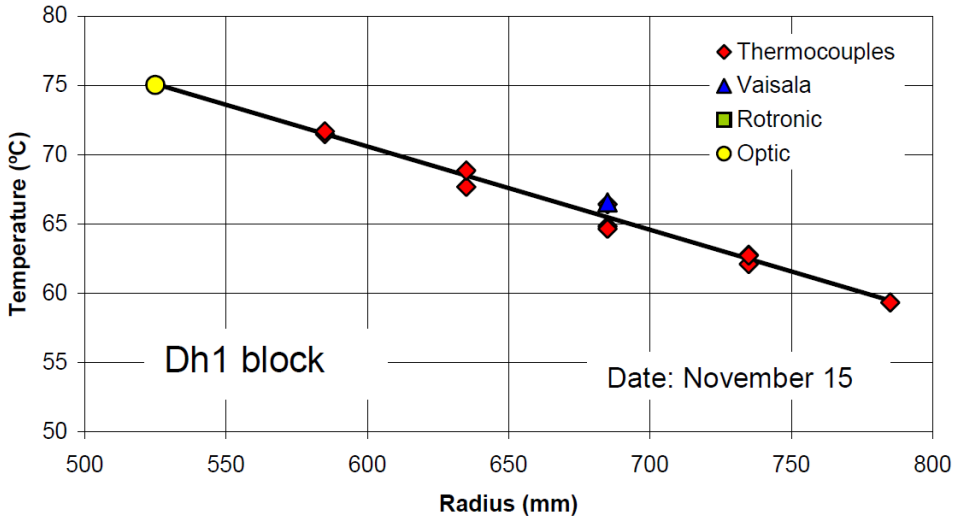


Fig. 8.10 Radial temperature distribution for DH1 R5 at day 1200; from /GOU 06/

The evolution of the highest and lowest temperatures in ring 5, together with the resulting temperature gradient, is depicted in Fig. 8.11. The highest measured temperature gradient was 0.57 °C /cm. The lowest temperature in a ring can apparently be estimated from the canister surface temperature by assuming a given temperature gradient.

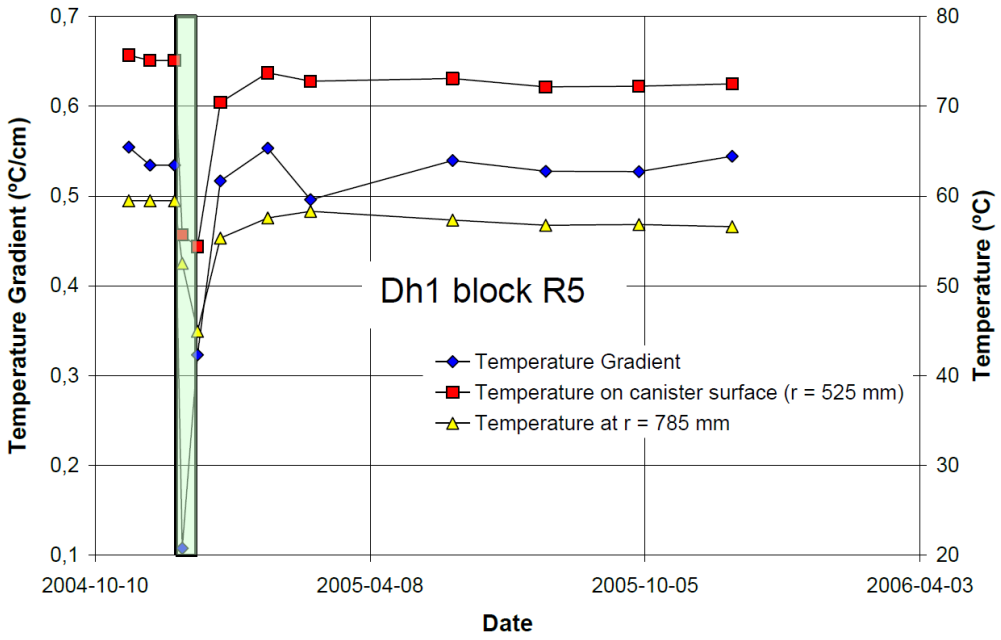


Fig. 8.11 Evolution of maximum and minimum temperature as well as the temperature gradient for DH1 R5; from /GOU 09/

8.4.3 Relative humidity / water content

In addition to temperature, the wetting state of the bentonite over time is of interest. However, determining this state is challenging. The large number of relative humidity sensors that could have provided relevant information remained operational for only slightly more than four years. Detailed data are available for this period, whereas no corresponding data exist for the subsequent period. Additional data are available only from the post-mortem analyses, which provide information on the conditions at the end of the test.

By way of example, two data plots for relative humidity and temperature from sensors located in DH1 R5 are shown in Fig. 8.12. They indicate that 90 % relative humidity was exceeded within less than one year, beyond which the Vaisala sensors become

increasingly unreliable. A state of high water saturation can therefore be assumed for DH1 R5 when this threshold was exceeded. A similar evolution is also expected for DH4 R7.

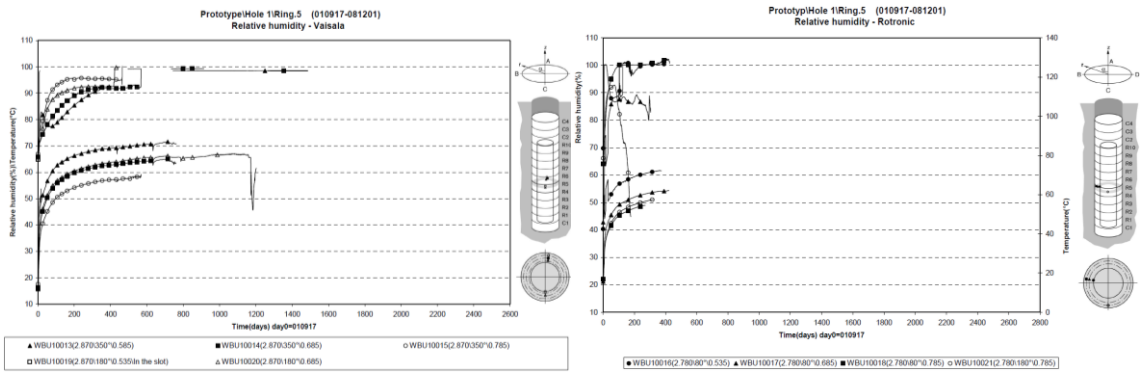


Fig. 8.12 Evolution of the relative humidity in DH1 R5; from /GOU 09/

In the post-mortem analyses for DH1 R5, a high degree of saturation was found, with values between 95 % and 100 % and the lowest values close to the canister (see Fig. 8.13). Essentially the same results were obtained for DH4 R7 (see Fig. 8.14), suggesting that the high degree of saturation and thus high relative humidity prevailed in these two blocks over the entire lifetime of the PR. However, it should be noted that DH1 was apparently wetted to a high degree in a comparatively homogeneous manner, whereas DH4 shows significantly lower water uptake in the lower part of the buffer.

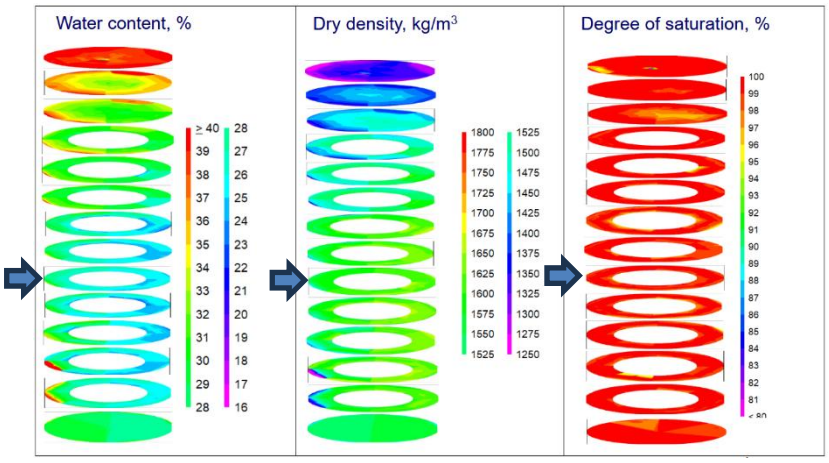


Fig. 8.13 Post mortem data on water content, dry density and degree of saturation for the whole buffer in DH1; arrows indicate the position of ring 5; from /San 25/

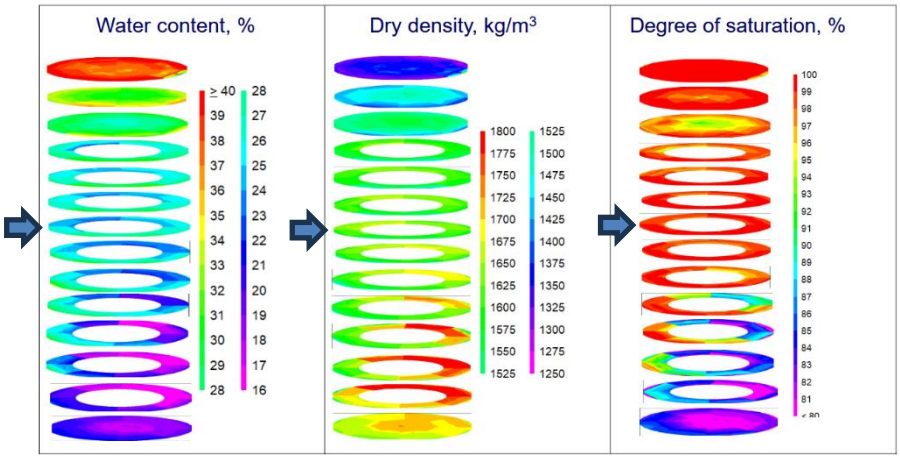


Fig. 8.14 Post mortem data on water content, dry density and degree of saturation for the whole buffer in DH4; arrows indicate the position of ring 7; from /San 25/

The conditions were apparently substantially different for DH2 R3. “The degree of saturation (for this ring) varied mainly between 75 % and 87 %, with the lowest values close to the canister. The sampling showed that this block had only taken up small amounts of water from the rock or from the bentonite above. The water content and the density were in the same range as when the block was installed.” /SAN 25/ (see Fig. 8.15). As in DH4, the buffer in DH2 also shows comparatively low wetting in the lower part of the deposition hole, whereas a very high degree of water uptake can be observed in the upper part. However, the sample material used in the present work for tests on DH2 material originates from the only slightly wetted part of the buffer.

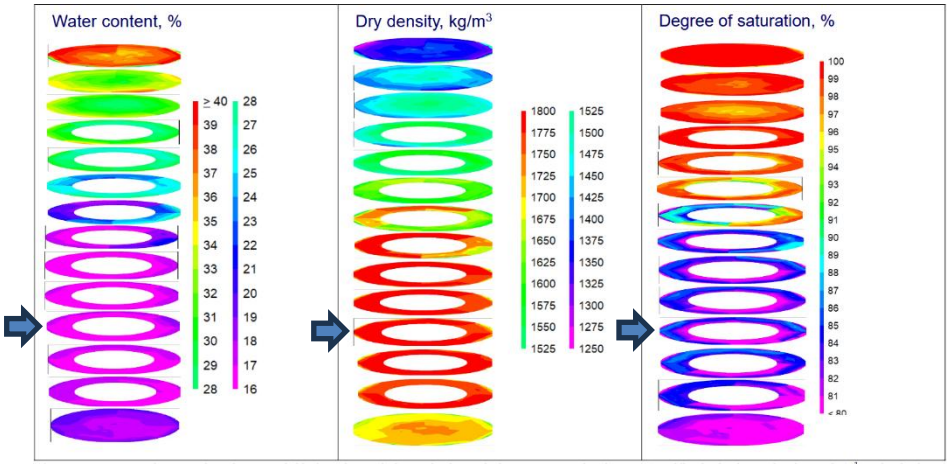


Fig. 8.15 Post mortem data on water content, dry density and degree of saturation for the whole buffer in DH2; arrows indicate the position of ring 3; from /San 25/

8.4.4 Essentials

The evolution of temperature and relative humidity in the three DHs examined here differed markedly. This was mainly caused by technical difficulties encountered during heating of the canisters. The total heating time was longest in DH4. Assuming that the canister surface temperature was related to the power input into the heaters, the maximum temperature was also maintained longest in DH4. However, the maximum temperature was reached in DH2 when the power management for this hole did not proceed according to plan. Consequently, the longest exposure to high temperatures occurred in DH4 R7. By contrast, the highest temperatures were applied to DH2 R3, although only for a period of time on the order of a few months.

The evolution of relative humidity, which indicates both water content and degree of saturation, was recorded in detail during the first three years of the PR. After this period, the next direct measurements were performed only within the framework of the extensive post-mortem investigations. These investigations showed that DH1 R5 and DH4 R7 were highly saturated at the end of the experiment. By contrast, DH2 R3 was located in a comparatively dry section of DH2.

The findings from the preceding subsections are summarized in Tab. 8.1.

Tab. 8.1 Summary of findings for DH1, DH2, and DH4.

	DH1 R5	**DH2 R3**	**DH4 R7**
Total heating time	6665 days	1200 days	7778 days
Maximum temperature on the canister surface	75 °C	96 °C temporarily up to 110 °C	88 °C
Duration of maximum temperature	4188	1200 days	5500 days
Evolution of relative humidity	reaching close to 100 % within a year	similar dynamics as in DH1 suspected	similar dynamics as in DH1 suspected
End state of degree of re-saturation	95 % to 100 %	75 % to 87 %*)	96 % to 100 %
End state of overall water content distribution in DHs	Homogeneous distribution at maximum water content	Top third: maximum uptake; rest: basically no uptake	Top three quarters: maximum uptake; rest: little uptake

*) basically no water uptake compared to installation

8.5 Experimental method

Complete hysteresis loops consisting of adsorption and desorption isotherms were measured using the Vapour Sorption Analyzer (see subsection 5.1.2). Samples were taken directly from the vacuum-sealed packages, milled to a powder, and placed in the VSA. The loops were determined for buffer material originating close to the heater and for the corresponding reference material from ring 5 in deposition hole 1 (DH1 R5), ring 3 in deposition hole 2 (DH2 R3), and ring 7 in deposition hole 4 (DH4 R7).

8.6 Measurement results

The hysteresis loops for the in-situ buffer material close to the heater in DH1 R5 and for the corresponding reference material were determined and superimposed. Although no significant differences between these two loops were expected, slight, increasing differences were observed along the adsorption isotherm. Since these differences could have resulted from measurement artefacts associated with the Vapour Sorption Analyzer, the reliability of the results was checked by repeating the measurement of the reference material twice. Accidentally, an incorrect test scheme had been selected for the third run, so that only a few data points on the desorption isotherm were meaningful. As depicted in Fig. 8.16, the first and second runs were essentially identical, and the four data points from the third run also fitted the desorption isotherm very well.

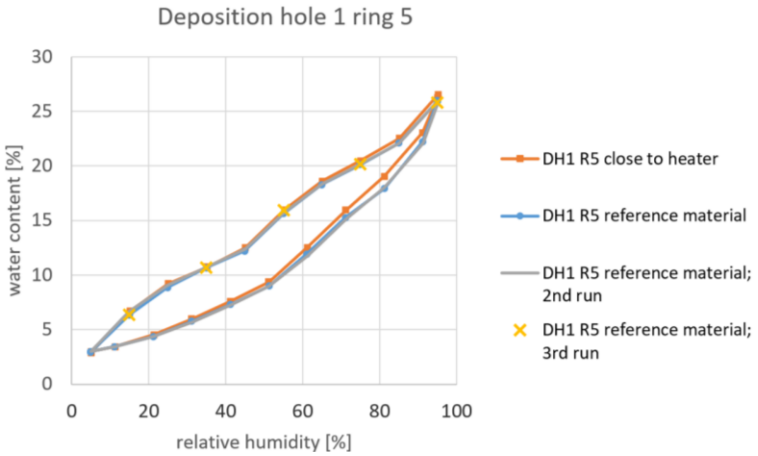


Fig. 8.16 Hysteresis loops for DH1 R5, in-situ and reference material

The results for DH2 R3 are graphically evaluated in Fig. 8.17. Here, the adsorption isotherm agrees comparatively well with the corresponding isotherm of the reference material. However, the desorption isotherm deviates comparatively strongly in the upper and lower thirds of the curve. As a result, the curve has lost the characteristic shape of MX-80 bentonite. Unfortunately, this test was disturbed at an unknown time for an unknown duration, so it cannot be excluded that the measured data were compromised. Since this test was also the last in the series, there was no opportunity to ensure proper functioning of the VSA and to repeat the test. The resulting curve is therefore not discussed further.

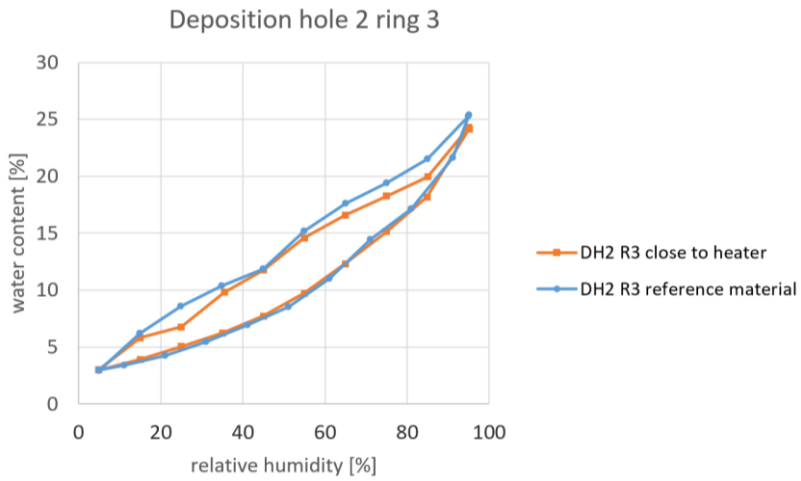


Fig. 8.17 Hysteresis loops for DH2 R3, in-situ and reference material

Fig. 8.18 shows the results for DH4 R7, where nearly the entire hysteresis loop is affected by a small upward shift. Finally, the hysteresis loops for all three reference materials were superimposed in Fig. 8.19, first to check the variability of the bentonite used for the PR and, second, to ensure an appropriate reference for the buffer material from DH2 R3. The plot again shows the repeatability of the results for the reference material from DH1 R5. Moreover, the hysteresis loops for the other materials also agree well with each other.

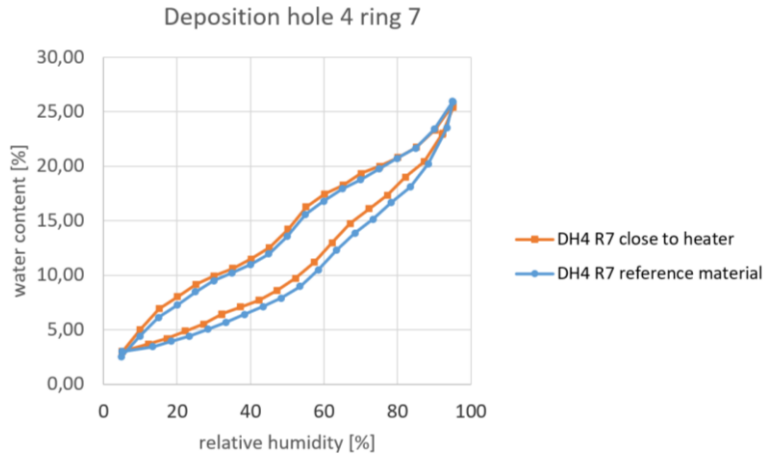


Fig. 8.18 Hysteresis loops for DH4 R7, in-situ and reference material

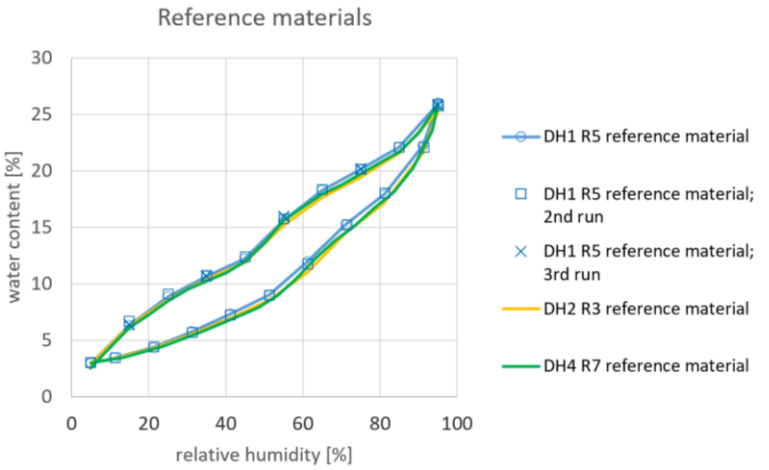


Fig. 8.19 Hysteresis loops for all three reference materials

8.7 Interpretation of the results

The high repeatability of the measurement results for the reference material from DH1 R5 lends a certain credibility to the admittedly small differences from the data for the in-situ material. The hysteresis loops for all three reference materials also appear to coincide well. The unusual results for DH2 R3 may therefore be related to the irregular heating history of DH2. However, an effect of the disturbance during the VSA test on the results for the in-situ buffer material appears more probable.

An upward shift of the isotherms essentially indicates a higher capacity of the bentonite to buffer water. For DH1 R5, this effect was observed for the in-situ buffer material during

water uptake, whereas the capacity to retain water during desaturation appeared unchanged. For DH4 R7, the bentonite not only took up more water than the reference material during wetting, but also retained more water during dehydration. However, the significance of this effect is probably low in the present case.

The deviation of the isotherms for the in-situ material appears to be greater for DH4 R7 than for DH1 R5. This is consistent with the fact that DH4 R7 was exposed to higher temperatures for longer periods. However, the data do not indicate whether this was caused by the absolute value of the maximum temperature or by the amount of heat energy supplied to the bentonite. Meaningful results for DH2 R3, which had experienced a higher maximum temperature for a short period of time, would therefore have been particularly informative.

It should be noted that the hysteresis loops were measured at room temperature, i.e. 25 °C. This clearly differs from the temperature conditions during PR operation, and it is known that increased temperatures result in a slight downward shift of an isotherm /KRÖ 20/. Repetition of the tests at an increased temperature may therefore be informative, as the VSA allows testing at temperatures of up to 60 °C.

9 Topic 7 – Extending the functionality of code VIPER

The thermo-hydraulically coupled code COMSOL-VIPER /KRÖ 23/, which is based on the balance equations of the experimental VIPER code /KRÖ 11/, has been further developed for simulating water uptake by bentonite. Traditionally, most hydraulic laboratory experiments that provided the basis for established modelling approaches addressed water uptake under conditions of unimpeded access of the bentonite to water (UA). Unimpeded access denotes a condition under which the bentonite can take up as much water as it is able to absorb.

However, experimental investigations at GRS /NOS 18/ have demonstrated that the hydration behaviour of bentonite is significantly affected by conditions of a limited water supply rate (LWSR). Such conditions are particularly relevant for low-permeability host rocks considered for DGRs, where the external water flux limits the potential uptake by the bentonite under UA-conditions. A comparison of outflow rates in typical repository-relevant rock formations with uptake under UA-conditions is provided in /KRÖ 18/.

To represent this effect in numerical simulations, a conceptual model for uptake under LWSR-conditions has already been described in /KRÖ 17/. A prescribed low water flux into the bentonite implies that the water content at the bentonite-rock interface increases according to the difference between inflow from the rock and subsequent water migration into the bentonite. This process can continue only until full saturation is reached at the interface. At this point, LWSR-conditions change to UA-conditions because the potential flow from the rock exceeds the water demand of the bentonite.

Within the framework of the VIPER-model, such a boundary therefore needs to be monitored to detect the change in water supply conditions, because this change is associated with a transition from Neumann to Dirichlet boundary conditions. This approach enables a more realistic representation of water inflow than conventional UA assumptions. For this purpose, Neumann boundary conditions have been implemented in the experimental code VIPER to account for LWSR conditions /KRÖ 18/, dynamically linking the external supply rate to the internal vapor diffusion flux at the bentonite interface.

To extend the VIPER-code in terms of dimensionality and functionality, the principles of the VIPER-model were transferred to a dedicated implementation in COMSOL

Multiphysics, which is referred to here as the COMSOL-VIPER model (/KRÖ 20a/, /KRÖ 25/). For this purpose, a specific VIPER-interface was developed in COMSOL. However, advanced features, particularly the capability to treat LWSR-conditions, were still pending. This functionality was implemented in the present project.

The corresponding implementation in COMSOL-VIPER required challenges related to the specific structure of the hydraulic balance equation to be addressed. When the original VIPER partial differential equation (PDE) was transformed into its weak form, a surface integral representing the Neumann boundary naturally emerged. This integral was incorporated directly as an additional weak-form equation using the COMSOL Physics Builder, thereby enabling, in combination with monitoring of the water content, dynamic coupling of the external water flux to the bentonite hydration process.

In parallel, the robustness of the VIPER interface was improved through targeted modifications. Some model variables in the original implementation had not been defined with sufficient clarity, which occasionally caused solver instabilities. By refining variable definitions, constraining admissible value ranges, and adjusting formulations, both model stability and applicability were substantially improved.

The updated interface was validated in a one-dimensional simulation against experimental data from a GRS water uptake experiment under LWSR conditions /NOS 18/. A comparison of experimental and modelling results is shown in Fig. 9.1. This experiment currently also serves as the basis for Task 14a within SKB's Task Force on Engineered Barrier Systems (EBS).

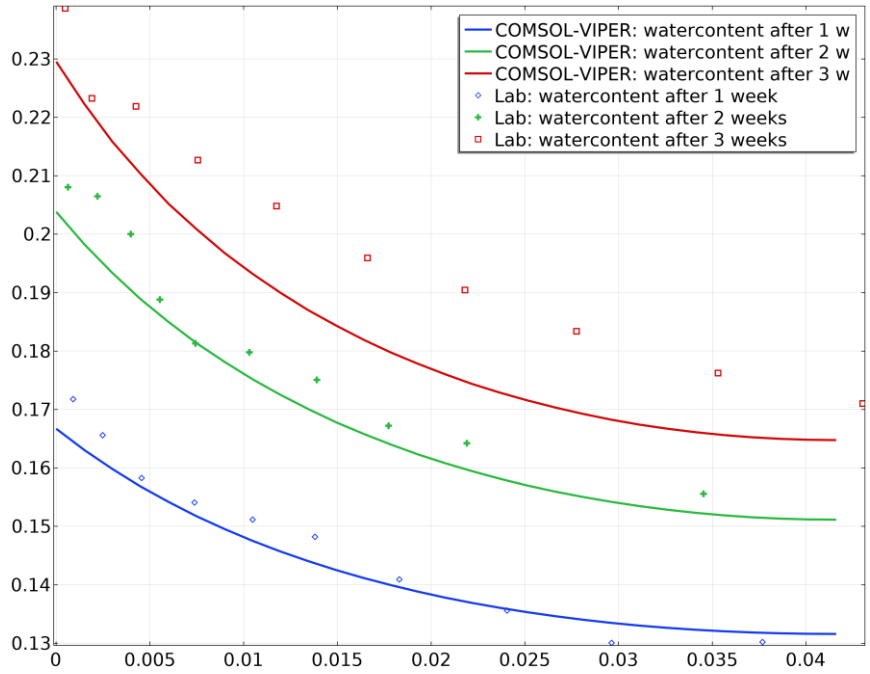


Fig. 9.1 Results from a water uptake test at restricted water inflow in comparison with the results of the advanced VIPER-interface in COMSOL; from /KRÖ 25/

The developments presented here not only enhance the stability and applicability of the VIPER interface but also enable more realistic simulations of bentonite saturation under LWSR conditions. The updated 1D COMSOL-VIPER implementation can now be applied to repository-relevant scenarios in which limited water inflow is expected under natural conditions, for example in the recently completed “Prototype Repository” in-situ experiment at the Hard Rock Laboratory Äspö in Sweden.

10 Assessment of the new measurement techniques

10.1 Technique (A): Non-destructive measurement of the water content

Three methods for detecting the water content of a bentonite sample were applied: (a) classic gravimetric measurement by heating and weighing, (b) visual observation with an optical camera based on greyscale values, and (c) absorption of SWIR-light detected with a spectrometer. The latter two alternatives to the classic method were considered attractive because method (a) requires cutting the sample into pieces, whereas methods (b) and (c) are non-destructive. In addition, substantially higher spatial resolution can theoretically be achieved with these methods than with method (a). However, it was found that methods (b) and (c) would have required more development effort than could be provided within the present project.

10.1.1 Classic gravimetric measurement

The classic method (a) is a robust technique because it depends only on weighing. It therefore provides a reliable reference for evaluating methods (b) and (c). However, gravimetric measurements yield only an integral value for a finite piece of bentonite. If a water content distribution in a sample is to be determined, the sample must be cut into several pieces, and each piece must be heated and weighed separately. The quality of the resulting distribution therefore also depends on the accuracy with which the integral value of each piece can be assigned to its representative position in the undisturbed sample. Consequently, preparation and geometrical control of the cut-off pieces also require the highest possible accuracy.

Because the impact of measurement errors decreases with increasing piece size, a trade-off exists between geometrical accuracy and the achievable resolution of the distribution. Practical experience indicates that discs cut from a compacted bentonite sample should have a thickness of at least a few millimetres.

10.1.2 Visual observation with an optical camera

By contrast, the visual method (b) provides much higher spatial resolution. However, a specific value for the resolution cannot be provided because it depends on both the sample size and the number of pixels available in the camera.

The achievable accuracy can only be estimated with difficulty because both the actual greyscale bandwidth and the covered range of water contents are not known beforehand. It can only be stated that scatter in the data caused by mineralogical differences at the sample surface reduces the accuracy. For granular bentonite, this scatter results in water-content variations in the one-digit percentage range, whereas it decreases to a few percent for powdery bentonite. Practical aspects therefore control the actual accuracy of the visual method.

Because a high-resolution camera was used for image acquisition, several thousand pixels provided data along the axial line of a sample, resulting in a spatial resolution in the range of 100 microns. Thus, essentially each grain at the sample surface was resolved in an image. Since accessory minerals cannot be expected to show the same optical properties as clay grains, a certain scatter in the optical data is unavoidable (see above). To minimize these scattering effects, powdery rather than granular materials are recommended.

In addition, the greyscale distribution across the sample must be scaled to the water content using at least two reference points. One point is used to correlate a specific greyscale value with a water content, whereas the second point is required to determine the range of water content across the sample. For practical purposes, it is therefore suggested that the water content be determined gravimetrically at both ends of a sample using method (a). However, if very high water contents are involved, as in the MX-80 samples investigated in Topic 1, the span may become too large to allow meaningful interpretation of most of the curve, which is characterized by comparatively low water contents and small variations.

The comparison of results obtained with methods (a) and (b) shows that trends in the water content distributions were roughly captured by the optical method. The achievable accuracy depends on the bentonite type considered. For MX-80 samples, the optical

method provides rather unreliable water content values because the reference curves from the gravimetric measurements are met only inconsistently. The results appear to be more reliable in the range of lower water contents. For Calcigel, only data for water contents below 15 to 25 %, depending on bentonite density, were reliable. The small fully saturated zone was generally not detected reliably. Where it was indicated by the data, either its extent was too large, its absolute value was too low, or both effects occurred.

Some of the strong deviations between the greyscale data and the gravimetric results appear to be attributable to non-linearity in the relation between greyscale and water content. These non-linearities seem to be less pronounced for samples with higher densities. In principle, non-linearities can be corrected by calibration. However, the observations from Topic 1 imply that such calibration would need to account for both water content and bentonite density. This made the required effort impracticable within the framework of the present project. The calibration problem is aggravated by the unexplained observation that, in the majority of cases (9 out of 14), the greyscale data at the wet end of the samples indicate a decrease in water content where an increase, or at least a constant value, should occur.

At the present state of development, the optical method can generally provide a qualitative impression of a water content distribution, but absolute values may deviate substantially. However, the dynamics of a transient water migration process can be detected convincingly.

10.1.3 Absorption of SWIR-light

Despite a promising preliminary investigation of water detection in bentonite by SWIR-photography, several approaches using different techniques had to be tested because some methods either failed or were not affordable within the framework of the present project:

- Direct SWIR-photography using an IR camera with a SWIR bandpass filter ultimately proved unsuitable.
- Multispectral illumination failed because a direct correlation between greyscale values and water content was not possible due to insufficient data for performing principal component analysis (PCA).

- Use of a multispectral camera would have been feasible but would also have exceeded the project budget. PCA is also required for processing the data.
- Working with a spectrometer yields results but provides only pointwise data and also requires PCA. The spatial resolution of the data points depended on the test set-up, more precisely on the minimum step size at which the motorized stage could be moved. This step size amounted to 0.3 mm.

The first component of a principal component analysis (PC1) appears to be reasonably well related to the water content at low bentonite densities, which applies to both MX-80 and Calcigel. However, this relation breaks down at medium and higher densities, so that only zones of low and high water content can be clearly distinguished.

As observed for the optical method, the relation between PC1 and water content appears to break down above a certain threshold. The critical water content that could not be exceeded was approximately 45 to 60 % for MX-80 and approximately 35 % for Calcigel. When these values were reached, PC1 decreased again. In this respect, the results of both non-destructive methods are similar. Apparently, additional factors also influenced PC1 in these ranges of water content; however, no satisfactory explanation was identified. This issue may become the subject of further investigations concerning the microstructural distribution of water molecules in the clay particles. In any case, knowledge of this effect nevertheless helped to identify the highly saturated narrow zone targeted in Topic 1, albeit in an unexpected manner.

Because the non-dimensional PC1 values require scaling to the water content in a similar way to the greyscale values from the optical method, two reference points are needed for this procedure. One point can again be obtained from the dry side of the sample, whereas the second point must be selected carefully to ensure that it is not located in a zone of very high water content.

10.2 Technique (B): Visual observation of hydraulic processes in fractures

As outlined in section 2.2, the production of realistic fracture replicas by 3D-scanning and 3D-printing and the subsequent laboratory testing constitute a complex and versatile task. The three main components, namely scanning, printing, and repeatability of tests, are discussed below.

10.2.1 Digital fracture models by high resolution 3D-scanning

Two major problems are encountered when hydraulic processes in fractures are to be observed. First, the surrounding rock is opaque, so that direct visual observation is not possible. If this limitation is circumvented by opening a fracture to characterize the fracture surfaces or to produce replicas, a second problem arises because the two opposing fracture surfaces must subsequently be realigned correctly. Because the surface topographies are complex down to the microscopic scale, the fracture halves can hardly be realigned without precise aids. The alignment problem can be solved with unparalleled accuracy by the scanning procedure described in subsections 2.2.1 and 2.2.2, whereas direct visual observation can be enabled by producing transparent replicas. It should be noted, however, that establishing a digital fracture model requires elaborate post-processing of the scanned elevation grid.

10.2.2 Producing fracture replicas by additive manufacturing

Once the correct alignment of the fracture surfaces has been established in a digital fracture model, mechanical aids added to this model by CAD methods help to preserve the alignment in a 3D-printed fracture replica. The accuracy of the transparent replicas is then determined by the accuracy of the scanner and the printer. In the technical equipment used here, the printer constitutes the limiting component, producing objects with an accuracy on the order of several tens of microns.

The printing procedure also includes several post-processing steps. Each step was found to introduce deformations into the printed object. Because the objective is to reproduce fractures with small apertures, these deformations may become critical. Although they cannot be completely avoided, they can be mitigated to some extent by optimizing washing times and curing parameters. Despite these adverse effects, reasonably accurate replicas can nevertheless be produced by 3D-printing, as demonstrated by checks based on scanning of printed objects.

10.2.3 Repeatability of hydraulic tests

Because all measurement techniques and production processes yield results with high but limited accuracy, it was clear from the beginning that a printed fracture replica cannot

constitute an exact copy of a real feature. However, for investigating basic hydraulic phenomena, it appears to provide a sufficient approximation. In this respect, the repeatability of flow and transport tests proved to be high even for the complex topography of a fracture. In addition, the results of a percolation test for a micro-DFN performed in Japan could be reproduced after a digital copy of the geometric model had been transferred to GRS.

However, the resin used as printing material exhibits some unfavourable properties. It takes up water over time and thereby deforms the replica. Mechanical stresses caused by grinding and polishing may also adversely affect a printed object. Additional 3D-scanning of the fracture replica is therefore recommended to ensure the best possible knowledge of the replica geometry during a hydraulic test. In particular, it is recommended that (a) the printed fracture be checked against the underlying digital model before hydraulic testing and (b) the replica be checked after a hydraulic test against its topography before testing.

11 Modelling of special groundwater flow and transport problems

11.1 Model Development and Validation of the Free Surface and Storage Term Using Analytical and Numerical Benchmarks

11.1.1 Introduction

Within the framework of the GRUSS project /SCH 20/, the d^{3}f++ simulator was enhanced by incorporating a storage term to account for transient incompressible flow processes. At that time, the implementation was tested using only two simplified benchmark problems.

A further verification case is provided by a benchmark problem published by /WAL 14/, which is based on a concept originally introduced by Theis /THE 35/. This benchmark is reproduced with d^{3}f++ in order to further assess and validate the implementation of the storage term. The agreement between the numerical results and the benchmark solution is used to evaluate the accuracy and robustness of the newly implemented functionality.

Grid generator ProMesh

For the generation of computational grids, the software ProMesh /REI 22/ was used. ProMesh provides a graphical user interface (GUI) for the creation and modification of both structured and unstructured grids and supports point, line, triangle, quadrilateral, tetrahedral, pyramidal, and prismatic elements. The software is an open-source development of the University of Frankfurt and is continuously maintained and extended. Its source code is publicly available on GitHub under the LGPLv3 license.

With ProMesh, mesh elements can be created, modified, and refined individually to meet specific modeling requirements. The software supports the import of raster data and allows the integration of scripts for automated mesh generation and adaptation. Different grid entities can be organized into so-called subsets, which can later be assigned distinct material properties, model parameters, and boundary conditions. The resulting computational meshes are exported in the ugx format, which serves as the standard input format for simulations with d^{3}f++.

Groundwater Flow and Transport Code d3f++

Density-driven groundwater flow simulations were carried out using the code d³f++ ("distributed density-driven flow"). d³f++ is a finite-volume simulator developed under the coordination of GRS in collaboration with several universities to address specific groundwater flow problems, with a particular focus on density-driven flow processes in large and complex geological systems (/FEI 99/, /FEI 04/, /SCH 20/, /RÜB 22/).

d³f++ is based on the generalized Darcy law (Eq. (11.1)), which describes fluid flow in porous media as a function of hydraulic conductivity, fluid properties, and the driving potential gradients:

$$q = -\frac{\mathbf{k}}{\mu}(\nabla p - \rho \boldsymbol{g}) \qquad (11.1)$$

Where $\rho = \rho(c,T)$, $\eta = \eta(c,T)$,

with

q Darcy velocity vector [m s^{-1}],
$\boldsymbol{k}$ intrinsic permeability tensor [m^2],
μ dynamic viscosity of the fluid, for water $1 \cdot 10^{-3}$ at 20 °C [kg m^{-1} s^{-1}],
p pressure [Pa],
ρ density of the fluid, for water 998.2 at 20 °C [kg m^{-3}],
$\boldsymbol{g}$ gravitation vector [m s^{-2}],
T temperature [°C],
c relative salt concentration [-].

The governing equations for groundwater flow and solute transport consist of the conservation equation for total fluid mass (Eq. (11.2)) and the conservation equation for salt mass (Eq. (11.3)),

$$\frac{\partial}{\partial_t}(\phi\rho) + \nabla \cdot (\boldsymbol{q}\rho) = F^f \qquad (11.2)$$

$$\frac{\partial}{\partial_t}(\phi\rho c) + \nabla \cdot (q\rho c - \rho\,(D + D_m I)\,\nabla c) = F^c \qquad (11.3)$$

with

ϕ porosity [-],

F^f source and sink term of the fluid [kg m^{-3}],

D dispersion tensor [m^2 s^{-1}],

D_m molecular diffusion coefficient [m^2 s^{-1}],

F^c source and sink term of the salt mass [kg m^{-3}].

In d^{3}f++, salinity is represented by the relative mass fraction of dissolved salt, defined as

$$c = c_{rel} = \frac{c_{abs}}{c_{abs,\ max}}\ ,\ c_{abs} = \frac{m_{Salz}}{m_{Salz} + m_{H_2O}} \qquad (11.4)$$

with

c_{rel} relative salt concentration [-],

c_{abs} density of the fluid [kg m^{-3}],

$c_{abs,max}$ maximal density of the fluid [kg m^{-3}],

m_{Salz} density of salt [kg m^{-3}],

m_{H_2O} density of water [kg m^{-3}].

Further details on the governing equations implemented in d^{3}f++ can be found in /FEI 99/, /SCH 12/ for groundwater flow and in /FEI 04/ for solute transport.

The post-processing, analysis, and visualization of the simulation results were performed with the software ParaView /KIT 24/. ParaView provides comprehensive tools for the visualization and quantitative evaluation of numerical simulation data, including scalar and vector fields, time-series analyses, and cross-sectional representations

11.1.2 Model concept and parameters

In /WAL 14/ a benchmark study was conducted to simulate groundwater extraction from a pumping well using the OpenGeoSys numerical simulator /KOL 18/ and to compare the numerical results with the analytical solution developed by Theis /THE 35/.

The benchmark problem considers a cylindrical aquifer with a radius of 100 m and a height of 10 m (Fig. 11.1). A pumping well is located at the center of the cylinder with a radius of 1 m and a screen of 5 m from the bottom. To exploit geometric symmetry and reduce computational effort, only one-eighth of the cylindrical domain is modeled. The porous medium is assumed to be homogeneous and isotropic, with uniform hydraulic properties in the whole model.

This benchmark provides a suitable test case for investigating transient groundwater flow and evaluating the implementation of the storage term in d^{3}f++. The numerical results can be directly compared with the analytical Theis solution, allowing the accuracy of the simulated drawdown behavior to be assessed.

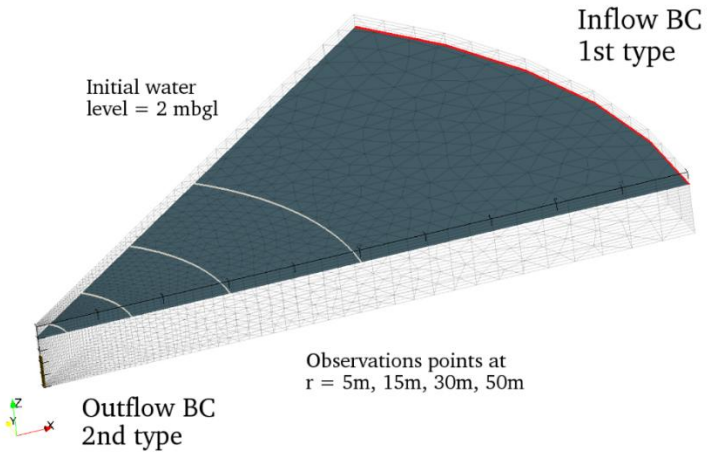


Fig. 11.1 Conceptual model including boundary conditions, computational mesh, and observation points according to /WAL 14/

For the present benchmark study, d^{3}f++ was applied using the boundary conditions and model parameters summarized in Tab. 11.1. Groundwater is extracted from the well, while a constant hydraulic head of 8 m is prescribed at the outer boundary of the model.

In /WAL 14/, the pumping rate is specified as $2.315 \cdot 10^{-4}$ m^3 s^{-1} for the entire well. Since the numerical model represents only one-eighth of the cylindrical domain, the corresponding extraction rate applied in the model amounts to $2.894 \cdot 10^{-5}$ m^3 s^{-1}.

The specific yield reported by /WAL 14/ is 0.2 and represents the fraction of water that can be released from the porous medium under the influence of gravity. In the present study, this parameter is assumed to correspond to the effective porosity by neglecting the compressibility of the rock and is therefore treated as porosity in the model formulation.

Fluid density and dynamic viscosity are assumed to remain constant throughout the simulation. Consequently, density effects are neglected. This simplification allows to investigate the influence of the storage term on transient hydraulic behavior independently of density-related effects.

Tab. 11.1 Benchmark parameters for the Theis solution according to /WAL 14/

Parameter	**Value**	**Unit**
groundwater extraction rate at the well[8]	$2.894 \cdot 10^{-5}$	[m^3 s^{-1}]
porosity ϕ (specific yield in Walther 2014)	0.2	[-]
density of the fluid ρ	$1.0 \cdot 10^{3}$	[kg m^{-3}]
viscosity of the fluid μ	$1.0 \cdot 10^{-3}$	[kg m^{-1} s^{-1}]
gravitation constant g	9.81	[m s^{-2}]
permeability constant k	$1.0194 \cdot 10^{-12}$	[m^2]
aquifer thickness	10	[m]
initial hydraulic head h	8	[m]
residual reduction factor	$1.0 \cdot 10^{-4}$	[-]
residual reduction pressure	5000	[Pa]

[8] 1/8 of the total pumping rate, corresponding to the modeled cylindrical sector representing one-eighth of the full circular domain.

The d³f++ computations are based on a prism grid with local refinement in the vicinity of the pumping well to ensure an adequate balance between numerical accuracy and computational efficiency. Fig. 11.2 shows the coarse grid. Computations are performed on grid level 2 with 22,272 prism elements.

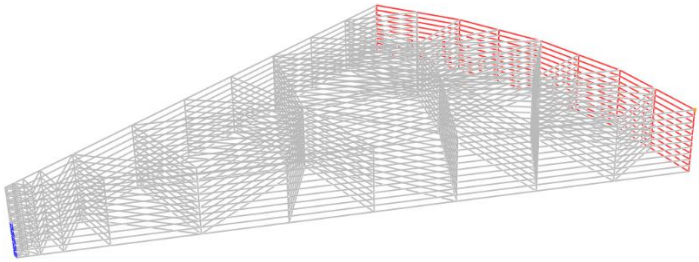


Fig. 11.2 Coarse grid generated with ProMesh (blue: Neumann boundary condition representing the pumping well; red: Dirichlet boundary conditions representing inflow at the outer model boundary)

11.1.3 Evaluation of the results

Modeling approaches for unsaturated groundwater flow can generally be divided into two categories. The first category represents saturation as a continuous field throughout the entire aquifer, while the second describes flow only within the fully saturated part of the aquifer and explicitly accounts for the temporal evolution of the saturated domain.

The first approach is typically based on extensions of the Richard's equation /BEA 88/, /GUE 23/, whereas the second relies on an explicit representation of the phreatic surface, e. g. using level-set methods /FRO 12/. Both approaches are implemented in d³f++ and can be tested through this benchmark /SCH 20/, /SCH 23/. However, in the present study the level-set approach is used.

Results neglecting the compressibility of the rock

In the following, the numerical results obtained with in d³f++ are compared with the results presented in /WAL 14/ and with Theis' analytical solution. The temporal development of groundwater drawdown at radial distances of 5 m, 15 m, 30 m, and 50 m from the pumping well shows good overall agreement among all considered models (Fig. 11.3). The analytical solution remains comparable to the numerical solutions up to

approximately $1 \cdot 10^7$ seconds. At later times, deviations occur due to the assumption of an infinite aquifer for the analytical solution, whereas the numerical models are based on a finite model domain. This behavior is also evident in the d³f++ simulations.

At a distance of 50 m from the well, no significant differences are observed between the numerical models with respect to the temporal evolution of the drawdown. At a distance of 30 m and 15 m, however, differences in the magnitude of the drawdown cone become visible. In the d³f++ simulation, the groundwater level is approximately 0.10 m lower than in the OpenGeoSys results, resulting in a slightly larger drawdown cone. At a distance of 5 m from the well, the difference increases to about 0.15 m. In this case, the d³f++ results are closer to the analytical solution of Theis than the corresponding OpenGeoSys results.

Overall, the comparison demonstrates good agreement between d³f++, OpenGeoSys, and the analytical solution. The observed differences are relatively small and can be attributed to differences in the numerical discretization, the treatment of the free surface, and the assumptions inherent in the numerical models. The results indicate that the free-surface formulation implemented in d³f++ provides a realistic representation of transient drawdown behavior and reproduces the benchmark solution with satisfactory accuracy.

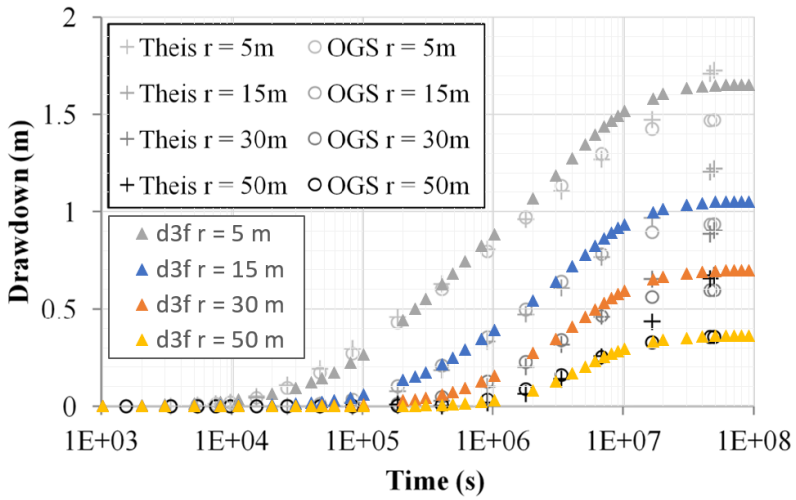


Fig. 11.3 Comparison of groundwater drawdown predicted by the analytical Theis solution, OpenGeoSys (OGS), and level-set approach of d³f++

The drawdown profiles plotted along the model radius show the same general trend observed in the temporal analysis (Fig. 11.4). The d³f++ results consistently predict a slightly larger drawdown cone than the OpenGeoSys simulations and are generally closer to the analytical solution of Theis.

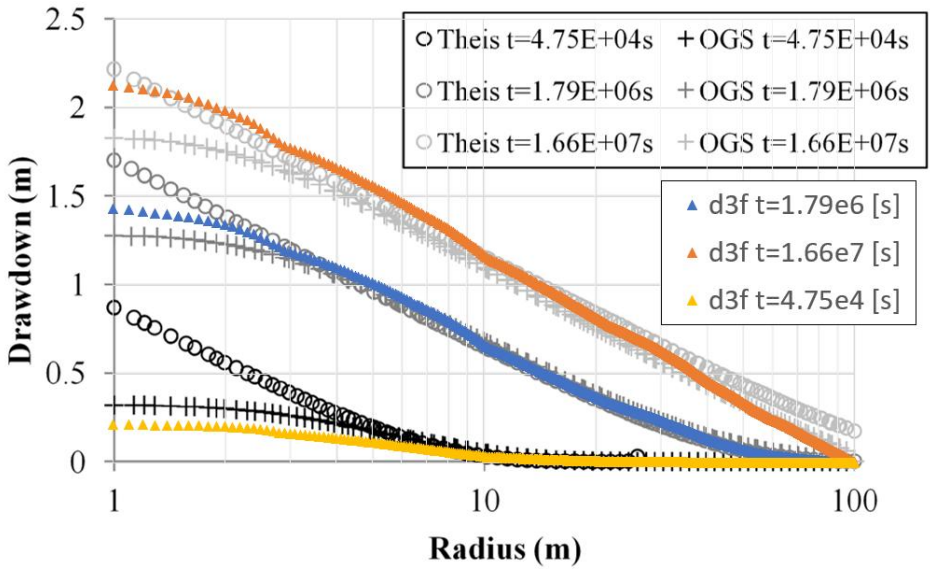


Fig. 11.4 Comparison of drawdown profiles predicted by the analytical Theis solution, OpenGeoSys (OGS), and the level-set approach of d³f++ at selected simulation times

Only at t = $4.75 \cdot 10^4$ s, the drawdown cone close to the well predicted by d³f++ is still slightly smaller than that obtained with OpenGeoSys, while at t = $1.66 \cdot 10^7$ s the d³f++ drawdown exceeds the OpenGeoSys results by approximately 0.15 m in the vicinity of the pumping well. At t = $1.79 \cdot 10^6$ s, the difference increases to about 0.30 m.

Walther /WAL 14/ notes that the OpenGeoSys results may be affected by several factors, including mass balance errors, insufficient mesh resolution, and the limited applicability of Theis' solution to an unconfined aquifer. Consequently, the small differences observed between the d³f++ and OpenGeoSys simulations may arise from numerical and conceptual assumptions inherent in both modeling approaches.

Despite these deviations, the overall agreement between the numerical and analytical solutions is good. Both models reproduce similar drawdown patterns and show a consistent temporal and spatial evolution of the cone of depression. The results therefore confirm

that the level set formulation for free surface implemented in d³f++ is capable of reproducing the benchmark problem with satisfactory accuracy. A limitation of this approach is the neglect of the compressibility of the rocks in the groundwater system.

Results Including rock compressibility effects

The movement of the phreatic surface including rock compressibility effects is described by the following governing equation

$$\mathrm{S}\frac{\partial h}{\partial t} + T_r\,\nabla \cdot (\nabla \mathrm{h}) = Q \qquad (11.5)$$

with

$T_r = \int_{z=a}^{b} K_f dz = K_f b$	transmissivity [m² s^{-1}],
$S = \varphi_0 + b\rho g(1-\varphi_0)\alpha$	storativity of the aquifer [m^{-1}],
$K_f = \rho g \frac{k}{\mu}$	hydraulic conductivity [m s^{-1}],
ϕ_0	reference porosity [-],
b	average thickness of the water body [m],
α	compressibility factor of the rock [Pa^{-1}].

Theis' solution for drawdown as a function of time and the distance r from the well is given in /SIN 17/. The groundwater drawdown d is defined as

where u is a dimensionless variable defined by

$$u = \frac{r^2 S}{4tT}\,. \qquad (11.6)$$

The integral in equation 11.6, often denoted as $W(u)$, can be numerically estimated as described in Tab 11.2 /SIN 17/, /MÜL 24/:

Tab. 11.2 Approximation of function $W(u)$

Range	Representation
$u < 0.05$	$W(u) \approx ln\ 0.562/u$ **(for practical calculations)**
$u <= 1$	$W(u) = -ln\,u - g + 0.99999193u - 0.24991055u2 + 0.05519968\,u3 - 0.00976004\,u4 + 0.00107857u5$
$u >= 1$	$W(u) = \frac{e^{-x}}{x} \cdot \frac{u4+8.5733287401\,u^3+18.059016973\,u2+8.6347608925\,u+0.2677737343}{u4+9.5733223454u3+25.6329561486u2+21.0996530827u+3.9584969228}$

The parameters for Theis' solution and for the simulation using Richard's equation implemented in d³f++ are shown in Tab 11.3.

Tab. 11.3 Benchmark parameters for Theis' solution and for Richard's equation approach in d³f++

Parameter	Value			Unit
Transmissivity T_r	$8 \cdot 10^{-5}$			$m^2\,s^{-1}$
Compressibility factor α	0	$1 \cdot 10^{-6}$	$1 \cdot 10^{-5}$	$[Pa^{-1}]$
Storativity of the aquifer S	0.2	0.262784	0.92784	[-]

The numerical results obtained with the storage term approach implemented in d³f++ were compared with the corresponding analytical solutions derived from the Theis model. The temporal evolution of groundwater drawdown at radial distances of 5 m, 15 m, 30 m, and 50 m from the pumping well was evaluated for compressibility factors of $\alpha = 0$ Pa^{-1}, $1 \cdot 10^{-6}$ Pa^{-1} and $1 \cdot 10^{-5}$ Pa^{-1} in d³f++, which leads to storativities of the aquifer of $S =$ 0.2, 0.262784 and 0.92784 in Theis' solution. Overall, the simulations show a very good agreement with the analytical solution, see (Fig. 11.5 - 11.8).

For all observation points, the simulated drawdown curves reproduce the general temporal behavior predicted by the analytical solution. However, the quality of the agreement depends on the assumed compressibility factor α. The best overall correspondence between the numerical and analytical r esults was obtained

for a compressibility factor of $\alpha = 1 \cdot 10^{-5}$ Pa^{-1}. In this case, both the magnitude and the temporal evolution of the draw-down closely match Theis' solution over the investigated radial distances.

The results indicate that the implementation of storage effects within the level-set approach significantly improves the representation of transient groundwater flow processes. The observed agreement with the analytical solution therefore provides additional verification of the storage-term implementation in d^{3}f++.

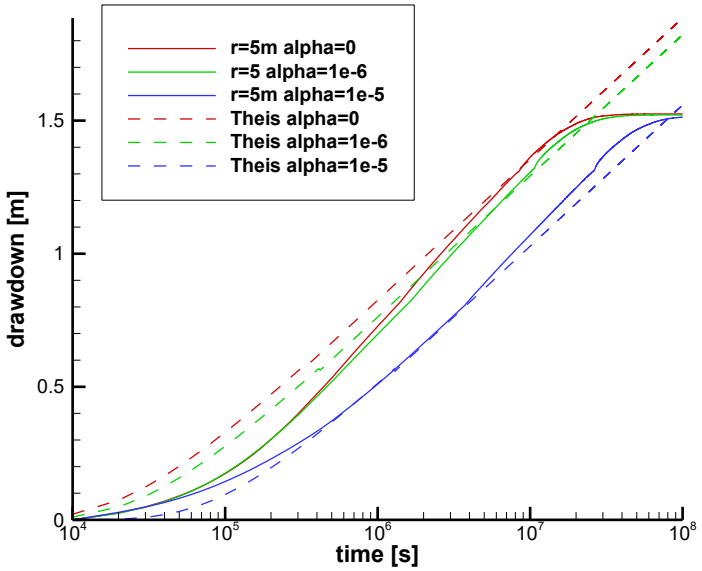


Fig. 11.5 Comparison of groundwater drawdown predicted by Theis' solution and the storage term approach of d^{3}f++ at a distance of 5 m from the pumping well

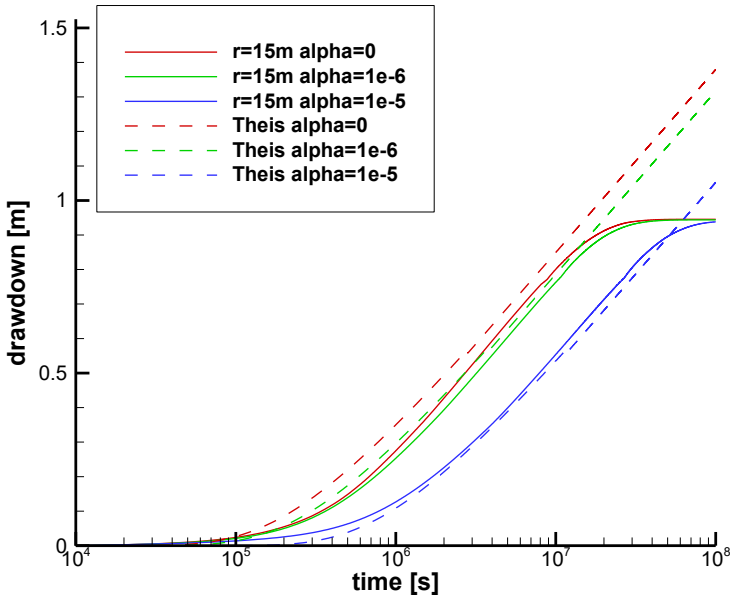


Fig. 11.6 Comparison of groundwater drawdown predicted by Theis' solution and storage approach of d^3f++ at a distance of 15 m from the pumping well

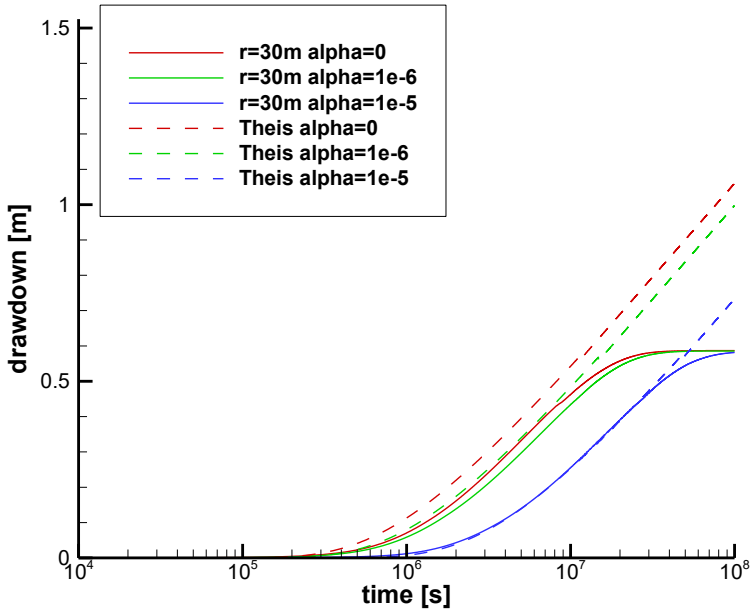


Fig. 11.7 Comparison of groundwater drawdown predicted by Theis' solution and the storage term approach of d^3f++ at a distance of 30 m from the pumping well

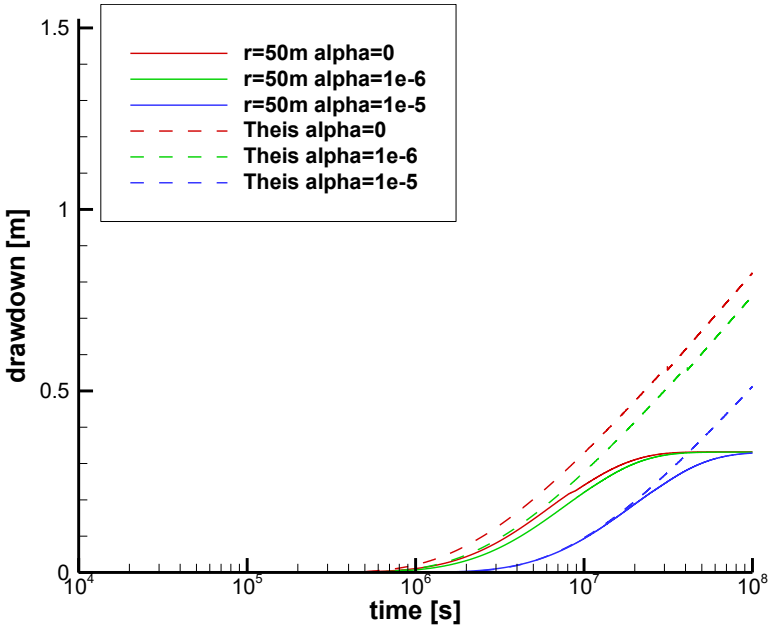


Fig. 11.8 Comparison of groundwater drawdown predicted by Theis' solution and the storage term approach of d^{3}f++ at a distance of 50 m from the pumping well

11.2 Modelling radionuclide transport in fractured rock

11.2.1 Background

This work is based on the work of the TRUE Block Scale Project at the Hard Rock Laboratory Äspö /WIN 02/. The hydrostructural model with a size of 200 m x 200 m x 200 m had been defined in the framework of Task 6c of the Äspö Task Force on Modelling of Groundwater Flow and Transport of Solutes. The original model consisted of 22 deterministic structures with an extension larger than 50 m which were all actually detected in-situ. Smaller fractures were called background fractures and can only be described in terms of geostatistics. Later on, the number of deterministic fractures was reduced to 11, and the background fractures were accounted for by adding 18 synthetic fractures /DER 03/. Although synthetically generated, these fractures were treated as deterministic features, resulting in a total of 29 intersecting discrete fracture structures. The complete hydrostructural model is shown in Fig. 11.9.

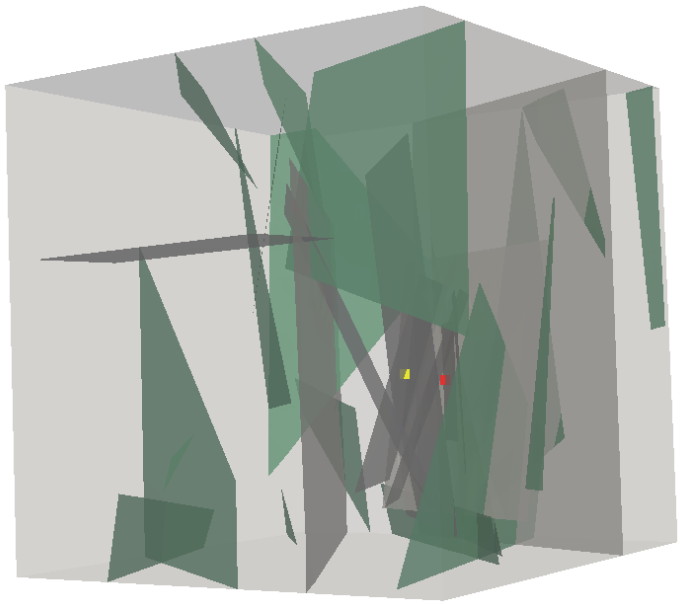


Fig. 11.9 Hydrostructural model with 11 real fractures (grey) and 18 synthetic fractures (green), /DER 03/

In the framework of the TRUE Block Scale project the tracer test “C2” was performed /AND 02/. It included the injection of various tracers in a certain structure and extraction from a different but hydraulically connected structure and formed the basis for Tasks 6D as well as 6E.

In /SCH 16/ the modeling of groundwater flow and the transport of an inert tracer using d³f++ in this complex model is described. The work package described here focuses on modeling radionuclide transport.

11.2.2 The tracer test C2

Fig. 11.9 shows the fractures that are considered as relevant for tracer test C2, see /DER 06/. The conservative tracer Re-186 and the sorbing tracers Ca-47, Ba-127, and Cs-137 were injected into structure 23 to-gether with water. The water injection rate was $1.67 \cdot 10^{-7}$ m^3 s^{-1}, while the pumping rate at the extraction location in structure 21 was $3.25 \cdot 10^{-5}$ m^3 s^{-1}. For details see /SCH 16/. The concentrations of the injected tracers were monitored at the extraction point, see Tab. 11.4 and Fig. 11.10. The straight-line distance between the injection and extraction points was approximately 17 m.

However, the actual transport pathway followed a connected, discrete fracture network (dfn) comprising structures 23, 22, 20, and 21, resulting in an effective flow path length of approximately 97 m /AND 02/.

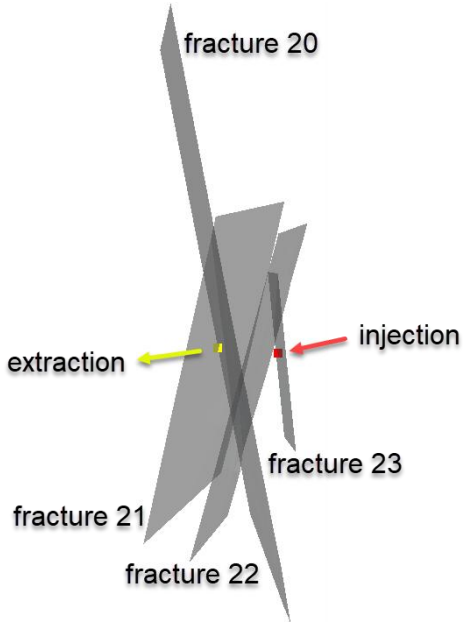


Fig. 11.10 Relevant fractures in C2 test (/DER 06/)

The measured concentration of Cs-137 in the extraction point remained below 0.2 Bq kg^{-1}, and Ba-127 could not be detected. Consequently, only the conservative tracer Re-186 and the sorbing tracer Ca-47 were considered in the present study. The tracer concentrations were reported in terms of activity per unit mass (Fig. 11.10). The total injected activities were $1.71 \cdot 10^{8}$ Bq for Re-186 and $5.64 \cdot 10^{7}$ Bq for Ca-47. As a result of the tracer test, breakthrough curves representing the measured tracer concentrations at the extraction point as a function of time were obtained, see Fig. 11.11.

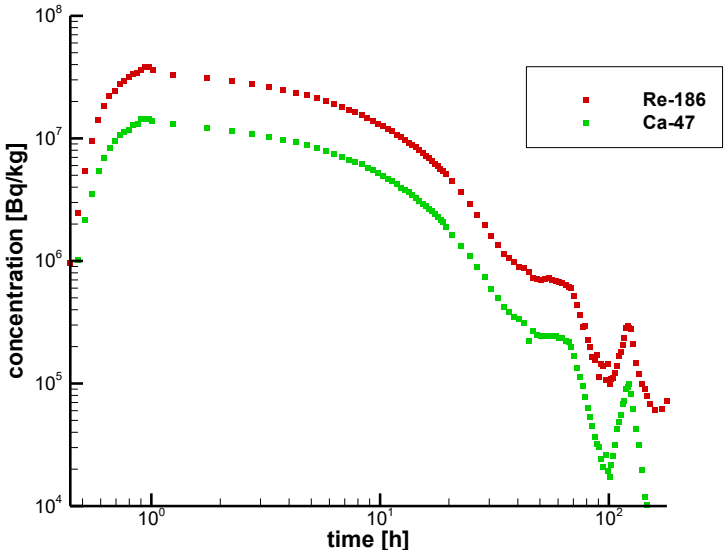


Fig. 11.11 Injection concentration of Re-186 and Ca-47

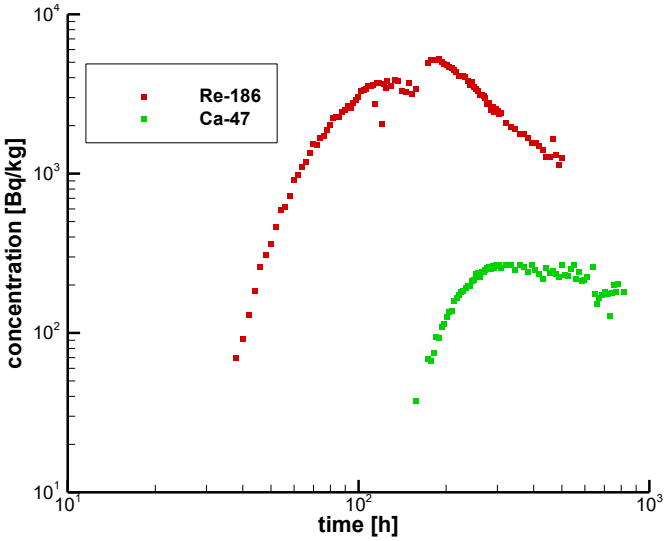


Fig. 11.12 Extraction concentration of Re-186 and Ca-47

11.2.3 Hydrostructural model and hydraulic properties

To simulate tracer test C2 with d³d++, the TRUE Block Scale hydrostructural model, a geometric model consisting of a cube with a side length of 200 m and the 29 discrete fractures was generated using ProMesh (Fig. 11.13). Since no statistical data on background fractures was available as a basis for

generating a porous equivalent medium, the rock matrix was assumed to be homogeneous.

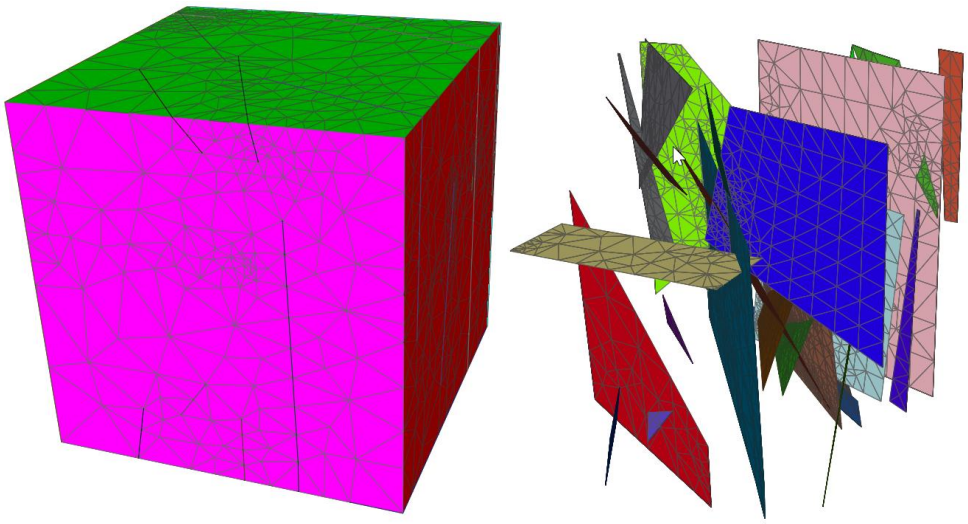


Fig. 11.13 Geometry of the hydrostructural model with 29 fractures

Characteristic hydraulic properties for each fracture within the TRUE Block were estimated based on in situ hydraulic testing and subsequent modeling studies in /DER 03/. The transport-relevant hydraulic apertures assigned to the deterministic fractures are listed in Tab. 11.4 /SCH 16/. Assuming laminar flow conditions, the corresponding fracture permeabilities could be derived from the hydraulic apertures using cubic law. The resulting permeability values are also compiled in Tab. 11.4. These parameters provided the basis for the simulation of groundwater flow and tracer transport in the discrete fracture network (dfn) in this study.

The existence of background fractures causes uncertainties in the model parameters for the rock matrix. According to /GRE 06/, a permeability of $1 \cdot 10^{-16}$ m^2 was proposed for an equivalent continuum representing both the rock matrix and the background fractures. In contrast, a value of $1 \cdot 10^{-17}$ m^2 was assumed in the Task 8 modeling studies /KRO 16a/, /KRO 16b/, /SCH 16/. Consequently, inverse modeling was required to reduce the uncertainties associated with these parameters and to achieve an improved fit to the tracer test observations. In the present study, a permeability of $1 \cdot 10^{-17}$ m^2 was used as the initial estimate for the equivalent continuum.

Tab. 11.4 Hydraulic properties of deterministic fractures /SCH 16/

structure	aperture [m]	permeability const. k [m^2]	structure	aperture [m]	permeability const. k [m^2]
5	$2.917 \cdot 10^{4}$	$1.405 \cdot 10^{10}$	7S	$3.865 \cdot 10^{4}$	$1.827 \cdot 10^{10}$
6	$2.010 \cdot 10^{4}$	$9.687 \cdot 10^{11}$	8S	$5.611 \cdot 10^{4}$	$2.656 \cdot 10^{10}$
7	$1.437 \cdot 10^{4}$	$6.923 \cdot 10^{11}$	9S	$2.552 \cdot 10^{4}$	$1.207 \cdot 10^{10}$
10	$7.941 \cdot 10^{5}$	$3.825 \cdot 10^{11}$	10S	$3.475 \cdot 10^{4}$	$1.643 \cdot 10^{10}$
13	$5.404 \cdot 10^{5}$	$2.603 \cdot 10^{11}$	11S	$6.528 \cdot 10^{4}$	$3.079 \cdot 10^{10}$
19	$1.469 \cdot 10^{4}$	$7.078 \cdot 10^{11}$	12S	$5.131 \cdot 10^{4}$	$2.417 \cdot 10^{10}$
20	$1.740 \cdot 10^{4}$	$8.378 \cdot 10^{11}$	13S	$1.037 \cdot 10^{3}$	$4.899 \cdot 10^{10}$
21	$1.129 \cdot 10^{4}$	$5.435 \cdot 10^{11}$	14S	$3.772 \cdot 10^{4}$	$1.782 \cdot 10^{10}$
22	$6.807 \cdot 10^{5}$	$3.280 \cdot 10^{11}$	15S	$5.810 \cdot 10^{4}$	$2.754 \cdot 10^{10}$
23	$1.874 \cdot 10^{4}$	$9.030 \cdot 10^{11}$	17S	$5.701 \cdot 10^{4}$	$2.701 \cdot 10^{10}$
24	$1.342 \cdot 10^{4}$	$6.464 \cdot 10^{11}$	18S	$4.946 \cdot 10^{4}$	$2.345 \cdot 10^{10}$
1S	$2.576 \cdot 10^{4}$	$1.219 \cdot 10^{10}$	20S	$5.336 \cdot 10^{4}$	$2.530 \cdot 10^{10}$
3S	$6.965 \cdot 10^{4}$	$3.288 \cdot 10^{10}$	21S	$4.688 \cdot 10^{4}$	$2.218 \cdot 10^{10}$
4S	$2.007 \cdot 10^{4}$	$9.466 \cdot 10^{11}$	24S	$4.581 \cdot 10^{4}$	$2.165 \cdot 10^{10}$
6S	$3.830 \cdot 10^{4}$	$1.809 \cdot 10^{10}$			

The suggested porosity values for the equivalent continuum are also varying in literature. While in /KRO 16a/ and /KRO 16b/ a porosity of $\phi = 0.005$ was proposed, in more recent studies a lower value of $\phi = 0.00025$ was adopted /SCH 16/. Accordingly, a porosity of $\phi = 0.00025$ was used as the initial estimate in the present modeling work.

In tracer test C2, Re-186 behaves like a conservative (non-sorbing) tracer, whereas Ca-47 shows weak sorption characteristics. For the sorption of Ca-47 in the rock matrix, an initial distribution coefficient of K_d = $7.1 \cdot 10^{-7}$ m^3 kg^{-1} was assumed, and the initial

diffusion coefficient was set to $1 \cdot 10^{-10}$ m^2 s^{-1}. These values were used as initial values for the inverse modeling analysis.

11.2.4 Hydraulic boundary conditions

Hydraulic boundary conditions were prescribed in terms of piezometric heads on the outer surfaces of the cube. These values were calibrated such that the hydraulic influence of underground excavations, including tunnels and boreholes, could be represented implicitly, thereby eliminating the need to model these features explicitly /DER 03/.

The boundary conditions are defined on a regular grid with a side length of 22 m on the model surface. Each of these boundary elements was assigned the corresponding pie-zometer heights (Fig 11.14). These head values were imported into d^{3}f++ and interpolated onto the computational grid to provide continuous hydraulic boundary conditions throughout the model geometry.

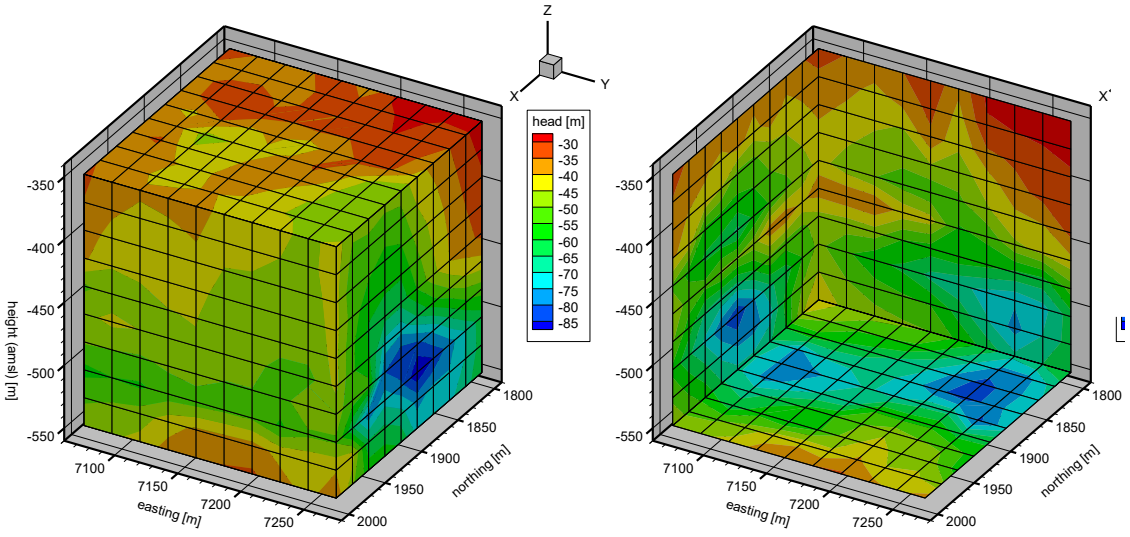


Fig. 11.14 Hydraulic heads on the surface of the 200-m model block /SCH 16/

The injection of water into structure 23 at the coordinates (1929.741, 7194.840, −476.100) is represented in the model as a point source with an injection rate of $1.67 \cdot 10^{-7}$ m^3 s^{-1}. The injections of the conservative tracer Re-186 and the sorbing tracer Ca-47 are specified as time-dependent source terms based on the injection histories shown in

Fig. 11.10. The tracer injection rates are interpo-lated at 4-hour intervals and implemented accordingly in the d^{3}f++ model.

Water extraction from structure 21 at coordinates (1914.628, 7186.294, −473.065) is modeled as a point sink with an extraction rate of $3.25 \cdot 10^{-5}$ m^3 s^{-1}. The tracer mass reaching the extraction point was removed from the system together with the extracted water, allowing the simulated breakthrough curves to be compared directly with the measured tracer concentrations at the extraction location.

These source and sink boundary conditions reproduce the hydraulic forcing applied during tracer test C2 and provide the basis for simulating tracer transport through the interconnected fracture network.

11.2.5 Primary results

Groundwater flow field and pressure distribution were computed firstly using the initial hydraulic parameters, including the preliminary estimates of permeability and porosity for the equivalent continuum. Fig. 11.15 shows the resulting pressure distribution on the model boundaries and the fracture surfaces, to-gether with the simulated flow field within the fracture network.

Fig. 11.16 gives a detailed view of the pressure distribution and flow field on fractures 20, 21, 22, and 23, which form the principal hydraulic connection between the injection and extraction locations. The results are shown from the perspectives of both the injection well and the extraction well. The simulated flow pattern clearly indicates groundwater movement from the injection point on fracture 23 toward the extraction point on fracture 21, primarily along the connected fracture pathway comprising fractures 23, 22, 20, and 21.

The computed hydraulic gradients confirm that this sequence of interconnected fractures constitutes the dominant transport pathway for water and tracer migration in tracer test C2. Consequently, the flow solution provided the basis for subsequent simulations of conservative and sorbing tracer transport through the fracture network.

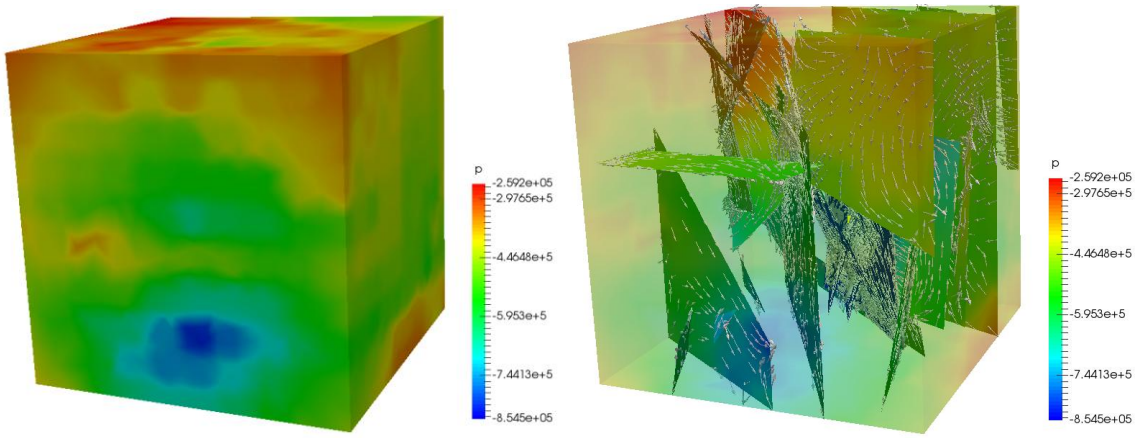


Fig. 11.15 Pressure distribution on the model boundary (left); pressure distribution and flow field in the fractures (right). The arrows illustrate the flow direction in the fractures.

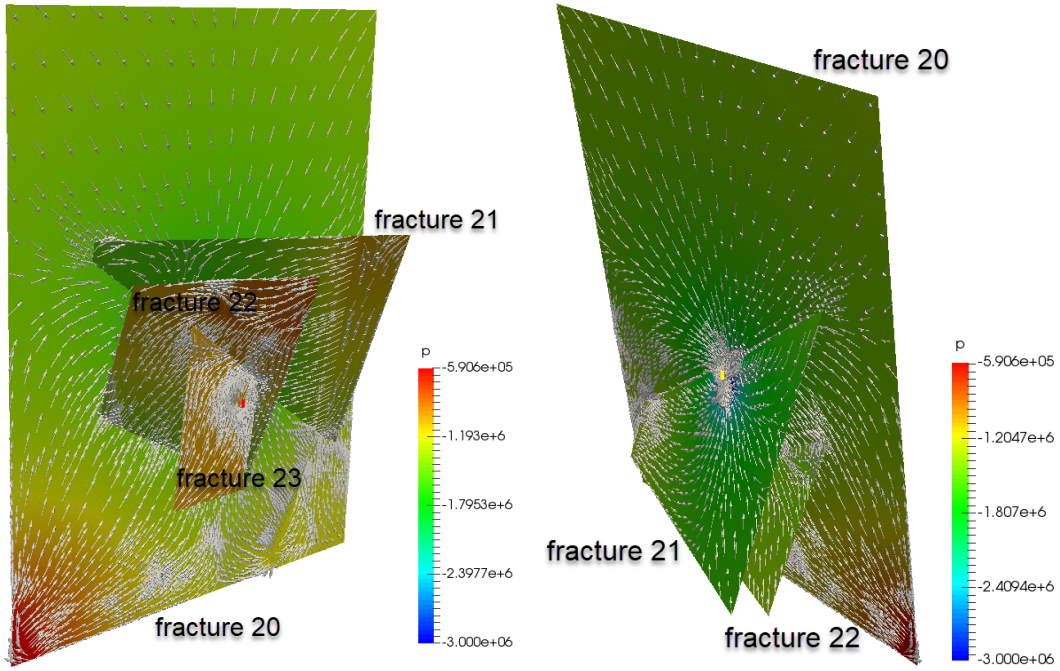


Fig. 11.16 Pressure distribution and the flow field on the relevant fractures for injection and extraction of water from point view of the injection well (left) and the extraction well (right). The arrows show the flow direction in the fractures

The transport of the conservative tracer Re-186 was simulated using the modified hydraulic parameters as described in section 11.2.3. Fig. 17 presents an example of the simulated Re-186 concentration distribution on the fractures that form the main

transport pathway, namely fractures 20, 21, 22, and 23.

In Fig. 11.18 the simulated Re-186 break-through curve at the extraction point is compared with the measured values. The comparison indicates that the model does not adequately reproduce the observed tracer behavior. In particular, the simulated tracer plume arrives at the extraction point later than observed in the field measurements, resulting in a delayed breakthrough peak. Furthermore, the predicted peak concentration is significantly lower than the measured value.

These discrepancies suggest that the initial parameterization of the flow and transport model does not fully capture the hydraulic and transport characteristics of the system. Consequently, further calibration of the model parameters, including the properties of the equivalent continuum and the fracture network, was required to improve agreement between the simulated and the observed breakthrough curves.

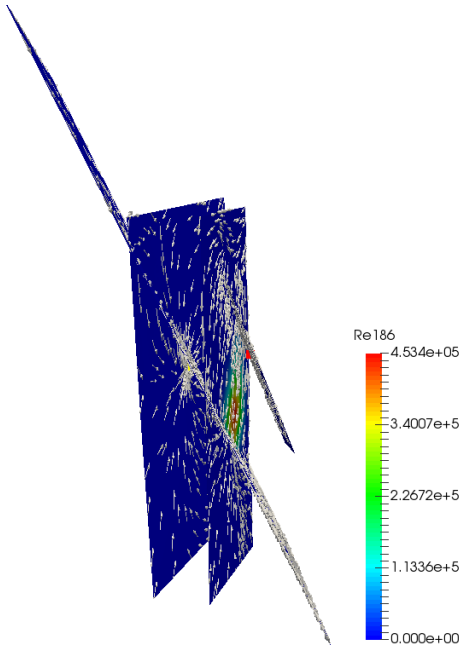


Fig. 11.17 Concentration of Tracer Re-186 and flow field in the relevant fractures at time of 200 hours

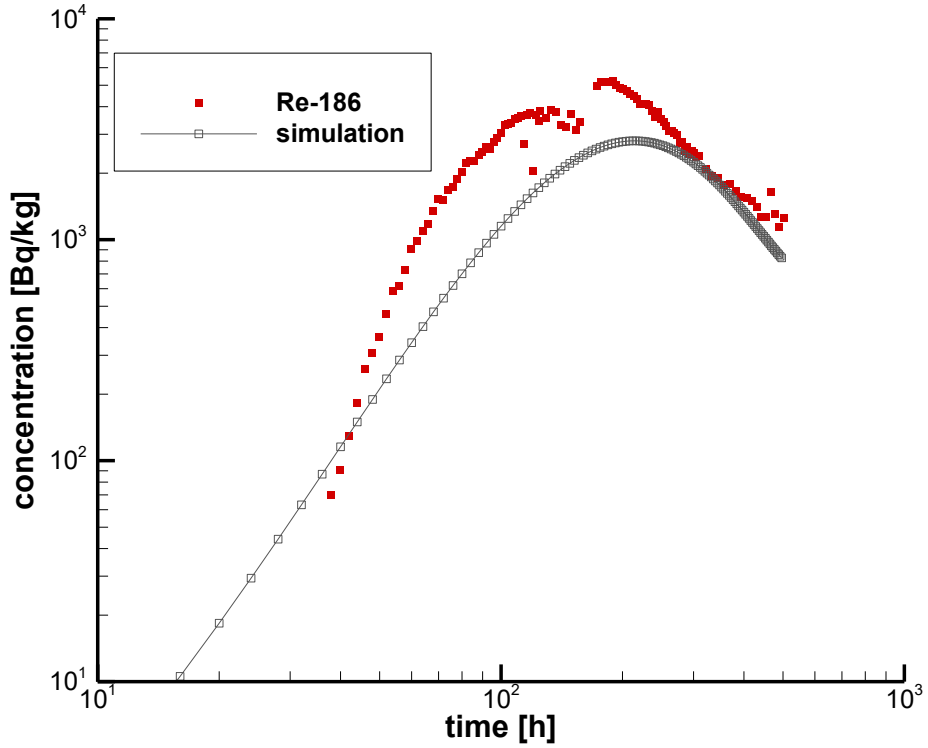


Fig. 11.18 Comparison of Breakthrough curve of Re-186 at the extraction point from simulation and experiment without calibration

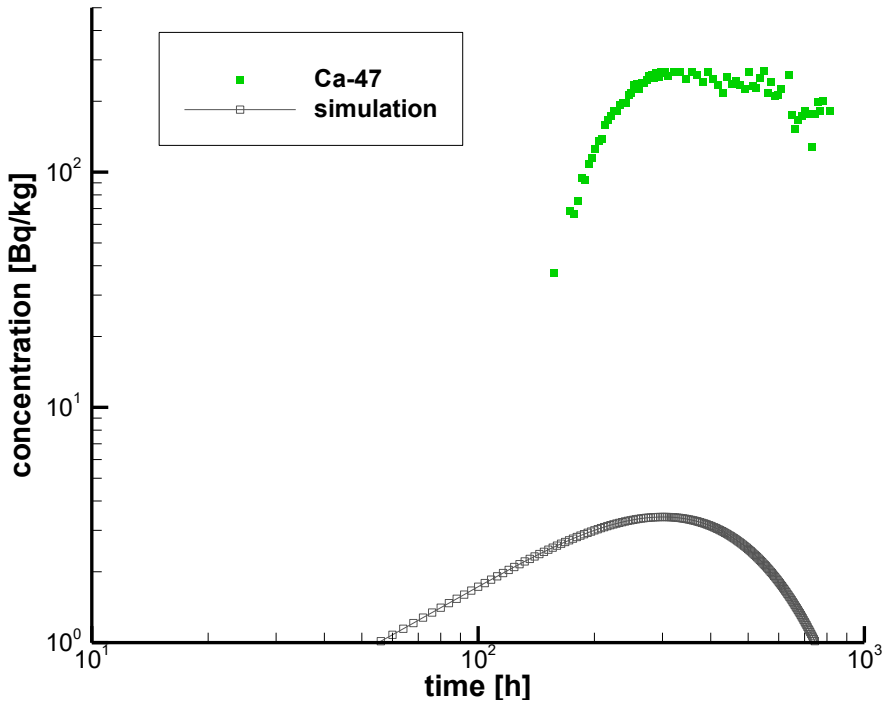


Fig. 11.19 Comparison of Breakthrough curve of Ca-47 at the extraction point from simulation and the experiment without calibration

The transport of the weakly sorbing tracer Ca-47 was simulated with the same hydraulic parameters and a first guess of the Kd-value. The concentration at the extraction point was compared to the measured breakthrough curve of the tracer (Fig. 11.19). The measured breakthrough curve was not satisfac-tory reproduced. The peak of the tracer plume took too long to reach the extraction point and did not reach the measured concentration.

The mismatch between the simulated and measured breakthrough curves suggested that the initial transport parameters, including the sorption coefficient K_d and the hydraulic properties of the equivalent continuum, require further calibration. Consequently, inverse modeling was applied to refine the model parameters and improve the agreement between the simulated and observed transport behavior of Ca-47.

11.2.6 Optimization of parameters with inverse modelling

For the transport simulation of the conservative tracer Re-186, the permeability and po-rosity of the equivalent continuum were selected as calibration parameters. A residual function was defined based on the differences between the simulated and measured Re-186 concentrations at the extraction well. The objective of the inverse modeling procedure was to minimize this residual and thereby improve the match between the simulated and observed breakthrough curves.

During each iteration, parameter sets consisting of initial values, lower bounds, and upper bounds were specified in d^{3}f++, and a transport simulation was performed over a model time of 250 hours. Based on the residuals obtained from the simulation, the Jacobian ma-trix was evaluated and a search direction for parameter adjustment was determined. The parameters were then varied along this search direction using a set of scaling factors to identify the parameter combination corresponding to the minimum value of the residual function.

This optimization procedure was repeated iteratively until no further reduction of the residual function could be achieved. Tab. 11.5 summarizes the initial values, parameter bounds, calibrated values, and the corresponding residuals for the permeability and porosity of the equivalent continuum after three iteration steps.

The calibrated simulation results for Re-186 are compared with the measured break-through data from tracer test C2 in Fig. 11.20. Obviously, the optimized parameter set resulted in a considerably improved reproduction of the observed breakthrough behavior, demonstrating the effectiveness of the inverse modeling approach in reducing parameter uncertainty and enhancing the predic-tive capability of the transport model.

Tab. 11.5 Porosity and permeability of equivalent continuum as result of model calibration for transport of inert tracer Re-186

	Start value	**Minimum value**	**Calibration**
Porosity	0.00025	0	0.000189
Permeability	$1 \cdot 10^{-17}$	$1 \cdot 10^{-25}$	$2.3137 \cdot 10^{-18}$
Residual	$8.67 \cdot 10^{7}$		$8.87 \cdot 10^{6}$

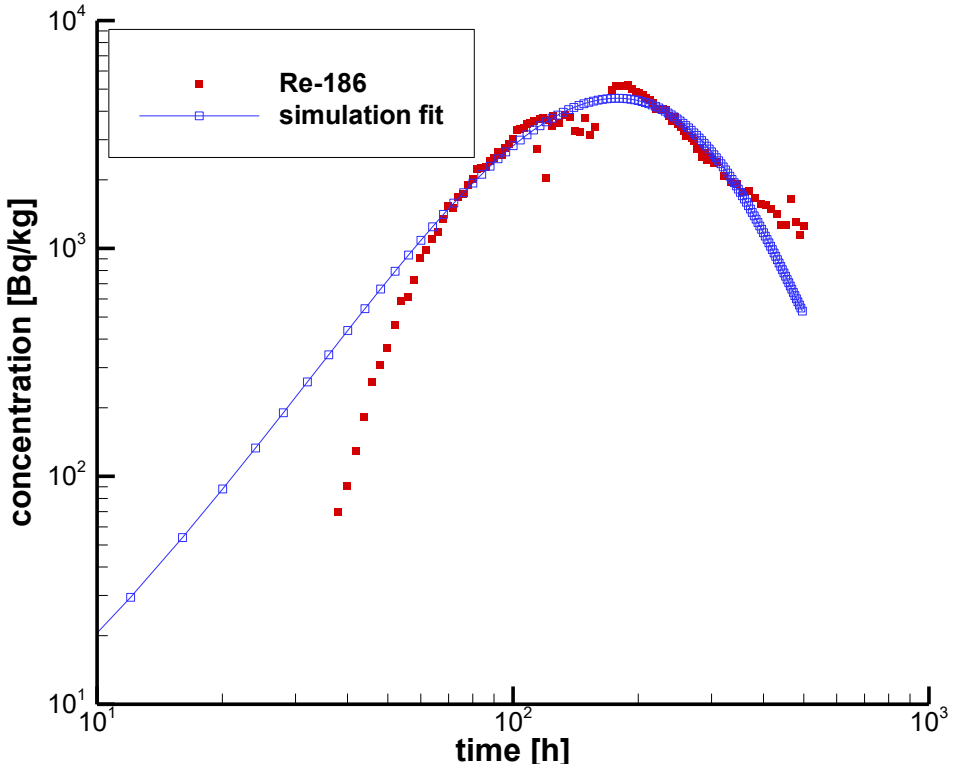


Fig. 11.20 Comparison of Breakthrough curve of Re-186 at the extraction point after optimization

For the transport simulation of the sorbing tracer Ca-47, the calibrated values for permeability and porosity could be adopted, but the specification of the diffusion coefficient and the distribution coefficient (K_d) are additional sources of uncertainties. Subsequently, in a second step diffusion coefficient and K_d value were selected as calibration parameters for the Ca-47 transport simulation. A residual function was defined based on the differences between the simulated and measured concentrations at the extraction well.

During each inverse modeling iteration, transport simulations were performed using parameter sets constrained by predefined initial values and parameter bounds. The resulting residuals were evaluated to guide the optimization process toward a minimum of the residual function. Tab. 11.6 summarizes the initial values, lower and upper bounds, calibrated values, and corresponding residuals for the diffusion coefficient and the K_d-value of Ca-47 transport in the equivalent continuum. After six iteration steps, the calibration converged to an optimized parameter set that provides the best agreement between the simulated and measured breakthrough data.

Tab. 11.6 Kd-value of equivalent continuum for the transport of Ca-47 as result of model calibration

	Start value	**Minimum value**	**Calibration**
Diffusion	$1 \cdot 10^{-10}$	0	$2.440 \cdot 10^{-8}$
Kd-value	$7.1 \cdot 10^{-7}$	0	$6.008 \cdot 10^{-8}$
Residual	$1.6 \cdot 10^{6}$		$7.5 \cdot 10^{5}$

Fig. 11.21 compares the calibrated break-through curve of Ca-47 with the experimental results obtained from tracer test C2. The optimized model achieves a substantially improved reproduction of the observed tracer behavior, indicating that the calibrated diffusion coefficient and sorption parameters ade-quately represent the transport processes controlling the migration of Ca-47 within the fracture network and the surrounding equivalent continuum.

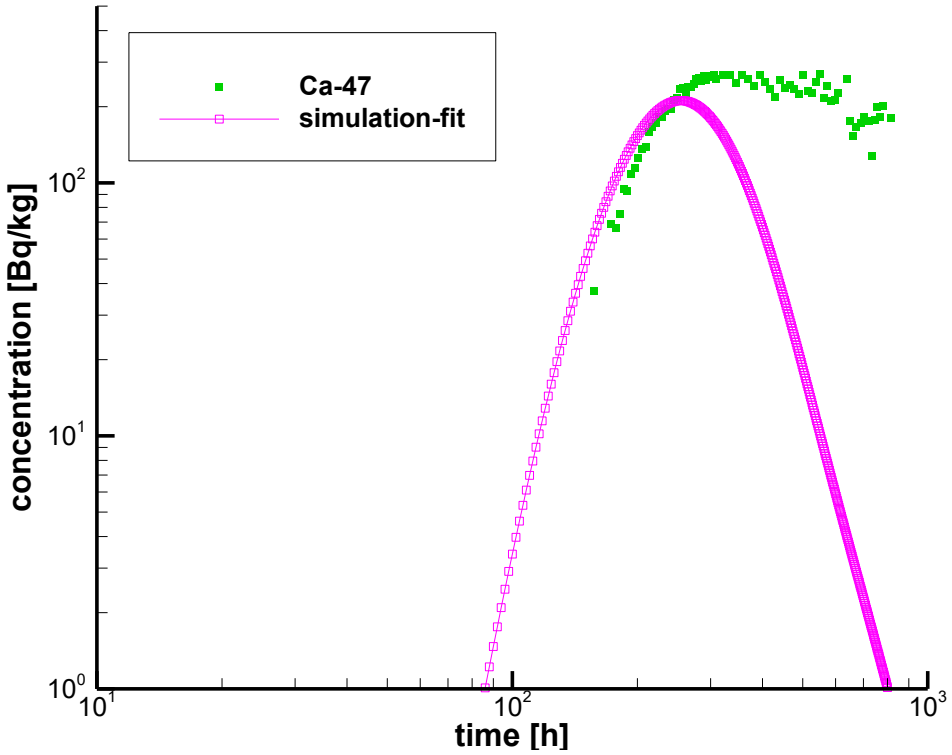


Fig. 11.21 Comparison of Breakthrough curve of Ca-47 at the extraction point after optimization

11.2.7 Conclusion

Tracer test C2 is successfully simulated using the d³f++ framework and the TRUE Block Scale hydrostructural model. Because some important input parameters could not be determined in advance without uncertainties, inverse modeling was applied for calibration. The permeability and porosity values were optimized based on the Transport of the conservative tracer Re-186, while the diffusion coefficient and sorption coefficient (K_d) were subsequently calibrated using the weakly sorbing tracer Ca-47. While the initial simulations were unable to reproduce the measured breakthrough curves of Re-186 and Ca-47 satisfactory, the calibrated model shows a very good agreement with the measured breakthrough data.

The results demonstrate that inverse modeling in d³f++ is an effective tool for reducing parameter uncertainty and improving the representation of flow and transport processes in fractured rock. The study confirms that tracer migration is primarily controlled by the

interconnected deterministic fracture network, while diffusion and retention in the surrounding rock mass play an important role in the transport behavior of sorbing tracers.

11.3 Colloid-facilitated contaminant transport

A generic test case was to be conducted on colloid-facilitated nuclide transport in fractured media. It is based on a block experiment performed by the organization UJV (Czech Republic) in an artificial, well described fracture in a granite as part of the EURAD program. The experimental granite block with dimensions 80 x 50 x 40 cm³ (TH02030543-V10) was constructed within the TACR project TH02030543 (https://starfos.tacr.cz/cs/project/TH02030543). The artificial fracture was generated by horizontal splitting of the Block (see Fig. 11.22, /JAN 19/). A fluid was injected via an injection point in the center of the fracture on one side of the block, and an outlet was constructed in the middle of the opposite side.

In EURAD, the code d³f++ was used to reproduce the flow field and the transport of nuclides in the fracture as result of the experiment. The goal of this work is to apply d³f++ also to colloid facilitated transport in the fracture. The transport of colloids and colloid-bound radionuclides is simulated. Of particular interest is the description of the interactions between radionuclides, colloids, and the fracture surface.

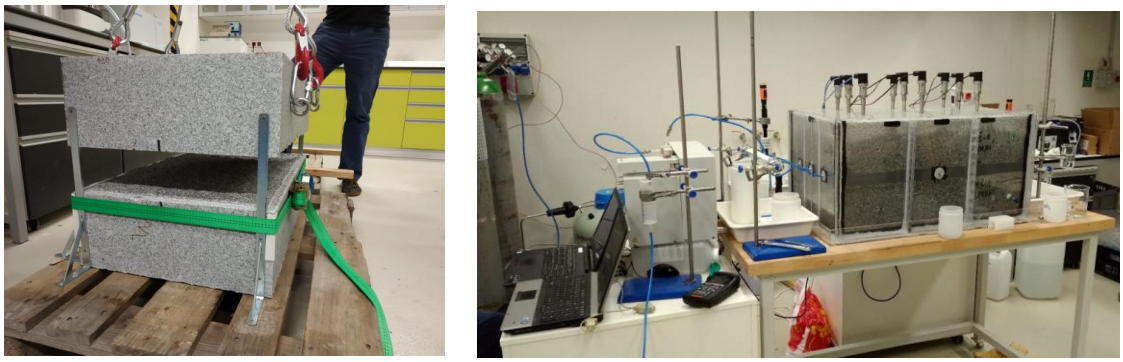


Fig. 11.22 Manufacture of the artificial fracture by splitting a granite block (left) and setting up the experiment in the UJV laboratory (right), /JAN 19/

11.3.1 Colloid transport

Transport calculations are based on the assumption of a steady-state flow field. The generalized Darcy law for two-dimensional groundwater flow can account for variable density and viscosity of the groundwater in the case of density-driven flow /FEI 99/, see equations (11.1)-(11.4). In the experiment the mineralization of the groundwater can be regarded as constant and the temperature in the entire model domain can also be assumed to be constant, such that the density and viscosity are treated as constant. Based on this, the general form of the Eulerian colloid mass balance equations in non-uniform, steady-state flow is:

$$\frac{\partial}{\partial \mathrm{t}}(\phi C_c) + \mathrm{div}(q_c C_c - \phi D_c \nabla C_c) = -F^t \qquad (11.7)$$

$$\frac{\partial}{\partial \mathrm{t}}(\rho_c C_c^*) = -F^{t*} \qquad (11.8)$$

with

q_c Darcy velocity of the colloids [L T^{-1}]
C_c Concentration of the colloids in the aqueous phase [M L^{-3}]
C_c^* Concentration of the colloids sorbed to the shear zone material [L^3 L^{-3}]
ρ_c Density of the colloids [M L^{-3}]

The tensor D_c [L^2 T^{-1}] describes the diffusion and dispersion effects. F^t and F^{t*} [M L^{-3} T^{-1}] are general expressions of the sink-source (exchange) term between the aqueous phase and the shear zone surfaces. Relevant expressions for F^t and F^{t*} are discussed in Section 11.3.2.

11.3.2 Colloid facilitated solute transport

In the model for the colloid facilitated transport two mobile and two immobile solute components and one mobile and one immobile colloid component are considered. These components and the interactions between them are depicted in Fig. 11.23, see e.g. /LÜH 98/, /REI 14/, /NOS 16/.

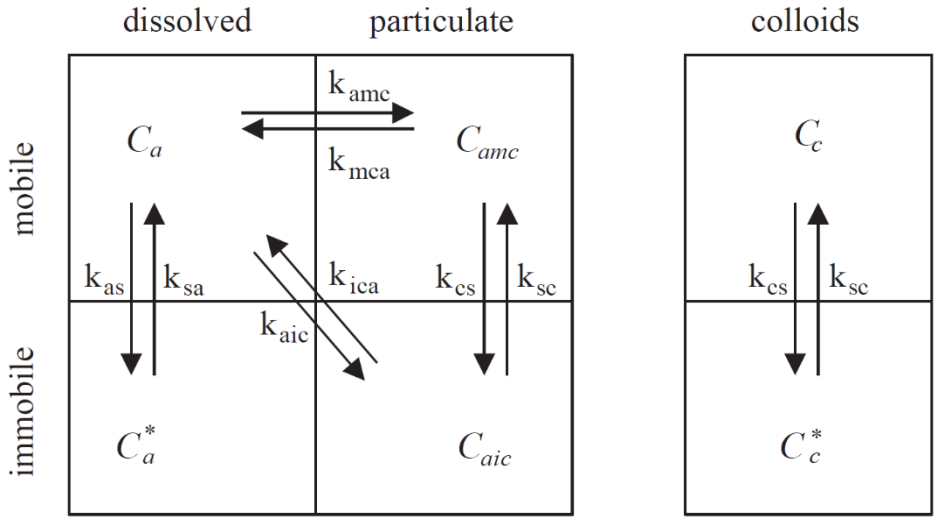


Fig. 11.23 General concept of considered mobile and immobile phases and interactions between them according to /NOS 16/

With the following denotation (cf. /NOS 16/):

C_c Mobile colloid concentration [M L^{-3}]

C_a Mobile solute concentration [M L^{-3}]

C_{amc} Solute concentration attached to mobile colloids [M(solute) $M(colloids)^{-1}$]

C_{aic} Solute concentration attached to immobile colloids [M(solute) $M(colloids)^{-1}$]

C_c^* Immobile colloid concentration [L^3(colloids) L^{-3}]

C_a^* Immobile solute concentration [M(solute) $M(solid)^{-1}$]

k_{cs} First-order transfer rate of colloids from mobile to immobile phase [L^3 $M(solid)^{-1}$ T^{-1}]

k_{sc} First-order transfer rate of colloids from immobile to mobile phase [T^{-1}]

k_{as} First-order transfer rate of solute from mobile to immobile phase [L^3 $M(solid)^{-1}$ T^{-1}]

k_{sa} First-order transfer rate of solute from immobile to mobile phase [T^{-1}]

k_{amc} First-order transfer rate of solute from mobile aqueous phase to mobile colloids [L^3 $M(colloids)^{-1}$ T^{-1}]

k_{mca} First-order transfer rate of solute from mobile colloids to mobile aqueous phase [T^{-1}]

k_{aic} First-order transfer rate of solute from mobile aqueous phase to immobile colloids [L^3 $M(colloids)^{-1}$ T^{-1}]

k_{ica} First-order transfer rate of solute from immobile colloids to mobile aqueous phase [T^{-1}]

The solute transport equations in the shear zone as presented in /NOS 16/ have essentially been given /IBA 95/. The continuity equations for the solutes dissolved in the aqueous phase or sorbed to the aquifer material are from /LÜH 98/:

$$\frac{\partial}{\partial t}(C_a) + div(v_a C_a - D_a \nabla C_a) = -F^a_{as,sa} - F^a_{amc,mca} - F^a_{aic,ica} \quad (11.9)$$

$$\frac{\partial}{\partial t}(\rho_b C^*_a) = F^a_{as,sa} \quad (11.10)$$

The mass balance equations for the solutes sorbed to mobile and immobile colloids are given by

$$\frac{\partial}{\partial t}(C_c C_{amc}) + div(v_c C_c C_{amc} - D_c \nabla C_c C_{amc}) = -F^a_{cs,sc} + F^a_{amc,mca} \quad (11.11)$$

$$\frac{\partial}{\partial t}(\rho_c C^*_c C_{aic}) = F^a_{cs,sc} + F^a_{aic,ica} \quad (11.12)$$

with

$F^a_{as,sa}$ Rate loss of solute from mobile to immobile phase [M L^{-3} T^{-1}]

$F^a_{cs,sc}$ Rate loss of solute sorbed on colloids from mobile to immobile phase [M L^{-3} T^{-1}]

$F^a_{amc,mca}$ Rate loss of solute from mobile aqueous phase to mobile colloids [M L^{-3} T^{-1}]

$F^a_{aic,ica}$ Rate loss of solute from mobile aqueous phase to immobile colloids [M L^{-3} T^{-1}]

D_a Tensor for diffusion and dispersion effects of the solutes [L^2 T^{-1}]

D_c Tensor for diffusion and dispersion effects of the colloids [L^2 T^{-1}]

v_a Flow velocity of the solutes [L T^{-1}] = Darcy velocity divided by θ

v_c Flow velocity of the colloids [L T^{-1}] = Darcy velocity divided by θ

The mass exchange between the phases shown in Fig. 11.23 is governed by the following source terms F:

$$F^a_{as,sa} = k_{sa}\frac{\rho_b}{\theta}\left(K_{d,as}C_a - C^*_a\right) = \frac{\rho_b}{\theta}\left(k_{as}C_a - k_{sa}C^*_a\right) \quad (11.13)$$

$$F^a_{amc,mca} = k_{mca}C_c\left(K_{d,amc}C_a - C_{amc}\right) = C_c(k_{amc}C_a - k_{mca}C_{amc}) \quad (11.14)$$

$$F^a_{aic,ica} = k_{ica}\rho_c C^*_c(K_{d,aic}C_a - C_{aic}) = \rho_c C^*_c(k_{aic}C_a - k_{ica}C_{aic}) \quad (11.15)$$

with the distribution coefficients $K_{d,i}$ [L^3 M^{-1}] for the respective linear sorption processes. All sorption / desorption processes in equations (12.14), (12.15), (12.16) are approximated by first order sorption and desorption rate expressions. Equilibrium sorption behavior can be approximated by using large values for the sorption and desorption rate constants: The ratio of sorption to desorption rate constant is equivalent to the $K_{d,i}$ value if both rates are fast.

The interaction of colloids with the fracture filling material can be described as a first order kinetic process according to /LÜH 98/:

$$F^c_{cs,sc} = k_{cs}\frac{\rho_b}{\theta}C_c - k_{sc}\rho_c C^*_c \quad (11.16)$$

with attachment and detachment rate constants k_{cs} and k_{sc}. Irreversible attachment or filtration of colloids is obtained by assigning a value of zero to the detachment rate constant. Accordingly, the contaminant concentration change caused by colloid interactions with the fracture-filling material can be expressed as:

$$F^a_{cs,sc} = k_{cs}\frac{\rho_b}{\theta}C_c C_{amc} - k_{sc}\rho_c C^*_c C_{aic} \quad (11.17)$$

11.3.3 Application of the model to a block experiment

A laboratory facility for assessing fracture flow quantification and conducting sensitivity analyses has been developed at ÚJV /AHU 21/, /JAN 19/. A physical granite block model (80 × 50 × 40 cm³) was constructed, and the artificially generated fracture was characterized using a 3D laser scanner. Tracer experiments employing various tracers (Cl^-, I^-, HTO,

and Pb^{2+}) were performed to develop methodologies for evaluating the migration and retention of potential contaminants in fractured rock environments /JAN 19/.

Based on the conditions of the granite block model a simulation for colloid facilitated radionuclide transport has been proposed and simulated with the flow and transport code d^3f++.

Set-up of geometric model in d3f++

The data set for the geometry of the model as well as for tracer experiments in the fracture, looking at different fracture variables and boundary conditions was provided by JV. The geometric description was made available in the form of raster data for fracture bottom, fracture top and fracture aperture with a resolution of 1 mm. Because of data inconsistencies, in addition to fracture bottom the fracture aperture information was used instead of the fracture top data to develop the model. Furthermore, based on the rock matrix properties and the estimated transport velocity the height of the model was reduced from 400 mm to 60 mm to safe computing capacity (diffusive transport deep into the rock matrix is not of relevance for the experiments). The model geometry is shown in Fig. 11.24. The coarse grid was refined three times (iso-tropically and anisotropically) to an element length of 2 mm during the solving process (geometric multigrid method). Finally, a special multigrid construction was chosen to optimize the relation between grid resolution and computational effort. The Raster Layer Projector Method /REI 20/ allows to apply the complete geometric information of the raster data in the grid refinement process. That means, the roughness of the fracture was almost completely reproduced in the model, while the coarsest grid consists of only 30 720 elements.

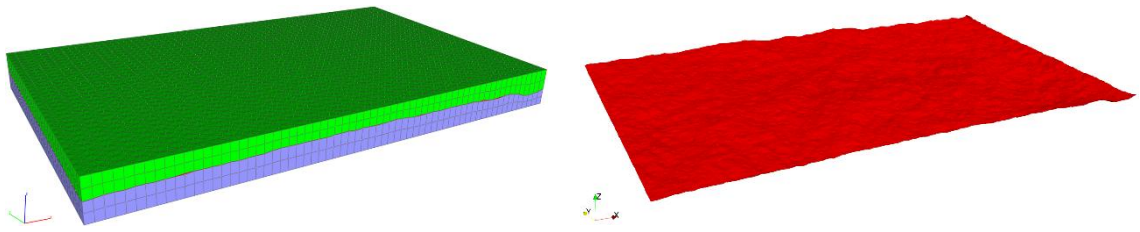


Fig. 11.24 Complete 3d geometric model (left; coarse grid) and fracture (right; fine grid)

Based on this model geometry, consisting of 7.9 million prism elements on the finest grid level, the code d³f++ was used to describe radionuclide transport in the block experiment. In the fracture, the porosity was set to 1.0 and a cubic law approach, based on the point-wise aperture measures, was chosen for the permeability. The matrix porosity was set to 0.007 and the permeability to 10^{-18} m². The model was calibrated by a conservative tracer experiment realized by UJV on 10.10.2019, see Fig. 11.25. Over a period of 60 s 20 ml/min of a NaCl tracer (358 kg/m³) were injected into the fracture in one central point, and outflow concentration was measured in one of the two outlets at the other side of the block.

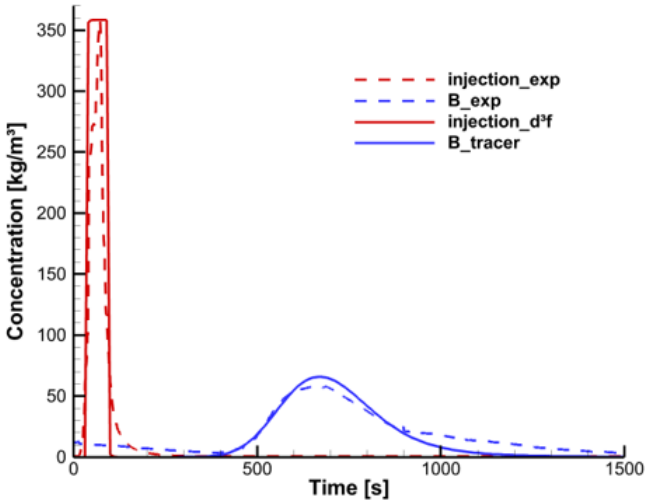


Fig. 11.25 Model calibration, based on the conservative tracer experiment of 2019

Fig. 11.26 shows the simulated tracer con-centration in fracture and matrix after a model time of 600 s. The concentration distribution in the fracture after 400 s is shown in Fig. 11.27. It illustrates the influence of the fracture roughness and the permeability distri-bution to the tracer transport. The measured concentrations at outlet B are met very well by simulation.

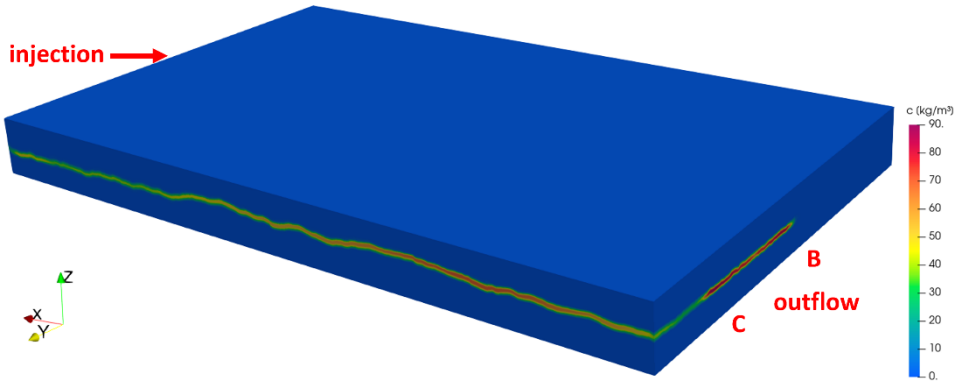


Fig. 11.26 Simulated tracer concentration in fracture and matrix after 600 s

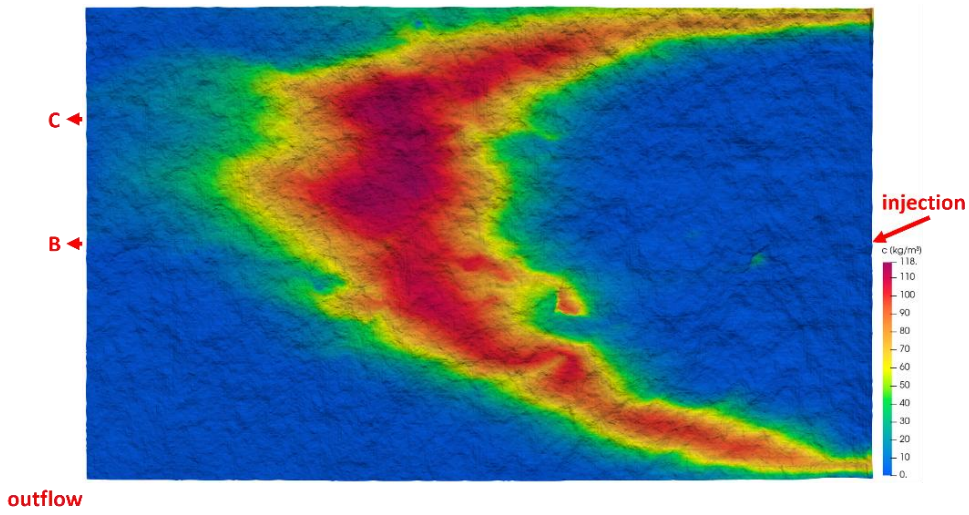


Fig. 11.27 Simulated concentration distribution of a non-sorbing tracer under the conditions of the block experiment performed by UJV on 10 October 2019

With regard to the block experiment the model pursued two objectives. Firstly, the calibrated model was used to predict concentrations and travel times of generic pollutants with different K_d values and different flow velocities in the fracture of the block experiment. This was done in order to plan the layout of the experiment. The main aim was to identify the duration of the experiment and the appropriate design to obtain tracer concentrations at the outlet significantly above the detection limits.

One important aim was to provide equilibrium conditions for sorption processes in the experiment, i.e., to reduce the flow velocity to as low as feasible values. Therefore, the computations were repeated with different inflow rates down to 2 ml/min and 0.2 ml/min

and an outflow only at point B (as later realized in the experiment). Fig. 11.28 shows the results for 0.2 ml/min and varying distribution coefficients. In Fig. 11.29 the simulated concentration distribution of a sorbing tracer with K_d = 0.01 m³ kg^{-1} after a model time of 28 days is depicted. This illustrates the strong influence of the sorption on the travel time and, therefore, the duration of the experiment required to recover the entire amount of substance. Tab. 11.7 compiles the travel times by d³f++ simulations.

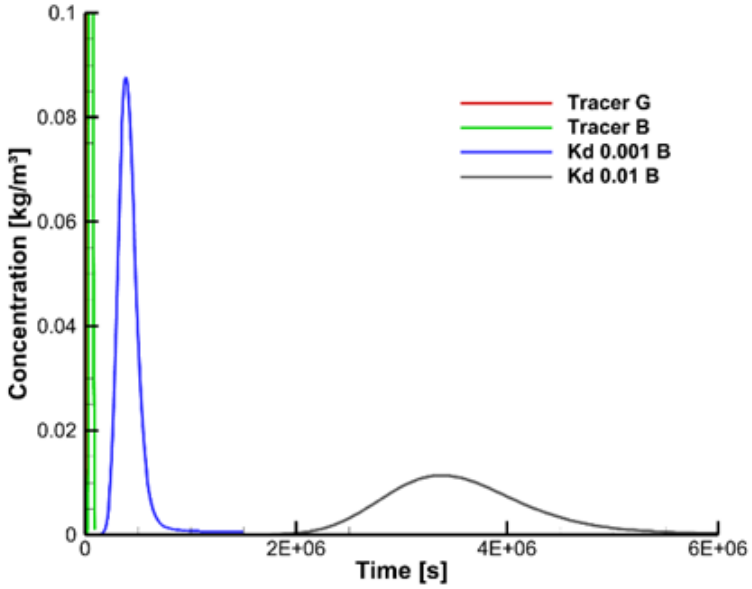


Fig. 11.28 Travel time predictions with an inflow rate of 0.2 ml/min and varying distribution coefficients

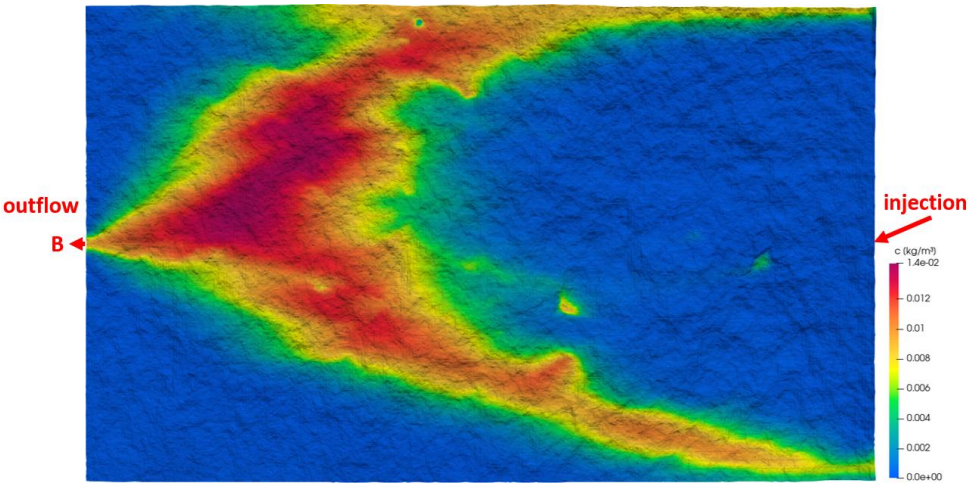


Fig. 11.29 Simulated concentration distribution of a sorbing tracer under the conditions of the block experiment with one outlet

Tab. 11.7 Results from predictive calculations of the break-through curves for the layout of the block experiment /JAN 23/

Kd [m³/kg]	time c_max in B [s]	time c_max in B	c_max in B [kg/m³]	Reduction factor c_max
Inflow 20 ml/min				
0	590	9.833 min	65.789	5.4
0.001	4899	82 min	9.618	37.2
0.01	42890	12 h	1.017	352
0.1	422419	4.875 d	0.103	3476
Inflow 1 ml/min				
0	9 900	2.75 h	88.6	4
0.001	78 000	21.70 h	9.92	36.1
0.01	680 000	7.78 d	1.28	278
Inflow 0.2 ml/min				
0	50 000	13.89 h	83	4.3
0.001	385 500	4.46 d	8.8	40.7
0.01	3 355 000	38.83 d	1.14	314

The experiments conducted as part of the ERAD program involved the transport of , Cs, Ba, Sr and Ni /JAN 23/. Based on the predictions, an inflow rate of 5 ml/min was chosen as a compromise between the requirement to meet equilibrium sorption conditions and a feasible duration of the experiment. Firstly, a test with an inert tracer was performed. The amount of the injected tracer was 98,01 g. The experiment was finished 20 hours after injection. The first arrival of iodide in the outlet was reached after 17.5 min and the maximum concentration after 40 min. The mass recovery was ca. 90 %. The reactive experiment was carried out in April/May 2023. The Block and the fracture were saturated with SGW2 water, and a cocktail with iodide as non-sorbing tracer and the elements U, Cs, Ni, Sr and Ba with concentrations as described in Tab. 11.8 was injected. In order to monitor on-line the progress of the advective fraction of the tracer cocktail it was decided to label the cocktail with 0.01 M NaI. For the results see Fig. 11.30 and Fig. 11.31.

Tab. 11.8 Nuclide concentration in the injected fluid

nuclide	SGW2 [mg/l]	injected concentration [mol/l]
U	3.07E-05	1.0E-04
Cs	2.23E-05	1.0E-03
Ba	2.50E-02	1.0E-06
Sr	2.80E-03	1.0E-04
Ni	1.14E-03	1.0E-03

When the experimental results became available, further transport simulations adapted to the results have been performed. The flow aperture and the dispersion lengths was slightly adapted to describe the breakthrough curves of the non-sorbing iodide and the uranium tracer, since the measured curves indicated that uranium has not been retarded at all. The results for simulated and measured curves are shown in Fig. 11.30.

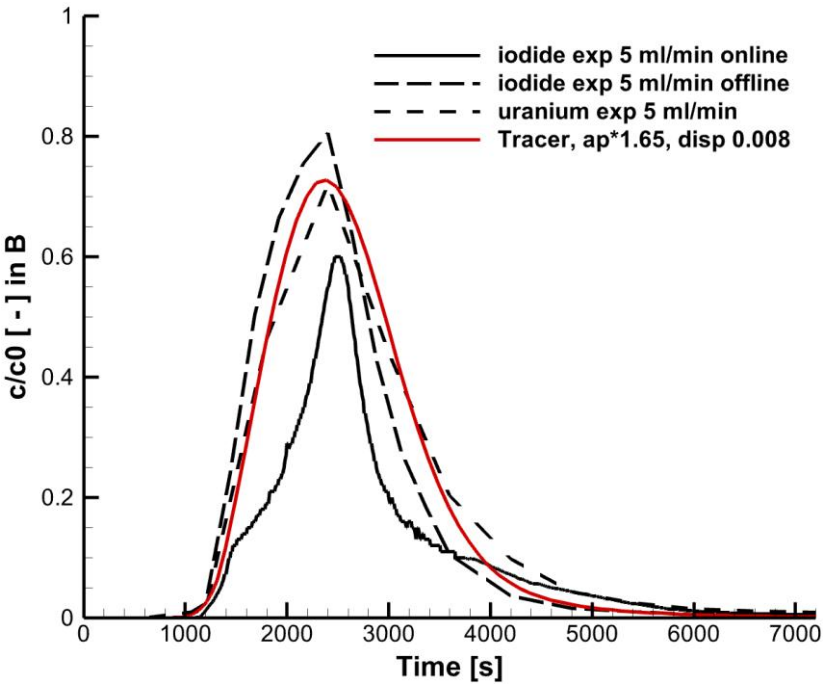


Fig. 11.30 Simulated breakthrough curves of a non sorbing tracer and measured breakthrough curves of iodide and uranium

Fig. 11.31 shows the same curves but also the measured breakthrough curves of the other elements of the injection cocktail. In addition, a simulation curve for a low sorbing element with a K_d value of 0.001 m^3/kg is. It is evident that the maxima of the breakthrough curves for Ni, Sr and Ba are similar to the non-sorbing tracer. However, these curves show a strong tailing. This could be due to matrix diffusion, but a more likely explanation is that the sorption processes are not in equilibrium, since the majority of the injected mass is transported through the fracture of the block in less than one hour. The breakthrough curve for Cs does not show a peak at ideal tracer arrival but a very broad, retarded curve, appearing much earlier but being broader than the curve obtained for tracer with equilibrium sorption and a Kd-value of 0.001 m^3/kg. Sorption experiments with Sr and Cs in a system with SGW2 water and granite reveal Kd-values in the range of 0.001 and 0.01. Speciation calculations for Ni indicate Kd-values above 0.1 m^3/kg. The differences between sorption values obtained in batch systems or from calculations on the one hand and the observations from the block experiment on the other hand gives evidence that the volume flow was too high to allow complete adjustment of equilibrium conditions. In order to check this hypothesis,

calculations applying approaches fo kinetically-controlled sorption processes should be performed. The complete description is given in /JAN 23/.

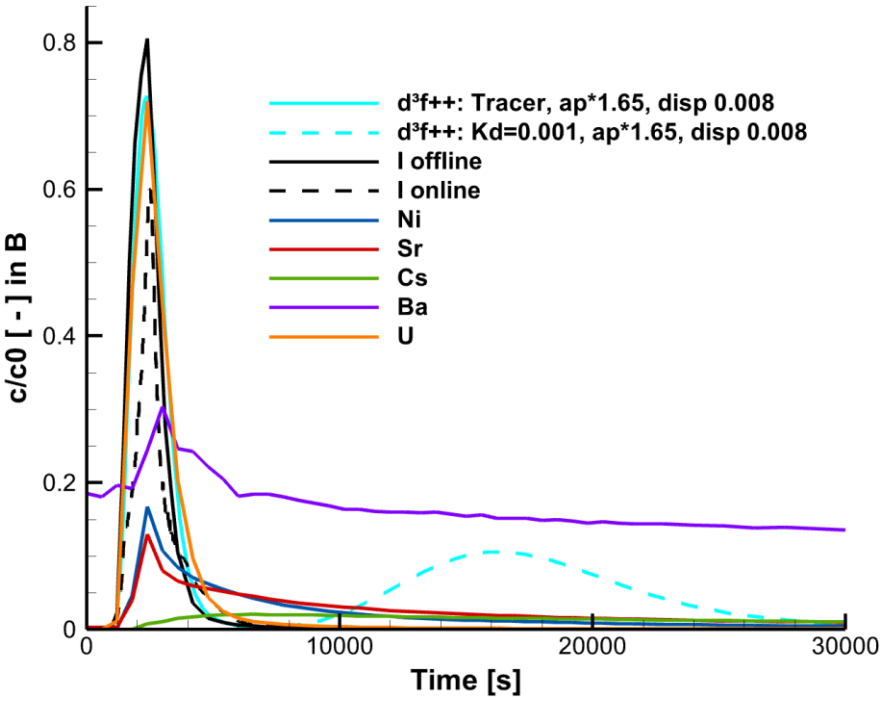


Fig. 11.31 Simulated breakthrough curves for a non sorbing tracer and a tracer with Kd=0.001 m³/kg and measured breakthrough curves of all injected tracers

Simulation of colloid facilitated transport under the conditions of the block experiment

In the next step, the colloide-facilitated transport model, described in Section 11.3.2, is applied. Based on the experiment with tracer experiment with iodide, a hypothetical simulation case for a colloid-facilitated radio-nuclide transport is developed. In this case the transport of Am and Pu as representatives of the trivalent and tetravalent elements in the presence of colloids is considered. In addition, transport of U as a non-colloid-bound element is simulated.

Flow and transport parameter

Relevant data for flow and transport are listed in Tab. 11.9. No distinction was made between the dispersion lengths for colloids and radionuclides. The values were derived from the experiments with the conservative tracer iodide. Due to the larger

radius the diffusion coefficients for colloids were selected as one order of magnitude lower than those for freely dissolved elements.

Tab. 11.9 Model system parameters for flow and transport

Parameter, unit; name	**Value**
Water inflow rate [m³/s]; Q	$3.33 \cdot 10^{-9}$
Colloid inflow [kg/s];	
Colloid molecular diffusion coefficient [m²/s]; $D_{m,c}$	$1.0 \cdot 10^{-10}$
Longitudinal colloid dispersion length [m]; α_{Lc}	0.002
Transversal colloid dispersion length [m]; α_{Tc}	0.0002
Nuclide molecular diffusion coefficient [m²/s]; $D_{m,a}$	$1.0 \cdot 10^{-9}$
Longitudinal element dispersion length [m]; α_{La}	0.002
Transversal element dispersion length [m]; α_{Ta}	0.0002
Porosity of undisturbed rock [-]; θ	0.005
Density of undisturbed rock [kg/m³]; ρ	2616

Interaction of radionuclides, colloids and matrix

Data for the interaction of tri and tetravalent radionuclides with bentonite colloids are derived from lab and field experiment results obtained at Grimsel test site (GTS) within the CFM project /HUB 16/, /NOS 20/, and are listed in Tab. 11.10. For uranium, in accordance with the observations under GTS conditions, no interaction with colloids is assumed.

Sorption coefficients for interaction of radionuclides with the solid matrix are based on laboratory reversibility experiments and related discussions from long-term tailings of Am and Pu in GTS field experiment CFM RUN 13-05 /HUB 16/, /NOS 20/. For uranium a value derived from the reversibility experiments has been chosen. In addition, a rather fast sorption rate as used in GTS field experiment simulations is applied for

all radionuclides. All data are compiled in Tab. 11.10.

For interaction of colloids with the solid matrix an irreversible colloid filtration was considered, namely the colloid remobilization coefficient was set to zero. Best estimate values for colloid filtration rates were derived from field experiment results at GTS /HUB 16/.

Tab. 11.10 Parameters for interaction of radionuclides, colloids and matrix

Parameter, unit; name	**Value**
Interaction of radionuclides with mobile and immobile colloids	
Sorption coefficient for trivalent elements [m³/kg]; $K_{d,amc,iii}$ $K_{d,aic,iii}$	1,500
Sorption coefficients for tetravalent elements [m³/kg]; $K_{d,amc,iv}$ $K_{d,aic,iv}$	1,600
Sorption rate for tetravalent elements [s^{-1}]; $k_{mca,iii}$ $k_{ica,iii}$	$2.2 \cdot 10^{-5}$
Sorption rate for trivalent element [y^{-1}]; $k_{mca,iv}$, $k_{ica,iv}$	$5.6 \cdot 10^{-5}$
Interaction of radionuclides with solid matrix	
Sorption coefficient for trivalent elements [m³/kg]; $K_{d,as,iii}$	0.2
Sorption coefficient for tetravalent elements [m³/kg]; $K_{d,as,iv}$	1
Sorption rate for trivalent and tetravalent nuclides [s^{-1}] k_{sa}	0.01
Sorption coefficient for U (VI) [m³/kg]; $K_{d,as,u}$	0.004
Interaction of colloids with solid matrix	
Colloid filtration coefficient [s^{-1}]; k_{cs}	$5.6 \cdot 10^{-6}$
Colloid remobilization coefficient [s^{-1}]; k_{sc}	0

The simulation results will be published separately in /SCH 27/.

12 Summary, conclusions, and recommendations

12.1 Topic 1 – Small saturated zone at the water-bentonite contact

Upon instantaneous wetting of bentonite with water under “unlimited” water supply, the formation of a small, highly saturated narrow zone in the bentonite was again observed. To identify this zone, determine its extension into the bentonite, and assess a possible dependence of its size on bentonite density, sodium bentonite samples with densities of 1.4 g/cm³ and 1.6 g/cm³ and calcium bentonite samples with densities of 1.4 g/cm³, 1.6 g/cm³, and 1.8 g/cm³ were investigated. Since the sodium bentonite was available only in granular form with grain sizes of up to 2 mm, part of the material was ground and subsequently compacted to 1.4 g/cm³ and 1.6 g/cm³ to assess a possible influence of grain size on the results.

The motivation for determining the water content by the new non-destructive methods instead of the established gravimetric method was to increase the spatial resolution of the results. An increase by a factor of 10 to 100 had been expected in this respect. This increase was achieved. However, the original intention to obtain data during the tests could not be realized for technical reasons.

After data had been acquired by both new detection methods, the water content distribution was also determined using the classic method of cutting, weighing, and drying. These data were used to calibrate the non-dimensional data obtained from both new detection methods and served as a reference for the resulting distribution as a whole.

However, once the technical equipment was operational, it became apparent that the assumed relation between greyscale values obtained by the optical method and water content is neither linear nor complete and therefore requires calibration. For Calcigel, reasonable agreement between greyscale and gravimetric data was found for water contents up to 15 % in samples of low and medium density and up to 25 % in samples of high density. Beyond these ranges, the greyscale data did not provide reliable values because the reference curve was met in some cases but substantially missed in others.

Furthermore, bentonite density appears to affect the results. Calibration with respect to both water content and bentonite density represented an unexpected and insurmountable

impediment, rendering the optical method, at the present state of development, unsuitable for improving the accuracy of detecting the highly saturated zone. Nevertheless, a general trend roughly indicating sections of low and high water content was captured, particularly for samples with low density.

Unfortunately, the SWIR-light method also failed to provide reliable absolute water content values. The relation between the first principal component and water content is apparently influenced by additional factors. Since principal component analysis detects changes but not their causes, identifying the undesired influencing quantities and correcting their impact on the results is particularly difficult. A more detailed investigation of microstructural water distribution appears necessary to understand the relation between water content and the first principal component obtained from spectrometer measurements.

Overall, the location of the narrow, highly saturated zone was detected in only 5 of 14 cases. Four of these matches were achieved with the SWIR-light method and only one with the visual method, suggesting that the SWIR-light method may be better suited in this respect. However, the overall ratio of 5:14 substantially limits the capability of the method to provide quantitatively correct data.

Although two new approaches for non-destructive determination of the water content could be developed and tested, the objectives of Topic 1 were therefore ultimately not achieved. At the present state of development, the new methods can generally provide only a qualitative impression of a water content distribution, because absolute values may deviate substantially.

Nevertheless, a useful result was obtained with the gravimetric measurement method. Particular attention was paid to the wet zone when the samples were cut for determination of the water content. The slices from the wet zone were cut as thin as possible because strong variations in water content were expected in this region. By this procedure, the thickness of the highly saturated zone was limited for all 14 samples to no more than 1.5 to 2 mm. Particularly noteworthy and potentially relevant for future investigations is the observation that this value was obtained irrespective of bentonite sample density, bentonite type, or material structure (granular or powdery).

In the corresponding pre-test, a thickness of 3 to 4 mm was determined based on the optical measurement method. However, because the gravimetric method is considered a robust reference method, greater weight is assigned here to the lower values.

Due to the difficulties encountered in making the non-destructive methods for observing water content operational, only limited time remained to provide a proof of concept, identify method limitations, and demonstrate general viability. It therefore remains highly desirable to continue the tests according to the initial test plan in the future.

The structural form of the loose bentonite material used to produce compacted buffer elements such as blocks or pellets, namely powdery or granular material, appears to affect the wetting dynamics. In the tests with granular and powdery MX-80, wetting of the granular material was faster than wetting of the powdery material. If this proves to be a general rule, the original structural form of the bentonite represents a parameter for the simulation of water uptake that has not yet been considered in numerical models. It is therefore strongly recommended that this conjecture be substantiated or disproved and, if necessary, suitably implemented in simulation codes.

12.2 Topic 2 – Free swelling into limited space

The swelling and wetting behaviour of cylindrical, compacted, and confined bentonite samples adjoining a water-filled limited free space for swelling was investigated for MX-80 and Calcigel bentonite. While sample size and density were kept constant, the width of the gap between the bentonite and the sinter plate limiting the free space was varied between 5 and 15 mm. The new optical and SWIR methods were again applied for non-destructive determination of the water content. Due to difficulties in obtaining clear infrared responses through the materials confining the samples, the spectrometer could unfortunately be used only after the samples had been pushed out of the cell at the end of the tests. However, under these conditions, high water contents causing failure of the SWIR detection method, as observed under Topic 1, were avoided.

The tests lasted 290 hours for the MX-80 samples and 522 hours for the Calcigel samples. Even without scaling the non-dimensional greyscale and PC1 data to the actual water content, several informative conclusions on the wetting process can be drawn.

In all samples, the gap was completely filled with bentonite particles within less than 10 minutes. Complete filling of the gap with bentonite particles was found to require approximately the same time for MX-80 and Calcigel. Overall, gap filling was again shown to be a rapid phase of the wetting process.

By contrast, water uptake by the bentonite required substantially more time and was completed in only 4 of 9 samples by the end of the tests. However, three further samples appeared to approach steady-state conditions sufficiently to allow an estimate of the remaining inhomogeneities. Only two of the three MX-80 samples did not approach an end state.

The optical data from the transient wetting process show that, after rapid filling of the gap, a steep wetting front extending over no more than 1 to 2 mm advanced into the bentonite. The steepness of this front remained stable for almost ten hours. Interestingly, the rate of water uptake increased with gap width. Larger gaps therefore appear to have provided less resistance to swelling, thereby also increasing the velocity of the wetting front.

This phase was followed by a levelling-off of the water content distribution, which eventually resulted in a steady-state curve shape. The results for MX-80 are less clearly pronounced than those for Calcigel but appear to be similar. Future experiments with longer testing times are therefore desirable to confirm this impression.

A remarkable result of the tests concerns the shape of the observed or estimated steady-state water content distributions. Samples with a small gap showed a persistent sharp transition from strongly wetted bentonite to an apparently still unaffected part of the bentonite that remained at the initial water content. The samples with an intermediate gap width had not fully reached steady state but indicated a steady-state distribution with a much broader transition zone that was also located much deeper within the samples. Samples with a large gap showed a completely homogeneous water distribution at the end of the tests. Thus, inhomogeneity generally became less pronounced as the initial gap for swelling increased.

These results support the hypothesis that the ratio of gap width to sample length determines the degree of steady-state heterogeneity. To corroborate this hypothesis, further tests are strongly recommended, for example by considering the effects of wall friction or

dry density. As for Topic 1, continuation of the initially planned test scheme using the now established observation techniques is highly recommended.

Final remark: The steady-state shape of the water content curve in the samples with the smallest gap resembles the narrow highly saturated zone that was the subject of Topic 1. Considering that the zone investigated in Topic 1 has been found in laboratory experiments to persist over long periods, the results from Topic 2 suggest a thought-provoking conjecture: in the test series for Topic 2, a transition zone from highly wetted bentonite to largely unaffected bentonite remains at steady state and represents a residual inhomogeneity. The sharpness of this zone increases with decreasing gap size. At the same time, the location of the transition zone shifts towards the original sample end as the gap size decreases. Extending this series to a gap size of 0 results in the set-up investigated in Topic 1. If the test set-up for Topic 1 can therefore be regarded as a special case of the test series under Topic 2, the narrow highly saturated zone investigated under Topic 1 may be interpreted as incomplete bentonite homogenization. Identifying the cause of incomplete homogenization therefore appears particularly urgent, because this effect should also be considered in numerical models for bentonite re-saturation.

12.3 Topic 3 – Scaling isotherms by bentonite types and clay content

Thirteen complete hysteresis loops, each consisting of adsorption and desorption isotherms, were determined for bentonite samples differing in smectite content and in the composition of mono- and divalent interlayer cations. Based on results from earlier measurement campaigns reported in the literature, a scheme and procedure for sampling data points along these isotherms were established with great care.

Twenty sampling points along each hydration path, using 5 % increments across the range of relative humidity, were found to represent the minimum requirement for resolving the complex shape of sodium bentonite isotherms; fewer points would probably have been sufficient for calcium bentonites. Furthermore, measurements of isotherms should principally begin at the start of the respective hydration path, i.e. under dry conditions for adsorption isotherms and under saturated conditions for desorption isotherms, to avoid inadvertently measuring scanlines instead of isotherms.

A comparison of measured isotherms scaled according to smectite content with theoretically predicted isotherms additionally scaled to the composition of interlayer cations revealed an excellent to reasonable fit in 23 of 26 cases. The remaining three results showed distinctly poor agreement. A reason for these outliers has not yet been identified. Although this casts some doubt on predictions based on scaling, the overwhelming majority of good fits appears to support the method. It therefore appears that isotherms can be predicted with high certainty for any bentonite from mineralogical data, if available, thereby avoiding long and costly direct measurements and providing a basis for rapid modelling. However, whether mineralogical characterization in the laboratory is more economical than direct measurements with modern techniques depends on the specific circumstances.

12.4 Topic 4 – Porosity at full saturation

12.4.1 General comment

The tests addressing porosity at full saturation via vapour (Test I) and via water (Test II) successfully provided evaluable data. Although measurements on individual sample segments were affected by inaccuracies, the medians calculated from all data for each sample yielded meaningful values or trends for the entire test ensemble.

In addition to end porosities, the water uptake dynamics were also investigated. Quite unexpectedly, very long times were required to reach full saturation. In Test I, full saturation was reached after approximately 498 days, whereas in Test II it was reached after 377 days. However, since Test I ran for 1231 days and Test II for 1232 days, it can nevertheless be concluded with confidence that all samples were fully saturated at the end of the tests. The results for the uptake dynamics provided considerable added value to Topic 4.

12.4.2 End porosity

The results of the uptake tests with water in Test II met the expectations for the fully saturated state derived from a late post-test analysis in /KRÖ 18/. The determined end porosities were in the range of 1 % to 2 %, whereas the present results yielded 1 % to 3 %.

Surprisingly, this observation applies to all 8 samples, indicating that the determined end porosity is independent of both bentonite type and dry density.

By contrast, this does not apply to the test results for uptake from vapour (Test II). MX-80 takes up markedly more water from vapour than Calcigel. Comparable end states show a difference of 10 % in terms of water content. For MX-80, the end water content in Test I exceeded the end water content in Test II at dry densities above 1.4 g/cm³, thereby exceeding the theoretical maximum degree of saturation and resulting in negative porosity values. These physically unreasonable results appear to be avoidable only by assuming a higher density for hydrated water than for free water. Further tests clarifying this issue conclusively are therefore highly recommended.

12.4.3 Water uptake dynamics

The evolution of sample weight (Test I) and water loss from the burettes (Test II) during the tests clearly indicates two phases in the water uptake dynamics. The first phase is characterized by an exponential decrease in uptake rates, consistent with a diffusion-like water uptake process. The second phase begins after approximately 81 days in Test I and after 52 days in Test II and is characterized by a disproportionate and much slower decrease in uptake rate. This finding is qualitatively confirmed by /KAR 86/, where uptake dynamics from vapour were investigated in a similar, although not directly comparable, manner.

Since the second uptake phase cannot be predicted from the evolution of the much better understood first phase, it must be assumed that, at the end of the first phase, either a different process becomes relevant, a process changes its dynamics, or a process ceases, thereby revealing the effect of a previously unnoticed secondary process at the microscale.

It may be hypothesized that this previously unconsidered phenomenon is responsible for an increase in the density of hydrated water. If this is the case, it has a noticeable impact on the safety function of the bentonite buffer because it may allow more water to be buffered than currently expected. In any case, the unexpectedly long times required to reach full saturation must be reproducible by numerical models. A closer inspection of hydration

processes at the microscopic level at high degrees of saturation and a corresponding representation in numerical models therefore appear strongly advisable.

12.4.4 Swelling of single bentonite pellets

Following a discussion at a meeting of the Task Force EBS, the swelling of single bentonite pellets in a vapour-saturated atmosphere was investigated. Three pellets were placed above water in a desiccator for almost two years and were measured with respect to shape by 3D scanning and with respect to weight. Although the pellets appeared unchanged to the naked eye, the water content approximately doubled to 24 % over the testing period. The scanned surface data acquired before and after the experiment were aligned and overlaid with a transparent representation of the swollen pellet, demonstrating pellet swelling of 1 to 2 mm over the entire pellet.

12.5 Topic 5 – Initial flow dynamics at the bentonite-rock contact

To date, the interplay between a freshly installed bentonite buffer and groundwater from fractures has largely been subject to speculation, because direct observation of fracture flow is not possible due to the opaque nature of crystalline rock. Even in the joint Task 8 of the Task Forces GWFTS and EBS, fracture flow could only be described by numerical models based on parallel plates.

To substantiate the speculations presented in /KRÖ 17/, a new technique based on realistic transparent fracture replicas (see section 2.2) was developed and applied. In addition, seven accompanying tests were performed to safeguard and further explore different aspects of the developed method using physical 3D-printed fracture models.

12.5.1 Accompanying tests

Long-term water uptake of the printing material

Water uptake by, and water loss from, a printed cube of clear resin due to ambient conditions were approximately exponential. In terms of water content relative to the initial cube mass, uptake converged towards a maximum value between 3.1 % and 3.55 %, whereas water loss converged towards a minimum value of less than -1 %. Steady state was

reached only after more than 2 years in the tests. The scatter of the obtained uptake curves cannot be explained satisfactorily by the post-printing conditions during washing and curing. Special post-printing conditions for minimizing water uptake can therefore only be inferred approximately.

Accuracy of printed planar surfaces

A test body was printed with three planar surfaces oriented at angles of 30°, 45°, and 65° relative to the printing platform. Since the 3D-body was manufactured in layers of constant thickness, the inclined surfaces are not smooth but are approximated by steps at their edges. Subsequent scanning with a higher spatial resolution than the step size revealed certain inaccuracies in the theoretically expected steps. However, these inaccuracies were smaller than the step size of 25 µm itself, thereby confirming the accuracy claimed by the printer manufacturer.

Deformation of printed bodys due to water uptake

The same test body was subsequently used for an additional water uptake test to investigate potential deformation. It was fully submerged in water for 24 hours and, after removal from the water, scanned again by 3D-scanning. The resulting datasets acquired before and after wetting were compared, and the geometric differences were visualized.

The comparison revealed systematic deformations of up to approximately 300 µm. The results suggest that water uptake primarily causes global expansion. Secondary amplification may be caused by residual internal stresses originating from the printing process in geometrically exposed regions such as edges and corners. It should be noted, however, that the geometry of the test body differed substantially from that of the printed fracture halves. Due to the more plate-like geometry of the fracture halves, substantially less non-uniform deformation is expected for this type of printed object.

Post-processing induced deformation of printed fracture replicas

The SLA-printing method used by the printer in the present project requires several post-processing steps, including washing, curing, machining (milling and grinding), and polishing. Although water uptake by a fracture replica is not a post-processing step, its potential influence was also investigated. A possible effect on the replicated fracture geometry was

systematically investigated and quantified by 3D-scanning before and after each individual processing step. This approach enabled deformation to be visualized and the workflow to be optimized to minimize geometrical alterations.

Since scanning prior to washing is not feasible due to residual resin remaining on the fracture surface, the first comparison was performed between the original digital dataset and a 3D scan of the printed fracture replica after washing, thus including both printing and washing. Deviations were predominantly found in the edge regions of the replica, indicating insufficient support structures. Dimensional accuracy could therefore be improved by increasing the number of support structures, particularly in the edge regions.

Curing was found to cause deformations of up to approximately 100 µm. UV exposure at elevated temperatures apparently induces additional crosslinking and redistribution of internal stresses within the polymer. Since the curing chamber supplied with the printer applies UV light predominantly from above, uneven exposure cannot be avoided completely despite an integrated turntable and an intricate mirror system. Based on the observation that shorter curing times and lower curing temperatures reduced geometric deviation, the curing parameters were optimized accordingly.

Subsequent mechanical processing steps include milling, grinding, and polishing, which introduce local temperature increases and direct mechanical effects. However, apart from awareness of these adverse effects and careful execution of this work, no specific remedy can be recommended.

Water uptake by the printing material had previously been investigated for printed objects with compact geometries, but not specifically for fracture replicas. Therefore, an additional test was performed in which a replica was submerged in water for 24 h. This exposure resulted in an overall expansion of 200 to 300 microns, which unfortunately obscured the expected small-scale deformations. Since water uptake cannot be avoided, water contact with the replica should be minimized, and possible deformations should be assessed by 3D-scanning before and after a hydraulic test.

Repeatability of a wetting test

Hydraulic tests in printed physical models must be repeatable to yield meaningful results. The method was therefore tested by injecting a coloured solution into an initially dry

fracture replica and repeating this test three times under identical conditions. Evaluation of the photographs acquired during the tests, followed by overlaying the resulting binary images, demonstrated satisfactory repeatability of the wetting pattern, particularly with regard to repeated air entrapment at several locations. It should be noted that the same type of test was also highly successful for tracer transport in water-filled fractures

Wetting patterns depending on flow direction

To investigate the dependence of wetting patterns on the flow direction through a fracture, two flow tests were performed on a single fracture replica. In both tests, tracer fluid was injected pointwise at a constant flow rate of 0.5 ml/h, while the injection point was shifted to the opposite side of the fracture after the first test. Despite identical injection rates and observation times, the resulting wetting patterns differed noticeably between the two flow directions, indicating a clear influence of flow direction on the spatial development of resaturation within the fracture.

Repeatability of a percolation test on a DFN

A further step towards assessing repeatability was taken by acquiring the geometry data of a micro-DFN that had been constructed and printed at Tohoku University, Japan, prior to the present project. Based on these data, a new replica was printed in Germany, and the percolation tests that had been the objective of the work in Japan were repeated. Despite differences in printing material, support material, and related processing parameters, the newly measured permeabilities were within the same range as those reported previously. The method of 3D-printed physical models therefore appears to be robust also for a micro-DFN, provided that the same digital model is used.

Combining optical 3D-scans with CT images

At the University of Jyväskylä, Finland, fracture surfaces have been measured using X-ray computed tomography (CT). This technique offers the advantages of identifying relevant fractures and enabling non-destructive data acquisition from undisturbed samples. Since the 3D-scanning method used by GRS provides surface data with higher spatial resolution than CT, complementary 3D scans were produced to combine the advantages of both methods. The results demonstrate that CT data and 3D-scanning data can be effectively combined to generate a comprehensive dataset. Application of this

methodology is expected to be particularly beneficial for future investigations of fracture intersections.

12.5.2 Main tests

In the main tests, the situation of a completely dried-out fracture in contact with air-dry bentonite was reproduced. The fracture was represented by a rectangular replica, with a water injection point located at one short side and compacted bentonite at the opposite side. The fracture replica was then filled with water at different inflow rates while the resulting water movement was recorded.

The results indicate that the interplay of flow dynamics and capillary effects controls the shape and stability of the fluid front. The configuration of the variable aperture field leads to the formation of water fingers that advance ahead of the main water body. These fingers do not necessarily move straight forward but follow an apparently irregular flow pattern. Since they may turn by 90° or even 180°, they also cause air entrapment. The effective permeability in the fringe region of the fracture around the buffer should therefore be lower than in a fully water-saturated fracture.

After the bentonite had been reached, repeated disruptions of water fingers were observed at low inflow rates, lasting from a few minutes up to 10 hours, depending on the inflow rate. The number of these disruptions decreased with increasing inflow rate. Disruption of water fingers due to suction was not limited to the immediate vicinity of the bentonite-water contact but was also observed relatively close to the inflow point. In addition to inflow rate and bentonite dry density, the configuration of the aperture field therefore also influences the location at which disruptions of the water fingers may occur.

The disruption of water flow delays bentonite re-saturation. Directly, this delay is caused by temporarily impeded inflow into the bentonite. Indirectly, it may also cause partial drying of the bentonite, thereby increasing suction and promoting repeated disruption of flow. However, the latter may represent a secondary effect.

The parameters identified as influencing buffer re-saturation dynamics could not be investigated to the originally intended depth. More comprehensive testing, particularly with

systematic variation of inflow rate, bentonite density, and fracture surfaces, is therefore recommended to identify the conditions that lead to delayed buffer re-saturation.

Furthermore, both the delay caused by flow disruption and the reduction in effective permeability caused by air entrapment need to be quantified for assessment purposes. If these effects prove to be significant, numerical codes for simulating bentonite re-saturation may require adaptation to allow realistic predictions of water uptake.

In general, these codes currently represent fractures as parallel plates. It would therefore be informative to compare bentonite water-uptake dynamics from a parallel-plate model with those from a corresponding physical fracture model in laboratory experiments.

12.6 Topic 6 – Stability of bentonite properties against long-term heating

The Prototype Repository (PR) experiment, conducted by SKB, represents the longest-running full-scale in situ test of its kind and was operated for more than 20 years at the Äspö Hard Rock Laboratory in Sweden. To investigate a potential impact of long-term heating on the water uptake behaviour of the bentonite buffer, samples were collected on-site from locations close to and distant from three of the four heaters in the deposition holes (DHs) of the inner section. Reference material corresponding to these samples, stored by SKB since production, was also obtained. The uptake behaviour was investigated by determining and comparing adsorption and desorption isotherms forming hysteresis loops. The hysteresis loops were determined using a Vapour Sorption Analyzer (VSA).

Samples were obtained from deposition hole 1 ring 5 (DH1 R5), deposition hole 2 ring 3 (DH2 R3), and deposition hole 4 ring 7 (DH4 R7). The temperature evolution in these rings differed considerably. Heating of the canisters in DH1 and DH2 was compromised by technical difficulties, which led to reduced heater power and ultimately to complete shutdown of heater 1 after 6665 days and immediate shutdown of heater 2 already after day 1200. Only heater 4 remained in operation until dismantling of the PR began on day 7778, although not at full power.

Humidity evolution had not been monitored directly beyond the early stages of the PR experiment, because the sensors had failed completely after slightly more than three

years. Where the post-mortem investigations indicated more or less full saturation of the bentonite rings, the wetting history appears to be relatively clear, as the sensors from DH1 R5 indicated an increase to very high relative humidities within one year. Similar dynamics can be assumed for DH4 R7. By contrast, DH2 R3 had essentially not taken up water during the 20-year runtime of the PR. DH2 was sufficiently dry that pellets from the gap fillings could still be retrieved individually. It can therefore be assumed that the wetting state remained stable at the initial water content throughout the entire test period.

A measurable difference between the hysteresis loops of the in-situ material from locations close to the heater and those of the reference material was identified for the samples from DH1 R5. This difference was even more pronounced for the sample from DH4 R7. Analysis of the heating history indicates that this may have been caused by the higher temperature at the canister surface in DH4. However, the total amount of heat energy transferred into the bentonite may also be decisive for this effect. Which of these alternatives is better supported by the data might have been resolved by comparing the hysteresis loops for DH2 R3, which had experienced the highest temperature of the three investigated DHs, although only for a short time. However, this comparison was compromised by a disturbance during the VSA test for determining the hysteresis loop of the in-situ material.

Continuation of the measurements on samples from DH2 R3 is therefore recommended to obtain results that can clarify the conditions relevant for the observed shift of the isotherms. Additional tests with bentonite samples from the buffer-rock contact should also be performed to investigate the impact of long-term intermediate heating on the isotherm shift.

Finally, it should be noted that the hysteresis loops presented here were measured at room temperature, i.e. 25 °C. This clearly differs from the temperature conditions during operation of the PR experiment. Repetition of the tests at elevated temperature may therefore provide additional insight, as the VSA allows testing at temperatures up to 60 °C.

12.7 Topic 7 – Extending the functionality of code COMSOL-VIPER

The thermo-hydraulically coupled code COMSOL-VIPER, which is based on the balance equations of the experimental VIPER code by GRS, has been advanced to simulate water uptake by compacted bentonite at a limited water supply rate (LWSR). LWSR-conditions

are particularly relevant for low-permeability host rocks considered for DGRs, because a primary function of the rock is to prevent water from reaching the waste canisters. However, most hydraulic laboratory experiments forming the basis for established modelling approaches have addressed water uptake under conditions of unimpeded access of the bentonite to water (UA).

Experimental investigations at GRS have shown that the hydration behaviour of bentonite differs significantly under these two conditions. In the conceptual framework of the COMSOL-VIPER code, LWSR-conditions are initially represented by Neumann boundary conditions, reflecting that the small amount of water supplied by the rock is readily taken up by the bentonite. Water therefore accumulates at the bentonite-water contact. Once full saturation is reached, water uptake is controlled by the uptake capacity of the bentonite, which corresponds to UA-conditions and requires Dirichlet boundary conditions.

The treatment of such a boundary requires numerical monitoring of the water content at the bentonite-water contact. Reaching full saturation then triggers a switch from Neumann to Dirichlet conditions in the code. In addition, the option of a Neumann boundary condition had to be implemented because it had not been included in the earlier version of the COMSOL-VIPER code. After completion of the implementation, the code was successfully tested against an uptake experiment from the GRS laboratory under LWSR-conditions, which was later adopted as a reference case in Task 14b of the Task Force EBS.

References

/AHU 21/ Ahusborde, E. et al. (2021): State Of the Art Report in the fields of nu-merical analysis and scientific computing. Final version as of 16/02/2020 of deliverable D4.1 of the HORIZON 2020 project EURAD. EC Grant agreement no: 847593.

/ÅKE 22/ Åkesson, M.: Prototype Repository Estimation of the buffer homogenisation. Report P-22-21, Svensk Kärnbränslehantering AB (SKB), Solna, 2022.

/AND 02/ Andersson, P., Byegård, J., Winberg, A.: Final report of the TRUE Block Scale project - 2. Tracer tests in the block scale. Technical Report TR-02-14, Swedish Nuclear Fuel and Waste Management Company (SKB), 2002.

/ASA 25/ Asaad, A., Nitsch, A., Baille, W., Emmerich, K.: Mineralogical and geotechnical characterization of two German bentonites from Westerwald and Bavaria. Applied Clay Science, Volume 276, 2025. https://doi.org/10.1016/j.clay.2025.107901

/BEA 88/ Bear J: Dynamics of fluids in porous media. Dover books on physics and chemistry, Dover, New York, 1988.

/BIS 19/ Bishop, J.L.: Visible and near-infrared reflectance spectroscopy of geologic materials. Chapter 4, pp. 68-101, in: Remote Compositional Analysis: Techniques for Understanding Spectroscopy, Mineralogy, and Geochemistry of Planetary Surfaces (J.L. Bishop, J.F. Bell III & J.E. Moersch, editors), Cambridge University Press, Cambridge, UK, 2019.

/BWT 26/ B&W TEK: Company pages. https://bwtek.com, as of 2026.

/COM 26/ Comsol Multiphysics GmbH: Product pages. https://www.comsol.de/products, as of January 2026.

/DER 03/ Dershowitz, W., Winberg, A., Hermanson, J., Byegård, J., Tullborg, E.-L., Andersson, P., Mazurek, M.: Äspö Task Force on modelling of groundwater flow and transport solutes; Task 6c - A semi-sythetic model of block scale conductive structures at the Äspö HRL. International Progress Report IPR-03-13, Swedish Nuclear Fuel and Waste Management Company (SKB), 2003.

/DER 06/ Dershowitz, W., Fox, A., Lee, G., van Fossen, M., Uchida, M.: Äspö Task Force on modelling of groundwater flow and transport solutes; Discrete fracture network flow and transport modelling at the rock block scale: Task 6D, 6E, 6F and 6F2. International Progress Report IPR-06-22, Swedish Nuclear Fuel and Waste Management Company (SKB), 2006.

/DES 17/ Dessirier, B., Åkesson., M., Lanyon, B., Frampton, A., Jarsjö, J.: Reconstruction of the water content at an interface between compacted bentonite blocks and fractured crystalline bedrock. Applied Clay Science, Vol. 142, p. 145-152, 2017.

/DUE 04/ Dueck, A.: Hydro-mechanical properties of a water unsaturated sodium bentonite - Laboratory study and theoretical interpretation. Doctoral thesis, Department of Building and Environmental Technology, Lund University, Division of Soil Mechanics and Foundation Engineering, 2004.

/ERI 25/ Eriksson, P. (SKB): personal communication, 2025.

/FEI 04/ Fein, E.: Software package r³t, Model for transport and retention in porous media. Gesellschaft für Anlagen- und Reaktorsicherheit (GRS) gGmbH, Bd. 192, GRS-192, 319 S., ISBN 3-931995-60-7, GRS: Köln, Garching b. München, Berlin, Braunschweig, 2004.

/FEI 99/ Fein, E. & Schneider, A.: d³f - ein Programmpaket zur Modellierung von Dichteströmungen, Abschlußbericht. Gesellschaft für Anlagen- und Reaktorsicherheit (GRS) gGmbH, Bd. 139, GRS-139, 261 S., ISBN 3-923875-97-5, GRS: Köln, Garching b. München, Berlin, Braunschweig, 1999.

/FRA 17/ Fransson, Å., Åkesson, M., Andersson, L.: Bentonite Rock Interaction Experiment. Characterisation of rock and installation, hydration and dismantling of bentonite parcels. Report SKB R-14-11, Svensk Kärnbränslehantering AB (SKB), Solna, 2017.

/FRO 12/ Frolkovič P.: Application of level set method for groundwater flow with moving boundary. Advances in Water Resources 47:56–66, 2012.

/FOR 24/ Formlabs : Company pages. https://formlabs.com/, as of May 2024.

/GAI 05/ Gailhanou, H.: Détermination expérimentale des propriétés thermodynamiques et étude des nanostructures de minéraux argileux. PhD Thesis, University Aix-Marseille III, 2005.

/GEN 19/ Gens, A.: Task Force on Engineered Barrier System (EBS), Task 1 Laboratory tests. Technical Report TR-14-24, Svensk Kärnbränslehantering AB (SKB), Solna, 2019.

/GOU 09/ Goudarzi, R., Johannesson, L.-E.: Äspö Hard Rock Laboratory. Prototype Repository – Sensors Data Report (Period 010917-060601); Report No: 15. SKB report IPR-06-26, Svensk Kärnbränslehantering AB (SKB), Stockholm, 2006.

/GOU 09/ Goudarzi, R., Johannesson, L.-E.: Äspö Hard Rock Laboratory. Prototype Repository – Sensor data report; Period 010917-090601; Report No 21. SKB report IPR-09-17, Svensk Kärnbränslehantering AB (SKB), Stockholm, 2009.

/GOU 23/ Goudarzi, R.: Prototype Repository – Sensor data report; Period 2001-09-17 to 2023-01-01; Report No 34. SKB report P-23-12, Svensk Kärnbränslehantering AB (SKB), Solna, 2023.

/GRE 06/ Grenier, C., Bernard-Michel, G.: Äspö Task Force on modelling of groundwater flow and transport of solutes; Modelling of Task 6D, 6E, 6F and 6F2, using Cast3M code. International Progress Report IPR-06-18, Swedish Nuclear Fuel and Waste Management Company (SKB), 2006.

/GUE 23/ Guevara M., Graf T.: A benchmark for variably saturated variable-density variable-viscosity flow and solute transport in porous media. Hydrogeology Journal 31(7):1903–1919, 2023.

/HAR 15/ Harjupatana T, Alaraudanjoki J, Kataja M.: X-ray tomographic method for measuring three-dimensional deformation and water content distribution in swelling clays. Appl Clay Sci.; 114: 386–394, 2015.

/HEX 26/ Hexagon AB: Company pages. https://hexagon.com/, as of January 2026.

/HUB 16/ Huber, F., Noseck, U., Schäfer, Th.: Stability of compacted bentonite for radionuclide retardation – Experiments and modelling (Project KOLLORADO-e; Final Report). Karlsruhe Institute of Technology, KIT_open-publishing, 2016.

/IBA 95/ Ibaraki, M., Sudicky, E.A. (1995): Colloid-facilitated contaminant transport in discretely fractured porous media: 2. Fracture network examples. Water Resour. Res. 31/12, 2961-2969.

/JAN 19/ Jankovský F., Zuna, M., Havlová, V., Kotowski, J., (2019): Contaminant migration experiments in an artificial block-scale granite fracture, in: Book Abstract. Goldschmidt 2019 conference. August 16 – 22. 2019, Barcelona, Spain.

/JAN 23/ Jankovsky, F., Zuma, M., Pospiech, S., Brendler, V., Noseck, U., Schneider, A., Becker, D.-A: Characterization and quantification of uncertainties in RN migration in crystalline formations. EURAD Deliverable

/PWI 26/ InnovMetric Software Inc.: PolyWorks Inspector. https://www.polyworks.com/en-us/products/polyworks-inspector, as of April 2026.

/PWM 26/ InnovMetric Software Inc.: PolyWorks Modeler. Company pages, https://www.polyworks.com/en-us/products/polyworks-modeler, as of March 2026.

/KAH 86/ Kahr, G., Kraehenbuehl, F., Müller-Vonmoos, M., Stoeckli, H. F.: Wasseraufnahme und Wasserbewegung in hochverdichtetem Bentonit. Technical Report NTB 86-14, National Cooperative for the Disposal of Radioactive Waste (Nagra), Wettingen 1986.

/KAU 08/ Kaufhold S., Dohrmann R.: Detachment of colloidal particles from bentonites in water. Applied Clay Science 39, 50–59, 2008.

/KAU 12/ Kaufhold S., M. Hein M., Dohrmann R. Ufer K.: Quantification of the mineralogical composition of clays using FTIR spectroscopy. Vibrational Spectroscopy 59, 29–39, (2012).

/KAU 13/ Kaufhold S., Plötze M., Klinkenberg M., Dohrmann R.: Density and porosity of bentonites. Journal of Porous Materials, 20:191–208, 2013.

/KOB 21/ Kober, F., García-Siñeriz, J.L., Villar, M.V., Lanyon, G.W., Cloet, V., Mäder, U., Wersin, P., Leupin, O., Sellin, P., Gens, A., Schneeberger, R.: FEBEX-DP Synthesis Summary of the Full-Scale Engineered Barriers Experiment – Dismantling Project. Technical Report 17-01, National Cooperative for the Disposal of Radioactive Waste (Nagra), Wettingen, Switzerland, 2021.

/KRO 20/ Kronberg, M., Johannesson, L.-E., Eriksson, P.: Strategy, adaptive design and quality control of bentonite materials for a KBS-3 repository. Report TR-20-03, Svensk Kärnbränslehantering AB (SKB), Solna, May 2020

/KRÖ 03a/ Kröhn, K.-P.: New conceptual models for the resaturation of bentonite. Proceedings of the Workshop on “Clay Microstructure and its Importance to Soil Behaviour” held in Lund, 2002, Applied Clay Science, Vol. 23, 2003.

/KRÖ 03b/ Kröhn, K.-P.: Investigation of uncertainties in the re-saturation model of bentonite as near-field buffer in a spent fuel repository in granite. Proceedings of the GRS/IRSN conference EUROSAFE, seminar 3, Paris, 2003.

/KRÖ 04a/ Kröhn, K.-P.: Modelling the re-saturation of bentonite in final repositories in crystalline rock. Abschlussbericht des BMWA-Vorhabens 02 E 9430, GRS-Bericht GRS-199, 2004.

/KRÖ 04b/ Kröhn, K.-P.: Proposal of an alternative re-saturation model for bentonite buffers - the conceptual model, the numerical model and the data base. In: Proceedings of the “Meeting on buffer & backfill modelling” held in Lund. SKB International report IPR-04-23, Stockholm, 2004.

/KRÖ 04c/ Kröhn, K.-P.: Results and interpretation of bentonite resaturation experiments with liquid water and water vapour. in: Schanz, T. (ed.): Unsaturated Soils: Experimental Studies. Proceedings of the International Conference “From Experimental Evidence towards Numerical Modelling of Unsaturated Soils”, Weimar, 2003, Springer, 2004.

/KRÖ 06/ Kröhn, K.-P.: About the role of vapour transport during bentonite resaturation. FKZ 02 E 9954 (BMWi), GRS-Report GRS-222, GRS, Köln, 2006.

/KRÖ 11/ Kröhn K.-P.: Code VIPER - Theory and Current Status. Status report, FKZ 02 E 10548 (BMWi), Gesellschaft für Anlagen- und Reaktorsicherheit (GRS) mbH, GRS-269, Köln, 2011.

/KRO 16a/ Kröhn, K.-P.: Hydraulic Interaction of Engineered and Natural Barriers – Task 8b-8d,8f of SKB. Summary report, FKZ 02 E 11213 and 02 E 11102 (BMWi), Gesellschaft für Anlagen- und Reaktorsicherheit (GRS) mbH, Köln, 2016.

/KRO 16b/ Kröhn, K.-P.: Hydraulic Interaction of Engineered and Natural Barriers – Task 8e of SKB. Summary report, FKZ 02 E 11213 and 02 E 11102 (BMWi), Gesellschaft für Anlagen- und Reaktorsicherheit (GRS) mbH, Köln, 2016.

/KRÖ 17/ Kröhn, K.-P.: Hydraulic Interaction of Engineered and Natural Barriers – Task 8b-8d,8f of SKB. Summary report, FKZ 02 E 10336, 02 E 10548, 02 E 10558, 02 E 11102, and 02 E 11213 (BMWi), Gesellschaft für Anlagen- und Reaktorsicherheit (GRS) mbH, GRS-430, Köln, 2017.

/KRÖ 18/ Kröhn, K.-P.: Re-saturation of compacted bentonite under repository-relevant flow conditions. FKZ 02 E 11102 (BMWi). Geomechanics for Energy and the Environment, Elsevier, 2018. DOI:10.1016/j.gete.2018.09.003

/KRÖ 19/ Kröhn, K.-P.: Bentonite Re-saturation – limited Access to Water and high Temperature Gradients. FZK 02E10548 and 02E11102 (BMWi), Report GRS-503, Gesellschaft für Anlagen- und Reaktorsicherheit (GRS) mbH, Braunschweig, 2019.

/KRÖ 20a/ Kröhn, M., Fromme, L.: An alternative equation-based model in COMSOL Multiphysics® for bentonite re-saturation. Proceedings of the COMSOL Conference 2020, 2020. doi:10.57720/4664

/KRÖ 20b/ Kröhn, K.-P. and Kröhn, M.: Project BIGBEN – constitutive equations for sodium and calcium bentonite. FKZ 02 E 11284 (BMWi), Report GRS-615, Gesellschaft für Anlagen- und Reaktorsicherheit (GRS) mbH, Braunschweig, 2020.

/KRÖ 20c/ Kröhn, K.-P. and Kröhn, M.: Producing fractures with a 3D-printer for flow experiments – The price to pay for the easy way out. Poster at the session HS8.2.3/ HS8.2 at the virtual conference EGU 2020, 2020.

/KRÖ 22/ Kröhn, M. and Kröhn, K.-P.: Pellet-scale investigations. In: Bernachy-Barbe, F., Bosch, J.A., Campos, G., Carbonell, B., Daniels, K.A., Ferrari, A., Graham, C.C., Guillot, W., Gutiérrez-Álvarez, C., Harrington, J.F., Iglesias, R.J., Kataja, M., Kröhn, K.-P., Kröhn, M., Mašín, D., Najser, J., Pingel, J.L., Real, E., Schäfer, T., Svoboda, J., Sun, H., Tanttu, J., Villar, M.V., Wieczorek, K.: Experimental work on bentonite evolution in the frame of BEACON – final report of WP4. European Commision, 2022. https://www.beacon-h2020.eu/wp-content/uploads/2022/04/D4.3_Experimental-work-on-bentonite-evolution-in-the-frame-of-BEACON.pdf

/KRÖ 25/ Kröhn, M.: Robust Implementation of Neumann Boundary Conditions in COMSOL-VIPER for Realistic Bentonite Hydration at Limited Water Supply. Proceedings of the COMSOL Conference 2025, Florence, 2025.

/LAN 15/ Lanyon, B.: Task 8: Analysis of BRIE “Bentographs”. Presentation at Workshop #33 of the Task Force on Groundwater and Transport of Solutes, Kalmar, 2015.

/LAS 26/ Laser 2000 GmbH: Product pages. https://www.laser2000.com/de/, as of January 2026.

/LÜH 98/ Lührmann, L., Noseck, U., Tix, Ch. (1998): Model of contaminant transport in porous media in the presence of colloids applied to actinide migration in column experiments. Water Resour. Res. 34/3, 421-426.

/MAT 26/ The MathWorks, Inc.: Product pages. https://de.mathworks.com/, as of January 2026.

/MEI 02/ Meijering, E.: *FeatureJ: An ImageJ plugin suite for image feature extraction*. https://imagescience.org/meijering/software/featurej/; 2002–2026.

/MET 23/ METER Group Inc., German branch: Web pages of the producer, last visited: January 2023. https://metergroup.de/food/produkte/vsa/

/MOO 52/ Mooney, R. W., A., G. Keenan und L. A. Wood: Adsorption of Water Vapour by Montmorillonite; I: Heat of Desorption and Application of BET Theory. Journal of the American Chemical Society, Nol. 74, No. 6, 1952.

/MÜL 24/ Müller, C., Flügge, J., Burlaka, V., Hassanzadegan, A., Johnen, M., Leonhard, J., Meleshyn, A., Richter, L., Wang, X., Wunderlich, A., Zhao, H.: Safety Analytical Investigations on Repository Systems in Crystalline Rocks (SUSE), Final report, FKZ 02E11577A and 02E11577B (BMUV), BGE Technology GmbH, 2024.

/NIK 24/ Nikkilä, K., Geologian tutkimuskeskus (GTK, Geological Survey of Finland): personal communication, 2024.

/NOS 12/ Noseck, U., Becker, D., Brasser, T., Flügge, J., Fahrenholz, Ch., Herbert, H., Ionescu, A., Kröhn, K.-P., Kull, H., Meleshyn, A., Mönig, J., Röhlig, K., Rübel, A., Rothfuchs, T.; Wolf, J.: Scientific basis for a safety case of deep geological repositories. Final report, FKZ-02 E 10548 (BMWi), Gesellschaft für Anlagen- und Reaktorsicherheit (GRS) mbH, GRS-298, 2012.

/NOS 16/ Noseck, U., Flügge, J., Reimus, P., Cvetkovic, V., Lanyon, G.W., Schäfer, Th., Böechschmict. I. (2016): Grimsel Test Site Investigation Phase VI. Colloid Formation and Migration Project: Modelling of tracer, colloid and radionuclide transport for dipole CFM 06.002 – Pinkel surface packer. NAGRA Technical Report ntb 16-06.

/NOS 18/ Noseck, U., Becker, D., Brasser, T., Buhmann, D., Fahrenholz, C., Flügge, J., Kröhn, K.-P., Meleshyn, A., Mönig, J., Moog, H., Rübel, A., Spießl, S., Wolf, J.: Scientific Basis for a Safety Case of Deep Geological Repositories. Final Report, FKZ 02E11102 (BMWi), GRS-501, GRS Braunschweig, 2018.

/NOS 20/ Noseck, U. & Schäfer, Th. (eds.): Integrity of the bentonite barrier for the retention of radionuclides in crystalline host rocks - experiments and modeling (Project KOLLORADO-e2; Final Report). KIT Scientific working papers 140, 2020, ISSN: 2194-1629.

/OLS 09/ Olsson, M., Markström, I., Pettersson, A., Sträng, M.: Examination of the Excavation Damaged Zone in the TASS tunnel, Äspö HRL. Report R-09-39, Svensk Kärnbränslehantering AB (SKB), Stockholm, 2009.

/PIN 13/ Pintado, X., Adesola, F., Turtiainen, M.: Downscaled Tests on Buffer Behaviour. Working Report 2012-100, B+Tech Oy, Helsinki, 2013.

/PIV 26/ PIV open source software. Internet pages: https://www.pivlab.de/, as of February 2026.

/REI 14/ Reiche, T., Noseck, U., Wolf, J.: Modellierung des Schadstofftransports in geklüftet-porösen Medien unter Berücksichtigung von Kolloiden mit den Transportprogrammen FRAME und COFRAME. Gesellschaft für Anlagen- und Reaktorsicherheit (GRS) gGmbH, GRS-333, Mai 2014. ISBN 978-3-944161-13-6.

/REI 15/ Reiche, T., Noseck, U., Schäfer, T.: Migration of Contaminants in Fractured-Porous Media in the Presence of Colloids: Effects of Kinetic Interactions, Transport in Porous Media, 111(1), 143–170, 2015.

/REI 20/ Reiter. S., Logashenko, D., Vogel, A., Wittum, G.: Mesh generation for thin layered domains and its application to parallel multigrid simulation of groundwater flow. Computing and Visualization in Science 23, 2, 2020, DOI: 10.1007/s00791-020-00322-5

/REI 22/ Reiter, S. B.: ProMesh. Erreichbar unter www.promesh3d.com, 2022, accessed at 17. Januar 2024.

/RIS 26/ RISE Research Institutes of Sweden AB (RISE): home page. https://www.ri.se/en, as of January 2026.

/RÜB 22/ Rübel, A. & Gehrke, A. C.: Modellierung des Radionuklidtransports im Tongestein, Aktualisierung der Sicherheits- und Nachweismethodik für die HAW-Endlagerung im Tongestein in Deutschland. Bd. 668, GRS-668, 161 S., ISBN 978-3-949088-59-9, Gesellschaft für Anlagen- und Reaktorsicher-heit (GRS) gGmbH: Köln, Garching b. München, Berlin, Braunschweig, 2022.

/SAN 25/ Sandén, T., Dueck, A.: Water content and density distribution in buffer and backfill of the inner section of the Prototype Repository. SKB report P-25-03, Svensk Kärnbränslehantering AB (SKB), Solna, 2025.

/SCH 12/ Schindelin, J., Arganda-Carreras, I., Frise, E., et al.: Fiji: an open-source platform for biological-image analysis. Nature Methods, 9(7), 676–682; https://fiji.sc/; 2012.

/SCH 16/ Schneider, A. (ed.): Modelling of Data Uncertainties on Hybrid Computers (H-DuR). Final report, FKZ 02 E 11062A (BMWi), Gesellschaft für Anlagen- und Reaktorsicherheit (GRS) gGmbH, GRS-392, 2016.

/SCH 20/ Schneider, A. (ed.): Groundwater flow and Transport in Complex Real Systems (GRUSS). Final report, FKZ 02 E 11476A-B (BMWi), Gesellschaft für Anlagen- und Reaktorsicherheit (GRS) gGmbH, GRS-566, 2020.

/SCH 23/ Schneider, A. (ed.): Hydrogeological Modelling at a Regional Scale (Hymne). Final report, FKZ 02 E 11809A (BMWi), Gesellschaft für Anlagen- und Reaktorsicherheit (GRS) gGmbH, GRS-750, 2023.

/SCH 27/ Schneider, A. et al: Modelling flow and nuclide transport with d³f++. In: Advances, Challenges, and Perspectives in Geological Disposal of High-Level Radioactive Waste, to be published, 2027.

/SEI 14/ Seiphoori, A., Ferrari, A. and Laloui, L.: Water retention behaviour and microstructural evolution of MX-80. Géotechnique 64, No. 9, 721–734 [http://dx.doi.org/10.1680/geot.14.P.017], 2014.

/SIE 26/ Siemens: Product pages. https://solidedge.siemens.com/en/home-7/, as of April 2026.

/SIN 17/ Sindalovskiy, L.: Aquifer Test Solutions: A Practitioner's Guide with Algorithms Using ANSDIMAT, Springer International Publishing, 2017.

/SKB 22/ SKB International: Invitation to participate in the retrieval of The Full-Scale Prototype Repository at Äspö HRL. Flyer, 2022. Internet: www.skbinternational.se/wp-content/uploads/2022/07/Excavation-of-prototype-repository-Flyer.pdf

/STE 01/ Stephansson, O., (ed.): DECOVALEX II. Special issue of Int. J. Rock. Mechanics and Mining Sciences, Vol. 38, no.1., 2001.

/STI 25/ Stigsson, M., Herbertsson, M., Kröhn, M., Lindvall, E., Spetz, J.: Scanning surface geometries of fracture intercepts in borehole KFM24. SKB report P-25-10, Svensk Kärnbränslehantering AB (SKB), Solna, 2025.

/SUZ 17/ Suzuki, A., Watanabe, N., Li, K., Horne,R. N.: Fracture network created by 3-D printer and its validation using CT images, Water Resour. Res., 53, 6330–6339, 2017. doi:10.1002/2017WR021032

/THE 35/ Theis, C. V. (1935): The relation between the lowering of the Piezometric surface and the rate and duration of discharge of a well using ground-water storage. Eos, Transactions American Geophysical Union, Bd. 16, Nr. 2, S. 519–524, 1935. DOI 10.1029/TR016i002p00519.

/THO 26/ Thorlabs GmbH: Poduct pages. https://www.thorlabs.com/, as of January 2026.

/TIS 26/ The Imaging Source Europe GmbH: Product pages. https://www.theimagingsource.com/de-de/, as of April 2026.

/TSA 87/ Tsang, Y.W. und Tsang, C.-F.: Channel Model of Flow Through Fractured Media. Water Resources Research, Vol. 23, No. 3, pp. 467-479, 1987.

/VID 17/ Vidstrand, P., Stigsson, M., Åkesson, M., Fransson, Å.: SKB Task Forces EBS and GWFTS - Modelling the interaction between engineeredand natural barriers - A compilation of Task 8 descriptions. Report P-16-05, Svensk Kärnbränslehantering AB (SKB), Solna, 2017.

/VYR 23/ Nuclear Waste Management Fund (VYR): Flow Pathways Within Faults and Associated Fracture Systems in Crystalline Bedrock (FLOP), part of the Finnish SAFER2028 research programme. Joint research project of University of Turku, University of Jyväskylä, Åbo Akademi, Geological Survey of Finland (GTK), 2023.

/WAD 04/ Wadsö, L., Svennberg, K., Dueck, A.: An experimentally simple method for measuring sorption isotherms. Drying technology, vol. 22, no10, pp. 2427-2440, Taylor & Francis , 2004.

/WAL-14/ Walther, M.: Variable-Density Flow Processes in Porous Media on Small, Medium and Regional Scales, Dissertation. Fakultät Umweltwissenschaf-ten, Fachrichtung Hydrowissenschaften, Institut für Grundwasserwirtschaft (Hrsg.), TU Dresden: Dresden, 2014.

/WIN 02/ Winberg, A., Andersson, P., Byegård, J., Poteri, A.,Cvetkovic, V., Dershowitz, B., Doe, T., Hermanson, J., Gómez-Hernández, J-J., Hautojärvi, A., Billaux, D.,Tullborg, E-L., Meier, P. and A. Medina: TRUE Block Scale Pro-ject; FinalReport – 4. Synthesis of flow, transport and retention in the block scale. Technical Report TR-02-16, Swedish Nuclear Fuel and Waste Man-agement Company (SKB), 2002.

/WIT 80/ Witherspoon, P. A., Wang, J. S., Iwai, K., and Gale, J. E.: Validity of cubic law for fluid flow in a deformable rock fracture. Waterresourcesresearch, 16:6 (1980): 1016–1024,1980.

Table of figures

Fig. 1.1 From project BRIE - left: sketch of empty borehole; middle: photograph of the retrieved bentonite column (from /FRA 17/; right: relation of greyscale and water content (from /LAN 15/) 4

Fig. 1.2 Sketch of a tunnel with deposition boreholes and a close-up of the re-saturating bentonite-rock contact 5

Fig. 1.3 Illustration of the principle of initial swelling of pellets into a limited free space 6

Fig. 1.4 Pictures from the TRANSU test; from /PIN 13/; left: experimental set-up, top middle: cross-section before wetting; bottom middle: cross-section after the test; right: close-up of bottom middle 7

Fig. 1.5 Water uptake by a cluster of MX-80 pellets in an acrylic glass tube; 1. Row: after 0, 1, 10, and 20 min; 2. Row: after 80 and 320 min and after 24, and 74 h; from /KRÖ 22/ 7

Fig. 1.6 A cluster of MX-80 pellets after long-term wetting in a steel cylinder 8

Fig. 1.7 Partially homogenized volume of a single pellet manually separated from the sample 8

Fig. 1.8 Water uptake by confined bentonite via water vapour 10

Fig. 1.9 Two schematic visualizations of hydraulic buffer-rock interaction 12

Fig. 2.0 Early set-up for an optical measurement of fracture flow 15

Fig. 2.1 Cylindrical bentonite sample confined in a plexiglas tube for testing SWIR-lighting 17

Fig. 2.2 Cylindrical MX-80 sample for testing a hyperspectral camera. 18

Fig. 2.3 Test setup for spectrometer measurements; complete setup (left) and spectrometer probe, sample and moveable stage (right). 19

Fig. 2.4 Workflow for the visual observation of hydraulic processes in fractures ... 23

Fig. 2.5 Visualised data of the 1N1 fracture from the data package for Task 10.2..24

Fig. 2.6 The cutting of slabs from the TASS tunnel at the HRL Äspö; from /OLS 09/ 25

Fig. 2.7 Cleaned rock surface at fracture traces of interest 26

Fig. 2.8 Scanning samples at a warehouse of SKB at Oskarshamn 26

Fig. 2.9 Hexagon SmartScan-HE R12 scanner on a photogrammetry tripod 28

Fig. 2.10 Sample surface with applied reference markers 28

Fig. 2.11 Left: scanning of the slab surface including markers before opening the fracture; right: close-up 29

Fig. 2.12 Confidence plot showing the quality of the obtained data. Green: high confidence, red: low confidence 30

Fig. 2.13 Photograph of two printed fracture surfaces; same scale, different scanners, different resolution of the resulting digital models; left: 40B03 cropout section (GRS); right: 1N1 (RISE) 31

Fig. 2.14 Surface artefact caused by misaligned single scans 32

Fig. 2.15 Realignment of the single scans; before realignment (left), afterwards (right) 32

Fig. 2.16 Surface of the fracture from slab VS0037B03 representing an area of about 40 cm x 13 cm 33

Fig. 2.17 Sample from slab VS0037B03; aperture distribution of the fracture along D1D5; scale in mm 34

Fig. 2.18 Digital model of a test cell including a cropped out fracture; top half in transparent green, bottom half in brown, additional test features in solid green and violet 35

Fig. 2.19 Simple test cell; lower half of digital model (left) and printing model including top plate (right) 36

Fig. 2.20 Completed printing of a fracture half with a Form 3-printer; from /FOR 24/ 37

Fig. 2.21 3D-printed fracture half 37

Fig. 2.22 Differences between digital model and 3D-printed testcell, plotted in mm 38

Fig. 2.23 The assembled test cell from the digital and the printing model in Fig. 2.20 39

Fig. 2.24 Wetting of a dry fracture by constant point-wise inflow; tracer solution in black; otherwise color-coded aperture 40

Fig. 2.25 Cell for tracer tests; from the description of Task 10.3.0.2 of the TF GWFTS 42

Fig. 2.26 Tracer distribution after continuous pointwise tracer injection; red colour: high tracer concentration, blue colour: no tracer 42

Fig. 2.27 Observed movement of a particle through a fracture from slab VS0040B03 43

Fig. 2.28 Overlays of four inflow tests at two different times; pixelwise colour-coding: water in four tests – red, in three tests – orange, in two tests – light green, in one test – light blue, in no test – dark blue 45

Fig. 3.1 Set-up of the pre-test 47

Fig. 3.2 Greyscale values over the sample as a function of time up to 36 s 48

Fig. 3.3 Greyscale values over the sample as a function of time up to 3 h 48

Fig. 3.4 Sketch of stage, spectrometer probe and light source 49

Fig. 3.5 Calcigel samples; left: before compaction of the final layer, right: after squeezing out at the end of the test; layer contacts indicated by arrows 50

Fig. 3.6 Cracks on the surface of a MX-80 sample with a dry density of 1.4 g/cm³ evolving during SWIR measurements 51

Fig. 3.7 Gravimetric and spectrometer data for sample 1 of granular MX-80 with a density of 1.4 g/cm³ 54

Fig. 3.8 Gravimetric, greyscale and spectrometer data for sample 2 of granular MX-80 with a density of 1.4 g/cm³ 55

Fig. 3.9 Gravimetric, greyscale, and spectrometer data for sample 1 of granular MX-80 with a density of 1.6 g/cm³ 56

Fig. 3.10 Gravimetric, greyscale, and spectrometer data for sample 2 of granular MX-80 with a density of 1.6 g/cm³ 56

Fig. 3.11 Gravimetric, greyscale, and spectrometer data for sample 1 of powdery MX-80 with a density of 1.4 g/cm³ 58

Fig. 3.12 Gravimetric, greyscale, and spectrometer data for sample 2 of powdery MX-80 with a density of 1.4 g/cm³ 58

Fig. 3.13 Gravimetric, greyscale, and spectrometer data for sample 1 of powdery MX-80 with a density of 1.6 g/cm³ 59

Fig. 3.14 Gravimetric, greyscale, and spectrometer data for sample 2 of powdery MX-80 with a density of 1.6 g/cm³ 60

Fig. 3.15 Gravimetric, greyscale, and spectrometer data for sample 1 of Calcigel with a density of 1.4 g/cm³ 62

Fig. 3.16 Gravimetric, greyscale, and spectrometer data for sample 2 of Calcigel with a density of 1.4 g/cm³ 62

Fig. 3.17 Gravimetric, greyscale, and spectrometer data for sample 1 of Calcigel with a density of 1.6 g/cm³ 63

Fig. 3.18 Gravimetric, greyscale, and spectrometer data for sample 2 of Calcigel with a density of 1.6 g/cm³ 64

Fig. 3.19 Gravimetric, greyscale, and spectrometer data for sample 1 of Calcigel with a density of 1.8 g/cm³ 64

Fig. 3.20 Gravimetric, greyscale, and spectrometer data for sample 2 of Calcigel with a density of 1.8 g/cm³ 65

Fig. 4.1 Sketch of the test principle (top left), photographic close-up of a flooded test cell at the beginning (bottom left), actual test set-up (right) 73

Fig. 4.2 Swelling of the sample into a gap of 1 cm width, initial conditions (left), after 1 minute (middle) and after 2 hours (right) 75

Fig. 4.3 PC1 scores for MX-80 samples with a target gap of 5 mm (top), 10 mm (middle), and 15 mm (bottom); wet end on the left, dry end on the right . 77

Fig. 4.4 PC1 scores for Calcigel samples with a target gap of 5 mm (top), 10 mm (middle), and 15 mm (bottom); wet end on the left, dry end on the right 78

Fig. 4.5 Evolution of greyscale values along the MX-80 samples; target gap size 5 mm (top), 10 mm (middle), and 15 mm (bottom); gap → left, dry end → right 82

Fig. 4.6 Evolution of greyscale values along the two Calcigel samples; target gap size 5 mm; sample 1 (top), sample 2 (bottom); gap to the left, dry end to the right 83

Fig. 4.7 Evolution of greyscale values along the two Calcigel samples; target gap size 10 mm; sample 1 (top), sample 2 (bottom); gap to the left, dry end to the right 83

Fig. 4.8 Evolution of greyscale values along the two Calcigel samples; target gap size 15 mm; sample 1 (top), sample 2 (bottom); gap to the left, dry end to the right 84

Fig. 4.9 Mean SWIR-data on MX-80 samples; fit by eye 86

Fig. 4.10 Optical end-of-test data on MX-80 samples 86

Fig. 4.11 Overlay of the curves from Fig. 4.9 and vertically mirrored curves from Fig. 4.10 86

Fig. 4.12 Mean SWIR-data on Calcigel samples; fit by eye 87

Fig. 4.13 Optical end-of-test data on Calcigel samples 87

Fig. 4.14 Overlay of the curves from Fig. 4.12 and vertically mirrored curves from Fig. 4.13 87

Fig. 5.1 Photo of the VSA during measurement (left), working principle (right); from /KRÖ 20/ 92

Fig. 5.2. Sections of the isotherms for MX-80 bentonite; a) full range, b) enlargement 93

Fig. 5.3. Comparing sampled isotherms with analytical solutions; left: MX-80, right: Calcigel; from /KRÖ 20b/ 95

Fig. 5.4. Principle sketch of isotherms and scanlines 96

Fig. 5.5. Measured scanlines for MX-80 including the data for isotherms for reference, left: desorption scanlines, right: adsorption scanlines; after /KRÖ 20b/ 96

Fig. 5.6. Data points for the adsorption isotherm from /DUE 04/ and analytical solutions for isotherms and scanlines from /KRÖ 20b/ 97

Fig. 5.7. Smectite content and fractions of mono- and divalent cations in the 13 samples 99

Fig. 5.8. Predicted and measured isotherms for bentonite B31; bounding isotherms for pure Na- and Ca-smectite added for orientation 101

Fig. 6.1 Failed pre-test with a 3D-printed test cell under Test II-conditions; left: broken cap – right: cracked coating..... 103

Fig. 6.2 Failed pre-test with aluminum plates as caps under Test II-conditions; left: open test set-up – right: aluminumchloride evolution at the bottom 104

Fig. 6.3 Test cells for water uptake via vapour in desiccators..... 105

Fig. 6.4 Temperature evolution in the eight desiccators 105

Fig. 6.5 Humidity in the desiccators 1 to 4, 2 and 4 being representative for all others 106

Fig. 6.6 Dynamics of water uptake from vapour by MX-80 and Calcigel for different dry densities 107

Fig. 6.7 Array for water uptake tests via liquid water, two different views 108

Fig. 6.8 Losses of water from the burettes over time..... 108

Fig. 6.9 Uptake rates of the bentonite samples in the desiccators..... 109

Fig. 6.10 Uptake rates in the desiccators; medians for MX-80 and Calcigel; left: semilogarithmic plot over the whole data range, right: linear plot for small values 110

Fig. 6.11 Evolution of the water content during uptake from vapour for MX-80 and Montigel; after /KAH 86/; left: linear scale, right: logarithmic scale. 111

Fig. 6.12 Uptake rates according to the burette readings 112

Fig. 6.13 Uptake rates via liquid water; medians for MX-80 and Calcigel; left: semilogarithmic plot over the whole data range, right: linear plot for small values 112

Fig. 6.14 Water content distributions for Calcigel (1.5 g/cm³); water (red), vapour (blue)..... 113

Fig. 6.15 Water content in all 16 samples over the determined dry density 114

Fig. 6.16 Degree of saturation in all 16 samples over the determined dry density 115

Fig. 6.17 Porosity in all 16 samples over the determined dry density 116

Fig. 6.18 Pellets in a desiccator for testing long-term uptake of vapour..... 120

Fig. 6.19 Swelling of a MX-80 pellet after 2 years exposure to high humidity 121

Fig. 7.1 Array of printed test cubes for different printing materials; from /KRÖ 20b/ 124

Fig. 7.2 Uptake of potassium permanganate by transparent printed cubes; from /KRÖ 20c/ 125

Fig. 7.5 Early water uptake; without blue series (left) including blue sries (right) 128

Fig. 7.6 Uptake of water in all test cubes over time 128

Fig. 7.7 Uptake of water in all test cubes over time, first enlargement 129

Fig. 7.8 Uptake rate in all test cubes over time..... 130

Fig. 7.9 Uptake of water in all test cubes over time, higher resolution 130

Fig. 7.10 Uptake of water in all test cubes over time, second enlargement 131

Fig. 7.11 Printed test body with differently slanted planes (left), close-up (right) . 132

Fig. 7.12 Scan of slanted plane (30°), without scanning grid (left), with grid (right) 132

Fig. 7.13 False-colour comparison, printed test body before and after 24h of exposure to water 134

Fig. 7.14 False colour comparison, printed dataset vs digital data; left: top surface; right: bottom surface..... 135

Fig. 7.15 False colour comparison, replica before vs after curing; left: top surface; right: bottom surface..... 136

Fig. 7.16 False colour comparison, replica before vs after wetting; left: top surface; right: bottom surface..... 137

Fig. 7.17 Repeatability of the wetting from the left of a single fracture including air enclosure; pixel-wise overlay of 3 tests; colour code: tracer detected in all 3 tests (black), in 2 tests (grey), in 1 test (light grey), no tracer (white)..... 139

Fig. 7.18 Repeatability of the wetting of a single fracture from the left including air enclosure; pixel-wise overlay of tests in replicas produced on 2 different printers; colour code: tracer detected in both tests (black), in 1 test (light grey), no tracer (white)..... 140

Fig. 7.19 Wetting patterns depending on the flow direction; top: inflow from the left, bottom: inflow from the right 141

Fig. 7.20 Micro-DFN used in /SUZ 17/ (left), DFN printed from the digital model (right) 142

Fig. 7.21 Permeability test on the 3D-printed DFN 143

Fig. 7.22 Total permeability of two 3D-printed micro-DFNs using different solutions for dissolving support material 144

Fig. 7.23 3D-data on a fracture 04B by different techniques, CT by University of Jyväskyla (top), 3D-scan by GRS (middle), overlay (bottom) 146

Fig. 7.24 Fracture apertures from 3D-scans 147

Fig. 7.25 Principle of the tests under Topic 5 148

Fig. 7.26 CAD construction of the reinforcement frame for the Topic 5 experiments 148

Fig. 7.27 Photos of the reinforced test cell for the Topic 5 experiments; frame and lower half of the replica (left), frame and complete replica (middle), and fully assembled reinforced test cell (right) 149

Fig. 7.28 Wetting test with potassium permanganate solution at an inflow rate of 0.5 ml/h applied to the top; images after 2.15 h (left) and after 4.1 h (right) 151

Fig. 7.29 Breaking off of water fingers after contact with bentonite; water in bright grey, air in structured dark grey; inflow from the top, bentonite at the bottom; pointwise water injection of 0.02 ml/h 153

Fig. 7.30 Almost breaking off of water fingers after contact with bentonite; water in bright grey, air in structured dark grey; inflow from the top, bentonite at the bottom; pointwise water injection of 0.1 ml/h 154

Fig. 7.31 Almost breaking off of water fingers after contact with bentonite; water in bright grey, air in structured dark grey; inflow from the top, bentonite at the bottom; pointwise water injection of 0.2 ml/h 155

Fig. 7.32 Breaking off of water fingers after contact with bentonite; water in bright grey, air in structured dark grey; inflow from the top, bentonite at the bottom; pointwise water injection of 0,1 ml/h, narrower but undeterminable aperture field 156

Fig. 8.1 Location (left), set-up of the PR (bottom right) and opening of the inner section (top right) of the PR; from /SKB 22/ 159

Fig. 8.2 Schematic drawing of a deposition hole with buffer and canister including standardized labelling of buffer rings and plates; rings 3, 5, and 7 marked for reference;after /VID 17/ 160

Fig. 8.3 Taking samples from deposition hole 3; sketch of deposition hole 1 during operation (top left), relation of sampling to the experiment (bottom left), position of samples in the buffer ring (bottom middle), lifting sample material in the ring (bottom right) 161

Fig. 8.4 Bentonite samples taken from deposition hole 1 161

Fig. 8.5 Storage of reference bentonite material for each buffer ring 162

Fig. 8.6 Number of still working sensors in the inner section; from /GOU 23/ 163

Fig. 8.7 Power consumption by heaters in DH1 (Top left), DH2 (top right) and DH4 (bottom); from /GOU 23/ 164

Fig. 8.8 Maximum temperature on the canister surface in DH1 (Top left), DH2 (top right) and DH4 (bottom); from /GOU 23/ 165

Fig. 8.9 Temperature sensor data for DH1 R5; from /GOU 09/ 166

Fig. 8.10 Radial temperature distribution for DH1 R5 at day 1200; from /GOU 06/ 166

Fig. 8.11 Evolution of maximum and minimum temperature as well as the temperature gradient for DH1 R5; from /GOU 09/ 167

Fig. 8.12 Evolution of the relative humidity in DH1 R5; from /GOU 09/ 168

Fig. 8.13 Post mortem data on water content, dry density and degree of saturation for the whole buffer in DH1; arrows indicate the position of ring 5; from /San 25/ 168

Fig. 8.14 Post mortem data on water content, dry density and degree of saturation for the whole buffer in DH4; arrows indicate the position of ring 7; from /San 25/ 169

Fig. 8.15 Post mortem data on water content, dry density and degree of saturation for the whole buffer in DH2; arrows indicate the position of ring 3; from /San 25/ 169

Fig. 8.16 Hysteresis loops for DH1 R5, in-situ and reference material 171

Fig. 8.17 Hysteresis loops for DH2 R3, in-situ and reference material 172

Fig. 8.18 Hysteresis loops for DH4 R7, in-situ and reference material 173

Fig. 8.19 Hysteresis loops for all three reference materials 173

Fig. 9.1 Results from a water uptake test at restricted water inflow in comparison with the results of the advanced VIPER-interface in COMSOL; from /KRÖ 25/ 177

Fig. 11.1 Conceptual model including boundary conditions, computational mesh, and observation points according to /WAL 14/ 188

Fig. 11.2 Coarse grid generated with ProMesh (blue: Neumann boundary condition representing the pumping well; red: Dirichlet boundary conditions representing inflow at the outer model boundary)..... 190

Fig. 11.3 Comparison of groundwater drawdown predicted by the analytical Theis solution, OpenGeoSys (OGS), and level-set approach of d³f++ 191

Fig. 11.4 Comparison of drawdown profiles predicted by the analytical Theis solution, OpenGeoSys (OGS), and the level-set approach of d³f++ at selected simulation times 192

Fig. 11.5 Comparison of groundwater drawdown predicted by Theis' solution and the storage term approach of d³f++ at a distance of 5 m from the pumping well 195

Fig. 11.6 Comparison of groundwater drawdown predicted by Theis' solution and storage approach of d³f++ at a distance of 15 m from the pumping well 196

Fig. 11.7 Comparison of groundwater drawdown predicted by Theis' solution and the storage term approach of d³f++ at a distance of 30 m from the pumping well 196

Fig. 11.8 Comparison of groundwater drawdown predicted by Theis' solution and the storage term approach of d³f++ at a distance of 50 m from the pumping well 197

Fig. 11.9 Hydrostructural model with 11 real fractures (grey) and 18 synthetic fractures (green), /DER 03/ 198

Fig. 11.10 Relevant fractures in C2 test (/DER 06/) 199

Fig. 11.11 Injection concentration of Re-186 and Ca-47 200

Fig. 11.12 Extraction concentration of Re-186 and Ca-47..... 200

Fig. 11.13 Geometry of the hydrostructural model with 29 fractures 201

Fig. 11.14 Hydraulic heads on the surface of the 200-m model block /SCH 16/ 203

Fig. 11.15 Pressure distribution on the model boundary (left); pressure distribution and flow field in the fractures (right). The arrows illustrate the flow direction in the fractures. 205

Fig. 11.16 Pressure distribution and the flow field on the relevant fractures for injection and extraction of water from point view of the injection well (left) and the extraction well (right). The arrows show the flow direction in the fractures 205

Fig. 11.17 Concentration of Tracer Re-186 and flow field in the relevant fractures at time of 200 hours 206

Fig. 11.18 Comparison of Breakthrough curve of Re-186 at the extraction point from simulation and experiment without calibration 207

Fig. 11.19 Comparison of Breakthrough curve of Ca-47 at the extraction point from simulation and the experiment without calibration 207

Fig. 11.22 Comparison of Breakthrough curve of Re-186 at the extraction point after optimization..... 209

Fig. 11.23 Comparison of Breakthrough curve of Ca-47 at the extraction point after optimization..... 211

Fig. 11.24 Manufacture of the artificial fracture by splitting a granite block (left) and setting up the experiment in the UJV laboratory (right), /JAN 19/ 212

Fig. 11.25 General concept of considered mobile and immobile phases and interactions between them according to /NOS 16/..... 214

Fig. 11.24 Complete 3d geometric model (left; coarse grid) and fracture (right; fine grid)..... 217

Fig. 11.27 Model calibration, based on the conservative tracer experiment of 2019 218

Fig. 11.26 Simulated tracer concentration in fracture and matrix after 600 s 219

Fig. 11.27 Simulated concentration distribution of a non-sorbing tracer under the conditions of the block experiment performed by UJV on 10 October 2019 219

Fig. 11.30 Travel time predictions with an inflow rate of 0.2 ml/min and varying distribution coefficients 220

Fig. 11.31 Simulated concentration distribution of a sorbing tracer under the conditions of the block experiment with one outlet 220

Fig. 11.32 Simulated breakthrough curves of a non sorbing tracer and measured breakthrough curves of iodide and uranium 222

Fig. 11.33 Simulated breakthrough curves for a non sorbing tracer and a tracer with Kd=0.001 m³/kg and measured breakthrough curves of all injected tracers 223

List of tables

Tab. 5.1 Sample characteristics after /KAU 12/ and /KAU 13/ 98

Tab. 5.2 Assessment scheme for the fit of predicted and measured isotherm. ... 100

Tab. 5.3 Assessment of the fits of predicted and measured isotherms. 102

Tab. 7.1 Post-processing conditions of the test cubes; colours according to Fig. 7.6 127

Tab. 8.1 Summary of findings for DH1, DH2, and DH4. 170

Tab. 11.1 Benchmark parameters for the Theis solution according to /WAL 14/ .. 189

Tab. 11.2 Approximation of function $W(u)$ 194

Tab. 11.3 Benchmark parameters for Theis' solution and for Richard's equation approach in d³f++ 194

Tab. 11.4 Hydraulic properties of deterministic fractures /SCH 16/ 202

Tab. 11.5 Porosity and permeability of equivalent continuum as result of model calibration for transport of inert tracer Re-186 209

Tab. 11.6 Kd-value of equivalent continuum for the transport of Ca-47 as result of model calibration 210

Tab. 11.7 Results from predictive calculations of the break-through curves for the layout of the block experiment /JAN 23/ 221

Tab. 11.8 Nuclide concentration in the injected fluid 222

Tab. 11.9 Model system parameters for flow and transport 225

Tab. 11.10 Parameters for interaction of radionuclides, colloids and matrix 226

A Appendix: Equations of the quantities of interest for Topic 4

As pointed out in sections 6.1 and 6.2, the individual discs were weighed before and after drying. The difference provides the amount of hydrated water m_w while the dry mass of the bentonite sample m_s was directly measured. From these two quantities, the water content w can be calculated:

$$w = \frac{m_w}{m_s} \tag{A.1}$$

The volume V of a cylindrical sample is determined from the disc's height h and the cross-sectional area A. Area A is calculated from the diameter of the cylindrical sample while the height involves a sensitive measurement. The latter can strongly influence all quantities that depend directly or indirectly on the volume V:

$$V = \mathrm{h} \cdot \mathrm{A} \tag{A.2}$$

The bulk dry density ρ_d is determined from the ratio of disc dry mass and the disc volume:

$$\rho_d = \frac{m_s}{V} \tag{A.3}$$

Next, the theoretical maximum water content w_{max} is determined as input for the degree of saturation. Equation (A.4) requires three density values: the density of the water in the bentonite ρ_w, the bulk dry density ρ_d and the density of the dry minerals in the bentonite ρ_s:

$$w_{max} = \rho_w \left(\frac{1}{\rho_d} - \frac{1}{\rho_s}\right) \tag{A.4}$$

The degree of saturation S is then determined as it indicates the state of the bentonite:

$$S = \frac{w}{w_{max}} \tag{A.5}$$

The porosity Φ can eventually be determined by

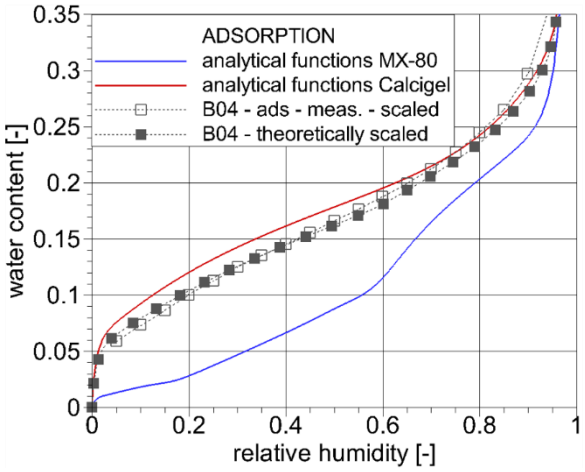
$$\Phi = 1 - \frac{\rho_d}{\rho_s} - w\frac{\rho_d}{\rho_w} \tag{A.6}$$

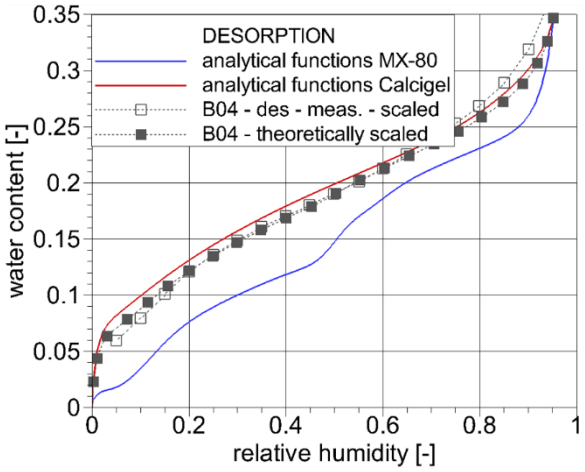
(All formulas presented in this section have been derived in /KRÖ 04/.)

B Appendix: Graphical comparison for Topic 3

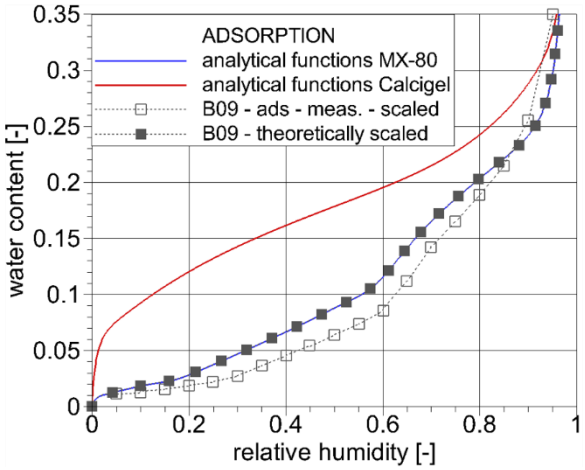
In the following, all 26 isotherms determined practically with the VSA as well as theoretically by scaling are graphically listed for the 13 bentonites in the same manner as for B31 in Fig. 5.8. Also the percentage of mono- and divalent interlayer cations as well as the analytical formulations for the isotherms from MX-80 and Calcigel are depicted for reference.

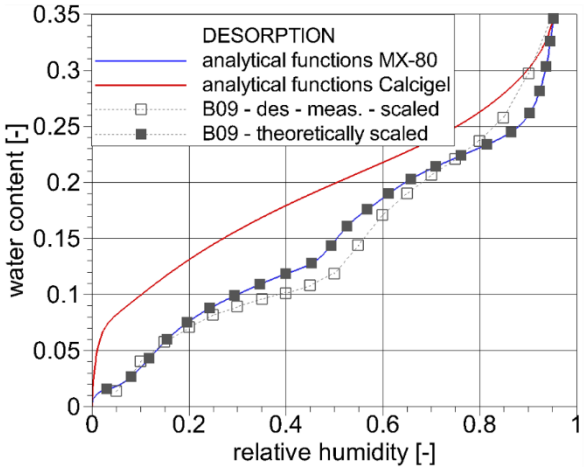
Bentonite B04 Na 18% Ca+Mg 82%



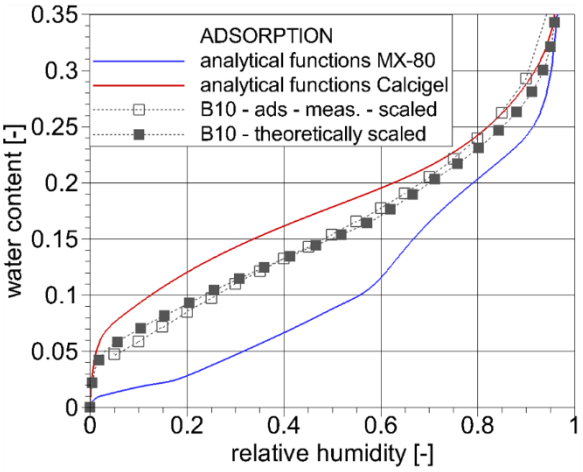


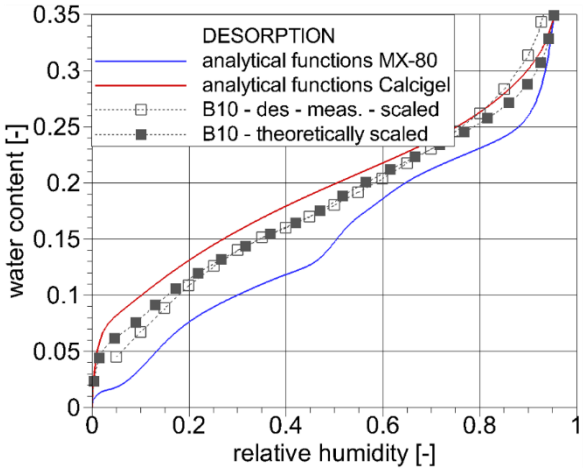
Bentonite B09 Na 100% Ca+Mg 0%



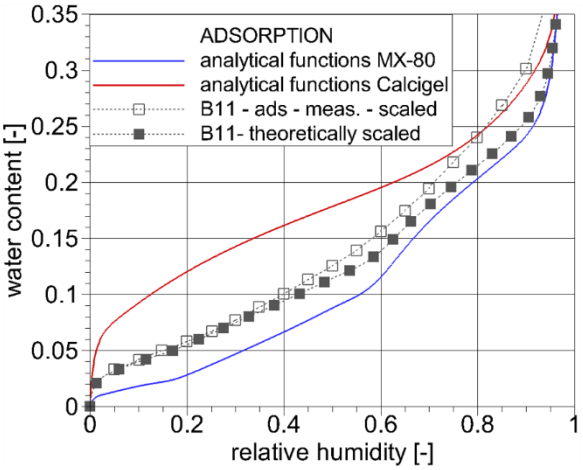


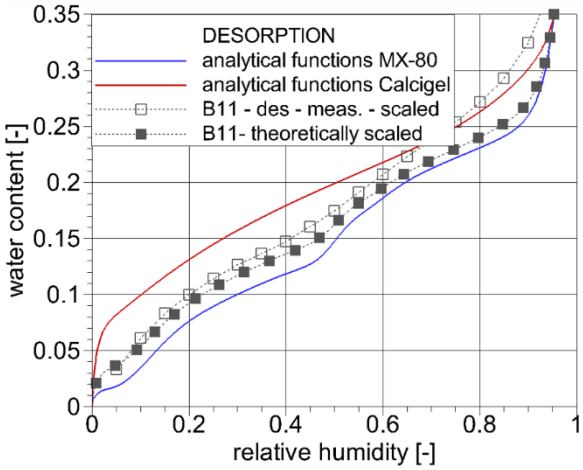
Bentonite B10 Na 31% Ca+Mg 69%



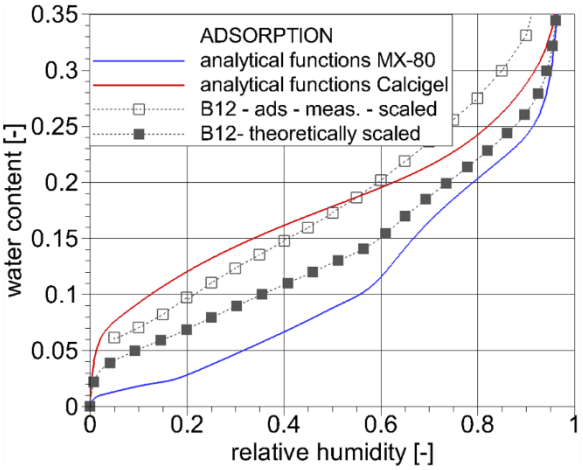


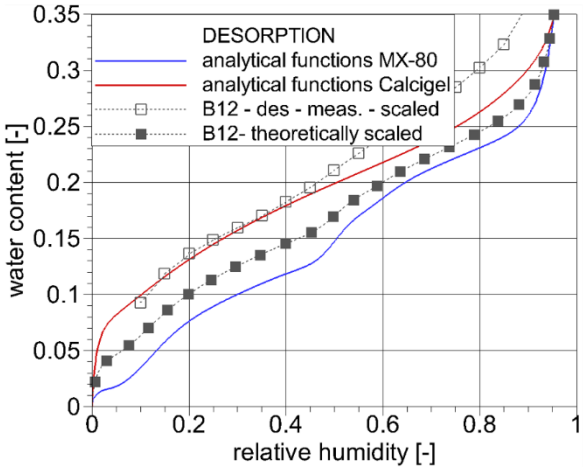
Bentonite B11 Na 71% Ca+Mg 29%



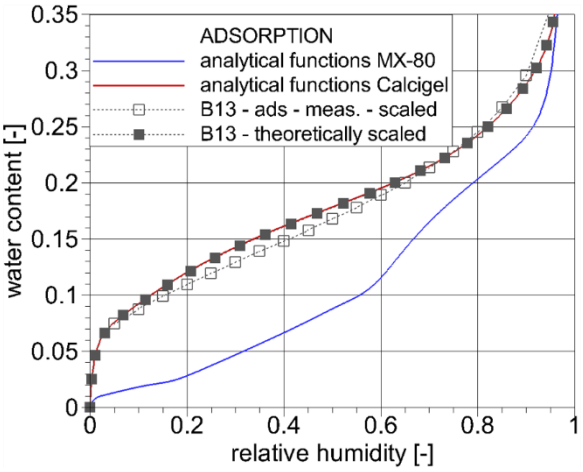


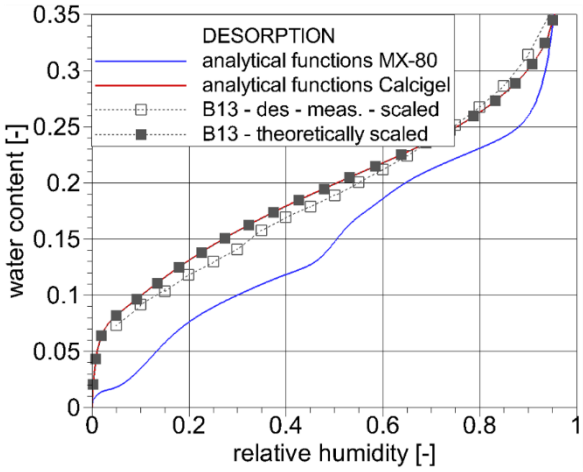
Bentonite B12 Na 56% Ca+Mg 44%



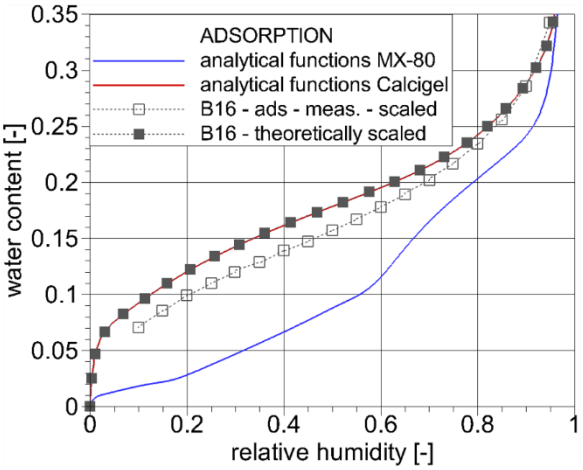


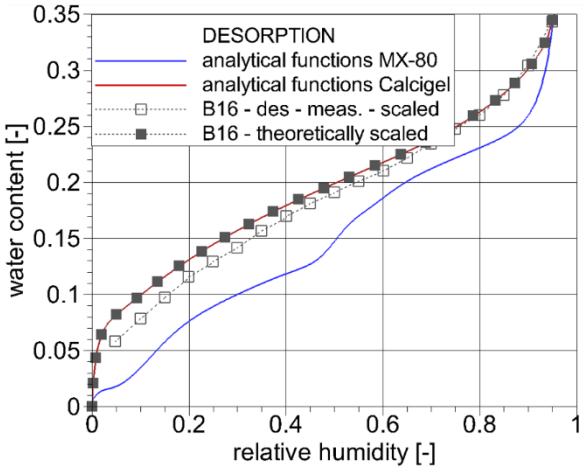
Bentonite B13 Na 1% Ca+Mg 99%



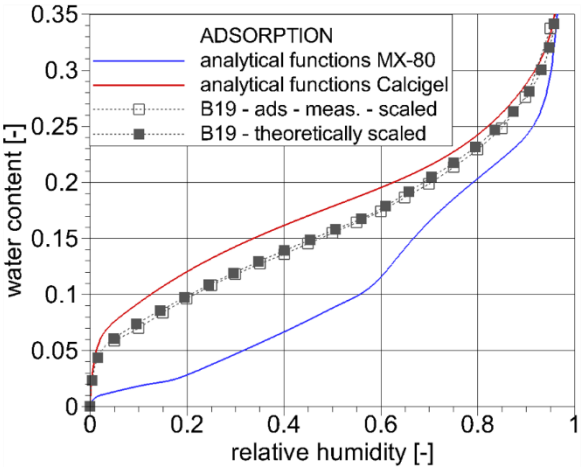


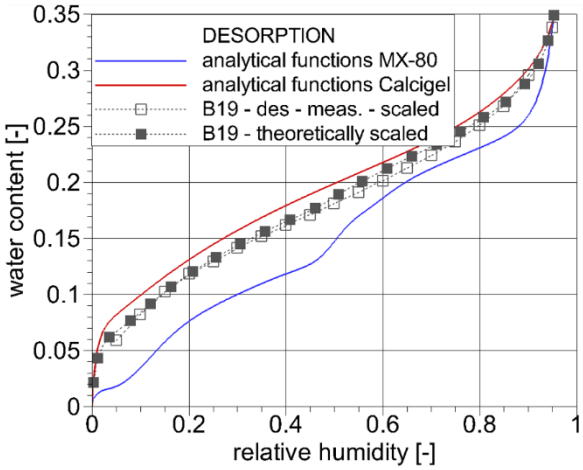
Bentonite B16 Na 0% Ca+Mg 100%



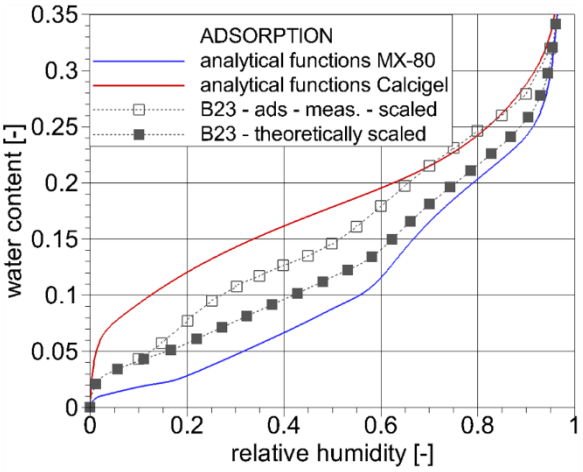


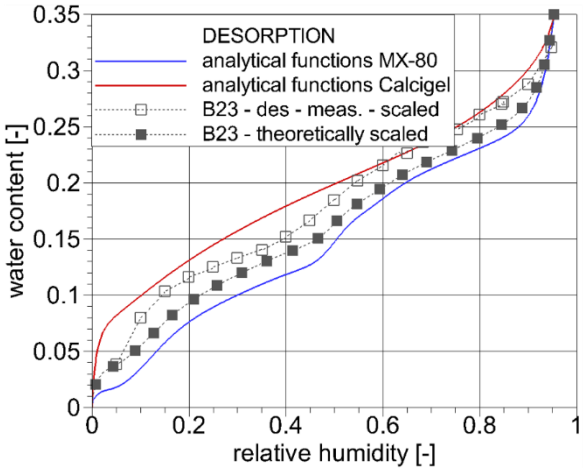
Bentonite B19 Na 24% Ca+Mg 76%



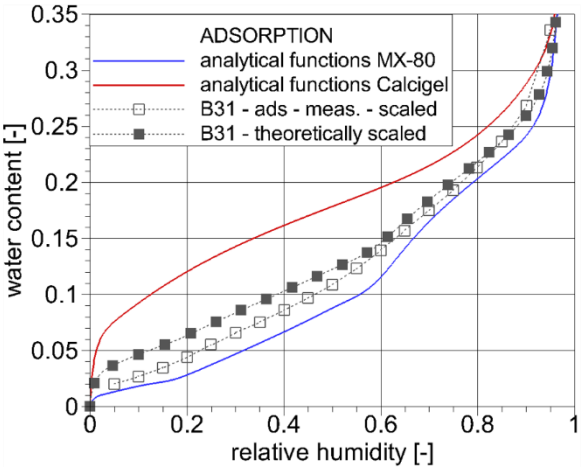


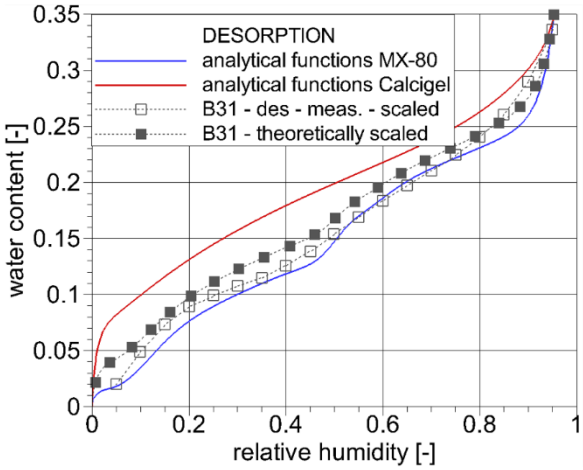
Bentonite B23 Na 69% Ca+Mg 31%



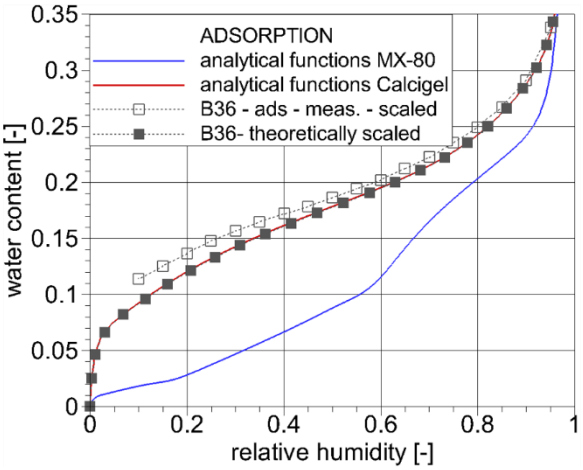


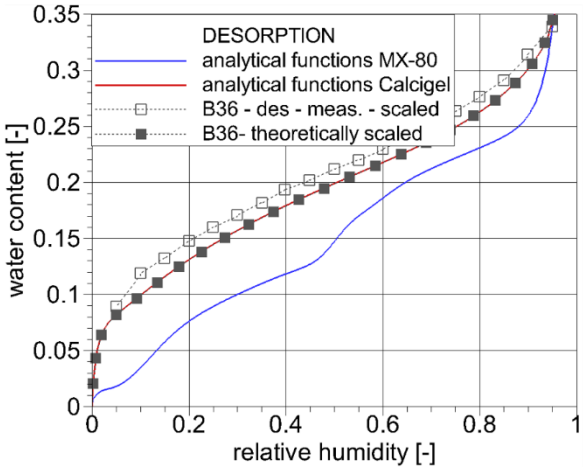
Bentonite B31 Na 62% Ca+Mg 38%



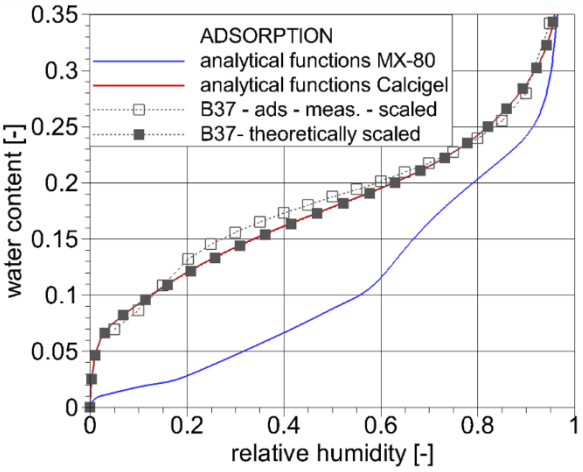


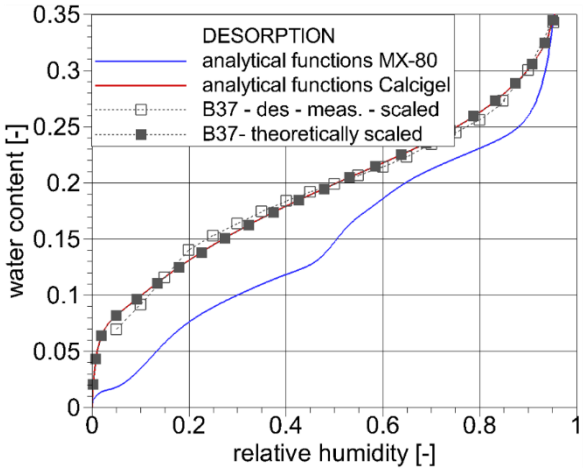
Bentonite B36 Na 1% Ca+Mg 99%



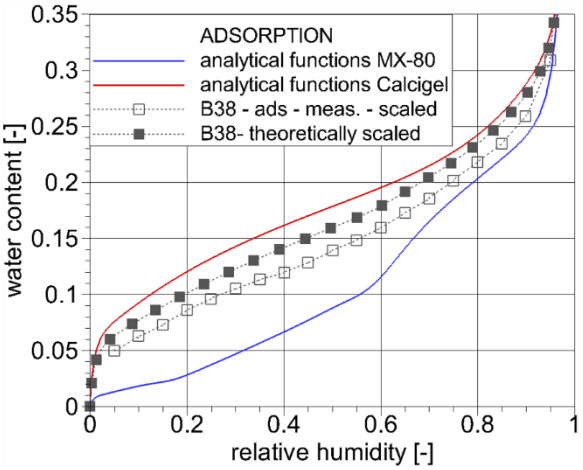


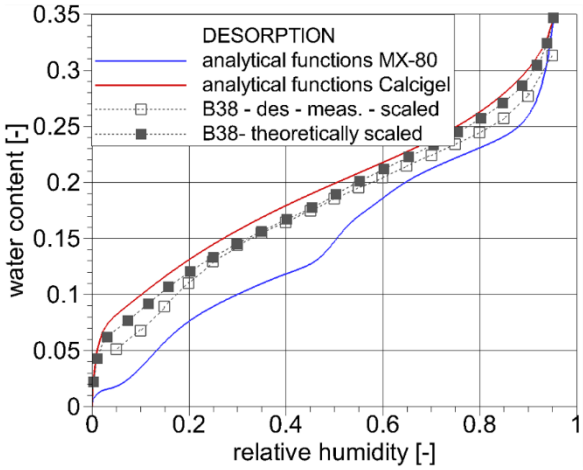
Bentonite B37 Na 1% Ca+Mg 99%





Bentonite B38 Na 21% Ca+Mg 79%





Gesellschaft für Anlagen- und Reaktorsicherheit (GRS) gGmbH

Schwertnergasse 1
50667 Köln
Telefon +49 221 2068-0
Telefax +49 221 2068-888

Boltzmannstraße 14
85748 Garching b. München
Telefon +49 89 32004-0
Telefax +49 89 32004-300

Kurfürstendamm 200
10719 Berlin
Telefon +49 30 88589-0
Telefax +49 30 88589-111

Theodor-Heuss-Straße 4
38122 Braunschweig
Telefon +49 531 8012-0
Telefax +49 531 8012-200

www.grs.de

ISBN 978-3-911727-47-1